RADIATION SHIELDING OF FUSION SYSTEMS

by

Andrew Davis

A thesis submitted to

The University of Birmingham

for the degree of

DOCTOR OF PHILOSOPHY

School of Physics and Astronomy

The University of Birmingham

April 2010.

Abstract

This thesis discusses the development, benchmarking and applications of activation dose analysis methods for fusion devices. The development and code logic of the Mesh Coupled Rigorous 2 Step (MCR2S) system is discussed. Following the development of the code, appropriate benchmarking studies were performed on the Frascati neutron generator, and revealed that the code was able to predict shutdown gamma ray dose rates to within $\pm 3\%$ of experimentally determined values, for decay times between 3×10^5 and 10^7 seconds.

The development of the Ion Cyclotron Resonance Heater (ICRH) with regards to neutronics is discussed. The ICRH went through a number of design stages and shutdown gamma ray doserates were determined for each stage. It was determined that of all the designs analysed only one of them, the first concept design for the internally matched design did not meet the shutdown dose criteria. This was due to a flaw in the system design, brought about by a lack of consideration towards nuclear design.

The ITER Light Imaging Detection and Ranging (LIDAR) system was subjected to a full shutdown nuclear analysis. It was found that the design of the LIDAR system supplied did not meet the ITER required shutdown gamma ray doserate limit of 100 μ Sv hr^{-1}, however use of the MCR2S system highlighted the components that contributed most to the shutdown gamma ray doserate and were shown to be the mirror holder and the laser beam pipe. Future designs should include additional shielding around the beam pipe.

Authors Contribution

The author of this thesis designed and wrote a computer program called MCR2S, based on the Rigorous 2 Step (R2S) method, that couples the radiation transport program MCNP to the nuclear inventory code FISPACT that facilitates high resolution activation analysis. The technical aspects of this code are described in Chapter 4. Fusion appropriate benchmarking was performed to validate the code for fusion neutronics calculations in two cases, one idealised case to compare MCR2S against a different code that performs similar analysis and one case from a well defined fusion neutronics experiment. The simulations performed and results of the benchmarking studies are described in Chapter 5.

The author performed nuclear analysis, including neutron and photon transport, nuclear heating and activation calculations on a number of Ion Cyclotron Resonance Heating (ICRH) designs for ITER. This involved creation of the MCNP model from CAD drawings and the subsequent use of MCNP and FISPACT to perform the analysis. The method used and results of the simulations performed are described in Chapter 6. A shutdown dose analysis was performed on the ITER Laser Imaging Detection and Ranging (LIDAR) system. The model was created by S Zheng, but the author performed neutron transport and MCR2S analysis. The results of the simulations performed are described in Chapter 6.

The author was fortunate enough to present the results of ICRH analysis as a poster presentation at the TOFE meeting in San Francisco, the results of ICRH and LIDAR analysis at the IAEA meeting on Fusion Safety. The second case resulted in a collaborative publication in the proceedings of the meeting. The results of the benchmarking of MCR2S were published in the peer reviewed journal Fusion Engineering and Design with the reference Fus. Eng. and Des., vol. 85, no. 1, pp. 8792, 2010.

"Adam, the first man, didn't know anything about the nucleus but Dr. George Gamow, visiting professor from George Washington University, pretends he does. He says for example that the nucleus is 0.00000000000003 feet in diameter. Nobody believes it, but that doesn't make any difference to him. He also says that the nuclear energy contained in a pound of lithium is enough to run the United States Navy for a period of three years. But to get this energy you would have to heat a mixture of lithium and hydrogen up to 50,000,000 degrees Fahrenheit. If one has a little stove of this temperature installed at Stanford, it would burn everything alive within a radius of 10,000 miles and broil all the fish in the Pacific Ocean. If you could go as fast as nuclear particles generally do, it wouldn't take you more than one ten-thousandth of a second to go to Miller's where you could meet Gamow and get more details."

-George Gamow

'Gamow interviews Gamow' Stanford Daily, 25 Jun 1936. In Helge Kragh, Cosmology and Controversy: The Historical Development of Two Theories of the Universe (1996), 90.

The author would like to extend his sincerest gratitude to; Thankyou to both of my supervisors, Drs Pampin and Norman, for without whom this thesis would not have been possible. To Dr R Pampin, at the Neutronic and Nuclear Data section of the Culham Centre for Fusion Energy, whose help, support and understanding have been invaluable. To Dr P I Norman, at the University of Birmingham, School of Physics and Astronomy, for giving me the opportunity to follow my dream. And to Dr M J Loughlin, now at ITER, for giving me a good start. To my colleagues at CCFE, all of whom have understood my lack of understanding; especially Dr D Ward, Dr R Forrest, Dr S Newton, Dr S Zheng and Mr L Packer. I also have to thank Mrs W Coombes and Ms K Samson, for without whom I doubt this thesis would have been completed.

I would also like to thank my family, friends and peers for the experiences of the past few years. And to my best friend and partner Jenny, who has been wonderful and understanding throughout.

This work was funded by the United Kingdom Engineering and Physical Sciences Research Council

Contents

List of Figures

List of Tables

List of commonly used abreviations

ASG - Activation Source Generator
CAD - Computer Aided Design
CTF - Component Test Facility
DPA - Displacements Per Atom
ECH - Electron Cyclotron Heating
ECRH - Electron Cylotron Resonance Heating
EMO - Externally Matched Option
JET - Joint European Torus
ICH - Ion Cyclotron Heating
ICRH - Ion Cyclotron Resonance Heating
IMO - Internally Matched Option
IFMIF - International Fusion Materials Irradiation Facility
ITER - International Thermonuclear Experimental Reactor
LIDAR - Light Imaging Detection And Ranging
MB - Mega Byte
MCNP - Monte Carlo N Particle
MPI - Message Passing Interface
NBI - Neutral Beam Injection
PKA - Primary Knock-on Atom
PP - Port Plug
RF - Radio Frequency
R2S - Rigorous 2 Step
TBR - Tritium Breeding Ratio
TS - Tompson Scattering
WWM - Weight Window Mesh

Chapter 1

INTRODUCTION

The ultimate goal of fusion research is to gain sufficient engineering and scientific knowledge to ensure fusion power as a credible, inexhaustible supply of energy for the future. Our current understanding is that magnetically confined fusion is the most promising method of achieving a fusion power plant.

Fusion is in an ideal position to replace coal, oil and gas fired power plants around the world. Fusion has no carbon footprint, except that carbon which is produced during construction and manufacture of the plant. The fuels of fusion, deuterium and tritium are abundant in nature or can be manufactured with little cost. The isotope deuterium occurs naturally and can be found in sea water in abundance. However, tritium does not exist in abundance in nature; it is a β^- emitter with a 12.3 year half life, it is 'bred' using lithium inside a fusion plant.

1.1 Nuclear Fusion

Thermonuclear fusion is the process by which two low atomic number elements are combined, or fused, to form a single higher atomic number nuclide. Fusion requires the particles to be close enough for the attractive short ranged strong nuclear force

to interact between the nuclei.

There are a number of fusion reactions that can be utilised for terrestrial applications. Deuterium is naturally occurring on earth and can be readily extracted from sea water where it appears in the ratio $\sim$ 1:6500. There are two possible reaction pathways for deuterium-deuterium (D-D) fusion;

$$^{2}\mathrm{H} + {}^{2}\mathrm{H} \rightarrow {}^{3}\mathrm{He} + \mathrm{n} + 3.2 \text{ MeV}$$

$$^{2}\mathrm{H} + {}^{2}\mathrm{H} \rightarrow {}^{3}\mathrm{H} + {}^{1}\mathrm{H} + 4.1 \text{ MeV}$$

Concerning D-D reactions there are issues extracting the Q-value of the reaction in a useful manner, since 4.0 MeV is given to the triton and proton, and 3.2 MeV is shared among the ^{3}He and a neutron, thus the neutron from DD fusion will have a kinetic energy of $\sim$ 2.4 MeV. The triton and proton are charged and will loose energy rapidly inside the plasma via Coulomb collisions.

The D-T reaction has a larger cross section than the D-D reaction and hence is more feasible for near term fusion power plants. It is clear from Figure 1.1 that the cross section for D-T fusion is at least 2 orders of magnitude larger than that for D-D fusion, except at impractibly large energies. The D-T reaction is;

$$^{2}\mathrm{H} + {}^{3}\mathrm{H} \rightarrow {}^{4}\mathrm{He} + \mathrm{n} + 17.6 \text{ MeV}$$

D-T fusion is the preferred reaction for a fusion power plant because of the larger Q-value and the larger cross section for the reaction. The kinetic energy of D-T neutrons is 14.1 MeV compared to 2 MeV for the average fission neutron kinetic energy.

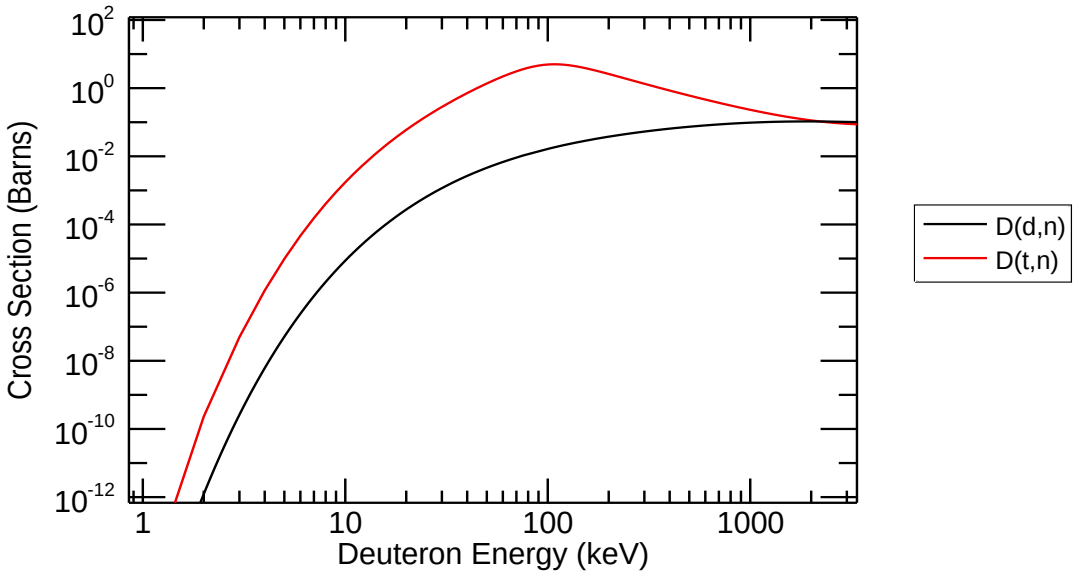

Figure 1.1: Cross section for D-D and D-T fusion

Tritium does not occur in large abundances naturally, it is a β-emitter with a 12.3 year half life. It has to be produced as part of the fusion fuel cycle. The process of creating tritium is known as tritium breeding, the following reactions describe the breeding process;

$$\mathrm{n} + {}^{6}\mathrm{Li} \rightarrow {}^{3}\mathrm{H} + {}^{4}\mathrm{He}$$

$$\mathrm{n} + {}^{7}\mathrm{Li} \rightarrow {}^{3}\mathrm{H} + {}^{4}\mathrm{He} + \mathrm{n}$$

With the exception of the neutron, all reaction products are charged, hence the kinetic energy of products is deposited within a very small distance from the site of the reaction, typically a few μm. There is of course the possiblilty that the neutron produced will react with the lithium atom.

Although the cross section of D-T fusion is higher than that of D-D fusion, high energies, and hence temperatures are required due to the Coulomb repulsion of the two ions. If we consider fusion to be attained by the thermal movement of nuclei,

then enough energy must be supplied to the reactants so that they can penetrate the Coulomb potential that exists between the reactants. Hence there is a need for heating a mechanism that increases the kinetic energy of reactants.

If we consider supplying kinetic energy to the reactants in the form of heat to overcome the Coulomb barrier, then a simple thermal argument can be considered

$$\frac{3}{2}kT = \frac{Z_1 Z_2 e^2}{4\pi\epsilon_0(R_0 A_1^{\frac{1}{3}} + R_0 A_2^{\frac{1}{3}})} \tag{1.1}$$

where A_i is the atomic mass of the ith reactant, R_0 is 1.22 fermi, Z_i is the charge of the ith reactant measured in electronic charges, ϵ_0 is the permittivity of free space 8.8542×10^{-12} F m^{-1}, k is the Boltzmann constant 1.3807×10^{-23} J K^{-1} and e is electronic charge 1.609×10^{-19} Coulombs.

If a deuteron and a triton are considered, then equation 1.1 results in a temperature in excess of 100 million K. This is higher than the temperature required to cause protons to fuse in the sun, which occurs at a temperature of around 20 million K. This is a classical interpretation of the physics, in actuality quantum tunnelling of the reactants is possible, and so fusion can occur at lower temperatures. When materials are heated to such high temperatures, atoms become totally ionised, and when confined in some potential well, the ion and electrons have too much kinetic energy to recombine and hence exist in the potential as a plasma of separated charges.

1.2 Physics of Plasmas

As described in the previous section, a plasma is a collection of seperated energetic ions and electrons, this plasma is globally electrally neutral because for every atom fully ionised the negative charge from the atom is evolved.

1.2.1 Confinement of Plasmas

If this plasma is placed in some isolating container then some of the kinetic energy of the plasma will be lost by collisions with the walls of the container. If we wish for the plasma to remain hot then we must insulate the plasma, or stop collisions with the walls of the container. There are a number of methods for the confinement of a plasma such as material, gravitational, electrostatic, inertial and magnetic. Due to the scope of this thesis, only magnetic confinement will be discussed.

Consider a constant magnetic field which extends to infinity along a single direction, then the force, F, upon a charged particle in the magnetic field is described by

$$F = m\frac{d\underline{v}}{dt} = q(\underline{v} \times \underline{B}) \tag{1.2}$$

where $\underline{v}$ is the velocity vector in m s^{-1}, $\underline{B}$ is the magnetic field in T and m is the mass of the particle in kg.

This implies that given an initial velocity for charged particles, their direction will be either parallel or anti-parallel to the magnetic field and will spiral about them with a radius of gyromotion r_g, of [2];

$$r_g \propto \frac{1}{|\underline{B}|} \tag{1.3}$$

This is shown qualitively in Figure 1.2. If this uniform magnetic field is bent around on its self forming a closed loop, then this particle will spiral around these toroidal field lines and remain confined. Scattering reactions may occur and when they do cause the particles to skip to adjacent field lines or break confinement entirely. However, a uniform magnetic field is far from what is found in a tokamak. To produce the magnetic field in a tokamak, coils are wrapped around the torus and

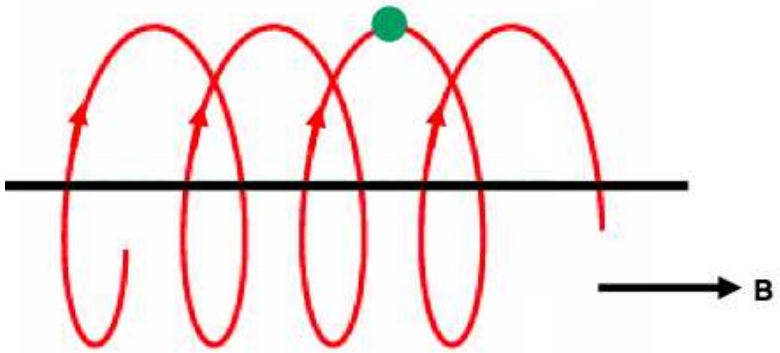

Figure 1.2: Charged particle confined to a magnetic field line

a current passed through them. A complication arises due to the placing of coils around the tokamak, which result in coils being placed closer together on the inboard (at the central axis of a torus) side of the tokamak than the outboard (outside surface) side. The placement of these coils results in a magnetic field configuration where the magnetic field strength varies inversely with the radial position within the device, hence a gradient in the magnetic field exists, which drives the postive ions in one direction and the electrons in another. This results in charge separation and hence generating a vertical electric field. This electric field causes further ion and electron drift towards the outboard, increasing the rate of loss of energy and particles.

1.2.2 Production of neutrons by plasmas

When the plasma is maintained at a high enough temperature and the particles are confined for sufficient time, some ions will eventually fuse. The ions are far more likely to coulomb scatter with other ions in the plasma and move radially outwards from the centre of the plasma. The distribution of ion energies in a thermonuclear plasma is governed by Maxwellian statistics, the number of particles at a given

energy is dictated by the temperature of the mixture

$$N(E) = \frac{2}{\sqrt{\pi}}(\frac{1}{kT})^{\frac{3}{2}} E^{\frac{1}{2}} e^{\frac{-E}{kT}} \tag{1.4}$$

where N(E) is the distribution of particle energies, k is Boltzmann's constant 1.3806×10^{-23} J K^{-1} and T is the temperature of the mixture in K.

Fusion neutrons from a D-T plasma are created with an average energy of 14.1 MeV. The constituent ions of the plasma are moving with an average ion temperature of T_i keV. The ion temperature distribution is a Maxwell-Boltzmann distribution. Hence there is a distribution of ion velocities, which smears out the pure delta function 14.1 MeV peak that would otherwise be seen if we could combine the reactants at rest. The energy spectrum of D-T fusion neutrons is approximately described by a Gaussian distribution with a full width half maximum (FWHM) [3];

$$\text{FWHM} = 2\sqrt{\ln 2}\sqrt{\frac{4mE_0kT}{m_1+m_2}} \tag{1.5}$$

where m_1 is the mass of ion 1 in kg, m_2 is the mass of ion 2 in kg, m is the mass of the neutron in kg, k is Boltzmanns constant 1.3806×10^{-23} J K^{-1}, T is the temperature of the particles in K, E_0 is the energy of the neutron produced in keV and T_i is the ion temperature in keV and FWHM is the full width half maximum of the distribution in keV.

1.3 Magnetically Confined Fusion

Tokamaks

The fusion devices world wide with the largest confinement times are the generation of devices known as tokamaks. The word "tokamak" is contraction of the Russian

"toroidal'naya kamera v magnitnykh katushkakh" or toroidal chamber with magnetic coils. There are a number of essential components to a tokamak, namely the toroidal field coils, the poloidal field coils, central solenoid and vacuum vessel, which are shown in Figure 1.3. A critical structure not shown in Figure 1.3 is the divertor, but is discussed later. The plasma torus acts like the secondary winding of a trans-

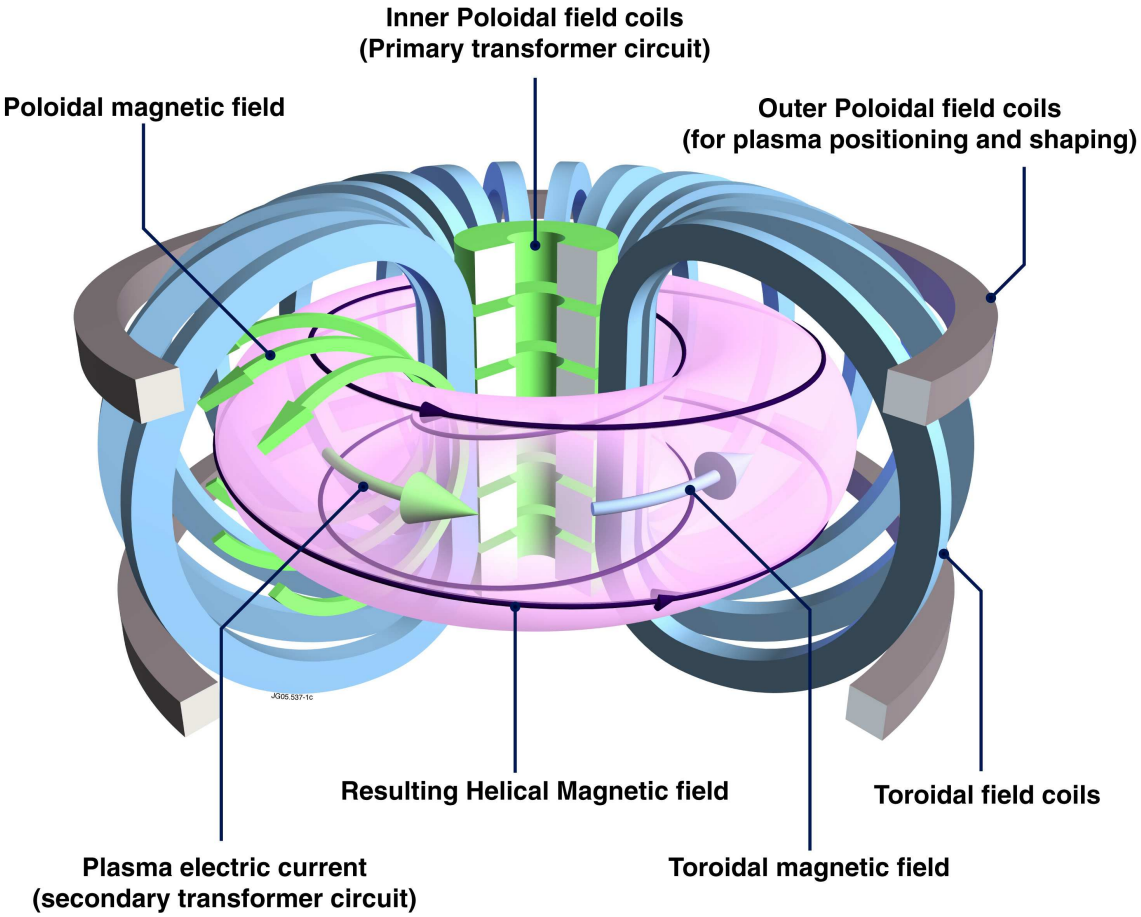

Figure 1.3: The magnet structure in a tokamak (EFDA-JET)

former. A current flow in the primary winding induces a current in the plasma. The plasma current that is induced, generates ohmic heating and also generates a further magnetic field in the poloidal direction. Furthermore, the toroidal magnetic field coils generate a tordoial field. The combination of poloidal and toroidal magnetic fields act to confine the plasma to a toroidal shape. There is an additional set of

coils, known as the poloidal field coils, the field they produce acts as a restraint to the ring of plasma which has a natural tendancy to expand, and are also used for shaping the plasma.

Stellarators

Stellarators were a concept developed around the same time as the first tokamaks, they are somewhat similar to tokamaks except with a few key differences. Stellerators do not rely on an externally induced plasma current. The helical field lines required for confinement are produced via a set of twisted coils, like those shown in Figure 1.4.

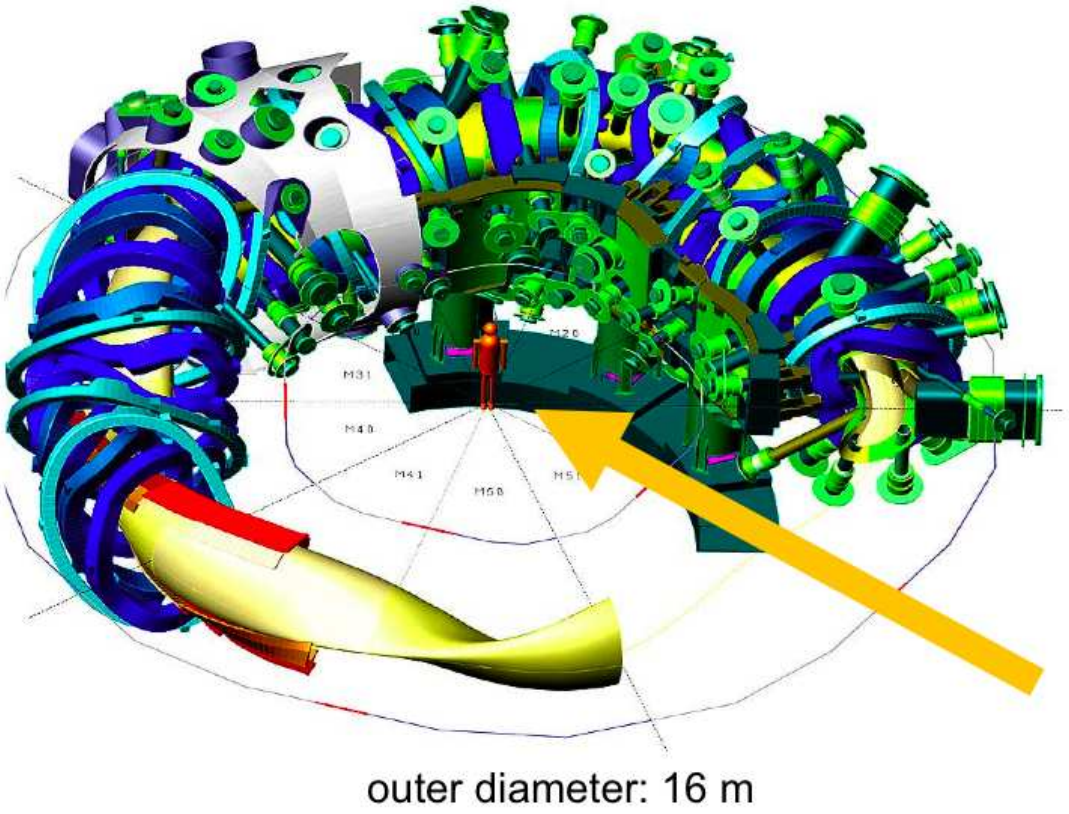

Figure 1.4: 3-D CAD rendering of the W7-X Stellarator [4]

1.4 Inertially Confined Fusion

Inertially Confined Fusion (ICF) has been considered as a possible alternative route to fusion power, examples of planned facilities are NIF [5], LMJ [6] and HiPER [7]. ICF is a different technological route to fusion energy, a frozen pellet of D-T is injected into the centre of a typically spherical vacuum vessel. A high power laser or particle beam is then shone upon the pellet from all directions, in order to produce an isotropic homogenous irradiation. This then causes the outer layers of the pellet to ablate into the pellet and increase the pressure on the internals of the pellet. Ultimately each layer of the pellet implodes and increases the pressure and temperature of the fusion fuel at the centre of the pellet. Eventually the pressure and hence density and temperature are high enough for fusion to occur. The challenges to ICF are similar to those of a standard power tokamak, however due to the frequent pulsing required to make an ICF device economically viable, will result in higher metal fatigue in ICF devices.

1.5 ITER

After the Joint European Torus (JET) tokamak was designed and construction had begun, the fusion community around the world began studies of a larger reactor, capable of sustaining a burning plasma and producing 1 GW of fusion power. This tokamak was called the International Thermonuclear Experimental Reactor (ITER). It was so much larger than previous designs, the cost would need to be spread across many countries. In 1988 the first ITER agreement was signed, marking the beginning of the ITER program. As progress was made finalising the design, it was determined that the fusion power should be made lower $\sim$ 500 MW, hence the reactor could be made smaller. The key parameters that define the performance of ITER are shown in the Appendix A Table A.1.

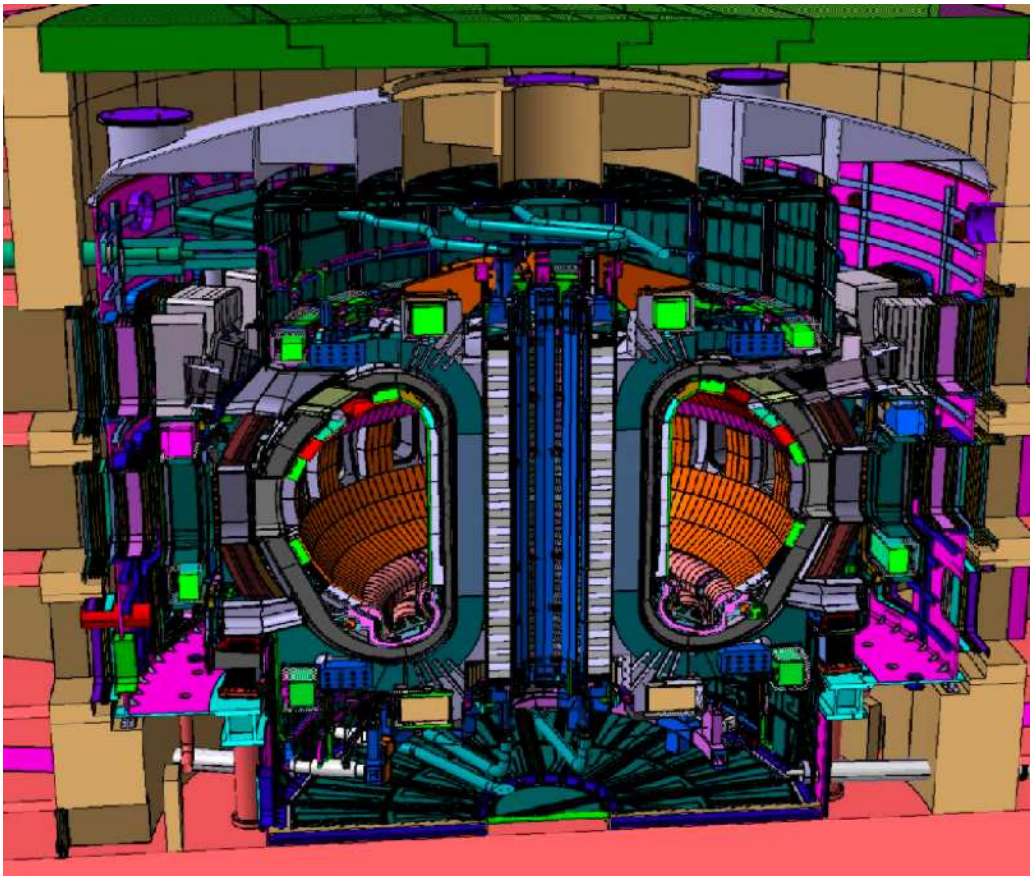

Figure 1.5: 3-D CAD rendering of ITER [8]

1.5.1 Geometry of ITER

The geometry of ITER shown in Figure 1.5, shares some similarities with JET as in that ITER is a conventional geometry tokamak. The plasma assumes a "D" shape when confined by the magnets.

1.5.2 Upper, Equatorial and Divertor Ports

The vacuum vessel is penetrated in a number of places by maintenaince ports, either at the upper, equatorial or divertor level. The ports are shown in Figure 1.6 and examples of the plugs that close them are shown in Figure 1.7. The divertor

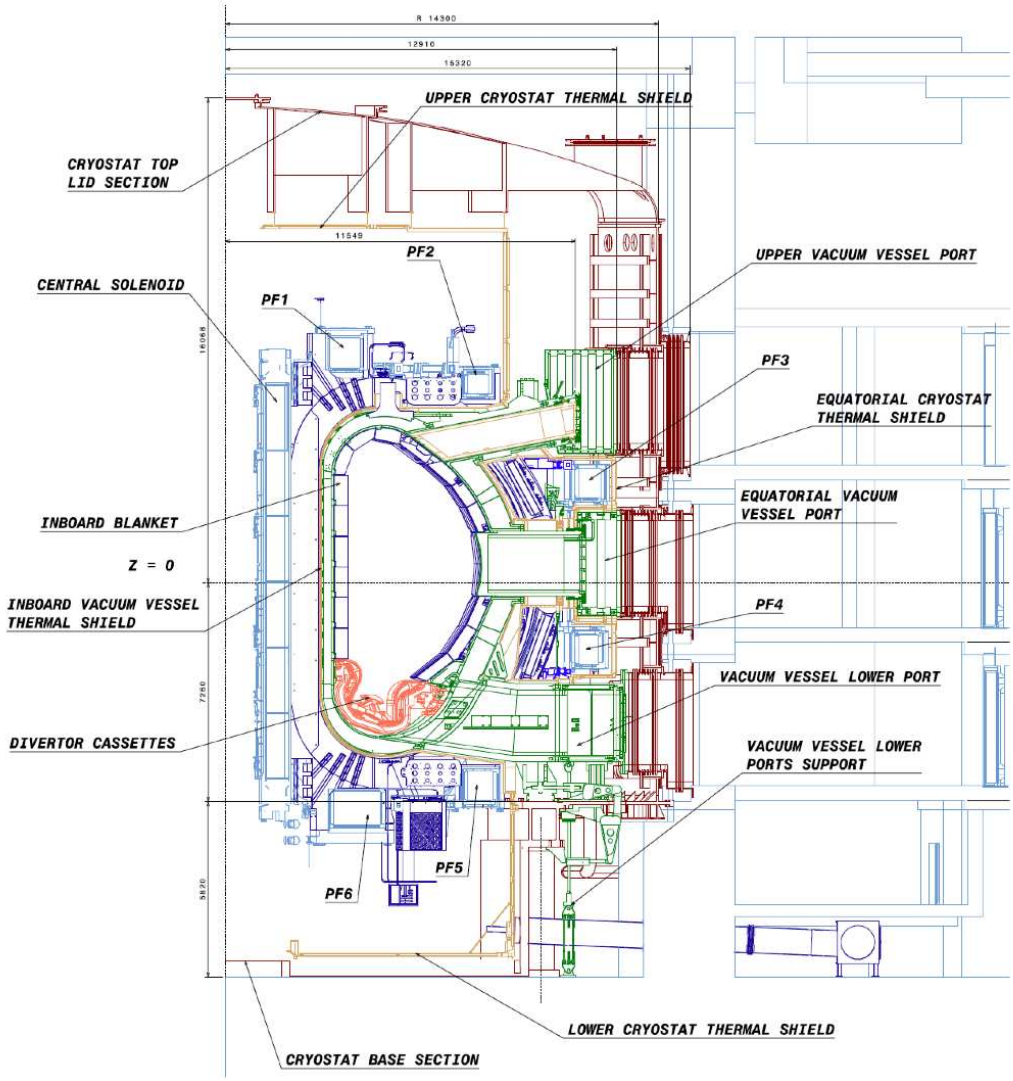

Figure 1.6: Cross section of ITER [9]

ports allow access to the divertor region of the device, and are large enough to allow the removal and replacement of divertor casettes. The equatorial ports lie around the equatorial mid-plane of the device. These ports typically contain equipment for the heating and diagnostic systems of the plasma. The upper port systems contain mostly diagnostic systems however the Electron Cyclotron Resonance Heater (ECRH) and Lower Hybrid Current Drive (LHCD) system also lie in the upper ports. In this thesis the nuclear analysis performed is concentrated on the equato-

rial port system, so more detail will be given to these.

The equatorial ports are centred at the equator of the vacuum vessel and are all a standard size. An equatorial port plug is 3.5 m in length, 1.7 m wide and 2.1 m high. Port plugs must stem the flow of neutrons through them so that the shutdown gamma ray dose after 14 days is less than 100 μSv hr^{-1} behind the plug, so that the port interspace area does not get excessively activated. The 100 μSv hr^{-1} after 14 days limit is an ITER requirement and is a voluntary target resulting from safety factor targets. In the majority of cases the front surfaces of the port plug match the surrounding geometry of blanket modules. The equatorial ports can contain a number of heating and diagnostic systems such as ICRH or LIDAR.

1.5.3 Heating Systems

Tokamaks require heating for a number of reasons;

- Particles are constantly escaping confinement, taking with them kinetic energy
- Tokamaks inherently rely on a circulating toroidal current to maintain stability, some of this current must be driven by heat injection
- Plasma instabilities arise during operation and must be controlled, these instabilities are often controlled with the injection of energy
- Orbiting charges emit radiation via Bremmstrahlung, reducing the temperature of the plasma
- Fuel is constantly being fed into the vacuum vessel and requires heating

There are two main methods for externally heating the plasma namely Neutral Beam Injection (NBI) and Radio Frequency (RF) heating. There is an additional heating

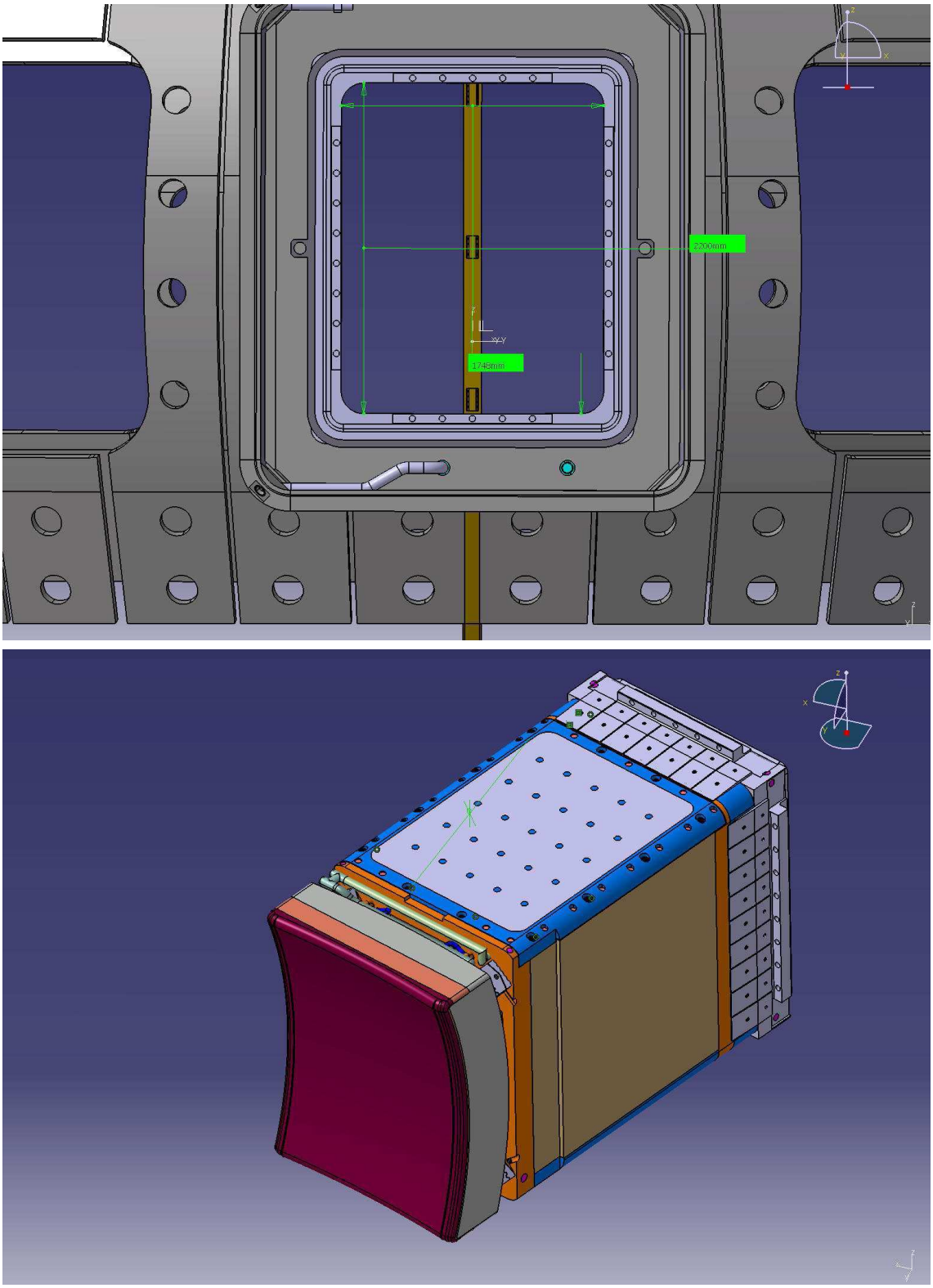

Figure 1.7: ITER equatorial ports and port plug [10]

	NB (1 MeV)	EC (170 GHz)	IC (50 MHz)	LH (5 GHz)
Power injected per unit equatorial port (MW)	16.5	20	20	20
Number of units for the first phase	2	1	1	0
Total power (MW) for the first phase	33	20	20	0

Table 1.1: ITER Heating [1]

method known as Ohmic heating within the plasma where the natural resistance of the plasma allows heating of the plasma up to a temperature of 1 keV.

Neutral Beam Injection

The Neutral Beam Injection (NBI) is a heating system with a dual purpose. A deuterium gas is injected into the beam unit, once the deuterium gas is into the beam unit, the deuterium atoms are ionised. The deuterium ions are then accelerated across an electric potential and then neutralised. Once neutralised they are unaffected by magnetic fields and travel along the beam duct. Once the deuterium atoms have entered the vacuum vessel they interact with the plasma transferring their kinetic energy and transferring momentum to the plasma. If the neutral beam is inclined at an oblique angle with respect to the plasma, the momentum transfer can cause the plasma to rotate faster in the toroidal direction.

Radio Frequency Heating

Ion Cyclotron Resonance Heating (ICRH) and Electron Cyclotron Resonance Heating (ECRH) uses MHz and GHz frequency EM radiation respectively to heat the plasma. The radio frequency (RF) radiation required is produced externally to the ICRH/ECRH system in RF sources, typically klystrons, situated in the RF power building. A diagram of the ICRH system for ITER is shown in Figure 1.8. The RF is propagated along waveguides or vacuum tranmission lines through the cryostat

and shielding up to the ICRH/ECRH system. A standing wave of voltage is setup along the length of the conductor and terminates in the antennae. The RF radiation propagates from the antenna into the plasma. The EM waves then interact with

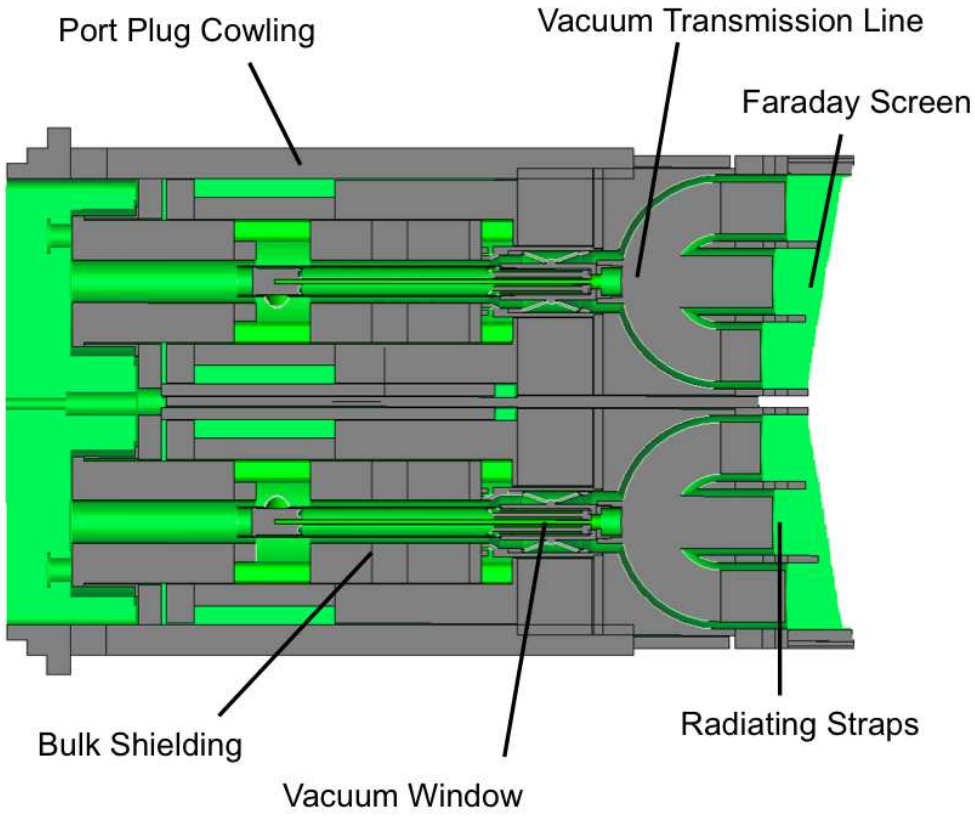

Figure 1.8: Diagram of the ITER ICRH system

the species, depending upon the frequency of the RF radiation it is either tuned to target electrons or ions. For deuterons and tritons, injecting RF with a frequency in the range of 30-120 MHz [11] will result in the greatest absorption. When the wave is absorbed the ions gyrofrequency, the frequency at which the particles orbit the magnetic field lines, is increased. These ions will go on to interact with other species in the plasma and thus overall the plasma energy is increased.

1.5.4 Magnets

In any tokamak the magnets are potentially the most important and expensive item. The magnets in older tokamaks like JET, ASDEX, MAST or TFTR are typically copper with a stainless steel jacket to provide strength against deformation. The issue with copper is that, although it is fairly conductive when passing tens of mega amps through them the heat deposition is significant. In JET the factor that limits

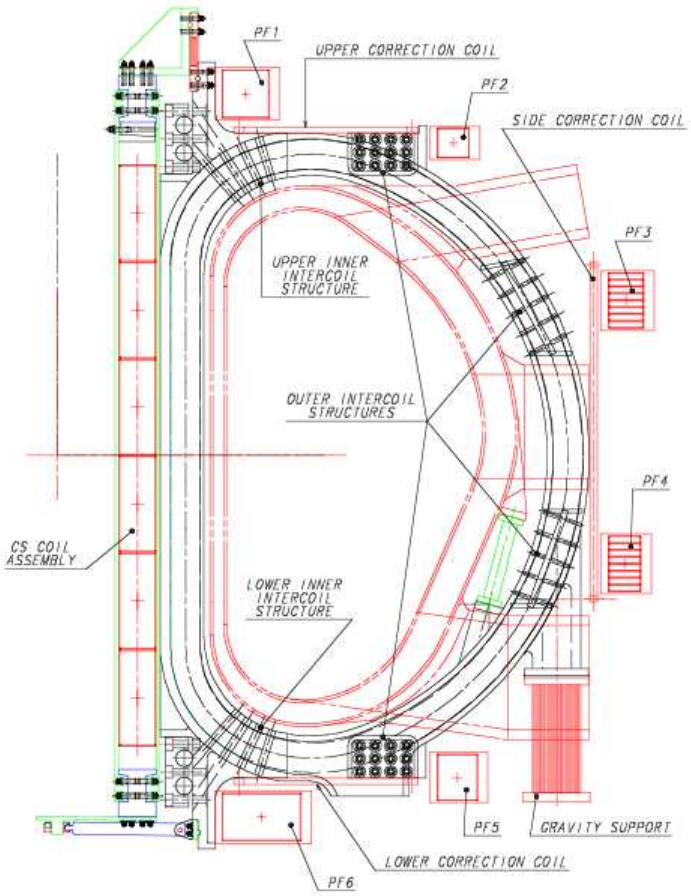

Figure 1.9: Location of the ITER PF coils [12]

the length of the plasma discharge is the temperature that the magnets reach when passing large amounts of current through the magnet system. To overcome this limitation ITER will use superconducting magnets cooled to 4.5 K, thus the current can flow nearly indefinitely. Due to the penetrating capability of neutrons, nuclear

heating must be minimised by placing as much shielding between the plasma and the magnets as possible. Space constraints arise however, because the magnets cannot be too far away from the plasma due to the $\propto 1/r$ decrease in magnetic field strength.

Poloidal Field Coils

The Poloidal Field (PF) coils, shown in Figure 1.9, are a set of toroidal coils that produce a magnetic field that is used to compress and shape the plasma and determines such parameters as the elongation and triangularity of the plasma.

The plasma shape is controlled by the currents distributed inside the six modules of the central solenoid (CS) and the six large PF coils placed outside the toroidal field coils. The magnetic configuration provided by these currents is such that the toroidal plasma current will experience a vertical force as soon as its centre is displaced vertically, and this force will increase with the displacement: the plasma with its elongated shape is in a vertically unstable equilibrium [12].

Toroidal Field Coils

The Toroidal Field (TF) coils are used to produce a toroidal magnetic field, current is passed around a coil with a poloidal geometry. If a toroid of these coils is constructed, then charged particles trapped by the magnetic field gyrate around the field lines along the length of the magnetic field. However, when particles undergo Coulomb scattering with other charged particles, they skip radially to another field line. Most particles will scatter many times before undergoing a successful fusion reaction, thus another field is needed which will provide some resistance to this radial diffusion.

The coils are packed into a strong stainless steel jacket, mainly to resist the toroidal

forces induced by interaction of the TF coil current with the transverse poloidal field from plasma and poloidal field coils. These local forces are pulsed, and therefore mechanical fatigue is a concern for the highly stressed structural steel of the coils [12].

Central Solenoid

The central solenoid of a tokamak is a further magnetic coil which via transformer action drives a toroidal plasma current. This plasma current not only heats the plasma, but also generates a further magnetic field. The sum of the toroidal field and the field from the central solenoid act to twist the total magnetic field structure which has the geometry of a toroidal helix.

1.5.5 Vacuum Vessel

The Vacuum Vessel (VV) of any tokamak acts to stop any ingress or egress of particles thus maintaining conditions required for the plasma. The VV must also act as a structural material maintaining its strength at high temperatures. The VV must also withstand any forces placed upon it by the plasma, such as those during plasma disruptions or by those created by halo currents [13].

1.5.6 Blanket

The role of the blanket modules is to shield the vacuum vessel from excessive neutron induced radiation damage, recover heat and also to breed tritium using lithium components within the blanket module.

In ITER, the inside of the vacuum vessel is covered with 440 stainless steel and water blanket shielding modules shown in Figure 1.10. The first wall is attached to the plasma facing side of the blanket module, the entire module is then bolted

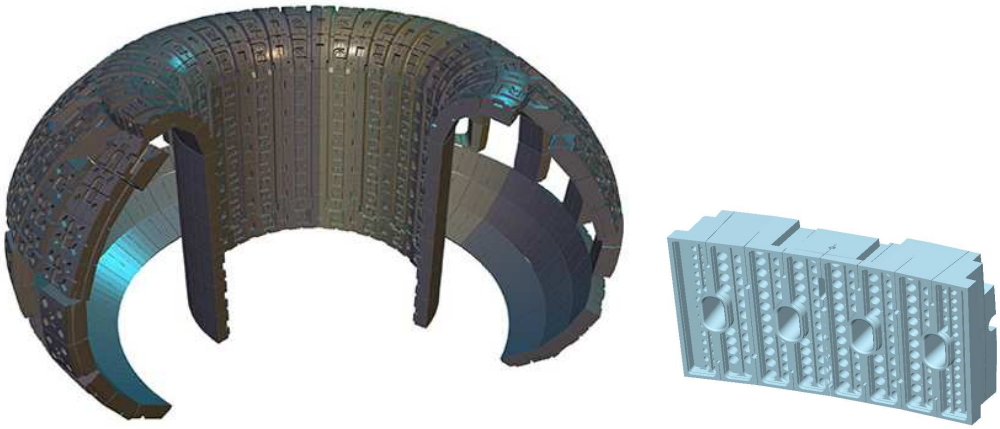

Figure 1.10: CAD rendering of the ITER blanket modules [8]

to the vacuum vessel along with cooling connections. Blanket shielding modules (BSM) provide radiation shielding only as there is no requirement to breed tritium.

First Wall

The first wall of a tokamak is required to stop high atomic number impurities entering the plasma and typically is a thin layer of material bonded to the blanket modules. The first wall is normally composed of beryllium, since beryllium is a low atomic number element, when Be ions are sputtered off the first wall into the plasma they induce bremsstrahlung losses similar to plasma itself, however an alternative material that could be used is tungsten. Although when tungsten atoms are sputtered into the plasma the high atomic number of tungsten causes large bremsstrahlung losses, the amount of tungsten sputtered into the plasma is much lower than that of beryllium [14].

Tritium Breeding

In a fusion power plant such as DEMO[1] tritium breeding blankets would be placed on the inside of the vacuum vessel, however in ITER the walls are covered with shielding blankets rather than breeding blankets. Instead, the design of breeding blankets will be investigated by placing a number of Tritium Breeding Modules (TBM) in a number of ITER equatorial ports. Each ITER member[2] have their own designs for testing tritium breeding.

1.5.7 Plasma Diagnostics

An extensive set of about 40 diagnostic systems will be available in ITER. Diagnostics are used for measuring plasma parameters such as density and temperature and for controlling the plasma. In general, very high levels of reliability are required from these systems as some are needed for real time control of the plasma. Most systems are based on the experience of similar ones on current machines, but in order to fulfill some measurement requirements it has been necessary to use techniques still under development [1].

Thompson Scattering System

The Thomson scattering (TS) systems in ITER are examples of the main optical diagnostics in ITER. The TS systems, shown in Figure 1.11, monitors both the core and edge of the plasma. The core TS system operates on the Light Imaging Detection And Ranging (LIDAR) principle. Light from a high power laser is transmitted to the plasma using a folded mirror arrangement inside a shielded labyrinth at an equatorial port.

[1]DEMO - is the working title of the planned DEMOnstration reactor to take place after ITER operations have finished

[2]The ITER Parties; European Union, India, the Russian Federation, China, Japan, South Korea and the United States

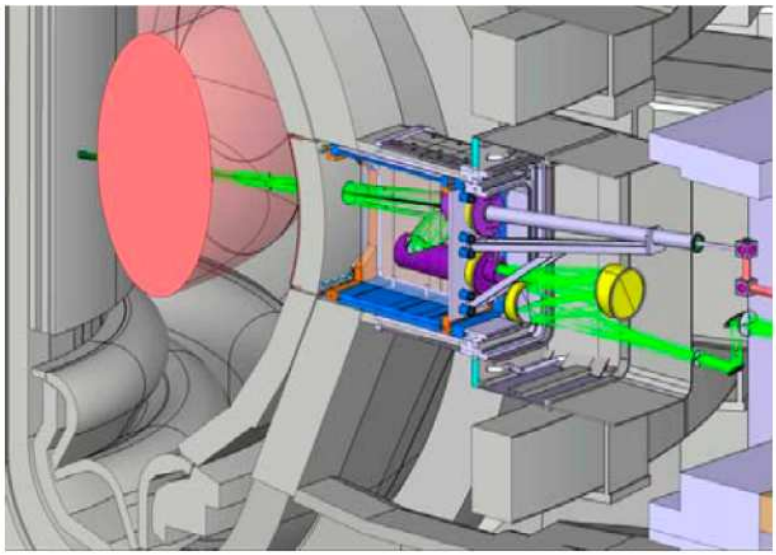

Figure 1.11: Schematic of the ITER LIDAR equatorial port plug [12]

The plasma-facing mirror is metallic and actively cooled. Scattered radiation returns along the same labyrinth to remote spectrometers. An active alignment system is employed to compensate for movements of different parts of the system. The key element in the system is the plasma-facing mirror. The mirror will be located at the bottom of a duct about 2 m in length and view the plasma through a 0.2 m diameter aperture in the blanket shield module.

The collection line is transmitted beyond the secondary confinement barrier using heated optical fibres. Using heated fibres reduces the effects of radiation induced fluoresence and luminescense [15], and also anneals out some of the radiation damage.

1.5.8 Divertor

The Divertor region of a tokamak is usually at the bottom of the vacuum vessel, it is a component designed specifically to service high heat and particle fluxes. Particles that escape confinement are guided to the divertor where they strike ceramic or

metallic plates known as strike plates. Some divertors require active cooling due to the large amounts of energy deposited, other divertors have a higher radiative cooling fraction by injecting a neutral gas in the region of the divertor, causing electrons to emit some kinetic energy in the form of Bremsstrahlung radiation.

In ITER, the divertor shares with the blanket a similar modular design. Besides providing shielding of the vessel, the modular cassettes support the divertor target plates, a set of components designed to withstand large heat fluxes, built with high conductivity armour of carbon fibre composite and tungsten.

These materials can be eroded by the plasma particles. This erosion process will not only call for replacement from time to time of the worn out divertor targets, but also may create dust, and in particular tritiated carbon dust.

1.5.9 Cooling

ITER is projected to produce 500 MW of fusion power when operating in D-T operation, with a peak neutron wall loading of 0.78 MW m^{-2}, thus an equatorial port is expected to have a maximum heat deposition rate due to neutrons of 2.9 MW, there will be additional heating due to neutron induced reactions that have large Q values. Hence an equatorial port must have an adequate supply of cooling to cope with such heat loads. There are a number of options that have been considered, however each ITER subsystem has its own requirement and heat deposition rate. There are however three standard ITER coolants namely water, LN_2 and helium. The only components cooled with helium are the magnet systems and the cryopumps (the cryopumps also take LN_2 cooling). The remaining systems are either uncooled or are cooled by water.

1.6 Thesis Outline

Chapter 2 describes the physical processes that determine particle transport through materials and how radiation safety parameters are determined. Definitions of key concepts are introduced. Finally the basic design processes of radiation shielding design with respect to fusion systems are discussed.

Chapter 3 deals with the computational aspects of this thesis, and it is where the computational methods used to determine key radiation safety parameters are described. In particular, why specific transport or nuclear inventory code were used.

Chapter 4 describes the inner workings of a shutdown gamma dose estimation software that was created as part of this PhD programme.

Chapter 5 discusses the comparison of the above code with regard to an alternative computional equivalent and ultimately the benchmarking of the code against fusion relevant experimental data.

Chapter 6 is a description of neutronic investigations of the ITER ICRH system, starting at the concept design stage and ending at the final design. Also in Chapter 6 is the neutronics analysis performed on the ITER LIDAR system focusing on the aspects determined by MCR2S.

Finally, Chapter 7 gives a summary of the work performed and what can be concluded from this work. Extensions to the work performed in this thesis are also discussed.

The work presented in this thesis with regard to ICRH Nuclear Analysis was con-

ducted as part of a contract between what was UKAEA Fusion and the European Fusion Development Agreement (EFDA). The remainder of this work was performed as part of an agreement between the Engineering and Physical Sciences Research Council (EPSRC) and the Culham Centre for Fusion Energy.

Chapter 2

RADIATION EFFECTS AND SHIELDING

2.1 Radiation Transport

In the study of thermonuclear fusion devices using a DT plasma, such as ITER, it is important to understand the spatial and energetic distribution of neutrons. The transport of neutrons through matter has been extensively studied and a number of seminal works are those of Ferziger [16] and Stacey [17]. Photon transport is more orderly than neutron transport, however much work has gone into developing codes for both neutron and photon transport. Calculation of radiation fields in nuclear devices allows other quantities to be predicted such as shutdown gamma ray dose, radiation damage and other parameters necessary for safety studies.

2.1.1 Neutron Physics

Neutrons are uncharged, and as such must rely on collisions with nuclei to loose energy or change direction. The parameter that determines how often a neutron will interact is known as cross section. Cross sections describe the likelihood of a

neutron undergoing a specific reaction as a function of energy and/or angle. Energy dependent cross section show specific traits such as the 1/v region, the resonance region and the fast region. Shown below in Figure 2.1, is the energy dependent cross section for ^{1}H(n,n')^{1}H, ^{10}B(n,α), ^{56}Fe(n,γ) and ^{235}U(n,fis). In the fast region

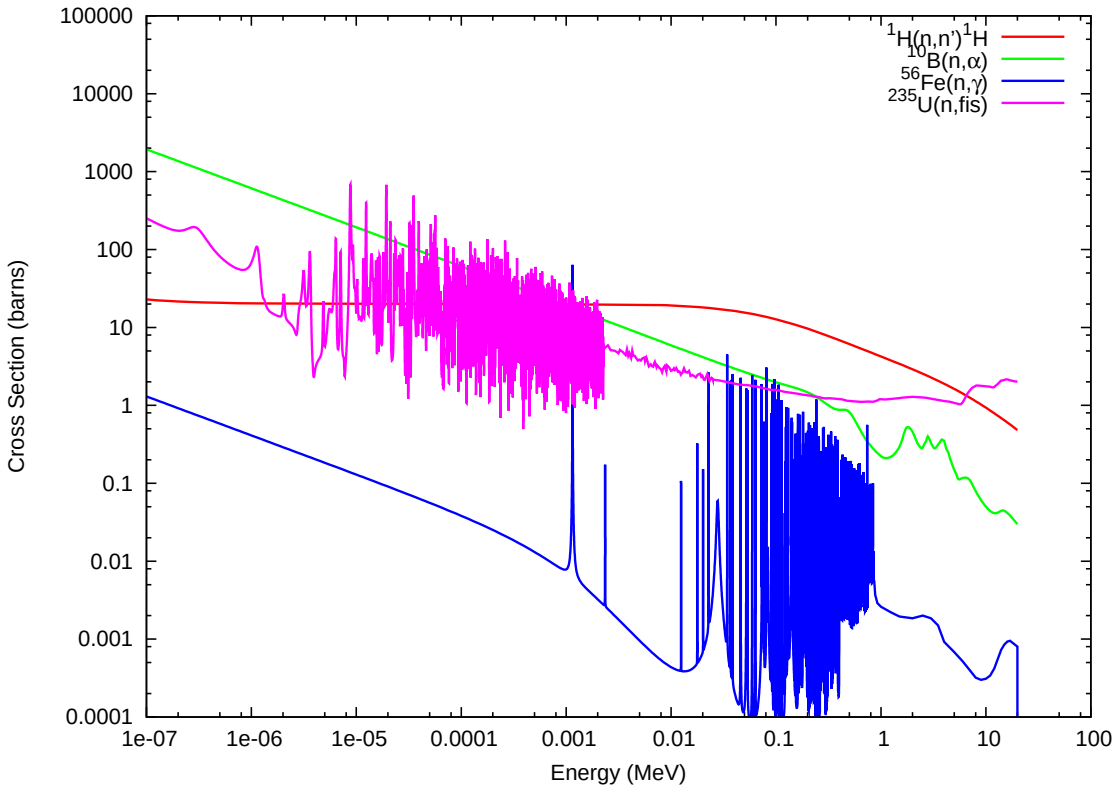

Figure 2.1: Cross section data for a number of different reactions

of the neutron cross section, typically greater than 1 MeV, the magnitude of the cross section can sometimes increase due to the increasing probability of reaction, this is where reaction channel widths are increasing and threshold reactions can take place. The resonance region of the cross section is due to nuclear resonances, which are discrete energy levels in the compound nucleus, these levels have a high probability of formation and very small widths, hence if there are a large number of these energy levels as is the case for ^{56}Fe and ^{235}U in Figure 2.1, and it can be very hard to distinguish between adjacent resonances. The so called "1/v" part of

the cross section is due to the neutron wave length being the dominating factor in the cross section. Very far from a resonance, when the exit channel is independent of the neutron energy [18], the Breit-Wigner formula shown in Equation 2.1;

$$\sigma \approx \frac{\pi}{k^2} \frac{\Gamma_a \Gamma_b}{(E - E_R)^2 + \Gamma^2/4} \propto \frac{1}{v} \tag{2.1}$$

where σ is the total cross section in cm^2, k is the neutron wave number in cm^{-1}, Γ_a is the width of the incoming reaction channel in eV, Γ_b is the width of the outgoing reaction channel in eV, Γ is the total width of the channels in eV, E_R is the energy of the resonance in eV and v is the neutron velocity in cm s^{-1}.

The thermal region of the cross section is where capture reactions typically take place due to the large increase in cross section.

It was found [19] that for neutrons with a kinetic energy of 14 MeV, the total cross section data approximately fits a scaling law, given by Equation 2.2;

$$\sigma_T = 2\pi(1.4A^{1/3} + 1.2)^2 \mathrm{fm}^2 \propto 2\pi r^2 \tag{2.2}$$

where σ_T is the total cross section in cm^2, A is the number of nucleons and r is the nuclear radius in cm.

It should be noted that the total reaction cross sections scale as the square of nuclear radius. Which implies that for fast neutrons the cross sections scales with the size of the nucleus, hence for fusion reactor shielding, we should choose materials with a high nucleon number in order to maximise the cross section. However, as will be discussed later, this conclusion is not correct, even if the cross section of interaction from low nucleon number materials is low, the potential energy loss is large, espe-

cially if hydrogen is considered. This so-called "moderation" must be balanced with the increasing reaction possiblity for the larger nucleon number nuclides.

Elastic Scattering

Elastic scattering is the process by which neutrons can loose energy by an elastic collision with a nucleus. The incoming neutron is deflected through some angle and by the laws of conservation of momentum and energy, the nucleus with which the collision occured must recoil. The neutron continues with a lower kinetic energy until another collision occurs and the process happens once more. This process of repeated collisions and slowing down of neutrons is known as moderation, for example a 2 MeV neutron in hydrogen will undergo on average 18 collisions before having its energy reduced to 0.025 eV however, the same neutron will undergo 110 collisions in graphite before reaching the same energy. The nuclides which tend to be better elastic scattering media are the lighter nuclides, which combine large cross section and energy loss.

Inelastic Scattering

Neutrons can scatter inelastically with certain nuclides [20], and is the result of the decay of a compound the nucleus formed, to an excited state of the target nucleus. Inelastic scattering can only occur once the neutron has enough energy (typically 0.1-1 MeV in medium mass nuclei) to raise the target nucleus to its first excited state. This process of excitation means that the nuclide has raised some of its consituent nucleons to higher energy levels. The neutron now continues on with less energy and a change in direction. The nucleus de-excites with the emission of one or more gamma rays, which can be quite energetic. Inelastic scattering tends to be the most effective method of downscattering neutrons in heavy metal media like iron.

Multiplication

When neutrons interact with heavier elements, there is a chance that the resultant reaction can result in two or more neutrons, (n,xn) being emitted from the compound nucleus. There is the possibility that the neutrons created may have higher energy than the inbound neutron, hence generally, it would not be beneficial to a neutron shielding system to have a multiplying material in the shield. However it is possible that the sum of the kinetic energy of the outgoing neutrons would be less than the energy of the incoming neutron, in which case there is a benefit to the inclusion of the material.

Radiative Capture

Neutrons entering a shield can be absorbed by the nuclei of atoms residing in the shield. Any kinetic energy of the neutron plus the binding energy in the resultant compound nucleus (typically 7-9 MeV) leaves the compound nucleus in a highly excited state [21]. This compound nucleus will now decay with the emission of one or more gamma rays, some of which can be quite energetic and hence penetrating.

2.1.2 Gamma Ray Physics

Photons are attenuated by 3 mechanisms; photoelectric effect, pair production and Compton scattering. A comparison is shown, in Figure 2.2, between two material extremes of photon attenuation namely hydrogen and lead. The difference between the attenuation factor for hydrogen and lead are quite marked. The lead attenuation curve has a number of features that the hydrogen curve does not, particularly the steps in the attenuation curve due to K and L shell electrons, where the energy of the incoming photon is equal to the binding energy of tightly bound orbital electrons.

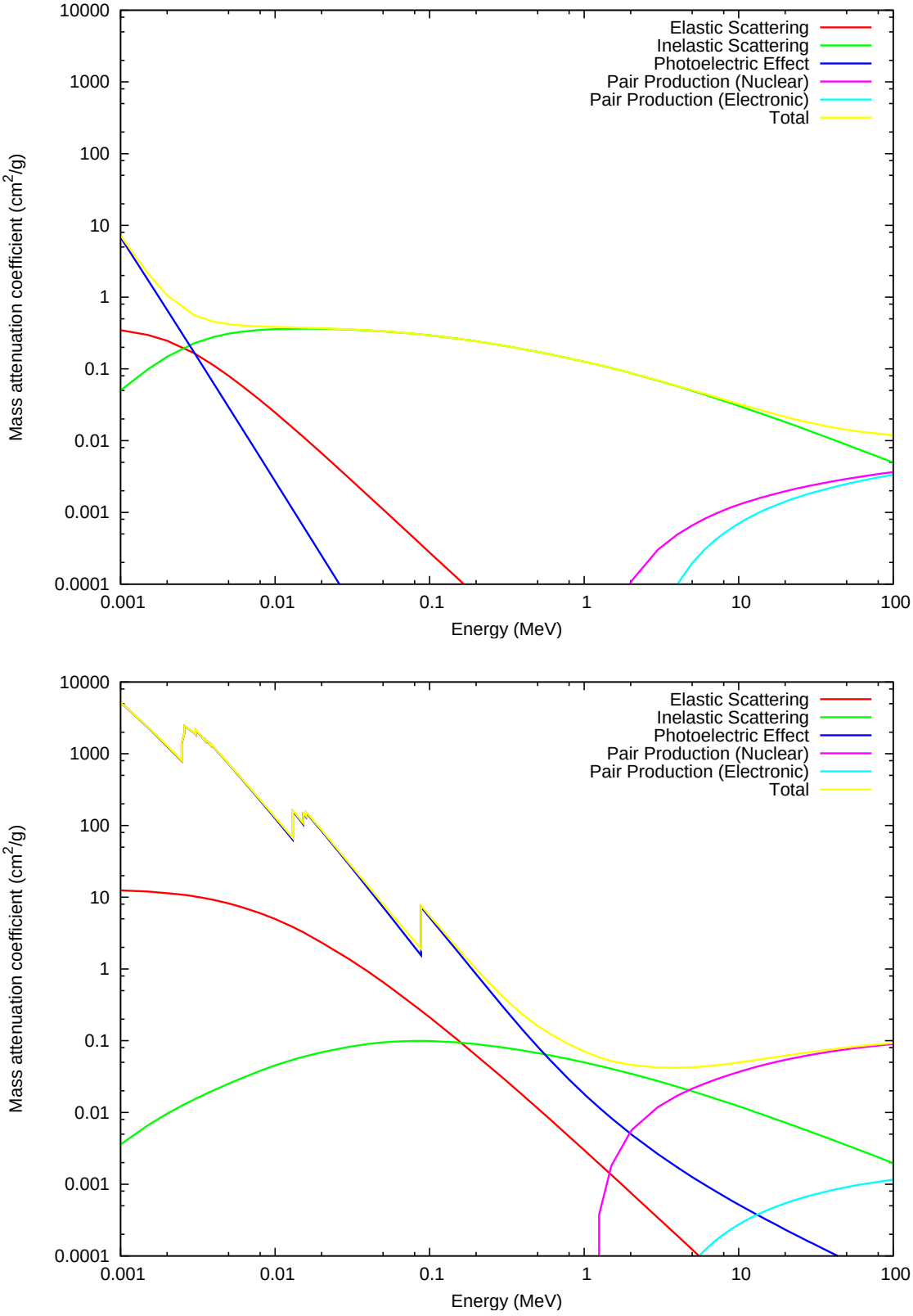

Figure 2.2: Photon mass attenuation coefficients for hydrogen (upper) and lead (lower)

Compton Scattering

Compton scattering is the process by which a photon scatters from a nearly free atomic electron, resulting in a less energetic photon and a scattered electron [18]. Compton scattering is typically the dominant process when photon energy is between 0.1-6 MeV. The cross section for Compton scattering is given by;

$$\sigma \propto Z \tag{2.3}$$

Photoelectric Effect

The photoelectric effect is a fairly simple atomic process. A photon is absorbed by an orbital electron, if the photon is of greater energy than the binding energy of the electron, the electron will be ejected from the atom. Photoelectric effect is the primary attenuation mechanism for photons less than 0.1 MeV. The cross section for the photoelectric effect away from the K and L electron shells is given by;

$$\sigma \propto \frac{Z^5}{E^3} \tag{2.4}$$

Pair Production

Pair production occurs when a photon with energy greater than 1.022 MeV can spontaneously create an electron-anti-electron pair, however, this can only occur near a nucleus. The electron and positron are created with equal kinetic energy but different momenta. The positron will eventually annihilate with an orbital electron in an atom, this process will produce two photons of energy 511 keV, which will travel almost directly away from one another. Pair production becomes the dominant attenuation mechanism when the photon energy is greater than approximately 6

MeV. The cross section for pair production is given by

$$\sigma \propto Z^2 \tag{2.5}$$

2.1.3 Boltzmann Transport Equation

We can describe the transport of radiation through a material using the Boltzmann transport equation. In certain simple cases the Boltzmann transport equation is readily solvable analytically, but for most cases when considering complex systems such as reactor or shielding systems, we can only solve the Boltzmann transport equation numerically, in an approximate manner.

The Boltzmann Transport Equation is;

$$\frac{1}{v}\frac{\partial}{\partial t}\phi(\underline{r}, E, \underline{\Omega}, t) + \underline{\Omega} \cdot \nabla\phi(\underline{r}, E, \underline{\Omega}, t) + \Sigma_t(\underline{r}, E, \underline{\Omega}, t)\phi(\underline{r}, E, \underline{\Omega}, t) = \int_{\underline{\Omega}'}\int_{E'} \Sigma_s(\underline{r}, E' \rightarrow E, \underline{\Omega}' \rightarrow \underline{\Omega}, t)\phi(\underline{r}, E', \underline{\Omega}', t)dE'd\Omega' + S(\underline{r}, E, \underline{\Omega}, t)$$

The term $\frac{1}{v}\frac{\partial}{\partial t}\phi(\underline{r}, E, \underline{\Omega}, t)$ represents the rate of change of flux with respect to time. This change may be due to the decay of isotopes, delayed neutron production or possibly if the particle source is pulsed.

The term $\underline{\Omega} \cdot \nabla\phi(\underline{r}, E, \underline{\Omega}, t)$ is the streaming term and is a measure of the directional dependence of the gradient of particle flux.

The term $\Sigma_t(\underline{r}, E, \underline{\Omega}, t)\phi(\underline{r}, E, \underline{\Omega}, t)$ is the total reaction rate, which includes terms for absorption, inelastic scattering, and elastic scattering. It it the total removal rate of particles from the energy, space, temporal and directional windows.

The term $\int_{\underline{\Omega'}} \int_{E'} \Sigma_s(\underline{r}, E' \rightarrow E, \underline{\Omega'} \rightarrow \underline{\Omega}, t)\phi(\underline{r}, E', \underline{\Omega'}, t)dE'd\Omega'$ is the scattering term and describes the probability of the scattering of particles from some direction range, $d\Omega'$ about $\underline{\Omega'}$, into our direction range of interest, $d\Omega$ about $\underline{\Omega}$, also probability of the scattering of particles of energy, dE' about E', into energy range dE about E.

The term $S(\underline{r}, E, \underline{\Omega}, t)$ is the extraneous source term for particles that are in the energy and direction but did not originate from the scattering reaction.

There are two main approximate methods that can be used to attempt to solve the Boltzmann transport equation numerically;

- Monte Carlo Methods
- Deterministic Methods

The two main methodologies are different from one another, the Deterministic methods try to numerically solve the Boltzmann transport equation and require simplification of a number of the important parameters. The Monte Carlo method does not solve the Boltzmann transport equation, instead it simulates the physics involved and often there are no simplifications made and typically determines $\phi(\underline{r}, E, \underline{\Omega}, t)$.

2.1.4 Monte Carlo Methods

Monte Carlo (MC) codes such as MCNP [22], GEANT [23], and PENELOPE [24] do not solve the transport equation as such. Instead, the codes simulate the microscopic physics of every particle collision, energy and direction change. Each particle is simulated according to source distributions and interaction coefficients. Particles are tracked through its history until it is absorbed or escapes the system. When enough of these particle histories are tracked the answer can be considered statistically significant.

2.1.5 Deterministic methods

Deterministic methods typically use one or all of the following approximations or methodologies;

- Discretise in energy (Multigroup Approximation)
- Discretise in angle (Discrete Ordinates)
- Spherical harmonics expansion of the scattering term

The main approximation used in the case of deterministic codes is the multigroup approximation, where it is assumed that the energy dependence of the problem such as the source and the cross section data are broken up into a number of discrete groups, where the energy centroid of the group determines the interaction energy. The main source of uncertainty with the multigroup method is ensuring that there is enough resolution in the energy groups to account for resonances in the cross section data, in some cases the averaging over resonances with insufficient resolution can lead to incorrect results.

The second approximation used in deterministic methods discretises the angular variation of the direction vector, $\underline{\Omega}$, into a number of discrete directions in space with associated solid angle elements. In a similar way to the multigroup approximation, the number of directions considered must be high enough in order to deal with the possibly highly anisotropic angular flux. This representation of the directions being split into groups is known as the S_n approximation.

The method of representing the cross section as Legendre polynomials, allows the scattering term to be expanded in terms of spherical harmonics, this representation in deterministic codes is known as P_n approximation.

2.2 Radiation Effects on Materials

When neutrons, heavy ions or highly energetic photons interact they can cause a number of effects detrimental to materials following their interaction with the nucleus, such effects are termed radiation damage.

2.2.1 Atomic Displacement

When neutrons interact with atoms in a material, the neutron can impart some of its kinetic energy to an atom via elastic or inelastic collisions [25]. If more energy than the displacement energy is supplied then the atom will leave its equilibrium position leaving behind a vacancy. The displaced atom is known as the primary knock on atom (PKA). If the atom has enough kinetic energy it can cause further displacements along its flight path, known as secondary displacements, and in turn these secondary displacements can cause tertiary displacements. The creation of the PKA, secondaries and tertiaries is known as a damage cascade. When the PKA has a kinetic energy less than the displacement energy, then the PKA has insufficient energy to create further displacements, it will then quickly loose the remainder of its kinetic energy via Coulomic repulsion and be absorbed into an existing atomic vacancy or could lie outside a vacancy and hence create an interstitial. The damage cascade is responsible for the majority of damage during irradiation by heavy particles (fast neutrons or heavy atoms) [26].

Dissociation Effect

A side effect of atomic displacements is a build up of internal energy in the atomic lattice [27], this is known as the dissociation effect or Wigner energy. The internal energy increases because atoms that have been displaced may end up lying between two crystal planes, the potential at this location is higher than in an equilibrium position. When the material is heated, the atoms that have been displaced to non

equilibrium positions will gain more kinetic energy and are likely to find a vacancy. The atom then has to de-excite as there is a difference in energy between the vacancy and the inter-planar position. This energy excess will be deposited into the atomic lattice and will increase the temperature of the material. The amount of energy deposited from de-excitation can become excessive if the applied dose is large.

2.2.2 Transmutation

When neutrons are absorbed in capture reactions such as ^{59}Co(n,γ)^{60}Co, the nuclide after absorption is different to that before the reaction due to the absorption of a neutron. This new nuclide may be stable or radioactive, in which case it can decay via a number of different decay schemes such as α, β, γ, Internal Transition (IT) or positron decay. When a nuclide undergoes decays via any decay but γ-decay or IT then the atomic number of the nuclide is changed. This new atom will affect the bonding structure of the crystal planes around the atom. If the neutron irradiation continues for a long period or is very intense, then a large number of material nuclides will transmute to other nuclides. If this occurs, then the material which was first put into the device will be different.

The rate of decay of a given nuclide is described by the Batemann equation, which describes the production and destruction of a given isotope

$$\frac{dN_i}{dt} = -N_i(\lambda_i + \sigma_i\phi) + \sum_{j\neq i} N_j(\lambda_{ij} + \sigma_{ij}\phi) + S_i \tag{2.6}$$

$$S_i = \sum_k N_k \sigma_f^k \phi Y_{ik} \tag{2.7}$$

where N_i is the amount of nuclide i at time t, N_j is the amount of nuclide j at time t, N_k is the amount of nuclide k at time t, λ_i is the decay constant of nuclide i (s^{-1}), λ_{ij} is the decay constant of nuclide j producing i (s^{-1}), σ_i is the total cross section

for reactions on i (cm^2), σ_{ij} is the reaction cross section for reactions on j producing i (cm^2), σ_f^k is the fission cross section for reactions on actinide k (cm^2), ϕ is the neutron flux (n cm^{-2} s^{-1}), S_i is the source of nuclide i from fission and Y_{ik} is the yield of nuclide i from the fission of nuclide k.

If we consider a simple system in a neutron capture reaction A(n,γ)B, then B is described by Equation 2.8 [20];

$$A_B(t) = \phi \Sigma_{act} V (1 - e^{-\lambda t}) \tag{2.8}$$

where A_B(T) is the activity induced in nuclide B at a time t in Bq, ϕ is the neutron flux in $cm^{-2}s^{-1}$, Σ_{act} is the activation cross section, e.g. that of the (n,γ) reaction in cm^{-1}, V is the volume of the sample in cm^3, λ is the decay constant of the excited state of the nuclide B in s^{-1} and t is the irradation time in s.

It can be seen from Equation 2.8 that when the exponential term is small, the activity of B is at its maximum, this is known as secular equilibrium. Thus when materials are irradiated activity builds up due to the activation of various nuclides, when the irradiation ends however, the activity will decay away, the timescale of which is determined by the half lives of the created nuclides. When materials are irradiated, the number of possible reactions, decays and half lives are huge. To compute this manually is possible but is very labour intensive and prone to mistakes. There are some activation-decay schemes that are impossible to solve analytically such ^{59}Co(n,γ)^{60m}Co(IT)^{60}Co(β-)^{60}Ni(n,2n)^{59}Ni, shown schematically in Figure 2.3. The reason that this reaction is analytically unsolvable is the backward step possible due to the decay of ^{59}Ni. The combination of analytically unsolvable reactions and the number of possible reactions means that a reliable computational technique must be found. Fortunately these problems have been examined previously and there are

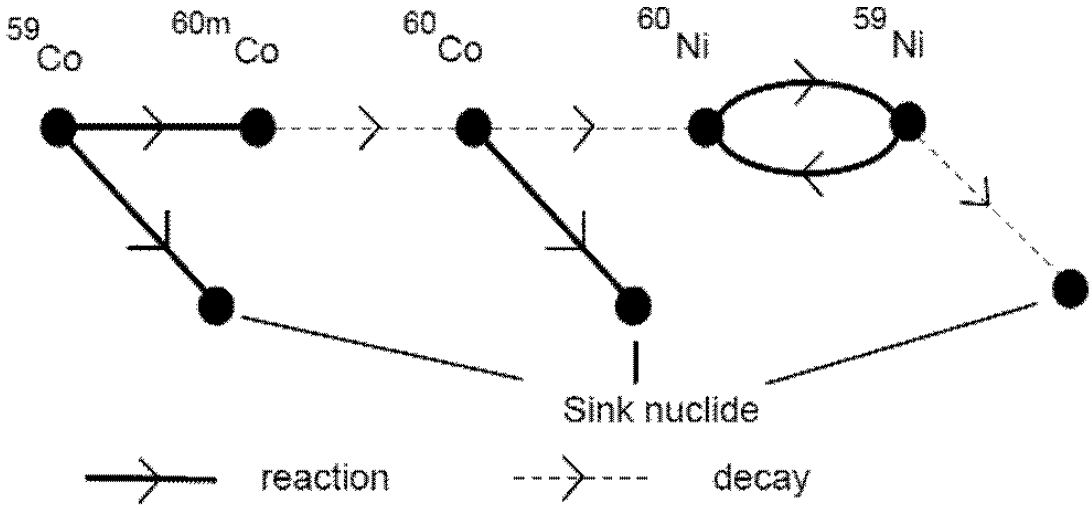

Figure 2.3: Example of analytically unsolvable activation-decay scheme [28]

a large number of nuclear inventory codes already in existence.

Gas Production

If the capture reaction was a (n,p),(n,d),(n,t) or (n,α) then either a hydrogen or helium nucleus is emitted. At some point the nucleus will absorb some electrons from the crystal lattice. These gas atoms tend to acrue along crystal grain boundaries or at voids in the crystal structure, which exert a pressure from the inside of the material. The production of gas, in particular production of helium, can affect the reweldability of steels if the helium concentration is above 1 appm[1] then it is not possible to make the welds stick. Helium is typically produced in (n,α) capture reactions such as that of ^{10}B(n,α)^{7}Li, although it can be produced via α decays.

2.2.3 Radiation Heating

When radiation interacts in matter some energy is transferred to the atom. The amount of energy transferred depends on the radiation type, the material and interaction type. This is known as radiation or nuclear heating. In the case of energetic

[1]appm - atomic parts per million

photons, the amount of energy deposited is proportional to the energy transfer coefficient, μ_{en}. Neutrons can heat material through the production of gamma rays from inelastic scattering and from elastic scattering events which knock on nuclei, and also via nuclear reactions which produce charged particles. The amount of heating is strongly dependant on the material in which the energy is deposited, the energy distribution and type of radiation impinging on the material. Nuclear heating is related to KERMA[2]. Nuclear heating is the sum of all processes which lead to the deposition of energy in a material.

2.2.4 Engineering Effects

When commerical fusion reactors are constructed, the materials from which they are made must last for the expected duration of the plant. This means that any components that maintains the structural integrity of the plant must not deteriorate to the point where plant safety is compromised. The effects of radiation by fission neutrons upon structural materials such as steel or concrete are well understood [29]. However, the placement of structural materials is often decided by how much radiation shielding can be placed between the radiation source and the supporting structures. The radiation fluence along with the spectrum of radiation incident upon structural materials determines how damaged a material will become. Hence load bearing structural materials must not exceed specified fluence limits or else suffer excessive levels of radiation damage. The uncertainty in material response to fusion neutron irradiation is large, and there is little or no data for prolonged fusion neutron irradiation. These issues could be addressed by the International Fusion Materials Irradiation Facility (IFMIF) [30] proposed to irradiate materials up to and beyond the expected operation duration of a fusion power plant. Another proposed facility to investigate these issues is the Component Test Facility (CTF), which will irradi-

[2]KERMA - Kinetic Energy Released in Matter

ate large material specimens in a high heat/neutron fluence environment [31].

The creation of vacancies and interstitals in materials are microscopic displacements, but macroscopic changes occur after large amounts of microscopic radiation damage. Such macroscopic effects are

- Radiation Swelling - When materials are irradiated some atoms will be displaced, some of these atoms will make their way towards the edges of the system, after a large amount of irradiation succesive displacements results in many atoms being dislocated from their original position. Any displaced atoms that lie at the edges of the system result in an increase in volume for that material, hence radiation 'swelling' occurs.

- Radiation Embrittlement - the presence of radiation damage decreases the strength of a material, particularly affecting the brittleness of a material, thus when load is applied to the material the elastic limit is reached sooner and plastic deformation will occur quicker.

A full discription of the above processes can be found in [32].

2.2.5 Optical Effects

Following radiation damage some displaced atoms will lie between crystal planes or other interstitial positions. They produce a change in the electronic structure and hence bonding structure in the material. It is these electrons that are used in chemical bonding and hence effect the absorbtion and emission spectra of photons. Hence when under irradiation the absorbtion and emission spectra will be different to when it is under steady state conditions.

Radiation Induced Absorbtion

For a material to be considered to be optically transparent it must not significantly absorb or scatter light in the visible wavelength region of the spectrum (350 nm to 750 nm). This also means there must be a band gap above the valance band of the material. When materials are damaged under irradiation, atoms are displaced from their equilibrium position thus changing the chemical bonding structure within the material. The displacement occurs so fast that orbital electrons are left in the vacancy. The electron sits in a potential well and acts as an 'oscillator' with a given strength and hence an absorber of visible light [29]. This effect is important when considering visible light diagnostics or optical relay data transfer along fibre-optic cables. Neutron and gamma ray irradiation can significantly affect the optical properties of such fibre-optic cables or diagnostic windows, however by using heated jackets for the cables, these affects can be minimised. Other radiation induced optical phenomena include radiation induced fluoresence and luminesence.

2.2.6 Electrical Effects

Radiation Induced Resistivity

The vacancies and interstitials produced by irradiation have numerous implications to the physical properties of the material. In conductors, the most important property is resistivity. The vacancies produced by irradiation scatter electrons. A vacancy is a postive potential, resulting in no clear path down which the electrons can travel without being scattered [33].

Radiation Induced EMF

Radiation induced electro-motive-force (RIEMF) is a transient effect on copper cables and other conducting devices that occur under irradiation. It is a thermo-

electric potential that is enabled by non-uniform radiation damage and energy deposition. It has been shown by [34], that it can have quite a large effect on cables in an ITER-like environment.

2.3 Biological Effects of Ionising Radiation

2.3.1 Effects of Ionising Radiation

The effects of ionising radiation upon humans can be broken into two discrete effects, namely deterministic effects and stochastic effects.

Deterministic Effects of Ionising Radiation

Deterministic effects of ionising radiation generally arise shortly after exposure to a radiation dose, only if this dose is greater than some threshold value. The severity of these effects, but not the probability of occurrence, depends on the total dose absorbed. An example of a deterministic effect is damage to body tissues such as the red bone marrow.

Stochastic Effects of Ionising Radiation

Opposing deterministic effects are stochastic effects, the dose influences the probability of occurrence, but not the severity. There appears to be no dose threshold with regards to stochastic effects. Most stochastic effects lay dormant after irradiation, such as the induction of cancer, or the damaged DNA inheritance to later generations.

2.3.2 Absorbed Dose

Absorbed dose, D, is defined by the relationship [35];

$$D = \frac{d\epsilon}{dm} \tag{2.9}$$

where $d\epsilon$ is the mean energy imparted by ionising radiation to the matter in a volume element and dm is the mass of the matter in this volume element

2.3.3 Effective Dose Equivalent

The International Commission on Radiation Protection introduced the concept of equivalent dose in ICRP Publication 60 [35]. Equivalent dose is defined as

$$H_{T,R} = w_r \cdot D_{T,R} \tag{2.10}$$

where $H_{T,R}$ is the equivalent dose over a particular mass of tissue T, due to radiation R, w_r is the radiation weighting factor the value of which depends on the type of radiation R and $D_{T,R}$ is the absorbed dose in a particular mass of tissue T, due to radiation R.

To account for differing amounts of organ and tissue radiosensitivity there are also tissue weighting factors, w_T, the product of the equivalent dose with the tissue weighting factor results in the effective dose, E [20];

$$E = \sum_T w_T \cdot H_T \tag{2.11}$$

The factors are normalised such that the sum over all tissues is equal to unity. The implication of this is that a uniform equivalent dose, H of 1 Sv to the whole body will result in an effective dose, E of 1 Sv.

Computer human models and neutron/photon transport codes have been applied to calculate energy deposition and dose for various tissues and organ systems. These calculations are sensitive to the direction of incidence of the radiation because of self-shielding and attenuation effects in the body through the tissue weighting factors recommended by the ICRP, the individual components can be then combined into an effective dose equivalent, H_E [35].

The effective dose equivalent represents an estimate of the overall biological effect of a uniform whole body exposure to the assumed fluence. The effective dose equivalent is then written as

$$H_E = h_E \cdot \Phi \tag{2.12}$$

where H_E is the effective dose equivalent in Sv, h_E is the fluence-to-dose conversion factor in Sv cm^2 and Φ is the radiation fluence in cm^{-2}.

There are several sets of fluence-to-dose conversion factors, in this thesis the factors used were ANSI-ANS-6.1.1-1977 [36] and ANSI-ANS-6.1.1-1991 [37]. The ANSI-ANS-1991 standard chooses to represent an analytic fit to the derived dose data at a fourth order polynomial

$$h_E(E) = 10^{-12} \times e^{(C_0+C_1X+C_2X^2+C_3X^3+C_4X^4)} \tag{2.13}$$

$$X = \ln E \tag{2.14}$$

where $h_E(E)$ is the fluence-to-dose conversion factor in Sv cm^2 and E is the particle energy in MeV.

The actual co-efficients used in this thesis can be found in the Appendix B.

2.3.4 Limits on Dose and Dose Rate

Due to the threshold of certain biological deterministic radiation effects and the non-threshold of stochastic biological effects, it is prudent to set radiation limits in any human activity in which personnel are subject to a radiation field. These limits are normally set to be at the upper level of tolerability. Therefore, during the design and operation of a radiation facility there must be a radiation protection system that ensures that actual recieved doses are well below the prescribed limits.

In the United Kingdom what was the National Radiation Protection Board (NRPB), which has now been merged with the Health and Safety Executive (HSE), sets guideline effective dose limits based on the findings and recommendations of the International Comission on Radiation Protection (ICRP).

It has been the case within the UK since 1999 [38] that the limits are,

1. for employees aged 18 years or over, 20 millisieverts in a calendar year (except that in special cases employers may apply a dose limit of 100 millisieverts in 5 years with no more than 50 millisieverts in a single year, subject to strict conditions)

2. for trainees, 6 millisieverts in a calendar year

3. for any other person, including members of the public and employees under 18 who cannot be classed as trainees, 1 millisievert in a calendar year

Since the ITER device will be based in France, the French nuclear authority limits, shown in Figure 2.4, will apply. Decree No. 2003-296 lays down the basic French nuclear safety standards for the protection of workers. It confirms the principle whereby individual and collective professional exposure to ionising radiation must be maintained at the lowest level reasonably achieveable, and it reduces the annual

effective dose for exposed workers from 50 mSv to 20 mSv. During a period of two years from the entry into force of the decree, the maximum sum of the effective doses recieved from external and internal exposure is set at 35 mSv per year, with a further maximum of 100 mSv over a period of 5 consecutive years, again from entry into force of the decree [39].

	Blue	Green	Yellow	Orange	Red
Time Spent		8 h per day	Controlled/ Monitored	Controlled/ Monitored	Controlled/ Monitored
Dose Rate Threshold (μSv/hr)	2.5	7.5	25	2000	100000
Dose Limit (effective dose)	15 mSv/a	50 mSv/a & 30 mSv/q	50 mSv/a & 30 mSv/q	50 mSv/a & 30 mSv/q	50 mSv/a & 30 mSv/q

Figure 2.4: Legal lower limits of radiation level zoning in ITER [1]

2.3.5 Maintenance Ports Dose Rate Limits

Due to the experimental nature of the ITER device it is expected that during the operation of the device, there will be unforeseen failures of components, hence it is imperative that person access is achievable at a maximum of 14 days after shutdown. In order for person access to be attained the gamma dose rate 14 days post shutdown must be less than 100 μSv hr^{-1}.

The equatorial ports in ITER lie in the region of highest neutron wall loading. The ports are filled with equatorial port plugs such as those discussed earlier like the ICRH or LIDAR system. The plugs perform a dual purpose of providing places to put diagnostics or heating systems and also provide radiation shielding. The main radiation concern with port plugs is typically the shutdown gamma ray dose rate at the rear of these plugs, although certain plugs may have penetrations for diagnostic lines of sight and hence radiosensitive components may lie within direct view of the

plasma, or provide direct lines of sight to highly activated components.

2.3.6 Bioshield Dose Rate Limits

Beyond the concrete bioshield the neutron dose rate must be less than 10 μSv hr^{-1} as personnel access must be maintained during operation. The ITER bioshield is to be composed of typical reactor concrete, possibly with an enhanced boron content. There is little concern that doses will be high beyond the bioshield during an ITER plasma. However, when transporting activated port plugs and other items there may be concern due to source of radiation being much closer to occupied areas.

2.4 Radiation Shielding

In order to mitigate the potentially harmful effects of radiation in materials and humans, and achieve the limits mentioned in the previous section we must shield radiosensitive (biological or inanimate) objects from the radiation field.

Before the design of any radiation shielding can take place, the radiation shielding designer must be aware of any consequences to their actions. Some general priciples of shielding design are as follows [21, 40].

A radiation shield must balance the following aspects while ensuring that the attenuation of the radiation field is sufficient;

- Activation
- Dose
- Heating/Cooling
- Handling

- Weight
- Radiation damage

The radiation shielding of a system must attenuate the primary radiation incident upon it and it must not become prohibitively activated. Ideally a shield would be made of a substance that cannot be activated, however in practice making a shield of such materials, for example a "low" activation material such as vanadium, would be rather expensive. Through careful shield design activation can be minimised or the effects of the decay radiation attenuated to a large degree.

Typically the purpose of a radiation shield is to reduce radiation dose to levels deemed acceptable. Although, there are a number of cases where thermal shields have been included in systems like the thermal shielding placed in front of the ITER TF coils, where its primary purpose is to reduce the nuclear heating of the coils.

The nuclear heating of the shield should not be so large as to cause excessive amounts of energy to be deposited in the shield, where this cannot be avoided as is the case when shielding intense charged particle sources, cooling methods must be introduced to the shield. Fluid coolants require some form of penetration through the shielding, these penetrations should not align with the major regions of the radiation source emission. Electrical cooling is a method of cooling that requires no penetrations, the heat generated inside the shield is conducted to the outside world via thermal conduits or cooling veins. The issue with electrical cooling in a radiation environment is the loss of conductity experienced by metals when damaged by ionising radiation.

The radiation shielding must not imbalance the system, where over head crane handling is requied the shield should sit balanced in the handling sling [21].

Shield weight is not typically a concern in stationary reactor applications, such as the reactor bioshield, where it can made as thick as is required, however certain parts of reactors may have strict weight limits if moving or maintenaince is required. In the case of these mobile shields it is important that shield weight is not excessive and that the equipment designed to move the shield around will not become damaged. This is the case for diangostic port plugs where the maximum dry weight of the plug is 50 tonnes.

One concern of radiation shielding is that of the time evolution of the shield, where radiation damage can cause many microscopic defects, which can lead to macroscopic effects such as embritlement and voiding. It is important to consider the level to which a shield will become damaged in the reactor application, and if this damage can not be avoided then shield replacement lifetimes should be recommended. Indeed, in severe circumstances the virgin shield will be more attenuating than the shield at its end of life.

2.4.1 Stages in Radiation Shielding Design

There are a number of stages when designing a radiation shield, the procedures used when moving from concept to final design can be broken down into a number of steps. Previously, radiation shielding calculations were challenging and error prone. With the advent of high power computing, these calculations have become less challenging. However, with increased computing power comes the desire for more accurate answers and inclusion of effects that otherwise would have been neglected.

The following stages are based on those of Price [40], however they have been modified to take into account the changes in radiation shielding design procedure in the

proceeding 50 years, such as digital computing.

Study of the Primary Radiation Source

It is the primary radiation source that determines the materials and geometry that the resulting shield is required to be constructed from. Knowledege of the spatial, angular and energetic distribution of the source is essential for any future calculations. Without an accurate source definition it is impossible to accurately estimate not only the uncertainty in the answer with respect to the source definition but also important transport effects such as streaming.

Formulation of the Basic Shield

Once the radiation type and energy distribution of the source particles is known, the primary shielding materials can be selected depending upon how much attenuation is required. For example when considering an energetic neutron source, a shield with a high density and with two component materials would be considered, one component for slowing down the neutron and another component for absorbtion. In the case of ITER, a high moderating fractional component would be selected, for example Stainless Steel (40%vol) and Water (60%vol).

The principal shield materials available to the designer can be divided into 2 categories according to their function: (1) materials that are used primarily to attenuate one kind of radiation, either neutrons or gamma rays, and (2) materials that serve a dual purpose and are used as the main attenuator of both types of radiation. Characteristic of the first category are hydrogenous materials, typically water, to attenuate fast neutrons by moderation down to energies where they can be captured, and dense materials of high atomic weight, typically lead, to attenuate gamma rays. Although each of these materials are chosen for their properties with regard to a

particular type of radiation, each, of course actually attenuates both types. In the second category are materials such as concrete which is effective at attenuating many different types of radiation.

The shield design at this point is subject to revision, as are the materials of which the shield is made. Revisions are made on the basis of calculated radiation levels, excessive heating, secondary radiation production, or material damage.

Calculation of the Attenuation of Primary Radiations

On the basis of the over-all system evaluation and the choice of material discussed above, approximate calculations can be performed to obtain the thicknesses required to attenuate the primary radiation. Calculation at this stage will be approximate with minimal details considered to give a reliable answer. Shield design is by its nature an iterative process and after each design stage more detail is added to the calculation.

Calculation of Production and Attenuation of Secondary Radiations

Once the attenuation of primary radiation has been calculated, the distribution and intensity of secondary radiations produced from interactions of the primary radation can be determined (if any). In the case of neutrons as primary radiation, an example of secondary radiation would be gamma rays produced via capture, transmutation and inelastic scattering reactions. There are many types of secondary radiations such as gamma rays, protons, alpha particles, bremsstrahlung and a number of the other processes. It is because of these secondary radiations that shield design can become a complex problem when considering shielding systems composed of many different materials.

Calculation of Heating in the Shield

Another important shield design problem, is that of the thermal heating in the shield. While heating is a common engineering problem, nuclear heating, because of the nature of neutron and gamma ray distributions throughout the shield, poses certain unique considerations. In many cases a specially designed thermal shield is incorporated, which, in contrast to the primary function of the over-all system, serves to absorb a large portion of the energy carried by the nuclear radiation and hence to facilitate shield cooling.

Optimisation of the Shield

The problem of optimisation is common to most engineering designs, whether the object is to minimise the cost or to reduce the size, weight, or some other parameter of the system. In shielding, the parameter of interest may be the cost, as in the case of a stationary reactor. The optimisation is usually carried out subject to certain constraints, or subsiduary requirements; for example, a limit may be imposed on post shutdown radiation levels at the surface of the reactor shield, or the shield dimensions may be restricted to some maximal value.

2.4.2 Neutron Shielding

There are a number of so called standard neutron shielding materials such as boron carbide, steel-water mixtures or concrete. The choice of material will usually be subject to a number of constraints.

Neutron shielding typically is partly composed of materials that both moderate and absorb, Bethe-Bloch for example boron carbide (B_4C) or even simple mixtures such as steel and water. Moderating materials are required to reduce the kinetic energy of the incoming neutron flux, when these neutrons slow down through a

number of collisions, its kinetic energy will be low enough to be in the "1/v" part of an absorber's cross section. Moderating materials differ from absorbers in that the absorption cross section in moderators are typically very low, but have large cross sections for scattering, either elastic or inelastic. There is a need to moderate neutrons to lower energies because typical absorbtion cross sections can be 6 orders of magnitude higher at thermal energies than at fast energies. Neutron shields have a dual purpose one of screening the primary radiation field from persons outside the shielding, and also attenuating any secondary radiation that is produced. A shield that is composed of only absorbant material will not shield as well as a mixture of moderator and absorber.

Consider a neutron source impinging from one side of a semi-infinite slab of material. It is known that a certain distance into a specific material the neutron spectrum is in equilibrium, this is due to the build up of neutrons scattered down in energy and the absorbtion of those neutrons accordingly either in the "1/v" part of the cross section or in the resonance region. This means that at depths greater than this equilibrium distance the neutron spectrum no longer changes in energy, only in intensity.

2.4.3 Photon Shielding

Photon attenuation is determined by 3 microscopic interaction methods; photoelectric effect, compton scattering, and pair production and as such the macroscopic design of shielding is determined by these interaction coefficients. However, since these cross sections scale with the number of electrons present in the material, the more effective shields tend to be high atomic number and high density materials such as lead and tungsten.

2.4.4 Charged Particle Shielding

When charged particles such as ionic species or electrons interact in materials they do so via the long ranged electric potentials of all the constiuent atoms in the material. Slowing down and attenuation of charged particles is described by the Bethe-Bloch stopping power [20], shown in Equation 2.15,

$$-\frac{dE}{dX} = \frac{4\pi e^4 z^2}{m_0 v^2} NB \tag{2.15}$$

$$B = Z[ln\frac{2m_0 v^2}{I} - ln(1 - \frac{v^2}{c^2}) - \frac{v^2}{c^2}] \tag{2.16}$$

where v is the velocity of the particle in m s^{-1}, ze is the charge of the particle in C, N is the number density of the shielding material in m^{-3}, Z is the atomic number of the shielding material, m_0 is the electron rest mass, e is the electronic charge 1.602×10^{-19} C, and I is the average excitation energy of the shielding material in Joules.

From Equation 2.15, there are a number of general rules that can be seen when shielding charged particles, which are;

- dense material
- high atomic number
- high ionisation potential

There is of course the possibility that the charged particle has such a high energy that nuclear reactions can be induced in the shielding material, as is the case when designing shielding for the Large Hadron Collider at CERN, in which a number of exotic reactions can take place.

2.5 Radiation Fields in ITER

The radiation field in ITER has two main components, neutron and photon. The neutron field is produced by the plasma and the photon field mainly by the interaction of neutrons with material surrounding ITER.

2.5.1 Neutron Field

The neutron field in ITER is due to the presence of the plasma neutron source at the centre of the plasma chamber. Neutrons born in the chamber from the t(d,n)α reaction are emitted isotropically, but being uncharged are not affected by the strong magnetic fields present in the chamber. The ions that produced the neutron are influenced by the magnetic field. This means that the intensity of fusion reactions and thus of neutron emission is linked to the magnetic field structure within the plasma chamber. The link between magnetic flux surfaces and neutron source emissivity can be described as in Equations 2.17, 2.18 and 2.19 [41], thus

$$R = R_0 + \rho\cos(\theta + \epsilon\sin\theta) + \delta_r(1 - \frac{\rho^2}{a^2}) \tag{2.17}$$

$$Z = k\rho\sin\theta + \delta_Z \tag{2.18}$$

$$S = S_0(1 - \frac{\rho^2}{a^2})^{\psi} \tag{2.19}$$

where R is the radial co-ordinate in cm, R_0 is the major radius in cm, ρ is the radial component in cm, θ is the poloidal angle, ϵ is the plasma elongation, δ_r is the radial shift in cm, a is the plasma minor radius in cm, Z is the vertical co-ordinate in cm, k is the plasma triangularity, δ_Z is the plasma vertical shift in cm, S is the neutron source strength at position ρ in s^{-1}, S_0 is the absolute neutron source strength in s^{-1} and ψ is the plasma peaking factor.

Thus given the parameters in Table A, we can predict the shape of the neutron source for ITER. The 14.1 MeV neutron peak is, however thermally smeared due to the temperature distribution in the plasma and is described by Equation 1.5 [3]. Due to the increased plasma density and ion temperature towards the centre of the plasma, there is increased fusion reactivity and hence neutron production. Once the neutron is created via the D-T reaction, it travels on until material is encountered. We can ignore neutron scattering events in the plasma due to the extremely low particle density.

Once the neutron leaves the vacuum chamber, a number of neutron interactions can occur, such as elastic and inelastic scattering, neutron capture alongside a number of other events. These neutrons then build up to form an equilibrium distribution of neutrons, known as the neutron field, shown in Figure 2.5. This neutron field is the cause of the neutron induced activation of materials around the ITER device. The neutron spectrum at each location can vary considerably depending upon the elemental and isotopic composition of the material.

Neutron interactions with materials are responsible for;

- Neutron Heating
- Radiation Damage
- Neutron Activation
- Photon Heating (indirectly)

2.5.2 Prompt Gamma ray Field

The prompt gamma ray field is created by neutrons that undergo inelastic scattering and radiative capture reactions with materials present in ITER, producing inelastic

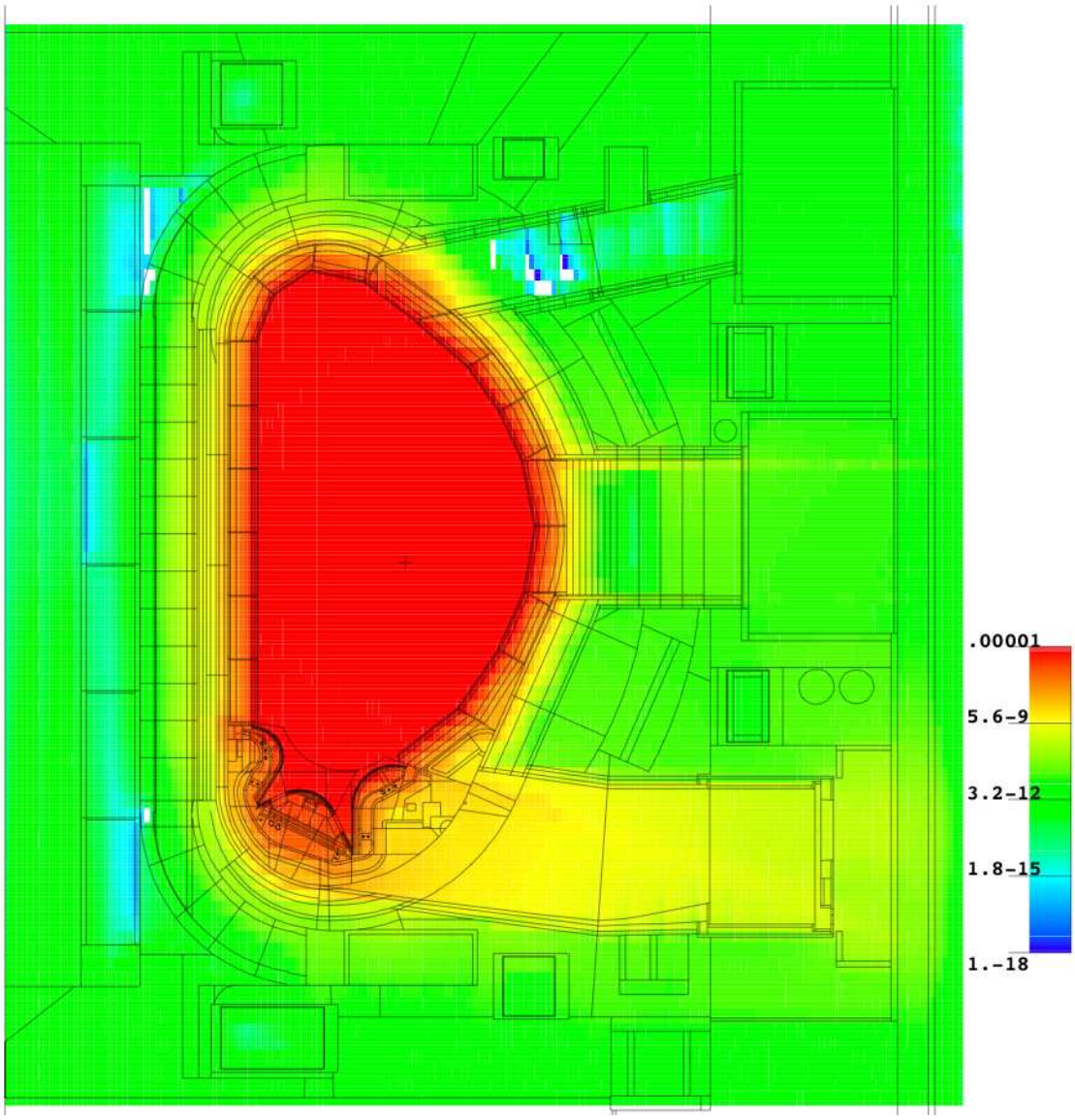

Figure 2.5: Neutron fluence distribution in ITER (per source particle cm^{-2})

gamma photons which can have energies of several MeV. These photons are typically absorbed fairly quickly by the material in which they were produced, however in ITER there are a lot of gaps and penetrations along which the photons can stream. When these photons are absorbed their energy is transferred into the kinetic energy of recoil electrons, and ultimately are transferred to the surrounding environment

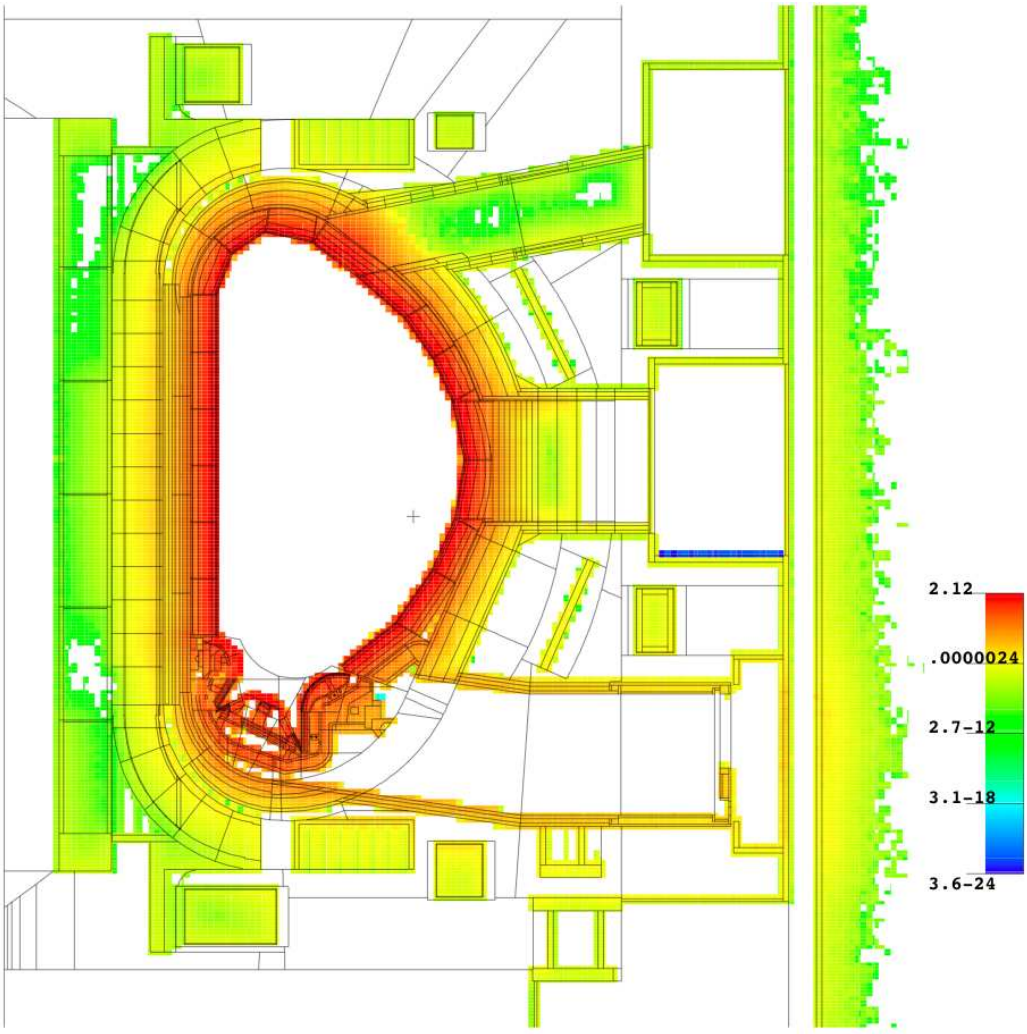

Figure 2.6: Photon heating in ITER (W cm^{-3})

as heat. This heating is known as photon nuclear heating. The photon induced heating, shown in Figure 2.6 is the main concern when calculating the prompt photon field. The dose caused by the inelastic scatter photons is very small beyond the concrete bioshield, since beyond this shield are maintainence and diagnostic areas, which sometimes may be populated hence the bioshield is very thick. It is the more penetrating neutrons that are of concern during operation.

2.5.3 Shutdown Gamma ray field

The shutdown gamma ray field is a direct consequence of the interaction between materials around the device and the neutron field distributed around ITER. The shutdown gamma ray field shares some similarities in the spatial distribution with the prompt gamma ray field. However, the intensity and energy distribution are quite different, shown in Figure 2.7. With regards to personnel dose, the shutdown

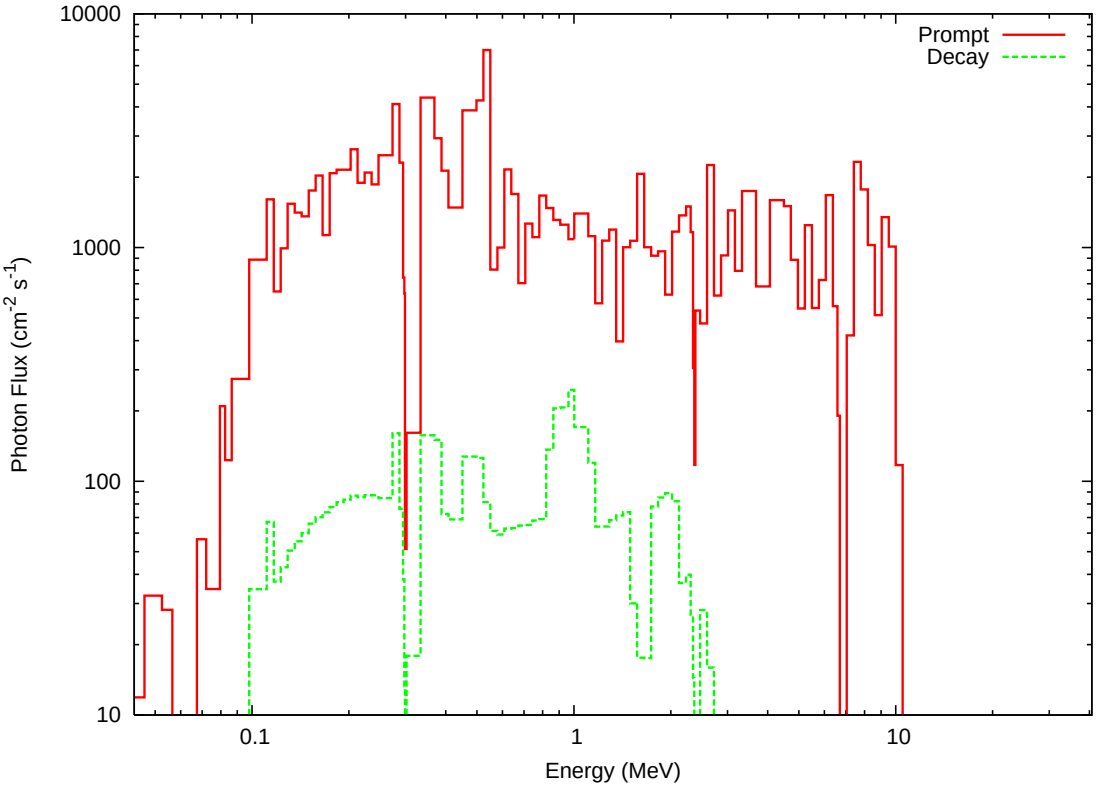

Figure 2.7: Prompt and shutdown gamma ray spectra from 316-LN Stainless Steel, where the shutdown spectra was performed for an irradiation of 1 year at the same constant neutron flux as the prompt photon case

gamma ray field is ultimately of more consequence than the prompt gamma ray field because no maintainence will occur when the device is operating. When the machine is offload, it is the gamma ray dose which determines maintainence procedures, such as whether or not remote handling is needed or a simple dose budget for workers

will be used.

2.5.4 Shutdown Neutron Field

Despite perhaps being counter-intuitive, there is a shutdown neutron field, which is estimated to be less than the shutdown gamma dose [42]. This field is produced by Be(γ,n) reactions in the first wall. The first wall, which is composed of beryllium, is subjected to a high flux of energetic shutdown gamma ray photons, which then undergoes (γ,n) reactions. This shutdown neutron field is proportional to the shutdown gamma ray field, so it shows a time dependence similar to the shutdown gamma ray field. There will be some deviation since the energy distribution of photons from the shutdown gamma ray field will change over time as the photon spectrum converges to an average photon energy around 1 MeV due to the production of ^{60}Co in steel during ITER's operation. However at shorter decay times ^{56}Mn,^{57}Ni and ^{58}Co are the dominant dose causing nuclides.

Chapter 3

COMPUTATIONAL METHODS

3.1 Radiation Transport

From the number of radiation transport codes mentioned in Section 2.1 the code selected for work in this thesis was MCNP. MCNP was selected for a number of reasons. MCNP takes ENDF[1] formatted data such as the FENDL libraries, which are pointwise cross section data. The use of pointwise data means that there is no approximation or averaging in the cross section data and hence a very good representation of transport is maintained. MCNP is the ITER reference transport code, and has been subject to a large number of experimental and code benchmarks [43]. A further reason was usage experience at CCFE. The source code is available for modification meaning that users can alter and add subroutines should they be required, and finally there are a number of code compilation test verifications to ensure that the code is correctly compiled to Los Alamos National Laboratory (LANL) standards.

[1]Evaluated Nuclear Data File

3.1.1 Monte Carlo N Particle (MCNP)

Monte Carlo N Particle (MCNP)[22] is a computer code used to simulate the transport of neutrons, photons and electrons in an arbitrary three dimensional geometry. The code tracks virtual particles through their "life" until they are "killed". During the "life" of a particle a number of events can occur, these are summarised in Figure 3.1. Uniform random deviates[2] are used to determine the result of the physical interaction between the virtual particle and the material through which it is traveling. For example, a neutron interacts in a given material, of which the fractional composition of each nuclide is known. A random number is used to sample with which nuclide the neutron interacts, another random number is used to determine for that neutron what reaction that nuclide undergoes, the direction and energy of emission of secondary particles and so on, until all required physical parameters of the neutron are determined. Particles are tracked by the code until their weight reaches zero at which point the particle is terminated by the code. In a real system when a particle is absorbed it is lots to the system, this is not a useful computational method. A technique known as implicit capture (weighted tracking) is used such that rather then let a particle be terminated by the code after absorbtion, it is instead allowed to continue with a modified statistical weight (multiplied by the probability of surviving).

A virtual particle is created according to the user defined source definition, with an accordingly distributed energy, direction and starting position. The distance to next collision is determined by

$$l = -\frac{1}{\Sigma_t} ln(\xi) \tag{3.1}$$

where l is the distance to next collision in cm, Σ_t is the total cross section in cm^{-1}

[2]Uniform random deviate - a random number uniformly distributed between 0 and 1

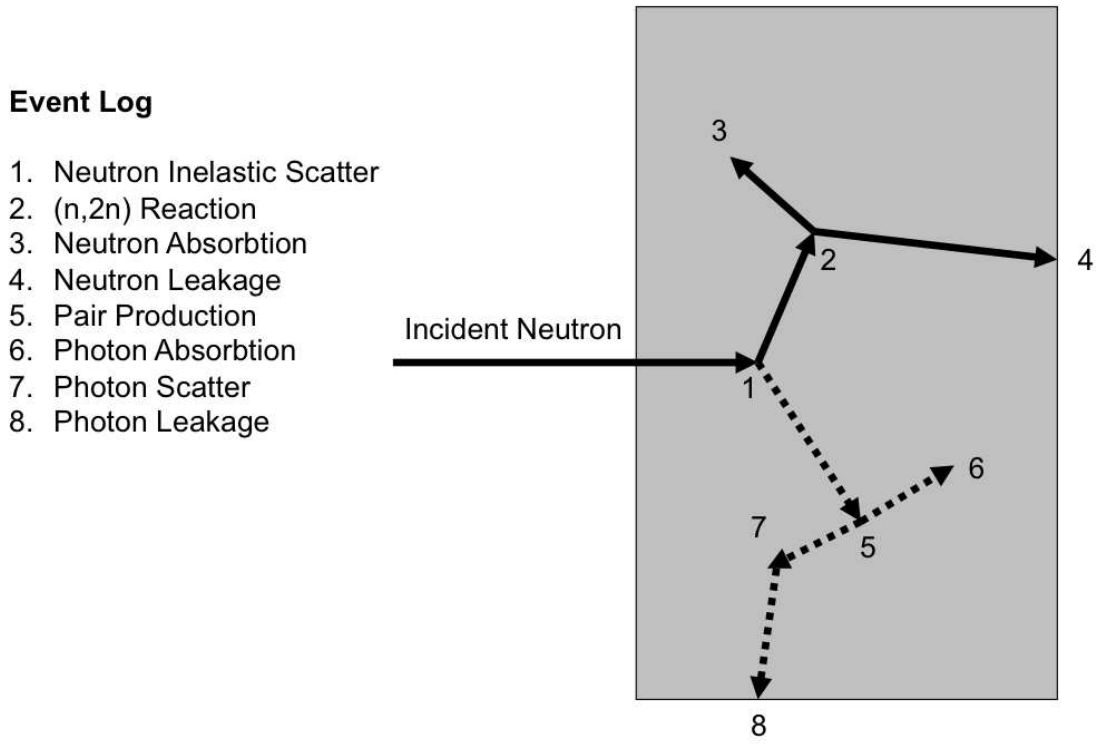

Figure 3.1: Neutron interaction events in MCNP [22]

and ξ is a continuous random number between 0 and 1.

Consider the case where the source particle is a neutron, which is incident upon a material, as shown in Figure 3.1. There are a number of steps which make up this particle history:

1. Undergoes an inelastic scattering reaction, the neutron is deflected through some angle, which is determined from the scattering distribution stored in the nuclear data and continues along the new trajectory. During the inelastic scattering event a photon was created, which is temporarily stored in memory for transport later.

2. The neutron is captured in some nuclide capable of an (n,2n) reaction and then the code creates two neutrons with energies and directions appropriate

to the reaction.

3. One of the neutrons from the previous (n,2n) reaction undergoes an absorbtion reaction.

4. The other neutron (which was retrieved from memory) produced from the (n,2n) reaction leaks from the system.

5. The photon (retrieved from memory) that was created from the inelastic scattering reaction undergoes a pair production reaction and produces two new photons of according energy.

6. One of the photons created from the pair production reactions is absorbed.

7. The second photon (retrieved from memory) that was created from the pair production reaction, undergoes a scattering reaction.

8. The photon leaks from the system.

This neutron history is now complete. As more and more such histories are followed, the neutron and photon distributions become better known. The quantities of interest are tallied, along with estimates of the statistical precision of the results [22]. The uncertainty in a tally is

$$\sigma = \sqrt{n} \propto \frac{1}{\sqrt{T}} \tag{3.2}$$

where n is the number of particles that contribute to the tally and T is the run time in minutes.

When a particle undergoes a reaction the type of reaction is determined alongside the energy loss, change in direction, and additional particle creation. An example of this are the cross section data shown in Figures 3.2 and 3.3. When the data are

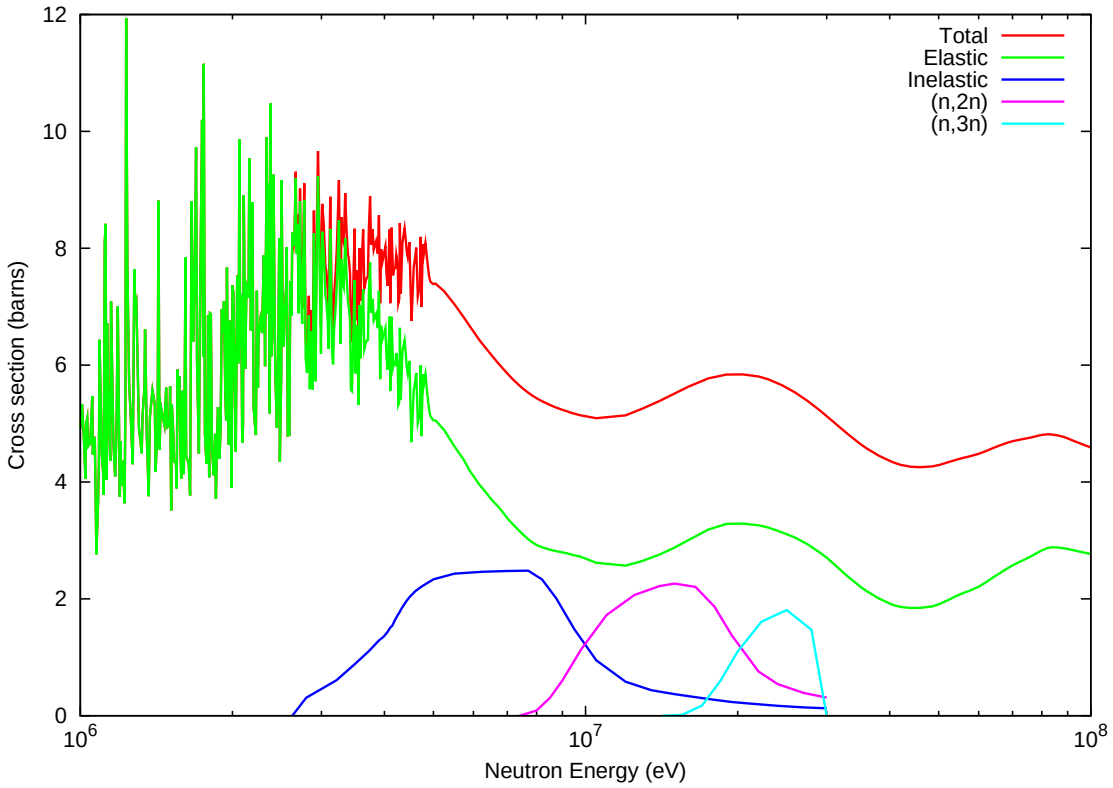

Figure 3.2: Various neutron interaction cross section data for ^{208}Pb

normalised MCNP can select the angle change, energy loss etc. The distance to next collision is then determined once more, and this process continues until the particle is absorbed (killed) or leaves the system. It can be seen that should the system be large or highly attenuating a large number of particles must be simulated in order to have a high confidence level in the simulation.

Geometry Creation

The combinatorial geometry input of MCNP is one of the features that has made its use popular. Combinatorial geometry is based on the definition of cannonical surfaces. In MCNP each surface is assigned a positive integer which is termed the surface number. Every surface has a type which defines the attributes of that surface, which for example may be a simple plane or the surface of a sphere. A number of surfaces are combined using boolean operators to create a volume; to do this

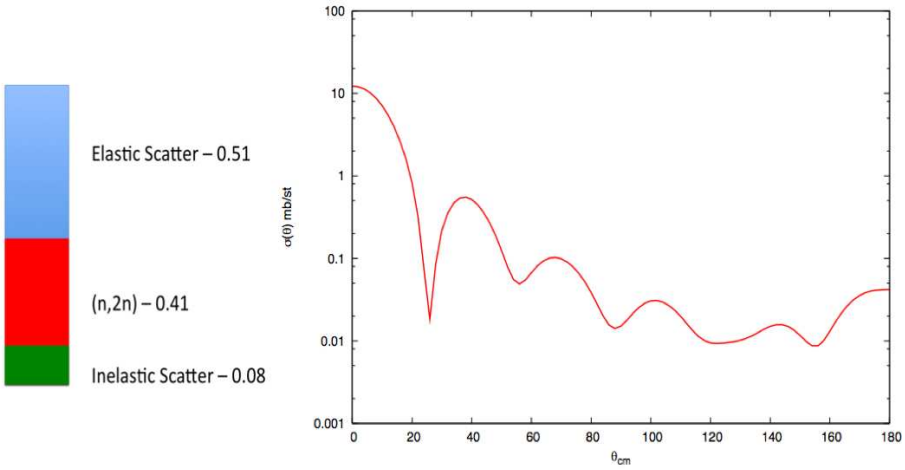

Figure 3.3: Interaction cross section probabilities for a 14 MeV Neutron incident upon ^{208}Pb (left), Elastic scattering cross section for 14 MeV neutrons incident upon ^{208}Pb (right)

each surface has a "sense" which is either positive or negative. Every surface has an equation which defines it, in the case of a plane situated at x=a, then equation of the plane would be x-a=0. Thus it can be seen that unless x is greater than a the term x-a is less than zero, which gives a negative sense to this surface definition.

Consider defining a cube of side 6 cm, then 6 surfaces are required, assuming we place the geometric centre of the cube at the origin then we have 6 plane definitions thus

$$x-3=0, x+3=0, y-3=0, y+3=0, z-3=0, z+3=0$$

If these planes are numbered in order of appearance 1 to 6 then to define the universe that belongs to the internals of the cube we would use -1 2 -3 4 -5 6, which define the region of space that has a negative sense with respect to surface 1, ie everything that is less than x=3, every region of space that has a positive sense with respect to surface 2, ie everything greater than x=-3 etc. For the transport calculation all space must be defined and there must be no doubly defined regions of space. If there were other volumes to include then they must now be defined, however in this

example, the universe shall be terminated at the outer boundaries of the cube. Thus the remainder of the universe is defined as (1:-2:3:-4:5:-6), where the ":" operator means logical union. The elegance of the CG method makes MCNP the most widely used radiation transport code worldwide.

Source Definition

Another crucial aspect of MCNP modelling is the source definition. MCNP has a number of internal probability distributions, such as the Watt fission spectrum, which allow a large number of potential source distributions to be created. It is beyond the scope of this thesis to fully describe all the possible source definitions, so an example will be given. Consider defining an electron source, which is uniformly distributed across a cube of side 6 cm centred on the origin, the electrons that are born are to be exponentially distbuted in energy from 3 to 18 MeV. The electrons are to be born with a vector pointing along the z-axis and have a uniformly distributed deviation from this vector of $\pm 45°$. Such a source would be defined thus;

```
SDEF X=D1 Y=D2 Z=D3 ERG=D4 VEC=0 0 1 DIR=D5 PAR=3
SI1 -3 3
SP1 0 1
SI2 -3 3
SP2 0 1
SI3 -3 3
SP3 0 1
D4 -5 3
SI5 -1 0.707 1
SP5 0 1
```

The keyword SDEF calls the MCNP source subroutine, which expects a number of parameters to be defined, otherwise the default values are assumed. In this case X,Y and Z are defined by distributions; D1, D2 and D3 respectively. In this case X,Y and Z are each sampled uniformly from -3 cm and 3 cm about the origin. Energy, ERG,

is defined by distribution D4 and is sampled from 3 to 18 MeV with an exponential probability distribution. The vector from which direction, dir, is sampled is defined as 0 0 1, hence the vector points along the z axis. The direction, cos(θ) is sampled from the distribution D5, and specifies that there is 0 probability of being between -1 and 0.707, with a probability of 1 for directions between 0.707 and 1.

Tallies

Another important concept within MCNP is the use of tallies. Tallies are particular regions of the model where either surface particle current or flux (F1 or F2), particle flux in a cell (F4), particle heating (F6), or other tallies as desired. Thus the code will now output the tally in average weight per source particle.

The two most important tallies for this thesis are the flux tallies, F2 and the F4 tally, and the F6 heating tally shown in equations 3.3, 3.4 and 3.5 [22] respectively, and are defined thus

$$F2 = \frac{W}{|\mu|A} = \Phi_S = \frac{1}{A}\int dE \int dt \int dA \int d\Omega \phi(r, \Omega, E, t) \tag{3.3}$$

$$F4 = \frac{WT_l}{V} = \Phi_V = \frac{1}{V}\int dE \int dt \int dV \int d\Omega \phi(r, \Omega, E, t) \tag{3.4}$$

$$F6 = WT_l\sigma_t(E)H(E)\frac{\rho_a}{m} = \frac{\rho_a}{m}\int dE \int dt \int dV \int d\Omega \sigma_t(E)H(E)\phi(r, \Omega, E, t) \tag{3.5}$$

where W is the sum of the statistical weights of all of the particles that have crossed area A, $|\mu|$ is the cosine of the angle that is between the direction vector $\underline{\Omega}$ and the surface normal, A is the area of the surface in cm, E is the energy of the particle in MeV, t is the time since the particle was created in shakes, $\underline{\Omega}$ is the direction vector of the particle, ϕ is the angular flux of particles in cm^{-2}, Φ_S is the surface averaged flux of particles in cm^{-2}, Φ_V is the volume averaged flux of particles in cm^{-2}, r is the position of the surface, T$_l$ is the track length in the cell in cm, V is the volume of

the cell in cm^3, m is the mass of the cell in g, σ_t is the microscopic total cross section in cm^2, ρ_a is the atom density in atoms/barn cm and $H(E)$ is the heating number in MeV/collision. These tallies could be energy dependent, hence the integrals over energy in Equations 3.3, 3.4 and 3.5 would be between two discrete values rather than across the entire energy range of the problem.

The F2 tally is the surface averaged particle flux and the F4 is the volume averaged particle flux. Another widely used tally is the mesh tally, which, in essence is a collection of F4 tallies, one for every voxel. A voxel, in analogue to a pixel (Picture Element), is a Volume Element, in this case the mesh tally is composed of a number of voxels each occupying a different position within the mesh. The mesh tally scores particles using a method identical to the F4 tally, except the tally is superimposed over the geometry. Qualitative examples of the 3 particle flux tallies are shown in Figure 3.4, where the arrow represents the history of a single particle. As shown in

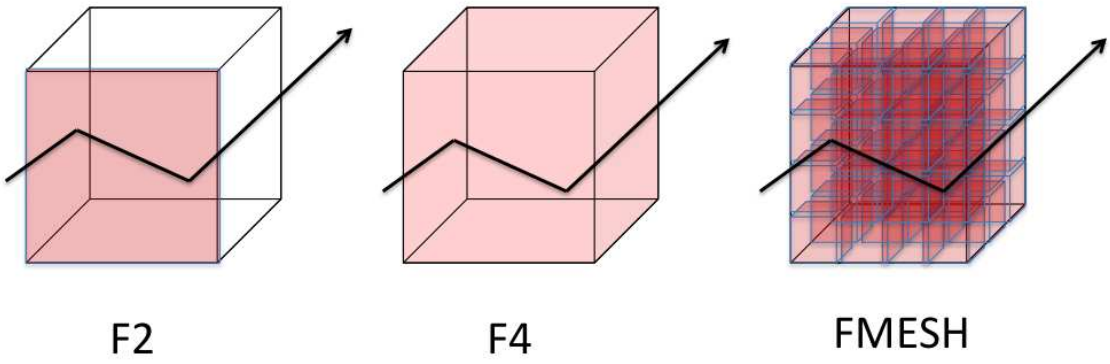

Figure 3.4: Examples of the use of MCNP tallies

left subfigure of Figure 3.4, the F2 tally records the weight of particles crossing the area of the front face of the cube, however the flux calculated is averaged over the area of the front face of the cube. The F4 tally records the weight and the track length of all particles that pass through the cube, however the flux is averaged over

the volume of the cube. However, in the right pane of Figure 3.4 is the FMESH mesh tally, which like the F4 tally gives a volume averaged flux determination, however the spatial resolution is much higher as the volume over which the average is performed is much smaller since the recording of weight and track length is performed on a regular basis within each mesh voxel.

Variance Reduction

There are some problems in MCNP where increasing the number of particles simulated by a factor of ten or one hundred will reduce the uncertainty in the result by the required amount. There is however a limit as to the number of particles than can be simulated, in 32 bit computers there is a limit in the size of an integer stored in the system, which is $2^{32} \sim 4\text{x}10^{9}$. However, the maximum signed integer is a factor of two lower than this. This ultimately means that the maximum number of particles that MCNP can perform on a 32 bit system is $2\text{x}10^{9}$. This problem is simply alleviated in the age of 64 bit computers where the largest signed integer is 2^{63}. However, this is computationally intensive and is not desirable. Thus techniques known as variance reduction are implemented. Variance reduction techniques reduce uncertainty in tallies by increasing the number of particles contributing to tallies in an unbiased way, thus reducing the variance of the tally. The mechanism of variance reduction is the killing of particles that travel to regions "unimportant" to the tally, and increasing the number of particles that travel through "important" regions to the tally. There are a number of variance reduction techniques namely; truncation methods, population control methods and modified sampling methods. There is a fourth technique that was never used in this thesis namely Partially-Deterministic methods.

Truncation methods include energy and time cutoffs, in that particle cuttoffs can be

controlled either globally or locally, and can be killed if their energy or time signature drop below specified values. A further example is that only important parts of the geometry are modelled, in that the geometry has been truncated to only include parts of interest. An example of a widely used truncation method is the energy cutoff. Particles can be tracked to an energy cutoff value, which can be defined on a cell by cell basis or globally. Once particles reach this threshold they are killed with a probability of 1. The most important cutoff is the weight cutoff, MCNP can track particles down to a weight comparable to machine precision, by this point the particle contributes negligibly to any tally, thus it is beneficial to kill particles that are below certain weight limits, and can therefore reduce computational time.

Population control methods use particle splitting and Russian roulette to control the number of samples taken in various parts of the geometry. In important regions many samples of low weight are tracked, while in unimportant regions few samples of high weight are tracked. A weight adjustment is made to ensure that the problem solution remains unbiased. Typically in shielding problems like those commonly encountered in fusion neutronics, importance splitting (importance map) and Russian roulette are the most important methods. Importance splitting dicates that every cell in the problem has an "importance" assigned to it. Low importances mean that few high weight particles are tracked in those cells, whereas high importance means that many low weight particles are tracked. If a particle of weight w_0, leaves a cell of low importance (I_1) and enters a cell of higher importance (I_2) and is absorbed in the higher importance cell, then a I_2/I_1 new particles are created with a statistical weight w, of $w_0.I_1/I_2$ each. If a particle of weight w_0, goes from a region of higher importance (I_2) to a region of lower importance (I_1) then a process known as Russian Roulette is performed, where the particle is killed with a probability of ($1\text{-}I_1/I_2$) and a new particle is created with weight w, $w_0(I_2/I_1)$. Thus, as in an

analog calculation, where all cell importances are unity, the number of simulated particles would decay with the attenuation coefficient of the problem, however in a problem with a good importance map, the number of particles would remain roughly constant throughout the problem, the total weight does not remain constant.

Modified sampling methods alter the statistical sampling of a problem to increase the number of sucessful scores per particle. For any Monte Carlo event it is possible to sample from any arbitrary distribution rather than the physical probability as long as the particle weights are then adjusted to compensate. Thus with modified sampling methods, sampling is done from distributions that send particles in desired directions or into other desired regions of phase space such as time or energy, or change the location or type of collisions. Modified sampling methods in MCNP include the exponential transform, implicit capture, forced collisions, source biasing, and neutron-induced photon production biasing [22].

Experience has shown that if neutron importance is tripled every 2 mean free paths or about 10-15cm, this means that the number of particles remains constant, although of course the statistical weight per particle is not. A new method was created during the course of this thesis, namely the MCNP Automatic Generation of Importances in Cells (MAGIC), described in the Appendix D. The method trivialises the determination of cell importances via an analog pre-run.

3.1.2 MCNP Nuclear Data

FENDL Nuclear Data Libaries

Fusion Evaluated Nuclear Data Libaries (FENDL) are now in their 3rd revision 2.1. The FENDL libraries contain ENDF formatted cross section data for various neutron induced reactions. The library contains 71 fusion relevant nuclides, which

are pointwise neutron interaction cross section information, containing information for a number of different reactions which are nuclide dependent. Pointwise data is important due to the exact nature of the data, resulting in an exact representation of transport. Pointwise data also requires no resonance correction factors, furthermore, the angular and emitted particle spectra are not approximated.

3.2 Nuclide Inventory

When materials are irradiated with neutrons a number of reactions are possible such as capture reactions (n,γ), (n,α),(n,p). Each reaction will change the nuclide that originated. Large numbers of reactions can occur such that after a long irradiation a large number of different isotopes can be generated. Due to the complexity of the number of isotopes, possible decay pathways, and analytically unsolvable reactions a consistent computational scheme must be found. The comutational problem of activation calculations have been previously examined and a number of computational schemes exist.

There are a number of nuclear inventory codes worldwide such as ALARA [44], ORIGEN [45], CINDER [46] and ACAB [47]. Each code has benefits such as speed of processing, accuracy of calculation etc. The only code that balances features and accuracy well is FISPACT (FISsion Products and ACTivation)[28]. FISPACT has its beginnings in FISPIN [48] (FISsion Product INventory), however since the 1970s FISPACT and FISPIN diverged, FISPACT was developed for fusion applications, with specific cross sections from the European Activation File (EAF) dataset. FISPACT is now the nuclear industry standard in the UK and is part the ITER benchmark code suite for activation calculations, and is the only code to include cross section uncertainties in the final activity.

The accuracy and relevance of a number of codes were benchmarked in an IAEA study performed in 1994 [49], the results of which are shown in Figure 3.5. The goal of the benchmark was to determine which codes were relevant for fusion activation calculations. FISPACT was initially tested and found to match analytic calculation to machine accuracy. The results from the remaining codes in the study were reported relative to FISPACT results. The outcome of the benchmark study that at

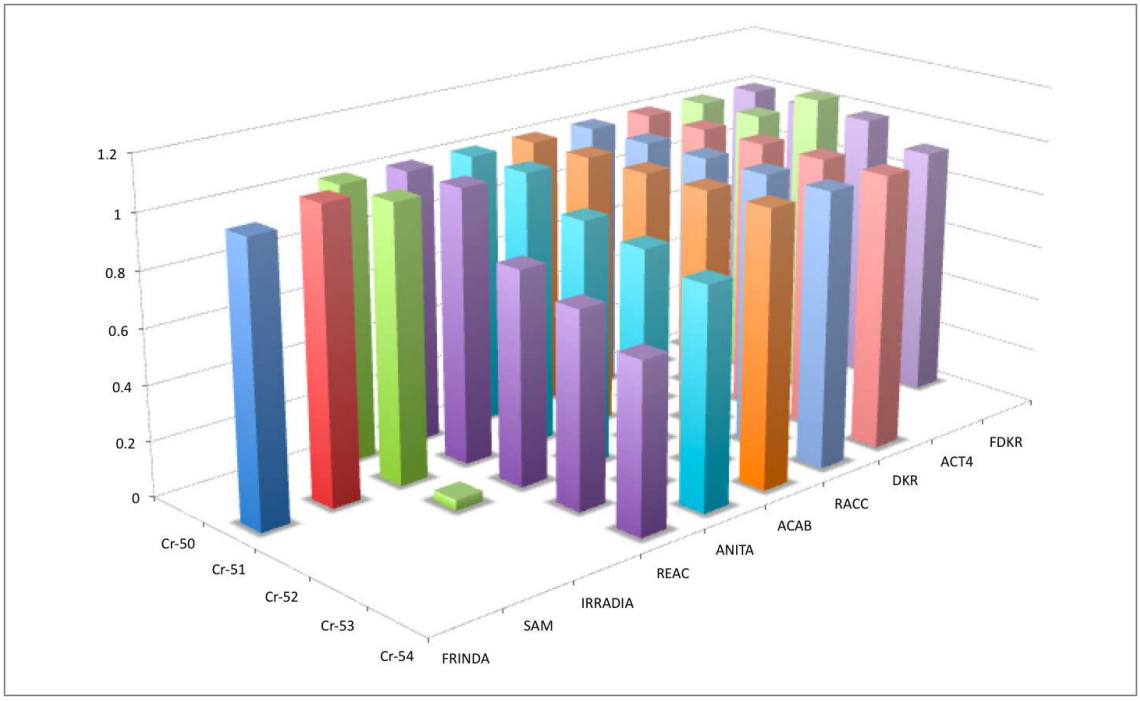

Figure 3.5: IAEA activation benchmark results [49]

the time of the report only the activation codes FISPACT and ACAB were reliable enough to perform fusion relevant activation calculations.

FISPACT was selected as the nuclear inventory code used for activation calculations in this thesis. Like MCNP there are a number of reasons for choosing FISPACT; large number of code benchmarks, use of EAF data, expertise within CCFE and personal experience.

3.2.1 FISPACT

The main task of inventory codes is to find the solution of a set of coupled differential equations that describe the amounts of atoms of various nuclides present following the irradiation of a given material in a neutron field [28]. FISPACT solves the Bateman equations, described in Chapter 2, using a number of numerical approximations.

The method used in FISPACT (and in FISPIN from which it was developed) is that of Sidell [50]. This method is an extension of the Euler (first order Taylor series) which uses an exponential function of the step length. FISPACT is a thoroughly benchmarked code with benchmarks across fission and fusion energy regimes. FISPACT has also been benchmarked with analytic problems such as those involving simple production and decay reactions.

Once the code has solved $N_i(t)$, any remaining parameters of interest can be calculated such as activity with knowledge of the decay constants, gamma ray spectra given decay gamma ray line data, and so forth. Data required for folding with the nuclide inventory in order to calculate derived data such as decay heat or hazard index are contained within the EAF libraries.

3.2.2 EAF Data Libraries

The EAF 2007 data libraries used in calculations for this thesis contain information on 65,565 possible reactions with interactions possible on 929 targets. The libraries include data for neutron, deuteron and proton induced nuclear reactions. The libaries also include decay data, IAEA A2 transport data, and a number of other important parameters. The data that make up the point-wise file are then processed into numerous group-wise files with different micro-flux weighting spectra to meet various user needs. Uniquely, an uncertainty file is also provided that

quantifies the degree of confidence placed on the data for each reaction channel.

3.2.3 Modelling Pulsed Irradiations

The nature of experimental tokamaks means that neutron production is pulsed due either to limitations in the systems or failure of components or power supplies. The computational difficulty is also increased as the bombarding neutron flux, ϕ, is no longer a constant in time and results in ϕ in Equation 2.6 becoming $\phi(t)$ resulting in Equation 2.6 becoming non-linear. The pulsing schedule for ITER is variable across the lifetime of the device, the start up phases contribute no activity, indeed, despite there being 3 years of DD operation prior to the first DT operation, it has been calculated that 3 years of DD operation is equivalent to a single 10 minute DT pulse, in DT mode there are projected to be some 41,751 pulses [51]. However, it is impractical to model such a high number of pulses, instead it is sufficient to model the majority of pulses as a single "equal fluence" irradiation, shown schematically in Figure 3.6. The method is that used by [52] summarised for convience here. There

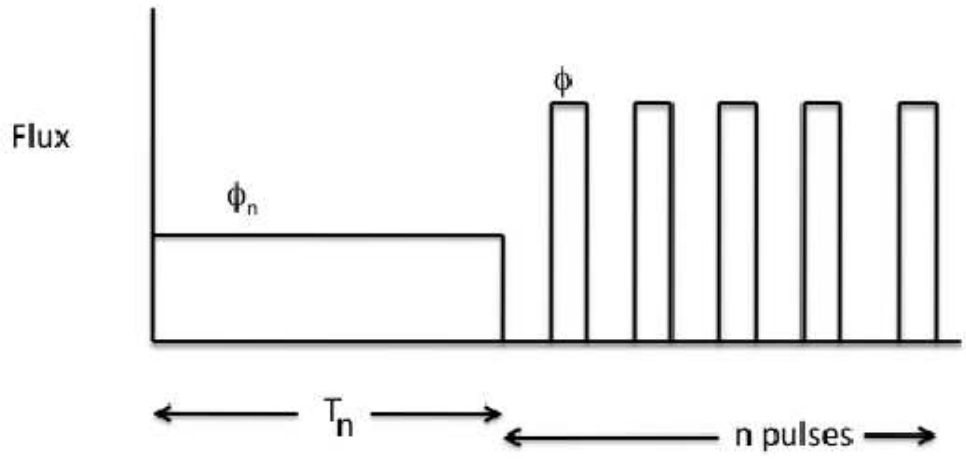

Figure 3.6: Schematic of an example pulsing schedule

are a number of criteria for this averaging technique to be accurate;

- total elapsed time before shutdown is constant
- total neutron fluence is constant

If the length of a pulse is θ and the length of the dwell (off) time is Δ, and there are N pulses in total, then the time for continuous operation, T_n and the value of this flux, ϕ_n, where n is the number of pulses to be modelled explicitly, are given by

$$T_n = (N-n)\theta + (N-n-1)\Delta \tag{3.6}$$

$$\phi_n = \frac{(N-n)\theta}{(N-n)\theta + (N-n-1)\Delta}\phi \tag{3.7}$$

Using this approximation for modelling irradations is convenient and accurate [52], in order to account for the correct build up of short lived nuclides it is necessary to model the last 20-40 pulses of an irradiation in order to be within 1% of the correct activity after 14 days decay time.

Chapter 4

ACTIVATION SOURCE GENERATOR FOR MCNP

This chapter describes the work completed on the activation source generator for MCNP. An activation source generator is a piece of software that produces a gamma ray source for a shutdown photon transport calculation, typically by using an inventory code. The main task was the development and benchmarking of a mesh based activation source generator. The benchmarking of the Mesh Coupled Rigorous 2 Step (MCR2S) system is described in the next chapter. MCR2S is a mesh coupled activation code that couples the results of neutron transport calculations to a nuclear inventory code in order to produce a shutdown gamma ray source for further photon transport calculations. Such systems allow more accurate shutdown gamma ray dose calculations to be performed than in previous analyses, for example [53, 54, 55, 56, 57].

4.1 Introduction

In magnetically confined fusion systems like JET or ITER, the shutdown gamma dose rate often is the defining safety parameter of neutronic studies. In the case of

ITER, an example is the port interspace behind the equatorial port plugs where the shutdown gamma ray dose rate must be less than 100 μSv hr^{-1} 14 days post shutdown. The ionising radiation dose limits are provided by the host country, which are those of the French nuclear industry, which can be found in Table 2.4.

In fusion nuclear systems like ITER and JET it is the distribution of activity that define the shutdown gamma ray dose. Accurate calculation of the shutdown gamma source and subsequent dose field is therefore an important goal of neutronic calculations for ITER and other fusion power devices.

The are a number of methods of calculating the shutdown gamma ray dose. Some include approximations in a number of the defining parameters. These are the three main computational methods of calculating shutdown gamma ray dose;

1. (FISPACT) contact doserate
2. Direct 1 Step method
3. Rigorous 2 Step method

In the list provided above the order is of relevance, the higher in the list the less accurate and more computationally fast the method is. For example FISPACT contact doserate is acceptable for the comparison between concept designs, but as an actual health physics calculation would be inadequate. The three methods are described and compared in the next 3 sections.

4.1.1 FISPACT Contact Dose

The inventory code FISPACT has the facility for the calculation of contact dose rate of the material being simulated. The contact dose approximation is based on that of Jaeger [58]. The approximation assumes a constant distribution of activity

throughout a semi-infinite slab of material. The dose at the surface of the slab is given by

$$D = 5.76 \times 10^{-10} \frac{B}{2} \sum_{i=1}^{24} \frac{\mu_a(E_i)}{\mu_m(E_i)} S_v(E_i) \tag{4.1}$$

$$S_v = E_g N_g A(t) \tag{4.2}$$

where D is the contact dose in Sv h^{-1}, E_i the mean energy of group i, μ mass attenuation coefficient of air (a) or material (m), B build-up factor, S_v rate of gamma emission in MeV kg^{-1} s^{-1}, E_g gamma energy in MeV, N_g line intensity and A specific activity. The build-up factor is a mathematical artefact accounting for scattered radiation in shielding applications, and has a default FISPACT value of 2.

The contact dose approximation provides valuable information for the comparison of the shutdown dose between different materials and neutron flux, and combined with powerful software such as FISPACT it can be used to investigate dominant nuclides and reaction pathways responsible for the activation dose, as shown in other parts of this thesis. The conditions assumed, however, are far from those encountered in a real activation problem with a largely distributed and spatially variable decay gamma source. Firstly, the contact dose approximation does not take into account the actual 3D geometry of the photon transport. Furthermore, the contact dose approximation does not account for variable activation levels within the geometry of interest; in most real situations of neutron-induced activation, neutrons are attenuated at an approximately exponential rate as they travel from the source and into the material, and the activation levels decay accordingly. The contact dose approximation will overestimate the dose in regions of the geometry where the activity is decaying with depth (e.g. plasma facing components) and underestimate it in regions where the activity increases with depth (e.g. at the rear of a thick shield) as a result of its over or under-estimation of the activity level, respectively; this is

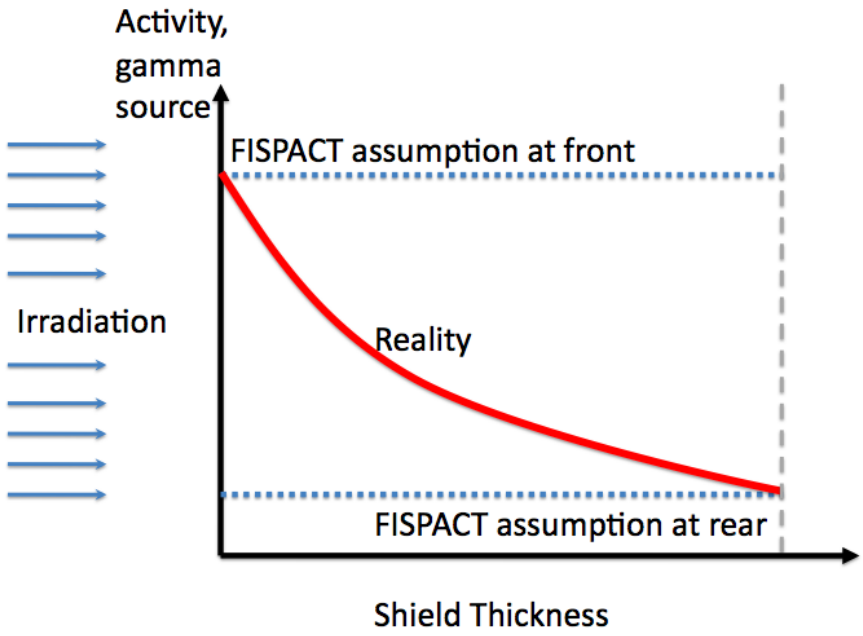

Figure 4.1: Description of the FISPACT contact dose approximation [59]

qualitatively illustrated in Figure 4.1. This overestimation comes from the fact that the real activity is distributed exponentially away from the neutron source, thus at the far side of the shield the photons born have the smallest amount of shielding to pass through, however the shielding thickness increases with depth into the shield, thus given that the contact dose approximation has assumed that the activity is distributed at the same level throughout the entire shield, missing the exponential increase of activity with depth, hence under-predicting the dose rate. Conversely, at the front of the shield the activity decreases with depth, but the contact dose approximation assumes that the activity remains constant with depth, hence compared to real situation overestimates at the front of the system. Furthermore, it does not account for penetrations the hot spots that can arise due to neutron streaming along them.

4.1.2 Direct One Step Method

The Direct One Step (D1S) method [60, 61] treats irradiations as one continuous irradiation at a single power level, and only treats single step reactions for example, (n,γ) reactions where a full inventory code would treat multistepped reactions such as (n,2n)X(n,p)Y(n,γ). Due to this simplified treatment, corrective factors must be introduced to account for the decay of the gamma emissions. These factors are usually determined by a full nuclear inventory code such as FISPACT. A further limitation is under conditions of extreme burnup.

The method is typically applied as a modified version of MCNP which replaces the prompt gamma ray data with decay gamma ray data. An example of this is replacement of the ^{59}Co(n,γ) gamma ray with gamma rays from the decay of ^{60}Co. The result of this calculation would be one where every isotope has the same production rate. The neutron/photon transport code must also be modified for the new data and there is a resulting "Activation level modification". This code modification would not be a problem, however the modifications required are in the `acegam.f` subroutine which is required even in non-activation photon problems, thus meaning there needs to be two MCNP executables when running standard problems, one for a normal neutron/photon run and one of the neutron/photon activation run.

When photons are created, each gamma ray coming from a specific nuclide is started with an identifying time index, for example the 1173 keV and 1332 keV gamma rays from the decay of ^{60}Co would start with the same time index, however the 811 keV from ^{58}Co would start with a different time index. This time index, shown qualitatively in Figure 4.2, is used to distinguish between gamma rays coming from multiple sources, such that the relative amounts can be modified at the end of the simulation according to the build up and decay of the nuclides. The simulation is

then performed, binned in both time and energy, thus allowing us to distinguish between each isotopes contribution to gamma ray flux or dose. Once the particular

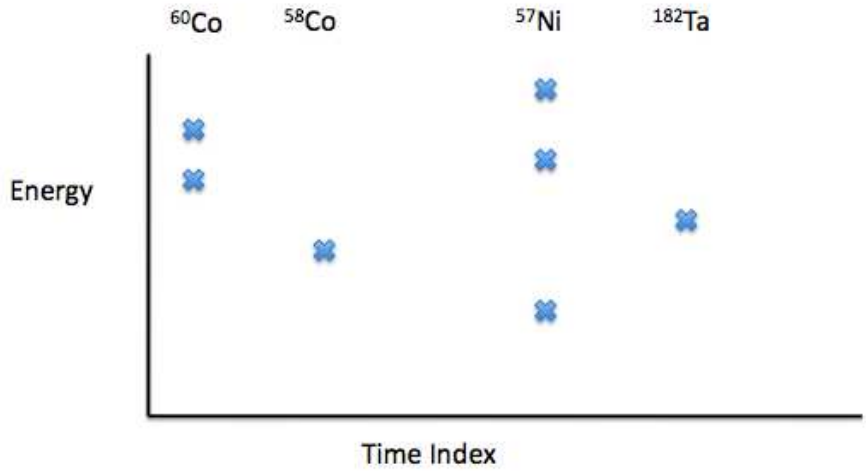

Figure 4.2: Qualitative illustration of the time binning in the D1S method

irradiation scenario has been determined, the ratio of the actual activation level and the direct production rate can be calculated, and this depends on the decay constant and cooling time for the isotope that has a simple activation chain. Complex activation chains such as those with backward steps are necessarily calculated using FISPACT. The results of the FISPACT calculation determine corrective factors for the D1S run. These corrective factors are necessarily imprecise since they are generated for a single neutron spectrum at a single location in the model.

In simple benchmark studies [60] the D1S method performs well and slightly overestimates the actual gamma ray flux. However, there are a number of limitations with regards to the D1S method. One of the main limitations of the D1S method is that the neutron transport and decay steps are performed at the same time, this means that the model can not be changed for the decay step, hence the removal of components can not be accounted for.

4.1.3 The Rigorous 2 Step method

The Rigorous 2 Step (R2S) method as the title suggests breaks the transport-activation calculation into 2 steps, firstly a neutron run is performed to calculate the neutron spectrum in locations of interest which may be a small number of specific locations or a large distributed volume. A nuclear inventory is calculated for every location specified using the appropriate neutron spectrum as input. When all the inventory calculations are complete, they define a number of gamma ray source distributions in space and time, which are then used in the second step of the calculation. The R2S method was concieved by Chen et al. [62]. These sources are then used to perform the gamma ray transport calculation in order to determine the shutdown gamma ray spectra or other such derived quantities.

The R2S method has proven to be the most accurate way of calculating almost any nuclear quantity involving neutron activation. The R2S makes no approximation with regard to transport, activation and subsequent gamma transport.

MC-FISP

A code exists for performing R2S calculations called MC-FISP (Monte Carlo - FISPACT) [62]. This C program is a link between a number of MCNP F4 tallies and FISPACT to perform the activation calculations. The use of FISPACT as the activation module of the code means that MC-FISP can use the high quality EAF nuclear data libraries and hence include all nuclides relevant for fusion. The entire sequence of neutron spectrum, activation and source definition are ultimately linked back to MCNP F4 type tallies, ie flux in a cell, which means that the calculation is implicitly coupled to the geometry. The implicit linking of F4 (volume averaged) flux tallies means that in the sometimes large neutron flux gradients very small cells often need to be used, for example as in the case of the upper port ECRH

launcher for ITER, shown in Figure 4.3. The fact the MCFISP is limited to the ge-

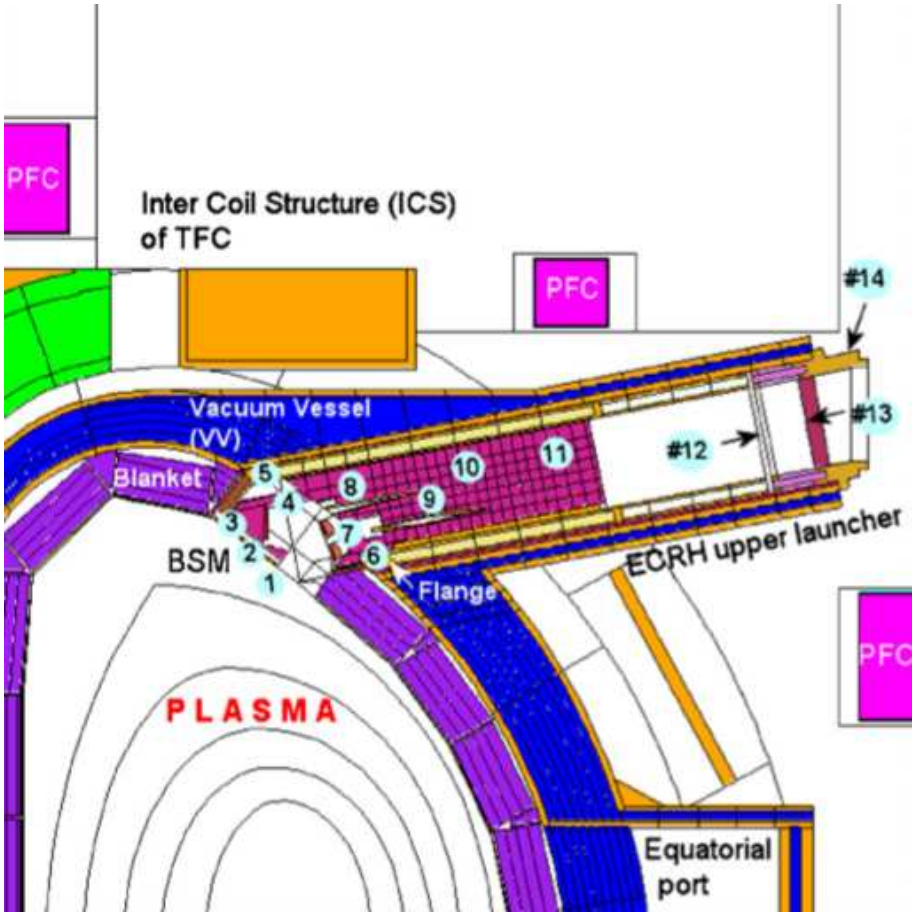

Figure 4.3: MCFISP cell splitting in the ITER ECRH [63]

ometry implies a number of considerations. When creating the transport geometry the requirements of MCFISP must be considered continually throughout the model creation process and leads to a finer geometry splitting than would optimally be considered to account for the activity variation. Furthermore, the cell splitting that is introduced will generally be larger than the photon mean free path, in some cases the cell splitting is several times the photon mean free path. This can have a large effect upon the accuracy of the final result. A further limitation is the shutdown gamma ray source defined for that specific transport geometry, meaning that this source can not simply be used on another geometry, which is desirable in certain circumstances.

ATTILA ASG

Recently the discrete ordinates neutron and photon transport code Attila by Transpire Inc includes a prototype activation source subroutine. At present it only includes a limited number of isotopes for fusion relevant applications in its nuclear data libraries. The activation solver is known as FORNAX [64] and is a modified version of the ORIGEN [45] inventory code. The purpose of FORNAX is to solve the Bateman equations for a given neutron field. FORNAX does this by considering the solution to the Bateman equations as a two dimensional matrix. Operations are then performed on this matrix in order to determine the concentration of various nuclides as a function of time.

One of the current limitations of the FORNAX solver is that of the quantity and quality of the nuclear data. Currently ATTILA only includes the ORIGEN-S [65] light element, actinide and fission product libraries. The data supplied is only in 3 energy groups namely thermal, resonance and fast.

4.2 Mesh tally Coupled Rigorous 2 Step

Due to the limitations of the previous R2S software, it was decided to develop a new tool that incorporates the most recent features of modern transport and activation codes. This software should overcome the limitations of previous software, which in summary are;

- Laborious splitting of the transport geometry
- Full treatment of neutron source pulsing
- Full accurate treatment of multistepped reactions
- Non portable photon source

- Be able to use the EAF dataset (eg FISPACT)

To remove the limitation of laborious geometry splitting we can use the newest feature of MCNP5 v1.4 which is the particle mesh tally. A mesh tally is a type of particle tally recently introduced into MCNP and is in essence, a collection of F4 tallies superimposed over the transport geometry. The mesh being superimposed over the geometry means that particles can be tallied and hence the spatio-energetic distribution of flux determined without the need to tally in every single geometry element of the model. Thus the geometry can be constructed almost arbitrarily or focussed on the optimisation with regards to neutron transport. The accurate treatment of pulsing and multi stepped reactions can be accomodated by the coupling of the neutron transport steps to a full inventory code such as FISPACT. The non portable requirement source problem can be solved, this will be discussed later in this chapter.

Thus in order to overcome the limitations of previous software the transport code MCNP5 v1.4 was selected in part due to the mesh tally capability of the code. The results of a neutron mesh tally are coupled in a consistent manner with FISPACT 2007, which are then processed into a photon source for a subsequent photon transport calculation using MCNP. This coupling of mesh tallies and activation calculations in a manner consistent with the R2S method led to the creation of the code Mesh Coupled Rigorous 2 Step (MCR2S).

The MCR2S code is a collection of Unix scripts and Fortran 90 programs that allow the calculation of R2S shutdown dose rates with input specifically designed for MCNP. A flow diagram showing the calculation flow can be seen in Figure 4.4. A description of MCR2S modus operandi and functionallity follows. In summary, two pre-MCR2S runs must be performed. The first neutron run determines the spec-

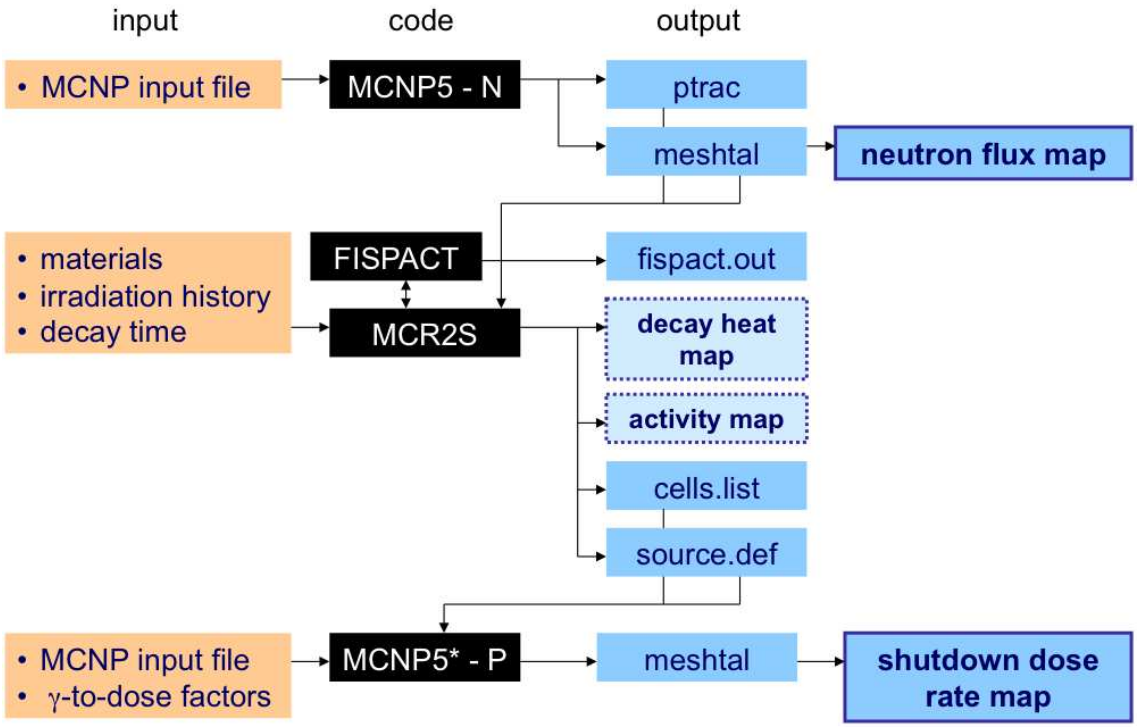

Figure 4.4: MCR2S Computational Flow Chart

trum in all locations of interest. The second determines the material distribution under that mesh.

4.2.1 MCR2S Input

Neutron Run

Firstly a neutron transport calculation must be performed with a mesh tally covering the geometry or the parts of the geometry that are to be irradiated. Variance reduction is important when performing calculations of this detail. When performing calculations using the mesh tally capability of MCNP, the resolution of the mesh determines the spatial accuracy of the calculation. If only considering the total neutron flux, resolution is strictly limited by computer memory. However, if the mesh resolution is very fine, a small number of particles are likely to enter that

particular voxel[1], an even smaller number of particles are likely to enter when neutron attenuation is factored in. Hence, variance reduction is required in order to reduce the uncertainty of the flux in any voxel. This is further complicated when considering the necessity of accurately accounting for cross section resonances of nuclides by tallying in a certain number of energy bins. In fusion problems the 175 group VITAMIN-J[2] format is typically used in order to account for the multitude of potential nuclide cross section resonances in the calculation. In order to avoid propagating a large uncertainty through the activation calculation it is necessary that the statistical error quoted for every voxel in the mesh tally to be less than 10% in every energy group, although ideally smaller. For fusion neutronics calculations it is recommended that the VITAMIN-J energy group structure be used, however MCR2S is capable of taking 69, 100, 175, 211 or 315 neutron energy group structures. These formats are standard energy binning formats in neutronics. The output of this computational step is the meshtal file, which fully defines in space and energy the neutron flux for the activation part of the run.

Ptrac file and Material Mapping

Having completed the neutron run and determined the neutron spectrum across the mesh tally to a sufficient accuracy, a so called "ptrac run" must be used with the geometry in which the decay gamma distribution is to be calculated. The decay gamma distribution geometry need not be the same as the irradiation geometry, this is to allow for the situation where certain parts of the model are removed which correspond to situations where items are removed for maintence, such as the ITER equatorial ports. An example of which is shown in Figure 4.5, where the first model represents the neutron transport geometry and the second the activation or decay geometry. This means that the neutron transport step is performed which deter-

[1]voxel - volume element, analagous to pixel - picture element
[2]Vitamin-J structure - with the structure shown in Appendix E

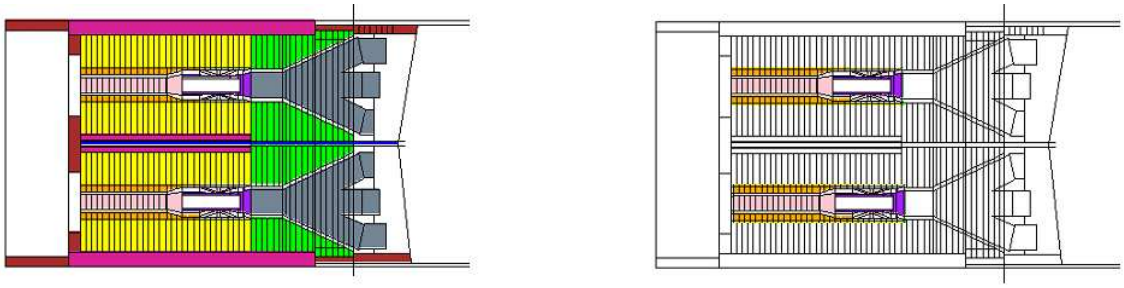

Figure 4.5: Example of differing transport and decay models, where different colours represent different materials and white represents void

mines the neutron spectra in situ, however the activation part of the code only needs to determine the gamma dose from the relevant parts of the geometry. The purpose of this calculational step is to determine the various material distributions in the geometry, allowing the volume fraction of all materials that lie under any particular mesh voxel. This information is used later in order to determine an average representative material for every voxel.

In MCNP the code word `ptrac` makes MCNP print out every particle's tracking history, which contains details of every interaction the particle underwent. The so called, ptrac run, is the calculational step where a particle source is uniformly distributed across the entire mesh, all other considerations of the source can be ignored such as the angular, energy and temporal distribution since they are irrelevant to the requirements of this calculational step. The most significant aspect is this, the source must be distributed across the mesh such that the probability of a single particle being born in any voxel, irrespective of voxel volume is equal. Hence with a ptrac run a list of the starting co-ordinates of every particle and the material in which the particle was created is sought. If, for example we consider a single mesh element, shown in Figure 4.6, where the left panel of the figure shows the geometry that underlies the mesh containing some material and some void, this is the geometry in which particles are created. The second frame of the figure shows the starting

coordinates of the particles that were born in this mesh voxel, when the number of source events are counted per material, the relative fractions of material and void can be determined, thus allowing the calculation of the average material composition of the voxel, shown in the last pane of Figure 4.6. The source must be uniformly

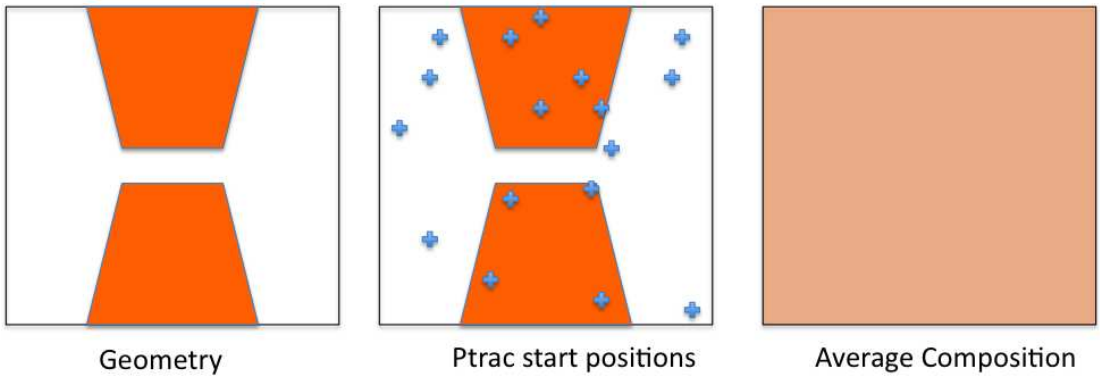

Figure 4.6: Diagram of stochastic volume fraction calculation for singe mesh element

distributed across the mesh, this requirement is for estimating the uncertainty in the material composition, it is however not a strict requirement. The ptrac run is generated by using an MCNP source thus;

```
SDEF X=D1 Y=D2 Z=D3 PAR=1
SI1 X_min X_max
SP1 0 1
SI2 Y_min Y_max
SP2 0 1
SI3 Z_min Z_max
SP3 0 1
```

Furthermore in the MCNP input which is being run to generate the ptrac file, the following ptrac options must be used;

```
ptrac event=src meph=1 file=ascii
```

This tells MCNP to only print src events, with a maximum number of histories per event to be 1 and for the output format to be ascii. This step is important as

the preprocessing of the code relies on the source events in the ptrac file. When MCNP outputs the source events it is an ordered list of starting: position (x,y,z), direction (u,v,w), energy, cell, material number, surface and event number. Thus the list of above variables is processed such that there is now a list of positions (x,y,z), cell number and material number, thus facilitating a 3-dimensional understanding of the material distribution.

The materials in the model must be renumbered from their arbitrary state to be sequentially ordered from 1 to N, where N is the last material. This step is for user satisfaction since MCNP prints out material number starting from 1, rather than the user specified material number which can be anything from 1 to 999. Furthermore, the void material must be renumbered to some dummy material, typically N+1. The ptrac file generated this way then allows the code to determine the materials distribution in the decay model, ultimately this means the creation of the `posmat.txt` and `cells.list` files. The `posmat.txt` and `cells.list` files contain the spatially dependent volume fraction information and the spatially dependent cell distribution respectively. The `cells.list` file is required for the final photon transport calculation. It is read during the starting phase of the calculations and allows the MCR2S MCNP subroutine to know the distribution of cells within each voxel.

Irradiation and decay times

The irradiation history must be included in FISPACT format and MCR2S can handle arbitrary irradiation schedules. The flux is quoted as a fraction of the neutron source normalisation, for example;

```
FLUX 1.0
TIME 360 DAYS
ATOMS
```

```
FLUX 0.05
TIME 5 DAYS
ATOMS
FLUX 0.0
TIME 6 HOURS
ATOMS
```

The above code would generate a fractional flux of 1.0 for 360 days, a fractional flux of 0.05 for 5 days and finally a zero flux for 6 hours. When this value is passed to the code, it is transformed from fractional flux to absolute flux, ϕ_r, by

$$\phi_r = S_n T_r f \tag{4.3}$$

where S_n is the neutron source normalisation, T_r is the mesh tally value at that voxel location and f is the fractional flux quoted in the `irradiation.dat` file.

Similarly, the decay times of interest must be included in FISPACT format, which tells the code to determine the photon source at specific decay times. This is done by including a file called `decaytimes.info`, the form of which is shown below.

```
TIME 1 HOURS SPECTRUM << 1 HOUR >>
TIME 4 DAYS SPECTRUM << 97 HOURS >>
TIME 10 DAYS SPECTRUM << 337 HOURS >>
TIME 300 YEARS SPECTRUM << 300 YEARS >>
```

The part of the code included between angled braces are comments, these allow the cumulatitive time to be monitored. It should be noted that this is standard FISPACT syntax, hence the decay times are cumulatitive, hence `TIME 4 DAYS SPECTRUM`, is actually after a decay time of 4 days plus 1 hour.

Material input

The material information must also be included, which is specified in standard FISPACT form. There must be a material file, `*.mat` file, for every material present

in the problem, including an extra material for the void, the material for which should be defined as hydrogen with a density of 0.00001 g cm^{-3}. The format of a material file is shown below.

```
DENSITY 8.3
MASS 1.0 4
H 0.33
O 23.4
C 13.67
W 62.6
```

Density is the mass density of the material quoted in g cm^{-3}. The `MASS` keyword specifies to the code that the irradiation of 1 kg of material should be performed, which is composed of 4 elements. The list of elements present follows and quotes mass fraction.

Thus having defined fully the `irradiation.dat`, `decaytimes.info`, `*.mat`, and the input file, the calculation can now be run.

4.3 MCR2S Activation Subroutine

When the calculation is finished, a shutdown gamma ray source file will be output for each decay step specified in the decay times file. These data are then preprocessed into a form which a bespoke MCNP subroutine can read. This subroutine uses MCNP global variables in order to assign photon weight, energy, direction of travel, starting position. Now a photon mesh with a dose response function or standard flux or heating tallies could be used. An example of the output, which is broken into two files namely the `files*.txt` and `ergs*.txt`, where * can be replaced by any of the decay times quoted in the `decaytimes.info` file. The syntax of the `files*.txt` file is shown below.

`int` x_{cen} y_{cen} z_{cen} s_n`(x,y,z)`

s_n(x,y,z)=V(x,y,z)*ρ_γ(x,y,z)

Where int is an arbitrary integer, x_{cen} is the voxel x centroid in cm, y_{cen} is the voxel y centroid in cm, z_{cen} is the voxel z centroid in cm, s_n(x,y,z) is the absolute source strength in this voxel in s^{-1}, V(x,y,z) is the volume of the voxel at x,y,z, in cm^3 and $\rho_\gamma(x, y, z)$ is the photon density at x,y,z in cm^{-3} s^{-1}.

The variable s_n(x,y,z) is used as the normalising factor, it is the product of the volume of the voxel and the photon density calculated by FISPACT. The other file(s) output by MCR2S are the `ergs*.txt` files. The `ergs*.txt` file is a voxel by voxel list of the total number of photons in every one of the 24 energy groups, in a format shown below;

int

E_1

E_2

E_3

...

E_{24}

Where the `int` is a dummy variable used in post processing and E_i are the photon densities in each group. The full file will have a long list of variables with the format shown above.

4.4 MCR2S Data Processing

In order for the MCNP source subroutine to sample as efficiently as possible, the absolute minimum of calculation should be performed by the source subroutine. Thus the output of the activation calculations are preprocessed to a specific format. The preprocessing subroutine `preprocess.f90` takes the `files*.txt` and `ergs*.txt` files and creates a `source*.def` file for each decay time and produces a file called `source.norm`, which contains the source normalisation (photons per second) for each decay time. The source normalisations are required to convert F2 and F4 (including mesh tallies) into a true photon flux.

The form of the `source*.def` file is shown below;

X_{min} X_{max} Y_{min} Y_{max} Z_{min} Z_{max} Pr(x,y,z) Cumpr(E_1).....Cumpr(E_{24})

where X_{min} the minimal x co-ordinate of the voxel in cm, X_{max} the maximal x co-ordinate of the voxel in cm, Y_{min} the minimal y co-ordinate of the voxel in cm, Y_{max} the maximal y co-ordinate of the voxel in cm, Z_{min} the minimal z co-ordinate of the voxel in cm, Z_{max} the maximal z co-ordinate of the voxel in cm, Pr(x,y,z) is the normalised probability of the voxel and Cumpr(E_i) is the cumulatitive probability of the ith energy group.

The file format was chosen such that the MCNP source subroutine had the least amount of calculation possible.

4.5 MCR2S MCNP Source Subroutine

In the previous section the logic of the activation module and preprocessing of MCR2S was described. Having performed these, the transport of the decay gamma photons must now be performed, with the positional variation of source strength and photon spectra defined according to the activation calculation. To define a source subroutine in MCNP a number of internal variables must be set, each particle that is started by MCNP has to have the following defined; `xxx,yyy,zzz,erg,wgt,tme,uuu,vvv,www,icl` and `sur`.

The variables `xxx`,`yyy` and `zzz` correspond to the x,y and z co-ordinates in cm of the starting particle. The variables `uuu`,`vvv` and `www` are the angle cosines of the direction vector in the x,y and z directions resepectively. The variables `erg`, `wgt` and `tme` are the energy (in MeV), the statistical weight and time (in shakes[3]) of the particle. The variables `icl` and `sur` are the starting cell of the particle and should the particle start on a surface in the problem it can be defined as such. However, due to the infinitesimal probability of a particle starting on one of the problem surfaces, the variable sur is set to 0.

Thus the MCR2S MCNP subroutine must define all of the above listed variables. At the stage of calling this subroutine, the code reads the `cells.list` and a specific `source.def` file. There are only two variables which are constant in all problems, namely `sur` and `tme` both of which are set to 0. When the `mcr2s.f90` subroutine is called by MCNP `uuu`, `vvv` and `www` are set by the code, and are always uniformly distributed random numbers, hence giving an isotropic distibution of direction in every voxel.

[3]Shakes - 10^{-8} s

Firstly let us consider the definition of x,y, and z co-ordinates of the starting particle. This is done by selecting a random x,y and z co-ordinate between the upper and lower spatial limits of the mesh, the method of which is described in Equation 4.4

$$\texttt{xxx} = (x_{max} - x_{min}) * \texttt{ranr()} + x_{min} \tag{4.4}$$

where `xxx` is the MCNP variable for the x co-ordinate in cm, x_{max} is the upper limit of the mesh in the x direction in cm, x_{min} is the lower limit of the mesh in the x direction in cm and `ranr()` is the intrinsic MCNP uniform random deviate generator.

Similarly there are equivalent functions for both the y and z directions. Thus the Equation 4.4 will return a uniformly distributed x co-ordinate in the range x_{min} to x_{xmax}. At this stage the subroutine has now assigned the starting coordinate of the particle. From knowledge of x,y and z, the subroutine determines which voxel these co-ordinates lie in. The subroutine now determines the probability of the particle being born in that specific voxel, read from the variable Pr(x,y,z). However, in selecting the x,y and z co-ordinates uniformly, we have already introduced a further bias, since the probability of selecting a particular voxel is proportional to the volume of the voxel, thus by multiplying through by the inverse of the fractional volume of the voxel we correctly modify `wgt`.

$$\texttt{wgt} = \frac{Pr(x,y,z) \sum_{x_i=1}^{N} \sum_{y_i=1}^{M} \sum_{z_i=1}^{L} V(x,y,z)}{V(x,y,z)} \tag{4.5}$$

Thus far `wgt`, `xxx`, `yyy` and `zzz` have been defined. Having determined the statistical weight of the particle, we must now determine the photon energy.

The energy data is input as the cumulative probability i.e. the first energy group contains the probability of the photon being born with an energy in the boundary 0→0.01 MeV, the 2nd group contains the probability of being born in either the first or the second group, and so on until the last group, where the probability of the photon having an energy between 0 and 20 MeV is 1. The energy of the particle is sampled by the canonical integral method. The energy groups are listed as those shown in Table 4.1. The cannonical integral method uses a uniform random deviate and another value to compare against. Consider a function, f(x), where

$$F(x) = \int f(x)dx \tag{4.6}$$

by definition

$$\int_{-\infty}^{+\infty} f(x)dx = 1 \tag{4.7}$$

Hence a uniform random deviate can be used to select a random value of x

$$F(x) = \int_{-\infty}^{x} f(x)dx = r \tag{4.8}$$

Comparing the value of this integral against a uniform random deviate, the corresponding value of x can be selected. Thus consider Figure 4.7 which shows the fractional value of the cumulatitive integral to that bin divided by the total value of the integral across all bins. For example, consider Figure 4.7, if the random number chosen was 0.6679321, then the corresponding x value selected would be 4.

Thus the code generates a uniform random deviate and compares to the value of each bin in turn until it locates the correct position. In MCR2S this sum is calculated for 24 photon energy groups, thus generating a random number and comparing it to this integral we determine the variable `erg`. The energy groups are limited to 24

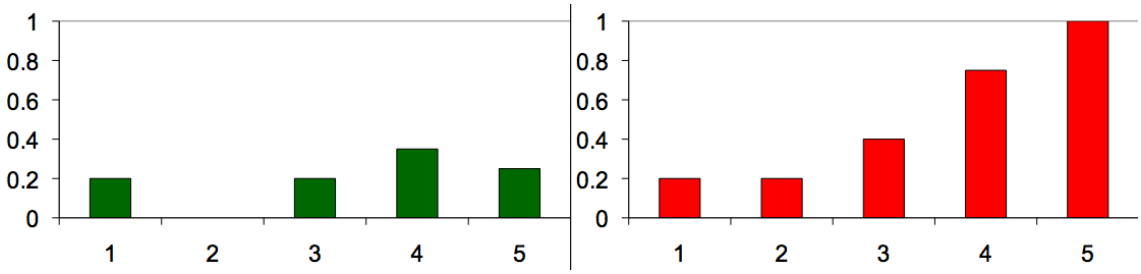

Figure 4.7: Cannonical integral method, f(x) - left and F(x) - right

due to this being the standard output group format for FISPACT photon spectra. The energy bounds are shown in Table 4.1, with the last energy group having no upper limit, however it is unlikely that many photons will ever be in the limit and in the MCNP subroutine the value is limited to 20 MeV.

There are also a number of checks during the course of the subroutine to maximise the efficiency of the source subroutine. The first rejection component of the subroutine that ensures that the source strength is greater than 0, if it is 0 then the code immediately generates new x,y and z co-ordinates. The main time saving routine is one that checks the newly assigned cell variable, `icl`, if the material attributed to this cell is 0, then the code trys the remaining possible cells, from the cells.list file for which there are up to 6 potential source cells for that particular voxel. If all voxels are void, then the code returns to the begining of the subroutine and selects new x,y and z co-ordinates, and thus begins the process again.

4.5.1 Treatment of voids in MCR2S

The treatment of voids and materials by MCR2S is paramount to the accuracy of the final shutdown dose calculation. The way different calculational steps treat materials are shown qualitively in Figure 4.8. When the “ptrac run” is performed, as described earlier in this chapter, the material volume fractions are determined for every material in the problem. The geometric information of the model is still main-

Lower Limit (MeV)	Upper Limit (MeV)
0.0	0.01
0.01	0.02
0.02	0.05
0.05	0.1
0.1	0.2
0.2	0.3
0.3	0.4
0.4	0.6
0.6	0.8
0.8	1.0
1.0	1.22
1.22	1.44
1.44	1.66
1.66	2.0
2.0	2.5
2.5	3.0
3.0	4.0
4.0	5.0
5.0	6.5
6.5	8.0
8.0	10.0
10.0	12.0
12.0	14.0
14.0	20.0

Table 4.1: FISPACT 24 Energy Group Boundaries

tained as the ptrac run is performed on the transport geometry. At the activation stage of processing the ptrac output, all information regarding geometry is lost, because all that is output from this stage of the calculation is the volume of the voxel and the material volume fractions. MCR2S then creates an average representative material from the constituent parts appropriately defined from the volume fractions of the materials including voids. The activation calculation is then performed on this average material, however, giving the appropriate shutdown gamma ray spectrum from the activated material. When output of all the activation calculations is processed by MCR2S, the list of source strength against position, the `files` file is produced. However, when this is read into MCNP, it is known by the code that cer-

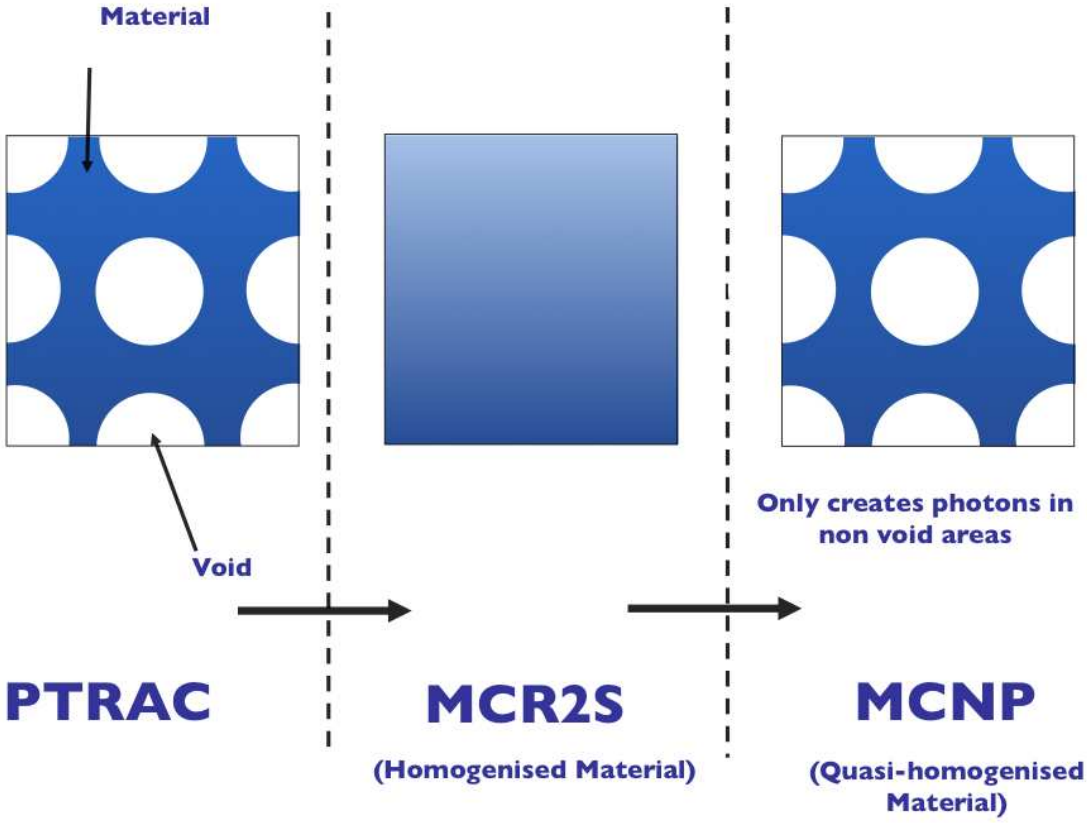

Figure 4.8: MCR2S material handling within a single voxel

tain parts of the geometry are void. Thus, a check is performed such that the source subroutine will not create photons in void regions of the model, ie only material that should emit decay photons will emit decay photons, although this spectrum is averaged over the constituent cells of the voxel.

4.5.2 The effect of mesh resolution

The resolution, or the total number of voxels, of the mesh determines the accuracy of the MCR2S calculation, since the resolution determines how well the mesh matches the geometry and the neutron flux distribution. The effect of cell resolution on MCFISP calculations was investigated in a PhD Thesis by F. Wastenerja [66]. Based on analytic calculations it was found that the dominant factor that determines the ac-

curacy of MCFISP calculations is the neutron and photon interaction cross sections. In analogy to this, since MCNP mesh tallies are in essence a large array of F4 tallies, the transport accuracy of the calculation is influenced in exactly the same way. It was determined by Wastenerja that in the case where the cell thickness equals both the photon and neutron attenuation coefficients this leads to an overestimation in activation/dose rate of $\sim 10\%$. In an extreme case where the size of the cell/mesh is 3 times the photon and neutron attenuation coefficients then the overestimation is a factor of ~ 2. Meshes with voxel dimensions smaller than a fraction of a mean free path do not influence the result of the calculation.

There is a second effect of mesh resolution which is related to how well the mesh fits the geometry in question. Consider the case shown in Figure 4.9, where a mesh is placed over shield with a duct running through it. In the case of the left pane

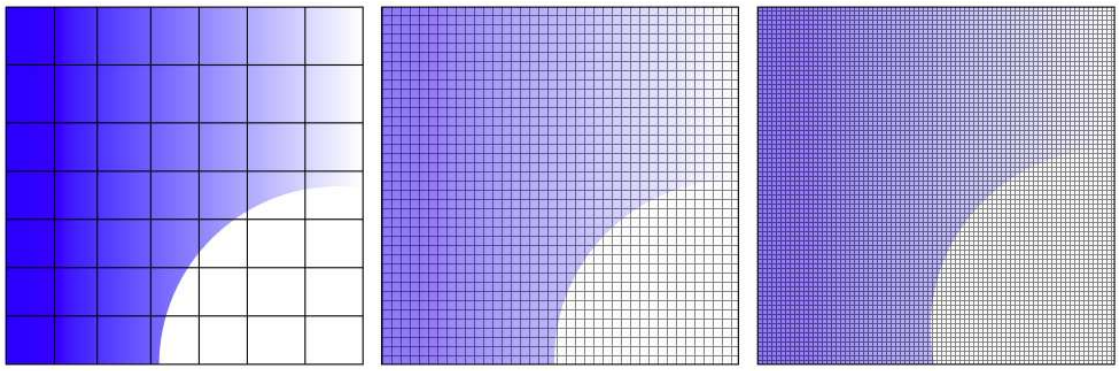

Figure 4.9: Effect of voxel size - (left) coarse, (middle) fine, (right) very fine

of Figure 4.9, the mesh is coarse and the mesh voxels that lie over both void and material will have a higher neutron flux than is truely the case, due to the summing of the diffusion and streaming components of neutron flux. This effect is reduced by increasing the resolution of the mesh, as shown in the remaining two panes. When the activation part of the calculation is performed, the average material of the voxel will be a irradiated with a higher total flux and faster neutron spectrum than is the

case, however the photon source that is created is geometrically correct.

4.6 Sources of uncertainty in MCR2S

There are a number of sources of uncertainty in an MCR2S calculations. Some can be controlled such as those due to the Monte Carlo method by running a large number of histories. Some, however, cannot be controlled such as those of the nuclear data.

Model Uncertainty

There is of course, as with any MCNP simulation the uncertainty introduced when creating the model such as those of approximating the true geometry to other geometric shapes and any other simplifications made when converting the true geometry to the model geometry.

Voxel Uncertainty

When the MCNP subroutine samples the photon source, it is sampled over a specific voxel i.e. photons are born across that voxel with a uniform probability, however the probability distribution in energy is according to the photon spectra in the voxel. This averaging means that on average the gamma spectrum is correct for the voxel, but is not correct for any specific material. The accuracy of this averaging technique is only an issue in a very small subset of cases, but it is important to be aware of how the software performs this process. Increasing the mesh resolution reduces the issues associated with the voxel averaged photon spectra. This is because the smaller the voxel the more likely it is that it lies in a single cell, making the uncertainty in composition zero. In the case of Figure 4.10, it possible to imagine a combination of materials or a strongly emitting source of gamma rays and weakly emitting source that will lead to incorrect source sampling. In the case of (a) in Figure 4.10, consider

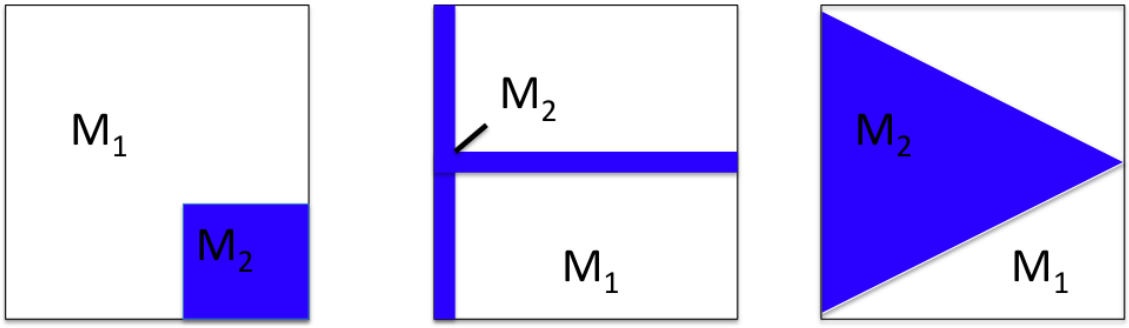

Figure 4.10: Voxel averaging issues (a) left, (b) centre and (c) right

M_1 being made of weakly emitting material and M_2 composed of strongly emitting material, the gamma ray source that is produced by voxel averaging of the photon source will have the correct energy spectrum, but the spatial distrbution of the photon source will be incorrect, hence giving the incorrect gamma flux away from the voxel. There are a number of other topologies that could be considered (b) and (c) in Figure 4.10 that will give incorrect gamma fluxes away from the voxel element. All issues associated with voxel averaging can be reduced by increasing the mesh resolution. This is a problem when one of the cells is smaller than the other cells under the voxel and also is the strongest emitter of gamma rays. One of the solutions to this issue is to increase the resolution of the mesh over that part of the model. However, this can only be done if there is sufficient memory remaining in the machine on which the simulations is being performed.

Neutron Transport Uncertainty

There is a source of uncertainty when the neutron transport part of the calculation is performed which stems firstly from the uncertainty in the transport nuclear data. Then there is a second source of uncertainty which is due to the monte carlo method. This related to the number of histories simulated and the amount of variance reduction in the model.

Activation data uncertainty

When the activation section of MCR2S is performed it is subject to a number of other sources of uncertainty, these being the cross section data, branching ratio's, gamma ray line intensities and energies, and half-life data. There are also uncertainties due to the inventory code used, although it has been shown that FISPACT is accurate to machine accuracy when perfoming analytic benchmarks.

Photon Transport Uncertainties

The photon transport segment of an MCR2S calculation is the smallest source of uncertainty, where the photon cross section data are well known. The main sources of error are due to the binning of the photon spectra 24 groups and the sampling of the shutdown photon source. The uncertainty in the sampling of the photon source can be reduced by running the simulation for a large number of histories.

None of the above uncertainties are propagated through the calculation, however these issues should be addressed when the calculation procedure is more mature. The estimation of the uncertainty in the final calculated dose rate or dose is currently a topic of great interest and further work should be performed.

Chapter 5

MCR2S BENCHMARK

In order to gain confidence in the reliability in a new software tool that is to be used to predict physical quantities, it is important to provide significant benchmarking. Benchmarking can be performed either against an already established code or against experimental data, or indeed both. In the field of neutronics there is already an experimental benchmark collection called the SINBAD database [67] maintained by the Nuclear Energy Authority (NEA) in Paris. SINBAD is a collection of experimental radiation shielding and neutronics benchmarks for fission, fusion and accelerator systems. Within the SINBAD collection of benchmarks there are a number of cases which are relevant to the benchmarking of the MCR2S software. The main results and description of the benchmark were reported in [59] and [68].

5.1 MCR2S and Attila ASG comparison

While the MCR2S code was being developed, UKAEA fusion was approached by Transpire Inc., the developer of the deterministic code ATTILA. Transpire wished to compare the results that their experimental ATTILA-ASG was producing in a simple test case. The ATTILA-ASG generates shutdown gamma ray sources using

the Origen-S libraries data set. Given the developmental status of both codes all other potential sources of error were removed, namely by using the same transport cross section data, model geometry and source definition. There are some sources of error that are intrinsic to the transport codes ATTILA, such as the use of multi-group transport cross section data and the method that ATTILA uses to solve the Boltzmann radiation transport equation.

The transport problem was one of Transipire's own standard neutron transport problems used for testing ATTILA. The geometry is comprised of six 20×20×10 cm slabs with reflecting planes on the y and z planes of the problem, thus making the problem essentially 1 dimensional. The geometry is shown in Figure 5.1. As

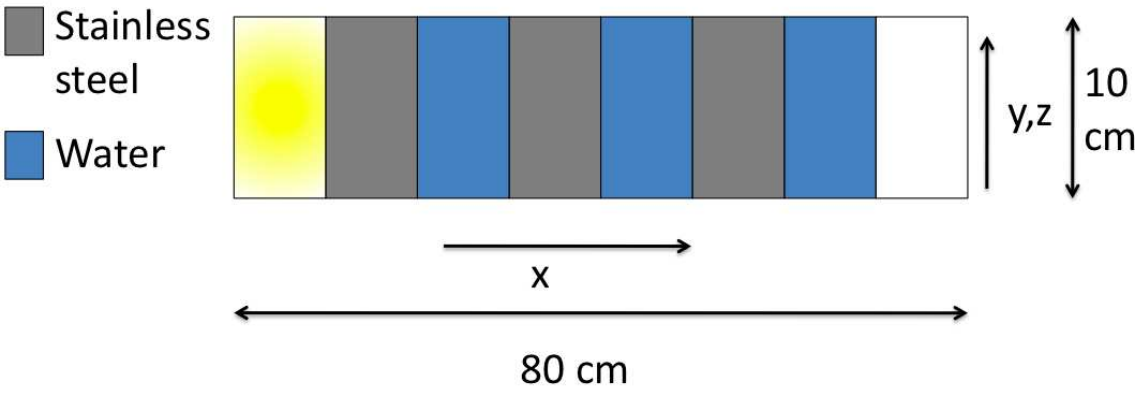

Figure 5.1: Geometry used in the ATTILA-MCR2S comparison (source cell - yellow)

for the materials, steel and water were alternated to provide both moderation and attenuation and thus different neutron spectra properties along the geometry; the steel composition is shown in Appendix C.1 Table C.1. Natural isotopic abundances were used throughout. Air slabs were placed at the front and rear of the model to provide source and dose tallying volumes respectively. The neutron source was located in the front air slab, and was isotropic in direction and mono-energetic in energy at 14.1 MeV. The source had a volume averaged intensity of 3×10^{11} n cm^{-3}

s^{-1}, which is typical of an ITER plasma.

The irradiation history selected was similar to an ITER pulsing schedule; a one year irradation at an on load factor of 5%, immediately followed by a single 600 second long pulse. This was chosen to roughly represent the three thousand 600 second pulses in projected ITER pulsing schedules. The last 10 minute pulse should help account for the build up of short lived nuclides.

Nuclide inventories and activation gamma sources were computed at four decay times following irradation; 1 hour, 1 day, 10 days and 1 year. The activation photon sources were used in photon transport calculations with MCNP and ATTILA to determine and compare the shutdown dose throughout the geometry at those same times. In both the ATTILA and MCNP neutron transport calculation the FENDL-2.1 nuclear data libraries were used. In both cases the neutron flux was calculated in 175 group VITAMIN-J format, in the case of ATTILA this meant using 175 multi-group cross sections. The nuclide inventory was calculated using neutron spectra generated in the 175 group format by folding the data with EAF-2007 activation data, using the inventory code FISPACT 2007. In the case of ATTILA, the combined FENDL-2.1 and FORNAX XML data were used. FORNAX was described in the previous Chapter in Section 4.1.3. Activation gamma sources were produced in the 24 group FISPACT format, shown in Table 4.1. However, ATTILA produced sources in the standard 42 group format for this code.

The spatial resolution was chosen to be 1 cm in the direction of the neutron flux gradient. An importance map was implimented in MCNP to ensure sufficient accuracy in the final answer. The ATTILA mesh size was selected to be 1 cm to facilitate comparison. The solver options S_8 and P_2 were selected together with a convergence

criterion of 0.01.

There have been a number of ATTILA benchmarks with comparison between experimental data [69, 70] which showed that there is often some deviation from the experimentally determined values, which was deemed acceptable by the authors. There have also been MCNP-ATTILA comparisions [71, 72] and deviations were once more deemed acceptable. Fig 5.2 shows the neutron fluence determined by MCNP and ATTILA, and the data are within 3% at all locations. Comparison

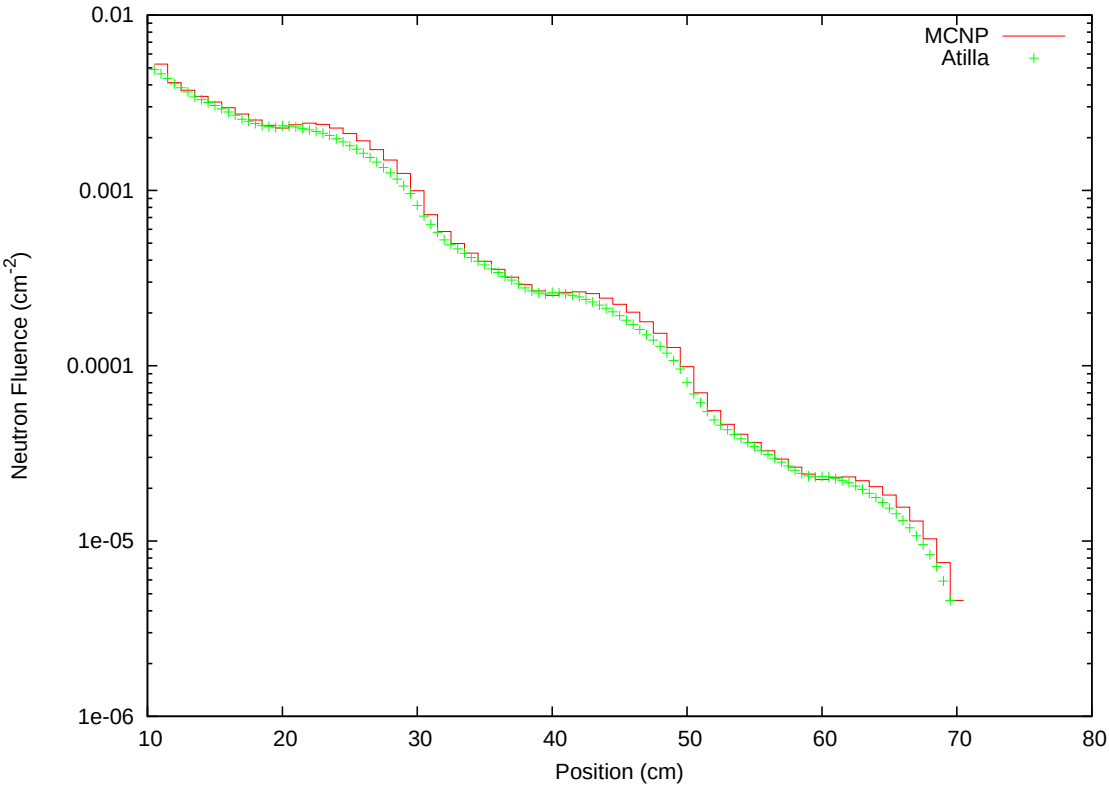

Figure 5.2: Neutron flux in the assembly calculated by MCNP and ATTILA

of the neutron spectra determined by both MCNP and ATTILA for the front and rear steel slabs of the problem, and are shown in Figure 5.3. The only deviations away from the MCNP determined value are due to the multigroup representation of ATTILA cross sections. The FISPACT contact doserate data were used to com-

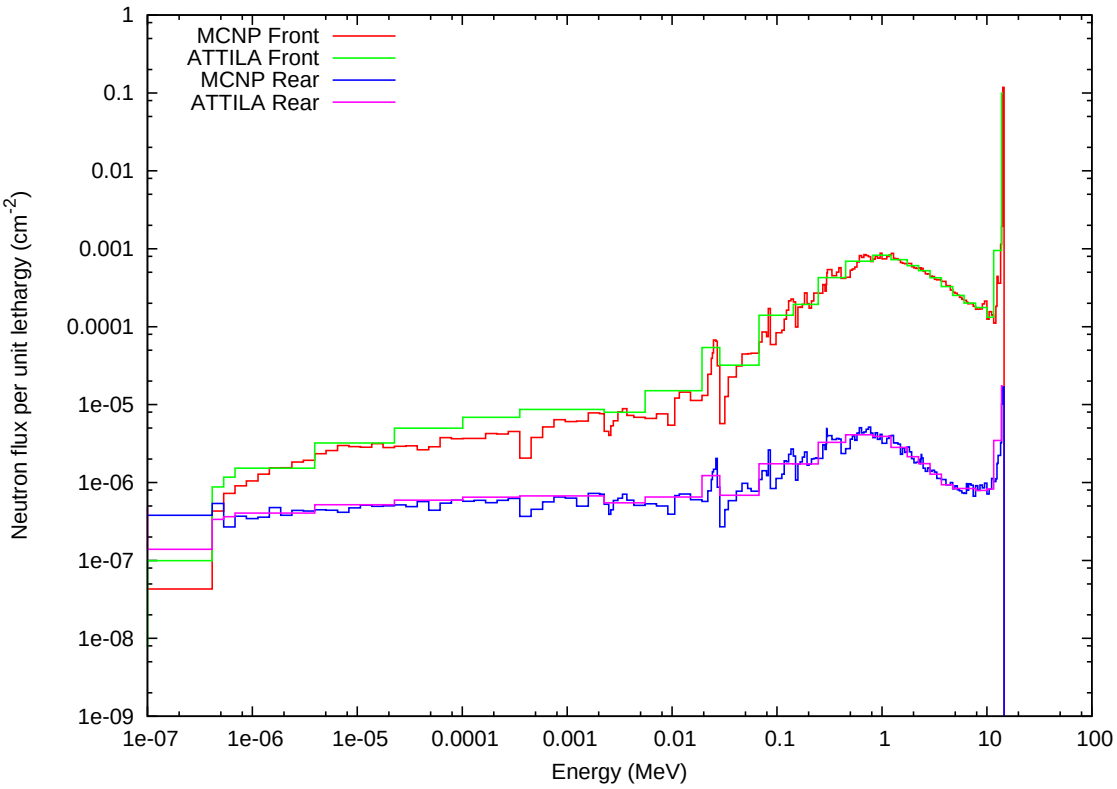

Figure 5.3: Neutron spectra at the front and rear of the assembly calculated with MCNP and ATTILA

pare isotopic production on the most important nulcides with regard to causing the highest dose, these were; ^{56}Mn, ^{57}Ni, ^{99}Mo, ^{51}Cr, ^{59}Fe, ^{58}Co, ^{54}Mn and ^{60}Co. Each nuclide contributes differing amounts of dose depending on the decay time and location (hence neutron spectrum). Figure 5.4 shows the production ratios of significant isotopes produced by both MCNP/FISPACT and ATTILA.

The results are all within 25%, the exceptions being ^{51}Cr and ^{99}Mo. Closer analysis of the EAF and FORNAX data show the reasons for the discrepancy in those two nuclides [59].

- ^{51}Cr a large difference was found in the ^{52}Cr(n,2n) and ^{50}Cr(n,γ) pathway cross section values between the two libraries

- for ^{99}Mo it was the absence of ^{100}Mo(n,2n) cross section information in the

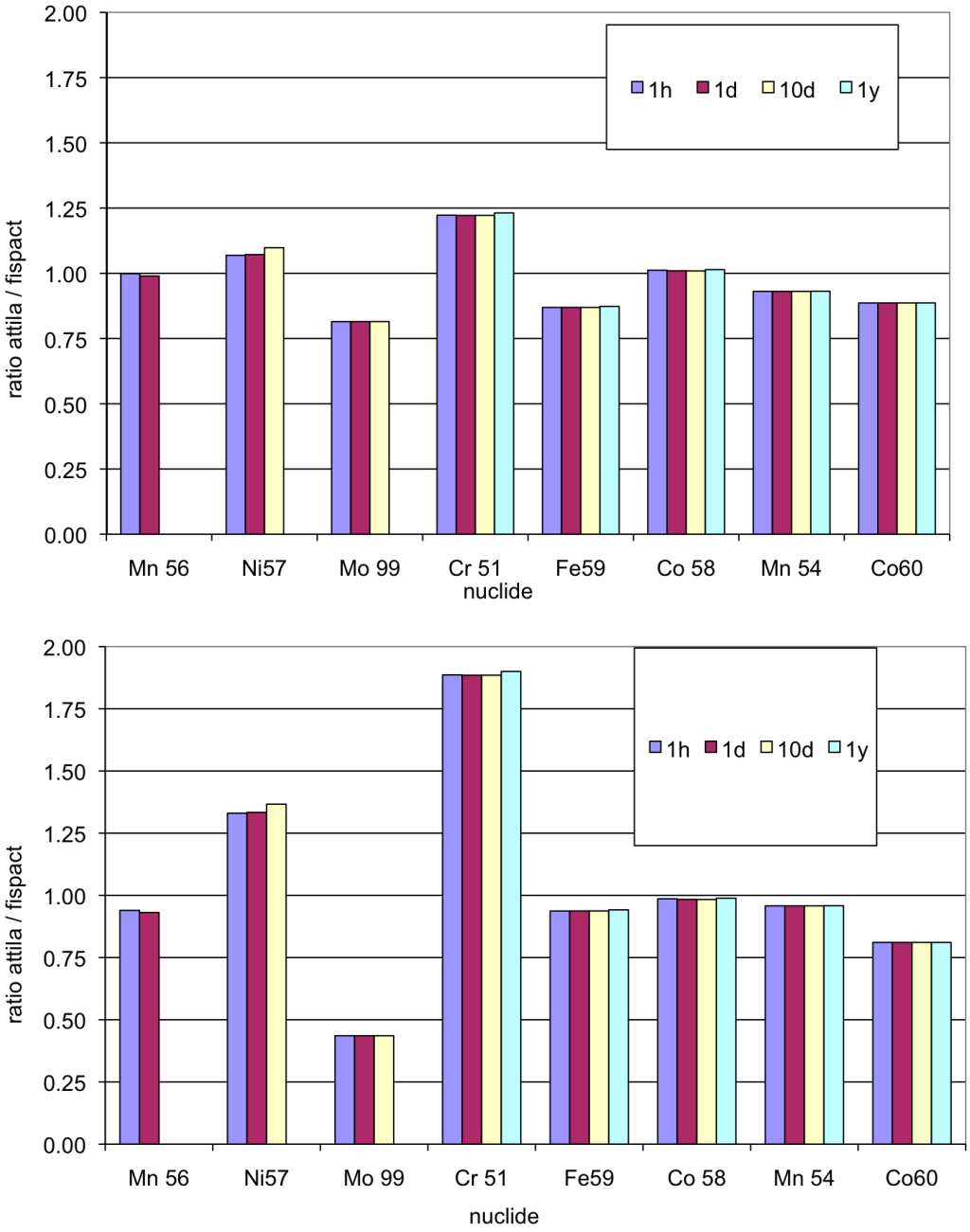

Figure 5.4: Isotopic production calculated by ATTILA in the first stainless steel block (upper) and last (lower) relative to FISPACT for 4 decay times

FORNAX data

- ATTILA isotopic production results also revealed the absence of a large number of isotopes produced by FISPACT and the EAF libraries, all of which had negligible contribution to the dose field due to their absence or the absence of their pathway reactions in the FORNAX XML library

Comparison of the gamma energies and decay data with EAF and FORNAX showed that decay constants agree to within 1%, gamma line energies to within 2%, and gamma intensities to within 5% [59]. Therefore most differences in the decay gamma source are those due to differing isotopic production. There are however, a number of exceptions;

- the absence of a high number of low-energy lines (X-rays) from the FORNAX data, compared with EAF libraries
- the absence from the FORNAX data of 511 keV lines corresponding to electron positron annihilation photons which occur in some nuclides following β^+ decay (e.g. ^{57}Ni and ^{58}Co in this case)
- an extra 141 keV line in ^{99}Mo has also been observed in the XML file; this line corresponds in fact to ^{99m}Tc, and is responsible for the significant difference in average gamma energy found for this nuclide

MCR2S and ATTILA activation source profiles for the four decay times are shown in Figure 5.5. The presence of all the extra X-rays in the EAF data make the ATTILA activation sources seem artificially low. These X-rays are unimportant for dose analysis, except when near the boundary of a radiation shield. A comparison is made between two sources for the same decay time, one produced by ATTILA and one produced by MCR2S, shown in Figure 5.6, in which the ATTILA data looks artificially low.

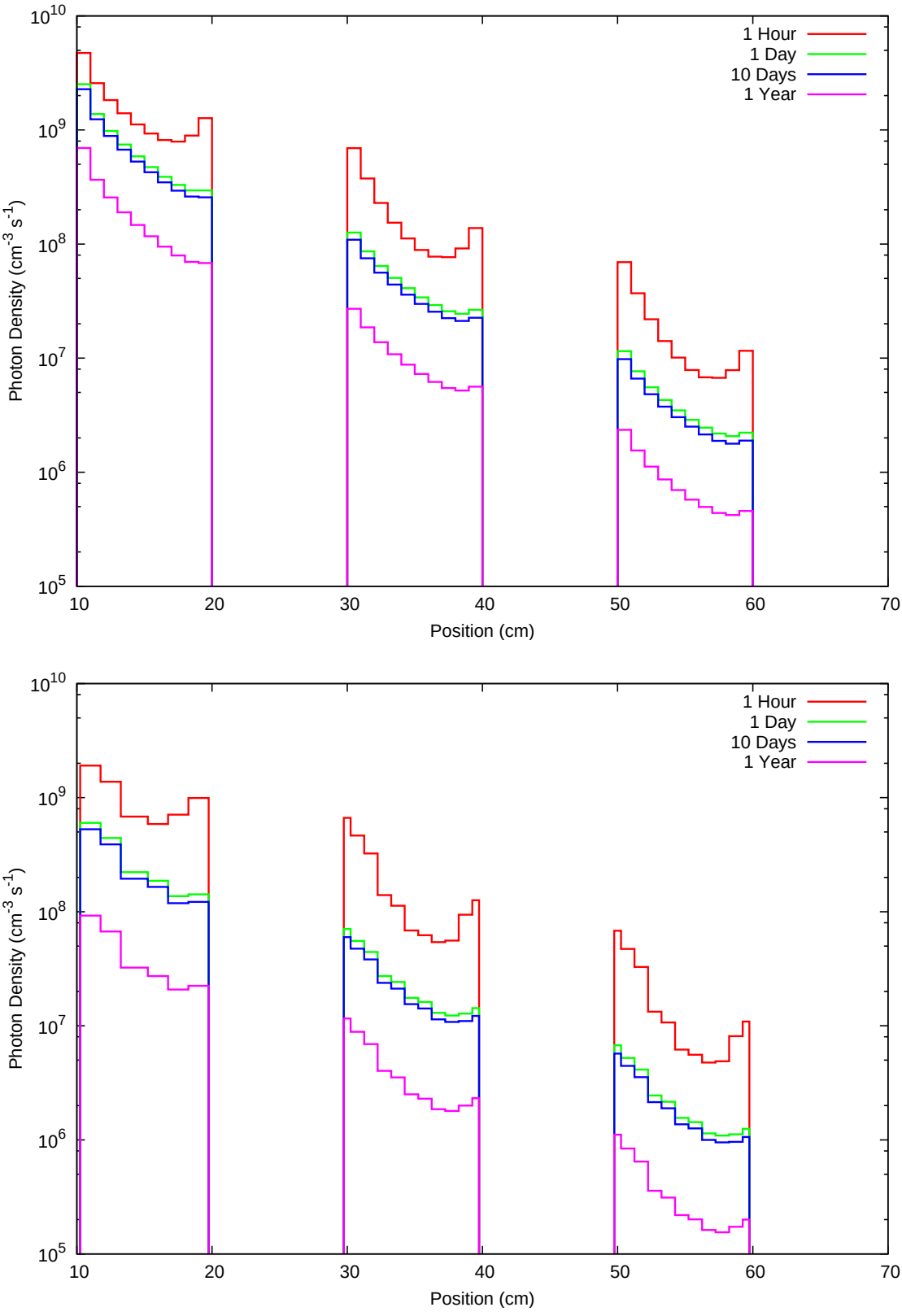

Figure 5.5: Photon source profiles for MCR2S (upper) and ATTILA (lower)

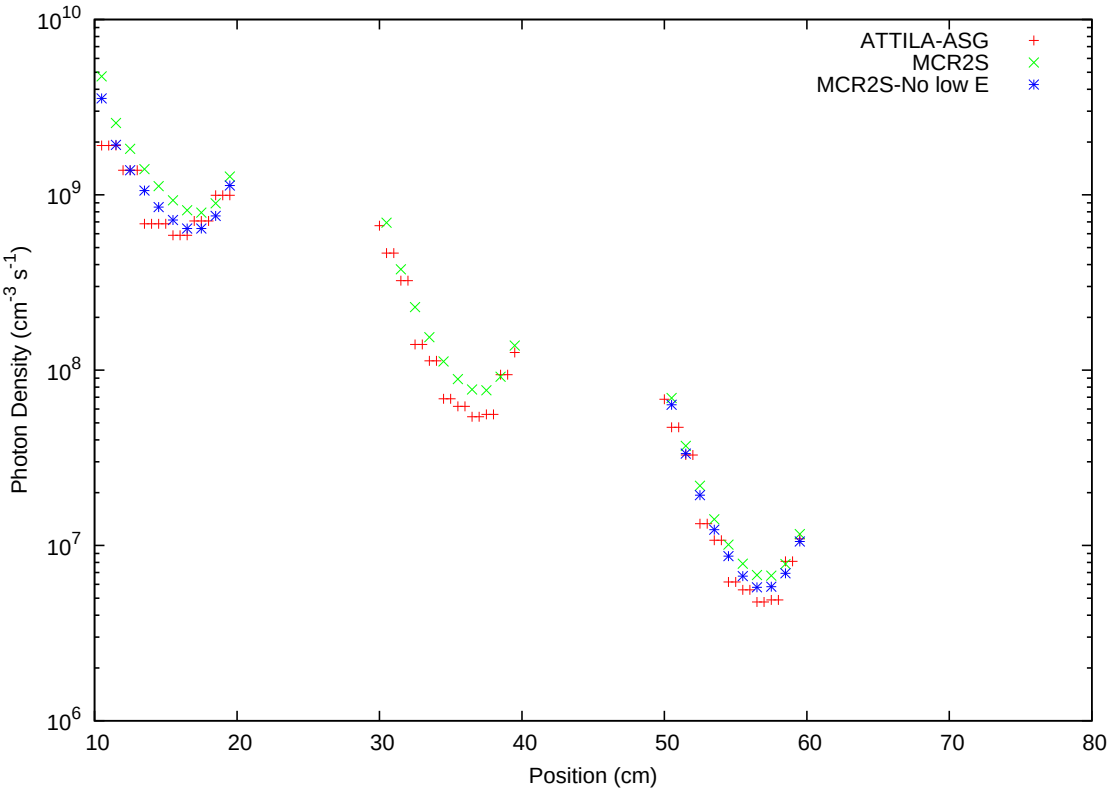

Figure 5.6: Photon source profiles for ATTILA, MCR2S and MCR2S with no low energy photons

When the contribution of these low energy X rays is removed, the source profiles are more similar. Results of photon transport calculations using these decay gamma sources are shown in Figures 5.7 and 5.8 in which the total photon flux from both MCNP and ATTILA is shown.

The activation photon densities used as sources are shown in Figure 5.5. Photon spectra are the outcome of the photon tranport calculation, including effects such as photoelectric effect, Compton scattering and pair production. The decay photon spectra from the two codes are shown in Figures 5.9 (MCR2S) and 5.10 (ATTILA).

The photon spectra match better at high energies due to the previously mentioned high abundance low energy X-rays present in the EAF data. Finally, the shutdown gamma ray dose in the problem was determined by using the shutdown

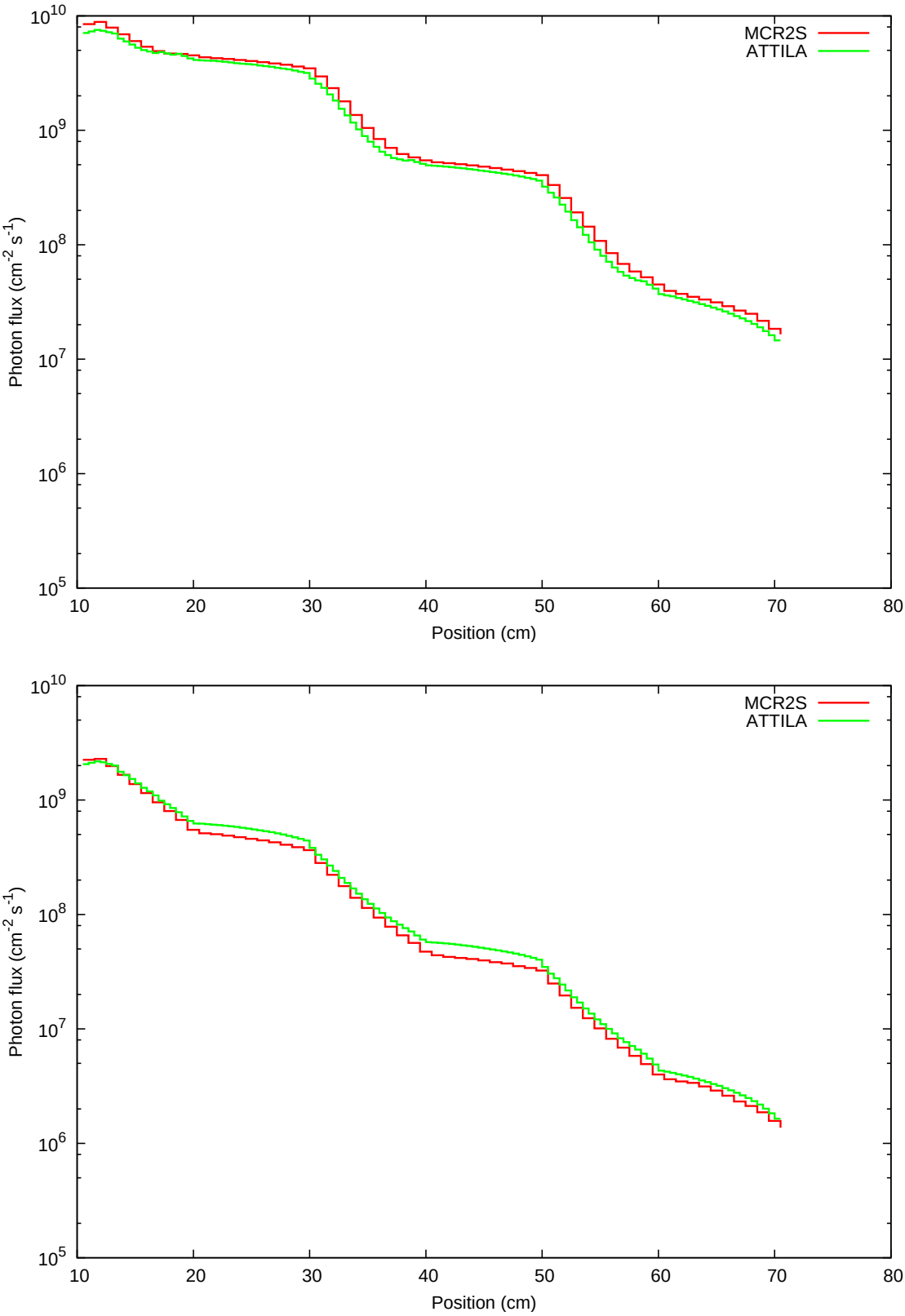

Figure 5.7: Photon flux profiles in the stainless steel assembly at decay times of 1 hour (upper) and 1 day (lower)

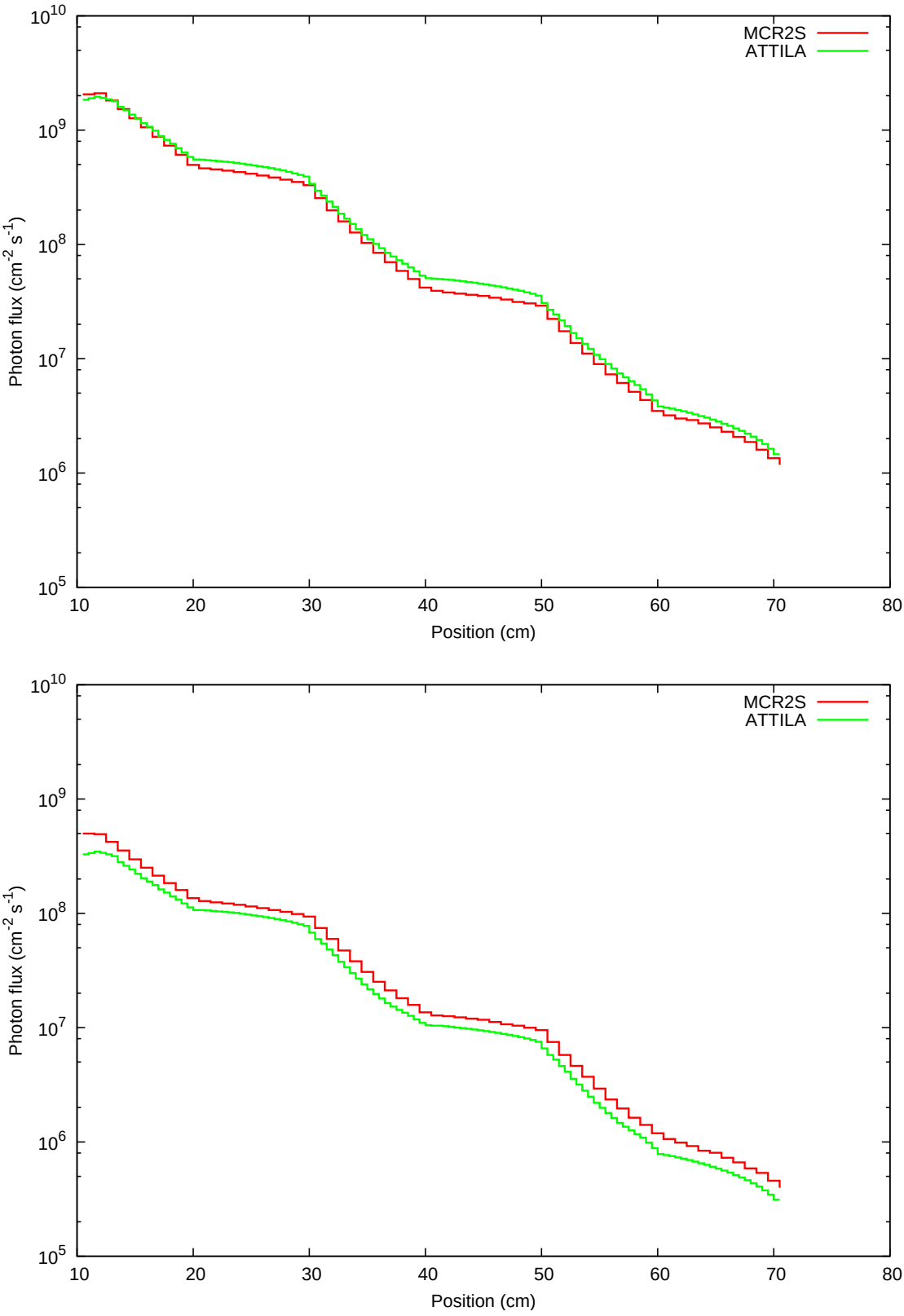

Figure 5.8: Photon flux profiles in the stainless steel assembly at decay times of 10 days (upper) and 1 year (lower)

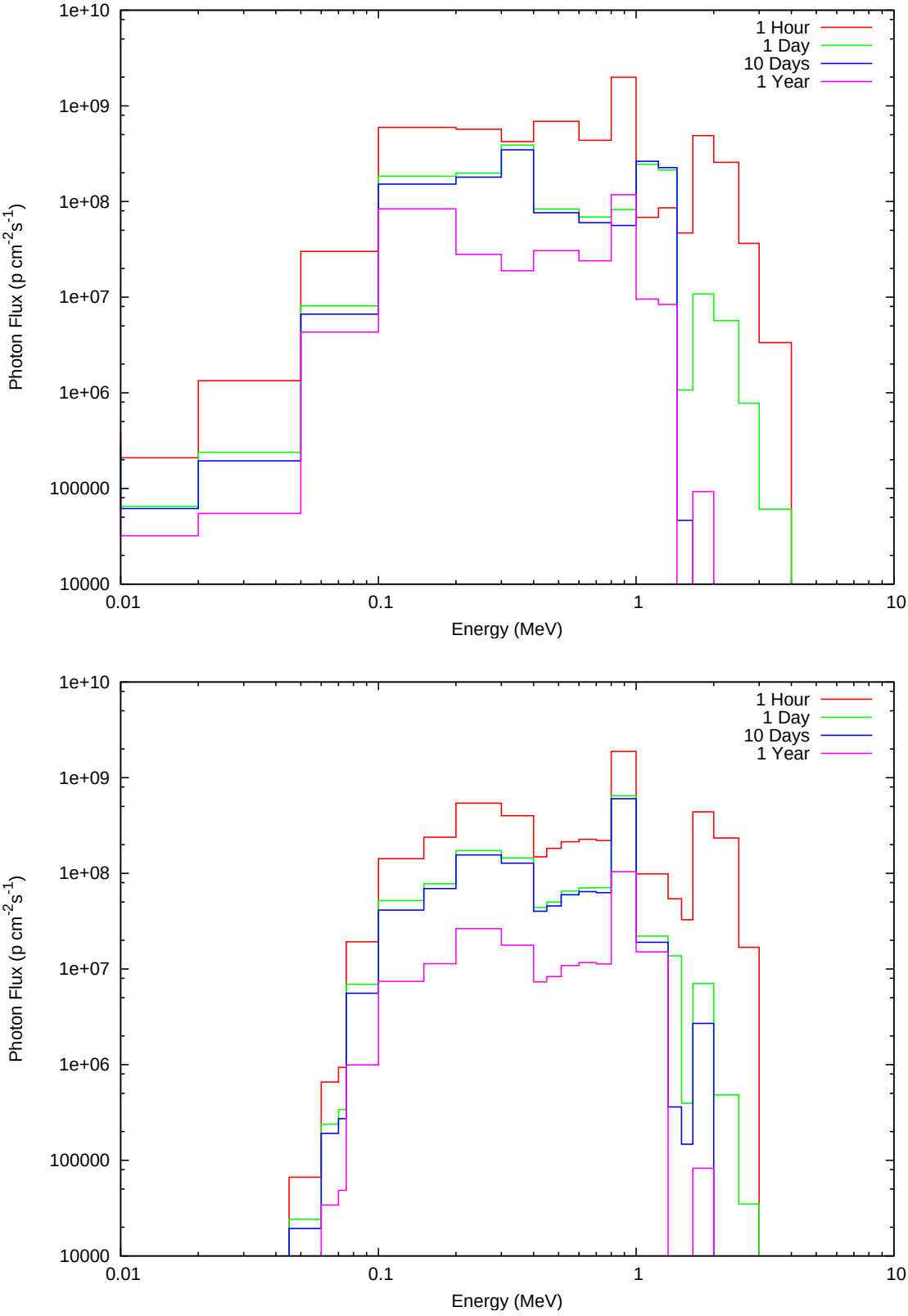

Figure 5.9: Photon spectra the front stainless steel slab, MCR2S (upper) and ATTILA (lower)

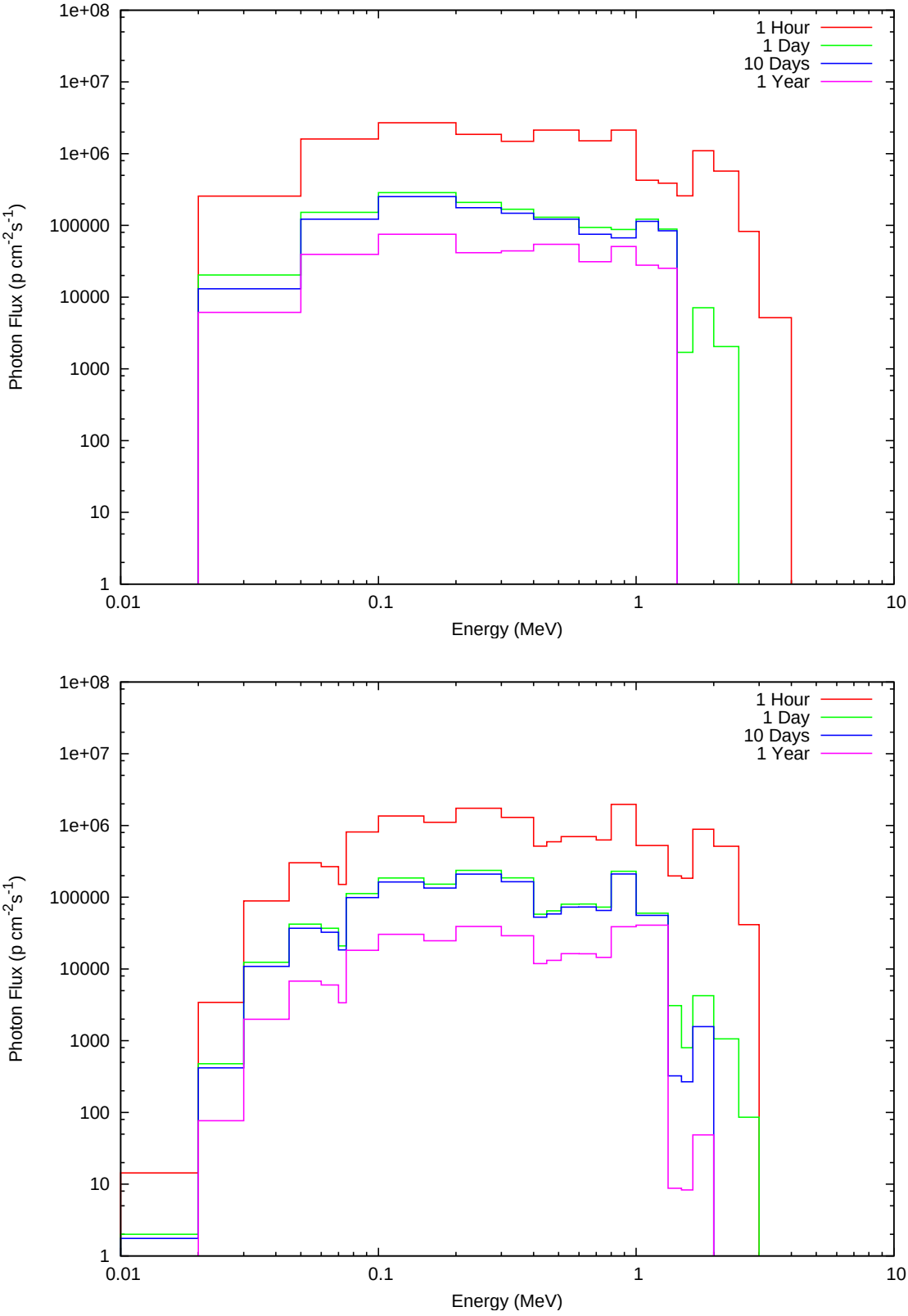

Figure 5.10: Photon spectra in the rear stainless steel slab, MCR2S (upper) and ATTILA (lower)

photon spectrum and flux previously calculated and the flux-to-dose gamma ray conversion ANSI/ANS-6.1.1-1991 factors [37].

Results are summarised in Table 5.1. At all decay times and locations, total doses are within 20% of each other. As mentioned previously the low energy contribution to total dose is insignificant as shown by the conversion factors. If the dose per unit

Decay time	ATTILA-ASG	MCR2S	ATTILA-ASG	MCR2S
1 Hour	62,000	67,000	134	150
1 Day	14,600	14,400	11.0	9.7
10 Days	13,000	13,600	9.8	8.3
1 Year	2,500	2,800	2.5	3.0

Table 5.1: Shutdown gamma ray doses (μSv hr^{-1}) at the front (left) and rear (right) for decay times of 1 hour, 1 day, 10 days and 1 year

lethargy is plotted, as shown in Figure C.1, shown in Appendix C then it can be seen that it is the high energy photons that cause the most dose, and it is therefore expected that the results compare well.

5.2 Frascati Neutron Generator Benchmarking

In the SINBAD shielding database are a number of carefully controlled and documentented neutron transport and shielding benchmarks. A number of them appear suitable for benchmarking the MCR2S code, namely a neutronics experiment for the validation of codes used to estimate ITER dose rates [73] and a dose rate validation experiment at the Fusion Neutron source in Japan [74]. The first benchmark was selected in order to facilitate comparison with the earlier MC-FISP code used in the original analysis and the original set of experimental data.

5.2.1 The Frascati Neutron Generator

The Frascati neutron generator (FNG) is a deuteron accelerator facility sited near Rome [75]. It accelerates deuterons up to a kinetic energy of 300 keV towards a tritiated titanium target. When the deuterons impinge on the target, a beam of neutrons are produced via the d(t,α)n reaction [76]. The neutrons that are produced are distributed as a Gaussian in energy with a mean of 14.08 MeV. The FNG typically is used for the benchmarking of neutron cross sections for fusion relevant neutronics and nuclear data. Shielding mock ups such as that shown in Figure 5.11 are placed in front of the beam and are used to determine the effect of neutron streaming, inelastic scattering gamma rays, or neutron activation in a specific geometry. Of particular interest to this thesis is the T-426 Experiment [73], where the FNG was used to activate a series of laminar sheets composed of alternating layers of 316L Stainless Steel and Perspex in two consecutive campaigns. At the centre of the steel-perspex matrix was a chamber in which doserate and spectrometers could be placed. Radiating away from the central chamber and toward the neutron source is a streaming channel. There are certain radiation detector configurations at the centre of the chamber depending upon the particular campaign being investigated. There is a plug at one side of the FNG, the removal of which allows a boom to be

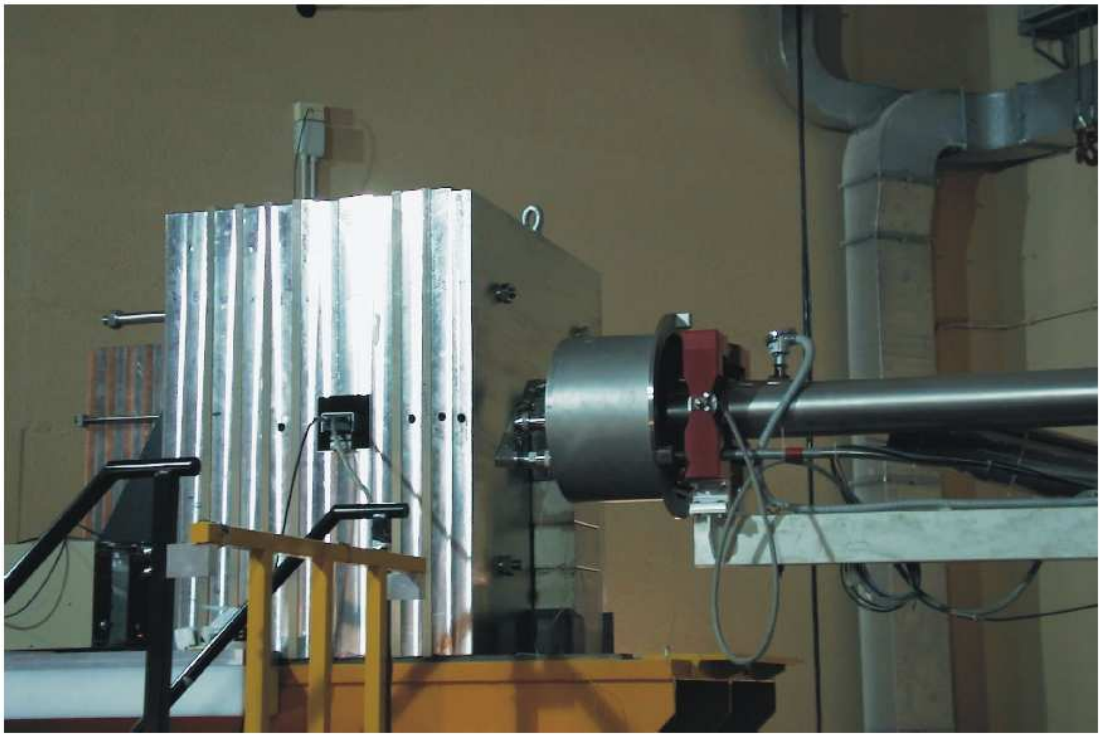

Figure 5.11: Experimental setup of the FNG [73]

inserted into the central cavity, attached to which are the fore mentioned radiation detectors. The composition and geometry of the FNG is very well known and the composition can be found in Table F.1 in the Appendix. The transport geometries are shown in Figure 5.12, where each colour corresponds to a different material, in this case green is air, blue is perspex, purple and pink are the two slightly different 316 stainless steels, and white corresponds to void. These models can be found in the SINBAD database and were used to benchmark MCFISP calculations during the original experiments.

5.2.2 Characterisation of FNG source neutrons

The angle and energy distribution of 14 MeV neutrons produced in the FNG were originally described using a combination of beam-target kinematics, Bethe-Bloch stopping and ion slowing down in the the target [76]. ENEA Frascati wrote a cus-

Figure 5.12: MCNP models for the irradiation (left) and decay (right) simulations and the material distribution shown by the colours

tom FORTRAN subroutine for MCNP 4C which was supplied along with the original data by SINBAD, however the subroutine is not compatible with later versions of MCNP.

In the supplied SINBAD database, there is an evaluation of the FNG neutron spectrum. This evaluation shows the intensity variation of the neutron source as a function of angle, and describes the variation of neutron energy at that angle, shown in Figure 5.13. A MCNP SDEF card was created which approximates the neutron source originally used. The full source is shown in the Appendix F.1.

5.2.3 Experimental Campaign 1

The shielding mock-up was irradiated for 18 hours over a 3 day period. The total neutron production in that time was 1.815×10^{15} neutrons. The actual and approxi-

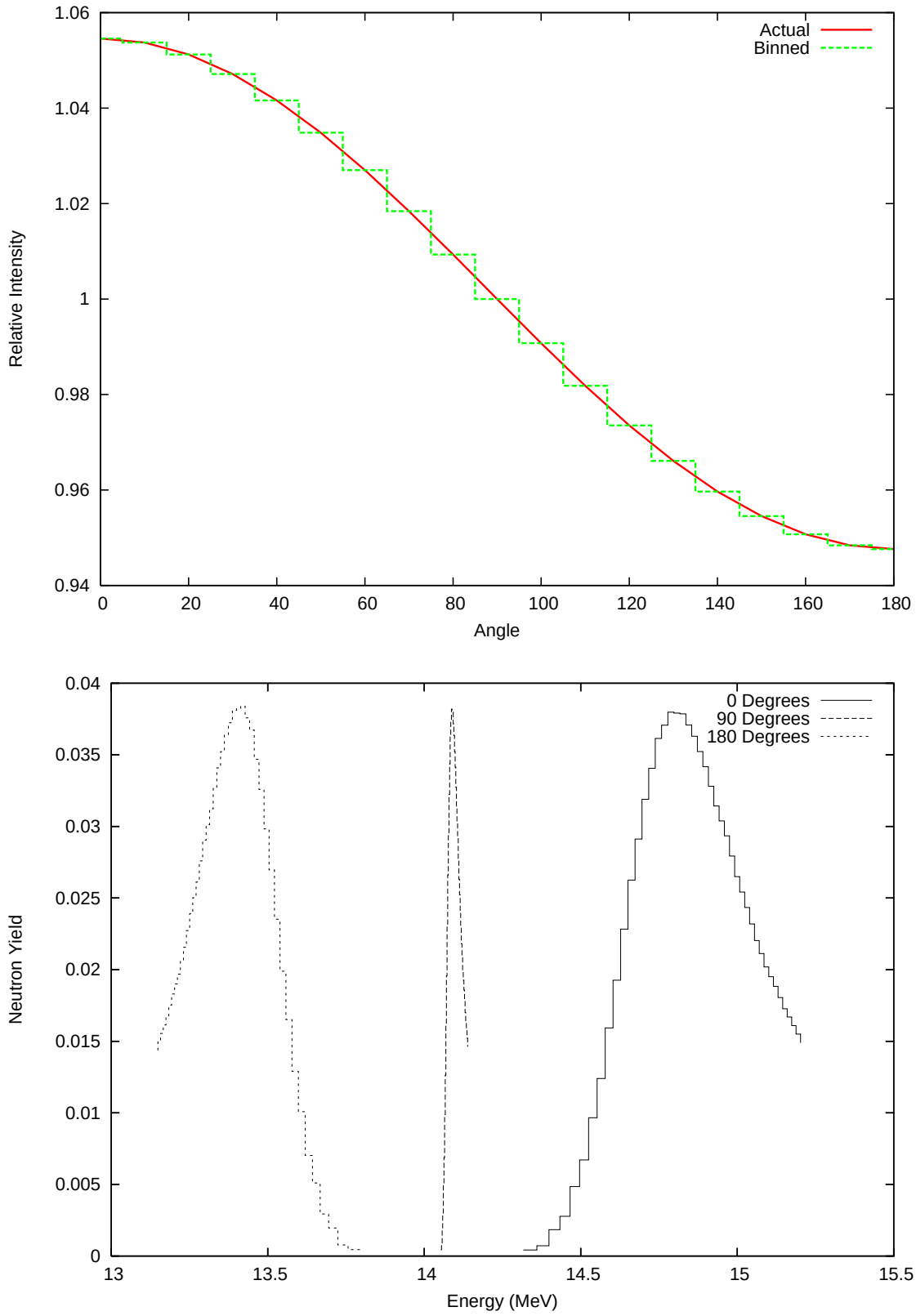

Figure 5.13: FNG source characterisation by angular strength (upper) and angular energy distribution (lower)

mated irradiation history for the 3 day period is shown in Figure 5.14. The neutron production is seen to be fairly variable due to the deuteron beam current and other factors such as the electrical supply of the Frascati site. Following the termination of the irradiation the following experimental quantities were measured by the ENEA team; dose rate by Geiger-Muller detector, gamma ray dose distribution by TLD[1], and the ^{58}Ni(n,p) and ^{58}Ni(n,2n) reaction rates by Ni activation foils.

^{58}Ni (n,p) and (n,2n) reaction rate measurements and calculations

In the central cavity of the FNG, six nickel foils, shown in Figure 5.15 were placed on the walls of the cavity in order to measure the ^{58}Co production, which was determined a priori to be an important isotope [77]. Due to the isotopic abundance of ^{58}Ni $\sim$ 68 % in elemental nickel the most important neutron induced reactions are ^{58}Ni(n,p)^{58}Co and ^{58}Ni(n,2n)^{57}Ni. In the original report [73] the reaction rates of these two reactions were calculated via three means; with MCNP directly using an FM card with appropriate ENDF MT numbers, with MCNP and IRDF-90.2 data and using MCNP and FISPACT with FENDL-2.0/A (EAF-99). Due to the similarity of results between FENDL-2.0 and IRDF-90.2 it was decided to only compare EAF-2007 and FENDL-2.1 in this new benchmark. All calculations rely on high quality evaluated nuclear data such as those present in the ENDF-VI and the FENDL libraries. The experimental reaction rates were determined by the placing of nickel foils in the cavity and then counted using a high resolution gamma spectrometer post irradiation. This method counts 811 keV gamma ray lines from ^{58}Co and the 1.38, 1.76 and 1.92 MeV lines from ^{57}Ni. In this work FENDL-2.1/MC was used for the neutron transport calculations and EAF-2007 was used for the activation calculations.

[1]TLD - Thermo Luminescent Detector

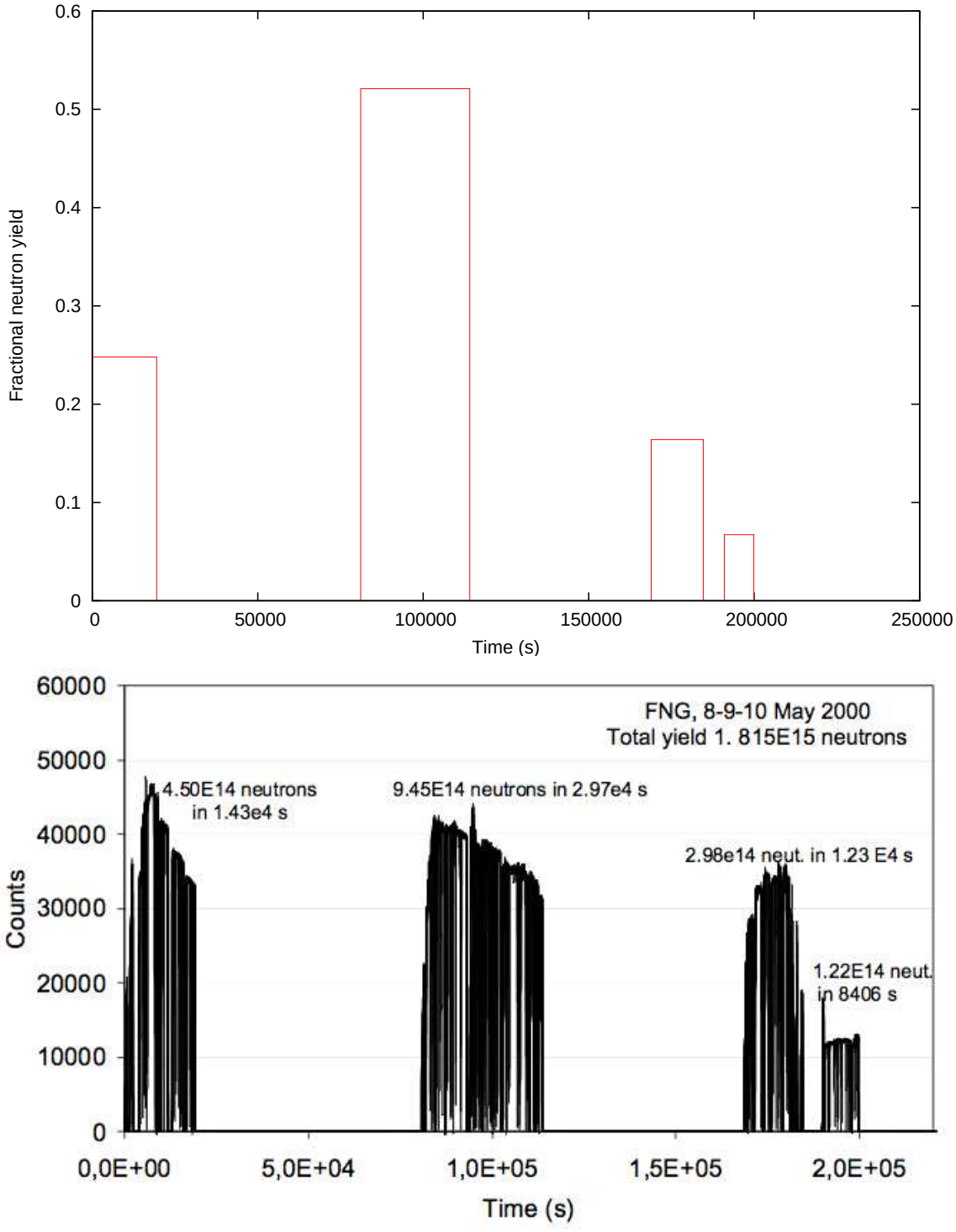

Figure 5.14: Irradiation schedule for campaign 1, computational (upper) and experimental comparison [73] (lower)

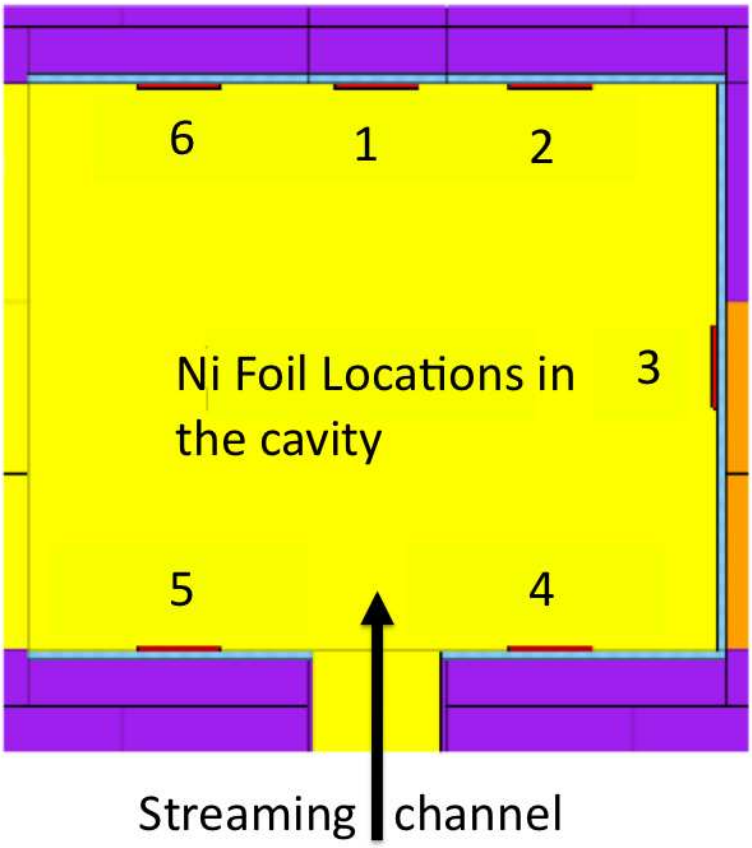

Figure 5.15: Nickel foil positions in the FNG Benchmark

In the benchmarking studies rather than to prove existing measurement and simulation techniques the nickel foil calculations were used to prove that the neutron spectra are equivalent in both this work and the original report. For the ^{58}Ni(n,p)^{58}Co and the ^{58}Ni(n,2n)^{57}Ni reaction, the ratio of the reaction rate calculated to the value experimentally determined (C/E) are shown in figures 5.16.

The C/E values in Figure 5.16 show reasonable correlation with the previous simulations [73, 78, 79] and with the experimental data. The total cross section uncertainty for ^{58}Ni(n,p)^{58}Co is 5%. The ^{58}Ni(n,p)^{58}Co reaction has a threshold energy of approximately 0.5 MeV; this fairly low threshold energy means that neutrons that have kinetic energies below the threshold do not react via this mechanism. The ^{58}Ni(n,2n)^{57}Ni reaction has a high threshold just over 12.5 MeV. The gradient of

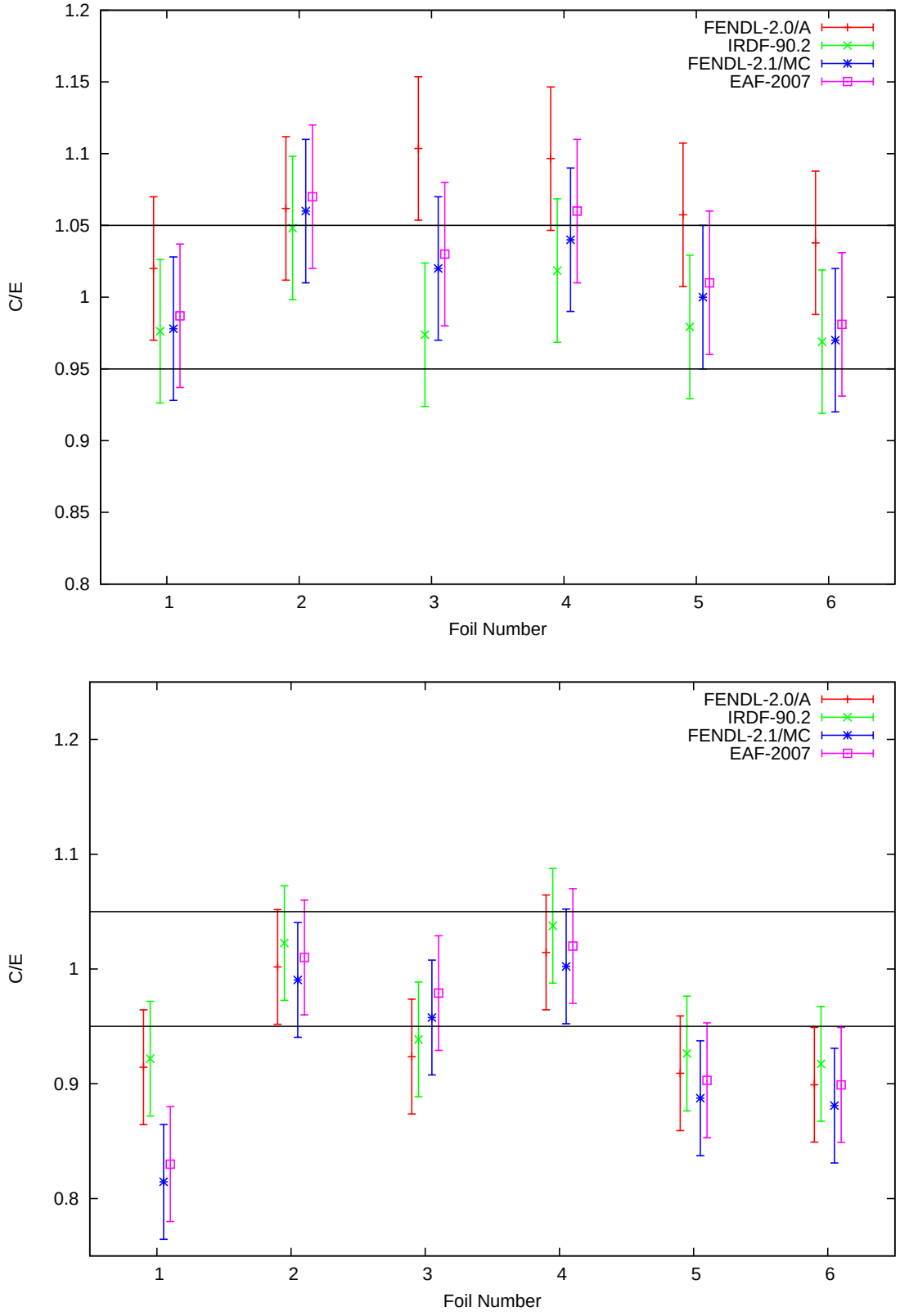

Figure 5.16: C/E data for ^{58}Ni(n,p)^{58}Co (upper) and ^{58}Ni(n,2n)^{57}Ni (lower) past and present

foil	experiment	A	B	C	D
1	2.15E-05	2.19E-05	2.09E-05	2.11E-05	2.12E-05
2	5.19E-06	5.51E-06	5.44E-06	5.54E-06	5.55E-06
3	4.13E-06	4.55E-06	4.02E-06	4.73E-06	4.26E-06
4	8.48E-06	9.29E-06	8.63E-06	8.88E-06	8.96E-06
5	7.86E-06	8.31E-06	7.69E-06	8.11E-06	7.97E-06
6	5.15E-06	5.34E-06	4.99E-06	5.04E-06	5.05E-06

Table 5.2: Reaction rates per atom for the ^{58}Ni(n,p) reaction, where A is MCNP (FENDL-2.0/MC) + FISPACT (FENDL-2.0/A), B is MCNP (FENDL-2.0/MC + IRDF-90.2) , C is MCNP (FENDL-2.1/MC) and D is MCNP (FENDL-2.1/MC) + FISPACT (EAF 2007)

the cross section near the threshold region is very steep, even a 0.01 MeV difference could cause large under or overestimations in the calculation of reaction rates. The lower C/E value seen in foil 1 shown in the lower part of Figure 5.16 are possibly due to the approximate source angle-energy definition that was used in the MCNP simulation. With the exception of foil 1 in the lower part of Figure 5.16 the remainder of the foils show acceptable C/E values, which have a similar spread to those of the original calculation. This is not surprising when considering that the total uncertainty in the cross section of ^{58}Ni(n,2n)^{57}Ni reaction is $\sim 30\%$.

Thus from the results shown in this section, it is argued that for the purpose of this benchmark the source definition used is adequate.

Geiger-Muller Tube dose rate measurements

Geiger-Muller (GM) tube measurements were performed after the irradiation by removing the shielding plug at one side of the stainless steel-perspex layer and inserting a GM tube on a boom, shown in Figures 5.11 and 5.12. The GM tube was calibrated at ENEA Frascati using a number of calibration gamma ray sources [73]. The GM tube measurements were taken continuously from 30 minutes after the irradiation until 3 months had passed. The GM tube is incorporated into the

model as a thin spherical shell of aluiminium with air internal to this sphere. The

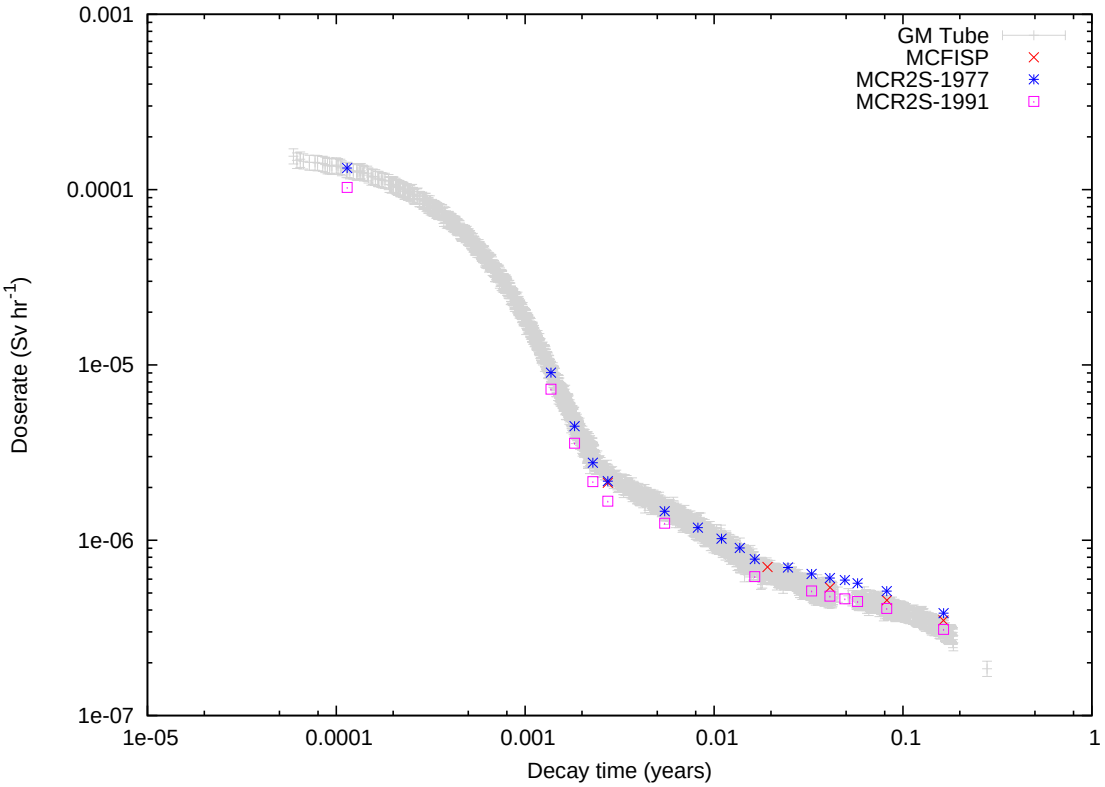

Figure 5.17: Shutdown gamma ray dose rate as a function of time in the FNG assembly

table below shows the ratio of the dose rate predicted by modeling and the actual dose rate given by the GM tube at each specific time. The dose rate calculated by MCR2S using the ANSI/ANS-6.1.1-1977 and ANSI/ANS-6.1.1-1991 dose response functions. The doserate calculated by MCFISP using an F6:P tally and the experimentally determined doserate are shown in Figure 5.17. The MCFISP values were originally calculated by the ENEA Frascati team by using an F6 tally in the region of the GM tube. As can be seen in Figure 5.17 the two sets of MCR2S data straddle the MCFISP data. The reason for the deviation of MCR2S-1977 and MCFISP is that the F6 tally (see Chapter 3) output data is in MeV/g, and this can trivially be converted to Grays (J/kg), i.e. absorbed dose, with a multiplicative factor. The

quoted output of the GM tube experiment data is in Sv/hr, i.e. effective dose, thus there is some unkown and unquoted factor applied to the MCFISP data to convert from absorbed dose to effective dose. Irrespective of this the MCR2S data folded with the ANSI-ANS-1977 dose response function are close to the experimental value for decay times between 1×10^{-4} and 1×10^{-2} years, deviating to doses greater than the experimental value for longer decay times. The MCR2S data folded with the ANSI-ANS-1991 dose response function fit poorly for decay times less than 1×10^{-2} years, however it fits well for decay times longer than this.

Taking the ratio of the calculated doserate and the experimentally determine doserate (C/E), allows deviations to be examined in the doserate data. The C/E values are shown in Figure 5.18 The straddling of the MCFISP data by the MCR2S data

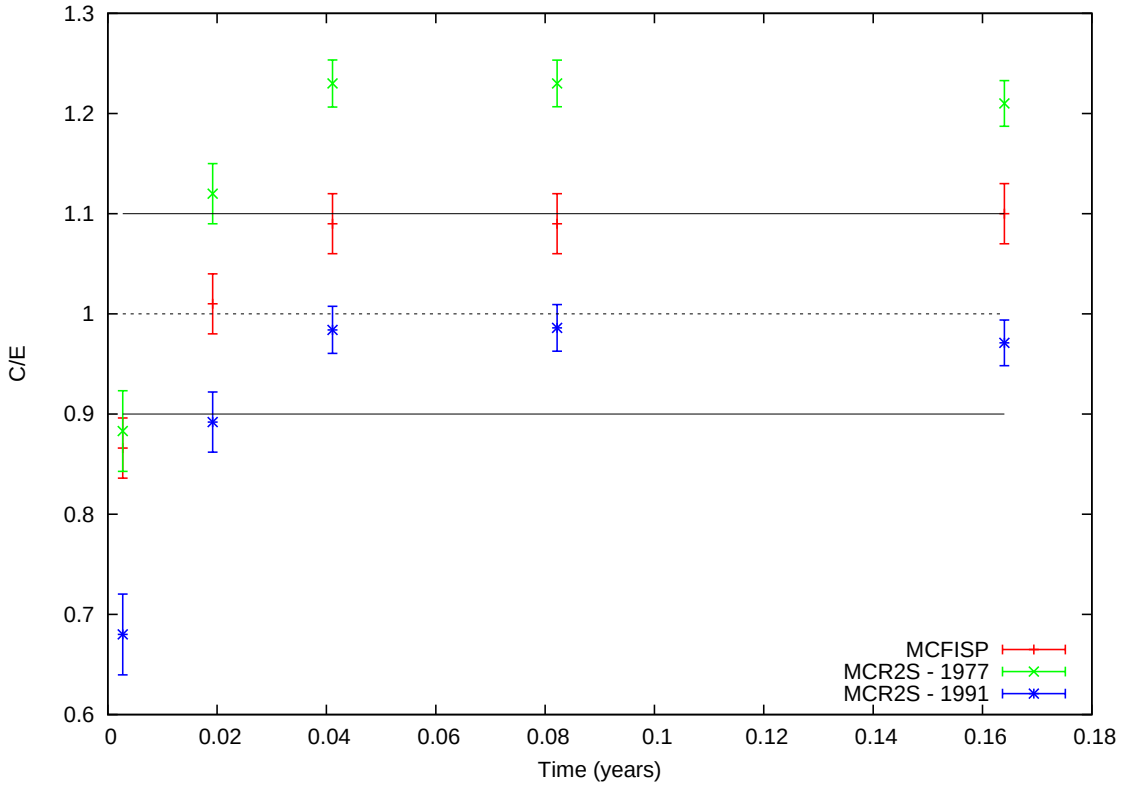

Figure 5.18: Calculated/Experimental values for doserate in Campaign 1

is more clear in Figure 5.18.

The shutdown gamma ray source

A shutdown gamma ray source is generated by MCR2S for every quoted decay time in the model, and an example of the decay gamma source produced is shown in Figure 5.19. Each vertical slice is shown below the main figure, which shows the total source strength across this horizontal slice. The effect the perspex sheets have on the source strength, and hence activation, is marked and the effect of neutron streaming along the duct is shown by the strong activation peak at the rear of the central cavity.

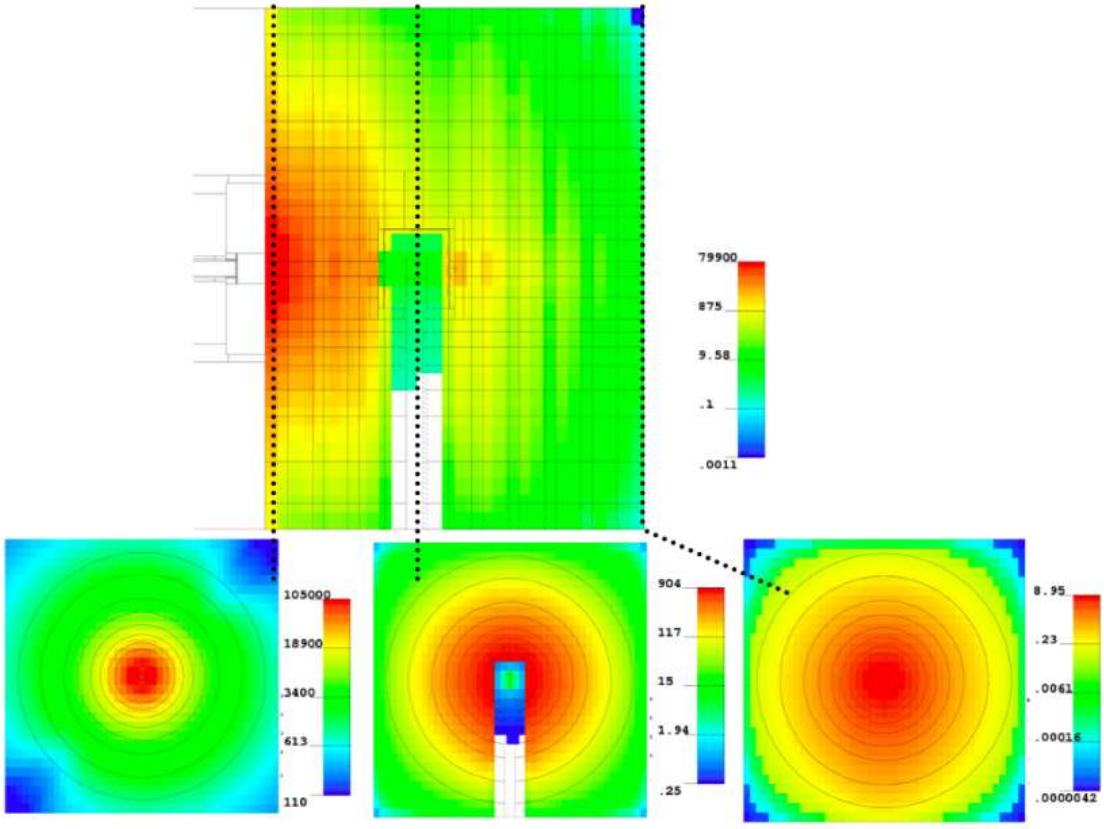

Figure 5.19: Shutdown gamma ray source for 1 hour decay time (p s^{-1})

5.2.4 Experimental Campaign 2

The second experimental campaign took place around 3 months after the initial irradiation. The second irradiation produced 1.95×10^{15} neutrons in 14 hours of on time over a period of 3 days, comprising of a total of 5 irradiation times and 3 dwell times. Due to the length of time between the first and second campaigns, it was shown to be unnecessary [80] to account for the first campaign in the inventory calculations. There are no changes to the input neutron source definition or the steel-perspex assembly. There are some differences in the duration of irradiation and dwell times as compared to the first campaign. This change in pulsing and the change in neutron fluence causes a higher dose rate following beam shutdown, due to the differing accumulation of short half life nuclides. However, the difference in fluence between both campaigns is relatively small (7%), and it would be expected that the total dose rate after long decay times would be almost equal, to within 7%. The photon transport geometry for the second campaign is shown in Figure 5.20. Two detectors are placed into the cavity once during the irradiation, and left in position following the irradiation.

NE-213 neutron and gamma ray spectra and calculations

During the second campaign the neutron spectrum in the internal cavity was determined by an NE-213 detector. The side plug in the FNG was removed and the NE-213 detector placed into the centre of the cavity suspended by a boom. The detector was operating neutron-gamma discrimination mode in order to remove the contribution from photons. The irradiation then continued for a short period. The number of source neutrons produced in this short period is a fraction of 7.5×10^{-5} [80] that of the main irradiation. To be certain, the experimenters determined the dose rate in the cavity as a function of time up to the begining of the long intense irradiation. This measurement confirmed that no additional background needed to

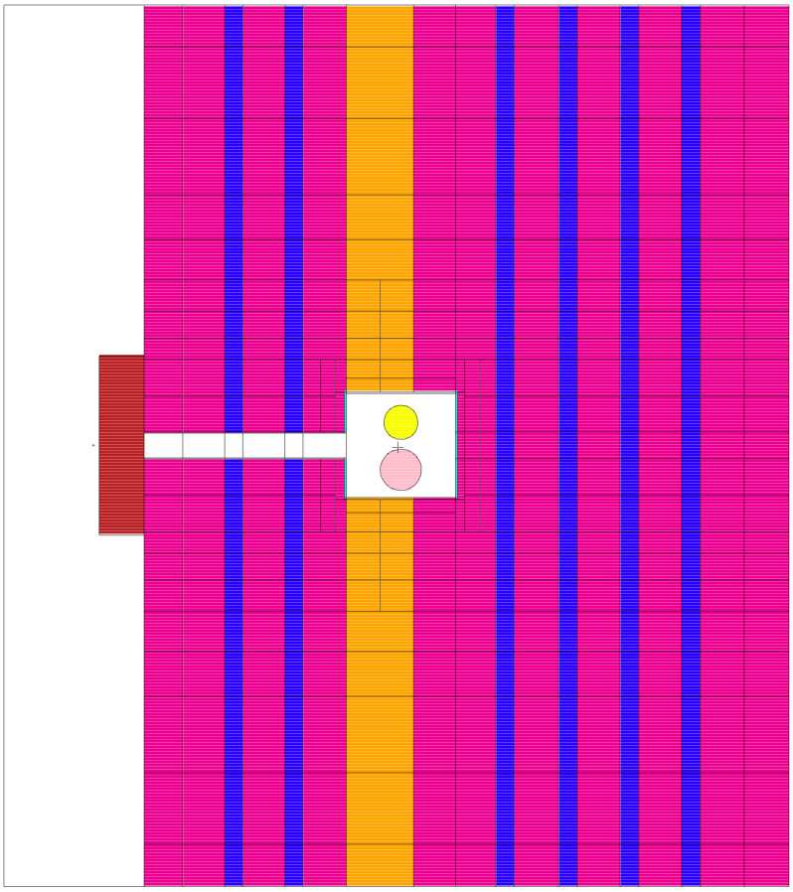

Figure 5.20: MCNP geometry for campaign 2 showing the detector setup

be taken into account [73]. The neutron spectrum calculated with MCNP and that determined experimentally are shown in Figure 5.21. It was reported in [80] that "The poor correlation between the simulation and experiment between an energy of 4 MeV and 12 MeV are due to poor counting statistics in the detector".

The gamma rays due to the activated material around the dose measurement cavity were measured using the same NE-213 liquid scintillator as the neutron spectra measurements. The scintillator was placed on a boom, which was then inserted into the dose measurement cavity. The detected signal was then converted to a gamma ray spectra using the unfolding program DIBFAS [81], which provided absolute fluxes. The spectra determination were performed at the same time as the dose

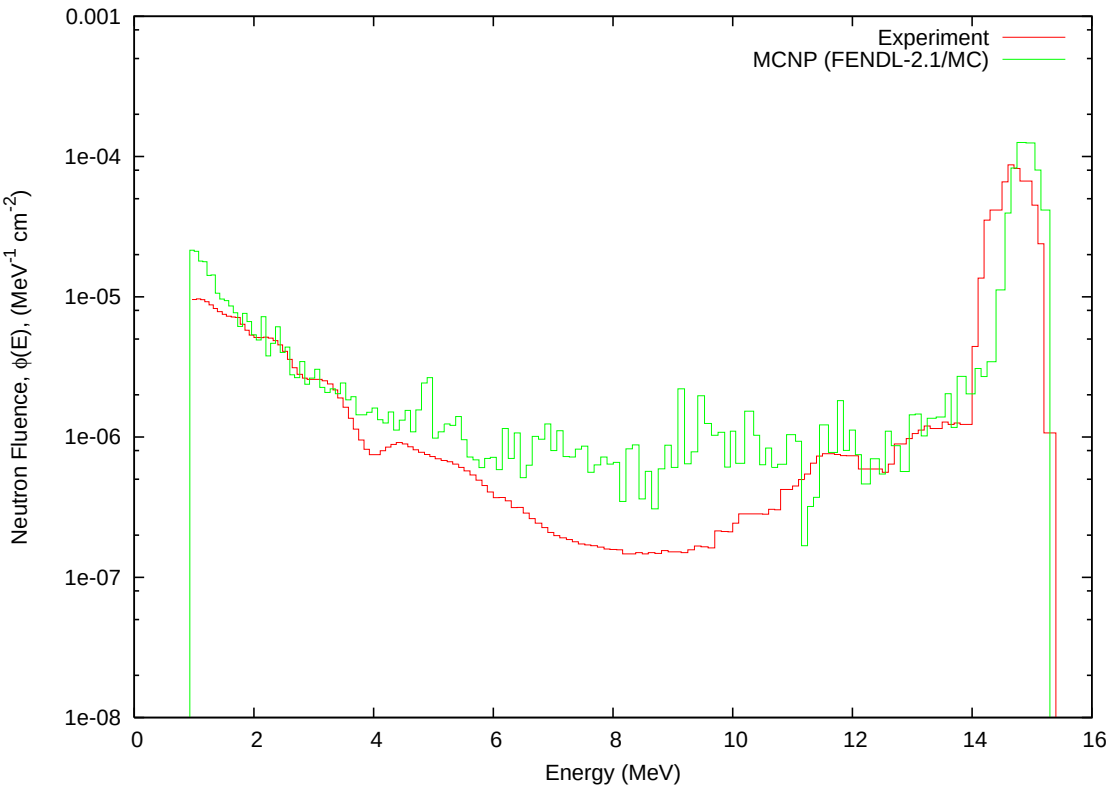

Figure 5.21: Neutron spectrum measured and calculated in the cavity

rate measurements, with the detectors lying adjacent to one another. The gamma ray spectra determined by MCR2S and those determined experimentally are shown in Figures 5.22, 5.23, 5.24 and 5.25. The results of this section also correlate with the findings in the original report, that the gamma ray spectrum generated by MCR2S and MCFISP under-estimate the gamma ray spectrum at low energies and over-estimate the gamma ray spectrum at higher energies. However, it is only a slight over-estimation and it is this high energy part of the spectrum that dominates the gamma ray dose, the difference gets smaller for longer decay times.

Second campaign dose rate measurements

The shut down dose rate was measured with a plastic scintillator (NE 105) which was inserted into the measurement cavity. The detector was calibrated at Physikalisch-Technische Bundesanstalt Braunschweig [80] and was determined to have a linear reseponse with photon energy [73]. The dose rate measurements started 73 minutes and ended 20 days after irradiation [80]. In the case of the shutdown photon transport calculations the doserate was determined in a volume with the same geometry and composition as the NE-105 scintillator.

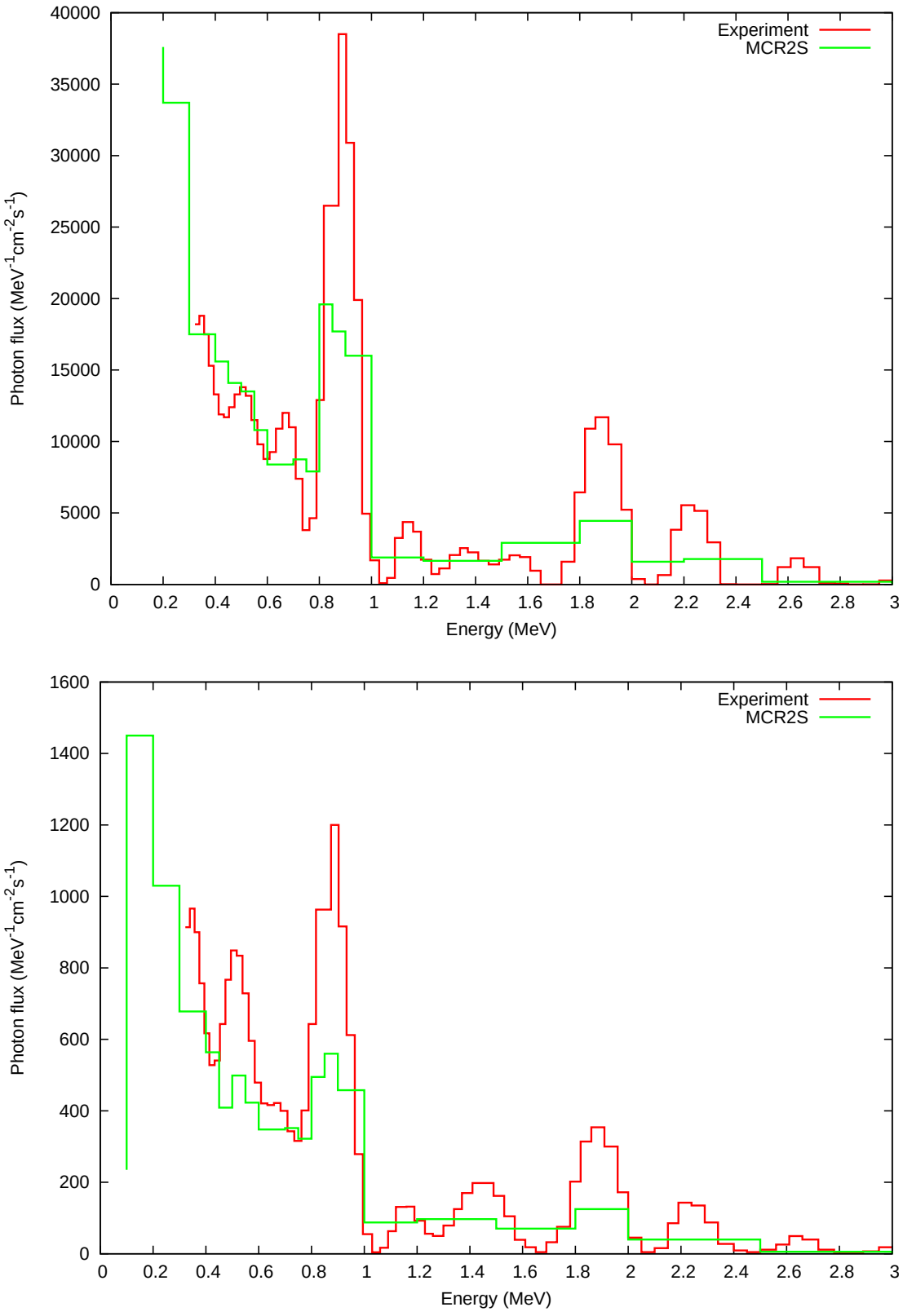

Figure 5.22: Shutdown photon spectra for 2.08 hrs (upper) and 15.9 hours (lower)

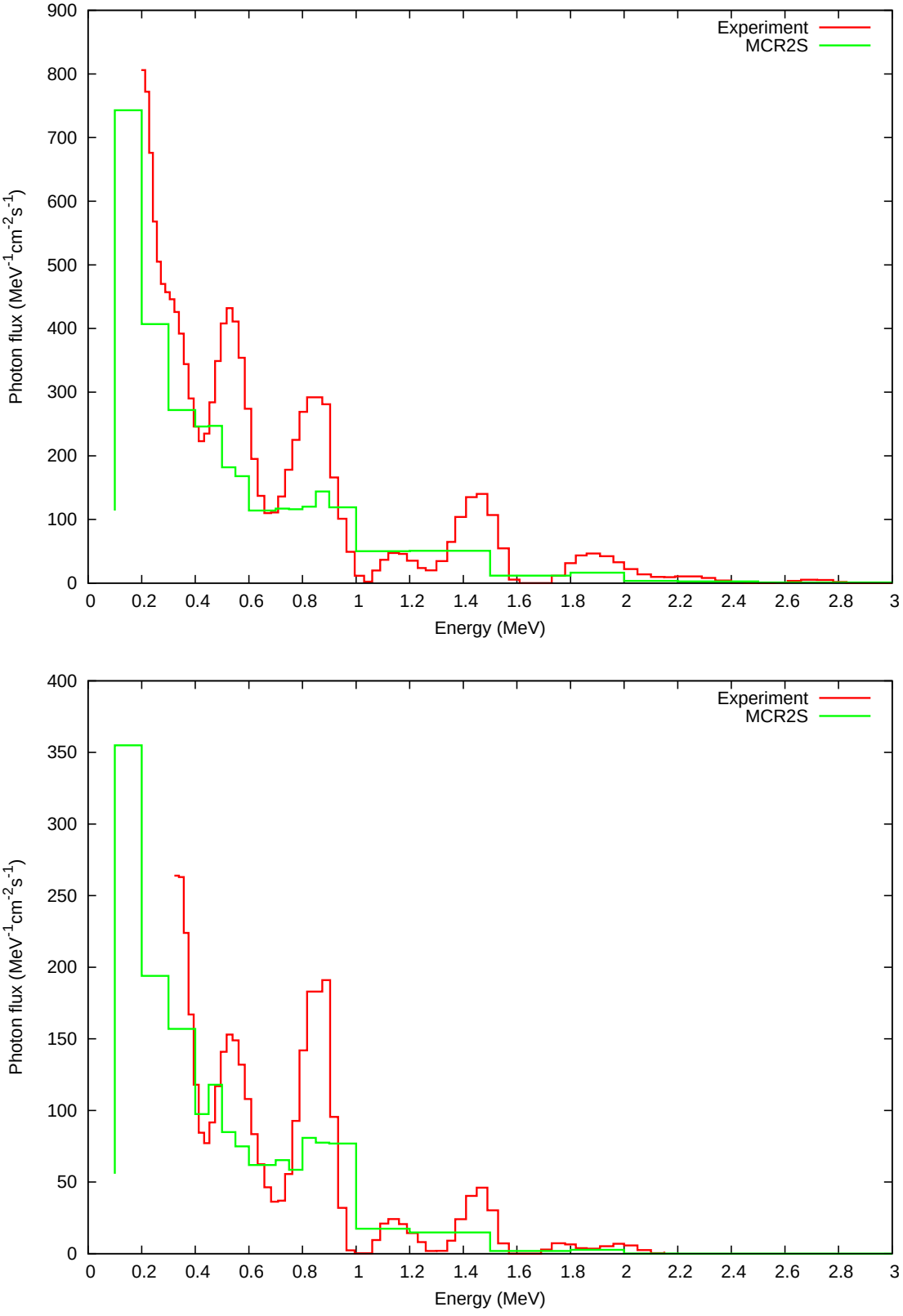

Figure 5.23: Shutdown photon spectra for 25.2 hrs (upper) and 4 days (lower)

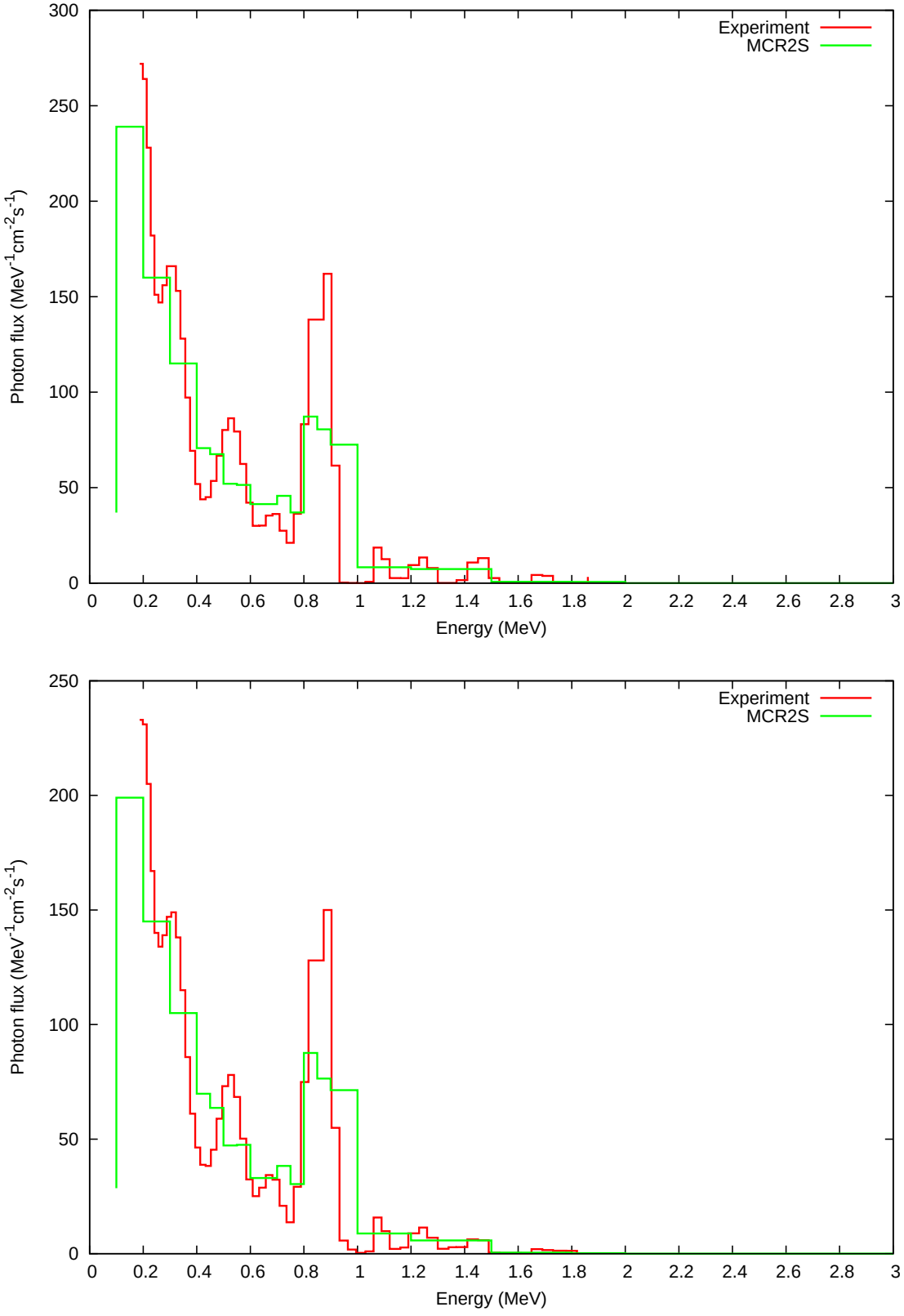

Figure 5.24: Shutdown photon spectra for 8.2 days (upper) and 12.2 days (lower)

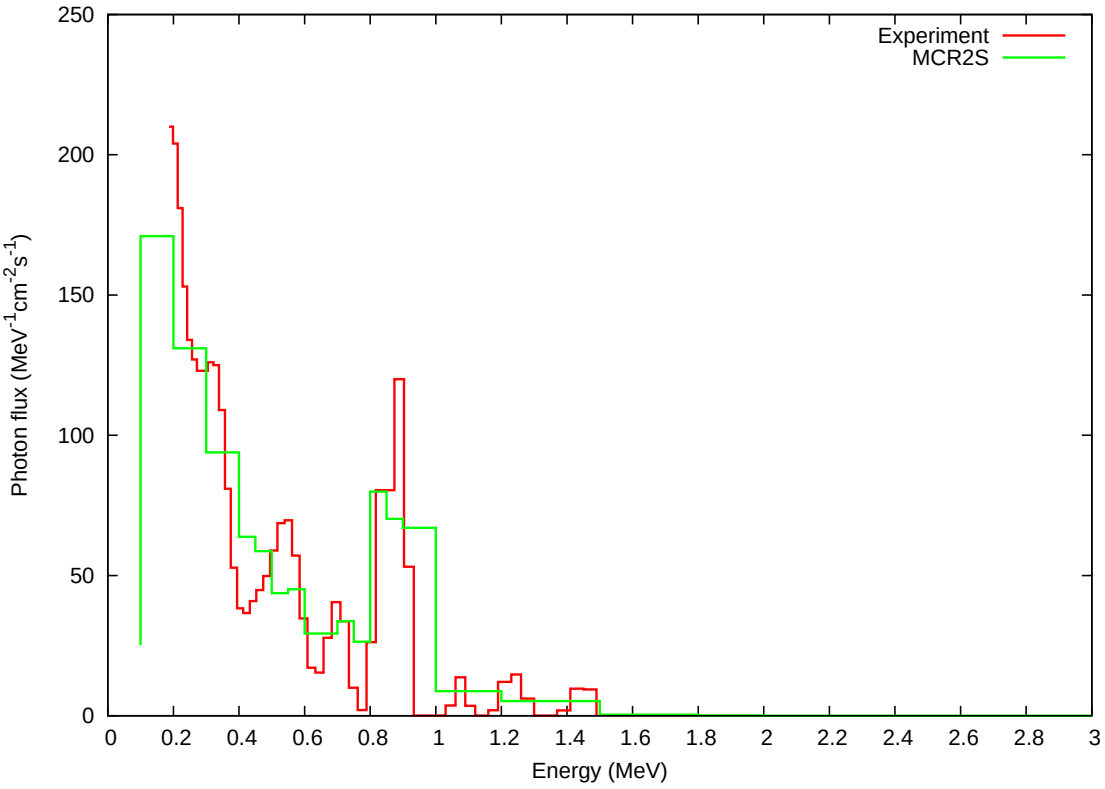

Figure 5.25: Shutdown photon spectra for 19.3 days (upper)

The doserate was determined by tallying in the detector volume and folding the derived photon spectrum with the same flux-to-dose conversion factors as previously performed in the first campaign. The shutdown gamma ray dose as a function of time for the doserate determined by the NE 105 scintillator, MCFISP and MCR2S using two different dose coefficients are shown in the lower part of Figure 5.26. As shown in Figure 5.26, the set of doserate data were determined for 19 decay times, shown in Appendix F Table F.2. The uncertainty bars shown in Figure 5.26 are those of the result of the MCNP tally uncertainty. The C/E results are shown in Figure 5.26 and show the deviation of the simulations away from the experimentally determined doserate. The two MCR2S trends follow a similar shape of curve to the original MCFISP data. Both the MCFISP and MCR2S-1977 (MCR2S spectra folded with ANSI/ANS-6.1.1-1977 dose response data) data match the experimentally determined dose data well. However, the MCR2S-1977 matches the experimental dose to within 3% after 4×10^5 s, and lies in the decay time range of interest to ITER, whose main shutdown dose targets are after decay times of 10^6 s. The dominant nuclides over the course of the decay gamma calculations were; ^{56}Mn between 0 and 4 Hours, ^{57}Ni between 1 and 5 Days and ^{58}Co for longer decay times.

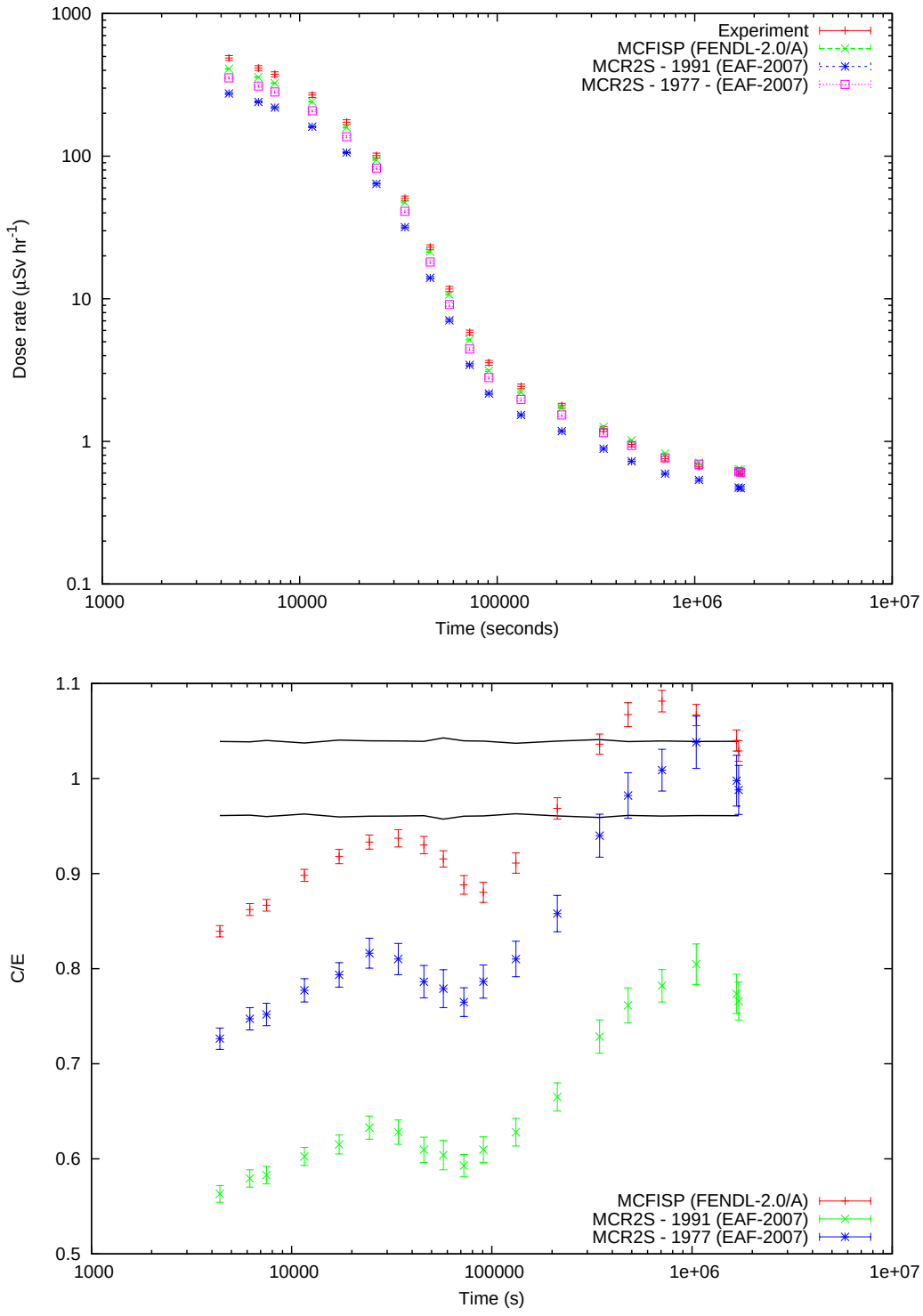

Figure 5.26: Doserates (upper) and Calculated over experimental (lower) doserates as a function of time for FNG Campaign 2, where the black line is the experimental uncertainty

Benchmarking of Attila-ASG by Youseff et al.

Youseff et al. [82] recently reported results of the ATTILA-ASG benchmarks on the FNG dose rate benchmark experiment. For the first campaign, ATTILA produces C/E's for a decay time of 1 day $\sim$ 0.8 (MCR2S 1977 $\sim$ 0.9) and at a decay time of 60 days C/E $\sim$ 1.3 (MCR2S 1977 $\sim$ 1.2). In the second campaign, for a decay time of 8×10^3s, C/E was 0.61 (MCR2S 1977 C/E 0.74), increasing to a C/E of 0.74 (MCR2S 1977 C/E 1.01) for a decay time of 7×10^5s. These values are similar to those found in the ATTILA-ASG/MCR2S comparison. They also found that at foil position 1 in the ^{57}Ni(n,2n) reaction rate measurement a 25% underestimation in the reaction rate, similar to what was found in the MCR2S FNG benchmark. The benchmarks compare favorably with one another, and it is the authors view that when EAF data is exported for use with ATTILA, results will be much closer.

Chapter 6

ITER PORT PLUG NUCLEAR ANALYSIS

This chapter describes the work performed on the nuclear analysis of a number of ITER equatorial port systems. The main task of these analyses was to estimate the shutdown gamma ray doserate at the rear of the port plug (PP) in and around the port interspace area. Each PP system has its own individual nuclear analysis needs, however there are some shared commonalities such as dose rate limits. The radiation transport code MCNP was used for the transport calculations using FENDL-2.1/MC cross section data. Activation calculations were performed using the inventory code FISPACT and the EAF-2007 activation libraries. The main results of ICRH nuclear analysis were reported in the papers A Borthwick et al. [83] and the result of ICRH and LIDAR analysis in A Davis, R Pampin and S Zheng [84]. A description of the computational tools used can be found in Chapter 3.

6.1 Port Plug Nuclear Requirements

Each port plug system, irrespective of its role in plasma operations, must adhere to strict nuclear saftey and machine operations guidelines. Some guidelines relate to

the cryogenic or material properties of the magnets, others to the radiation induced effects on the port plug system.

In the case of the ITER TF coils, the integral nuclear heating must be limited to less than 14 kW, hence the port plug system must not increase the nuclear heating to this critical value. This is an issue since the TF straddle either side of the equatorial ports. Nuclear heating is not the only value that must be limited. Other parameters such as dose or neutron fluence are equally important, thus there must be no directional biasing in the neutron transport of the port plug, such as to increase the lateral transport of neutrons.

There is also a need to produce detailed nuclear heat maps for the design of cooling systems. The results of high resolution heat maps can be used as input for CFD codes to determine if there is adequate provision of cooling for the entire plug. There is also a need to determine if there are any local heating hotspots due to neutron streaming, which may affect the temperature distribution in the plug.

There are also a number of structural requirements that must be met such as rewelding. Many components will require maintainence and port plugs are no exception. If components internal to the port plug system require rewelding, such as those of water connections, adequate shielding must be in place to ensure that the reweldability limit has not been passed. Weldability of irradiated stainless steel is mainly determined by helium production. The helium production limits specified by ITER are [51];

- $<$ 1 appm for thick plate welding
- $<$ 3 appm for thin plate or tube welding

The production of helium in stainless steels with some boron content is mainly via neutron capture reactions. ITER expects this mainly to be a problem in steels near water pipes due to the increase in neutron moderation. Hence boron content is also limited, and it is recommended that;

- < 0.002 wt.%B in steel for the first wall
- < 0.001 wt.%B in steel for the vacuum vessel cooling tubes

It is already known from a number of studies that the dominant dose causing nuclides in steels placed in a fusion neutron environment are mostly the alloying element impurities, with unstable transmuted isotopes being the remainder, and are ^{54}Mn,^{56}Mn,^{55}Fe,^{57}Co,^{58}Co,^{60}Co,^{57}Ni,^{51}Cr and ^{94}Nb. These nuclides are produced from transmutation reactions with the original steel matrix, and are responsible for the majority of the activation dose; the specific contribution from each isotope depends on the time elapsed since machine shutdown.

The port plug must also maintain the shutdown gamma ray dose limit of 100 μSv hr^{-1} at the port interspace flange, 14 days post shutdown. However, different port plugs have different projected lifetimes, for example the ICRH system is expected to have a maximal lifetime of 4 years which is projected to be due to neutron induced embrittlement of the vacuum windows.

6.2 The ITER ICRH Systems

The Ion Cyclotron Resonance Heater (ICRH) is one of four heating mechanisms planned for ITER. Electromagnetic radiation with a frequency of $\sim$ 50 MHz is propagated into the plasma. The exact frequency of the RF radiation depends on the ionic species being targeted. This RF radiation interacts with ion species in the plasma and causes the ions to increase their gyro frequency. Ultimately when these

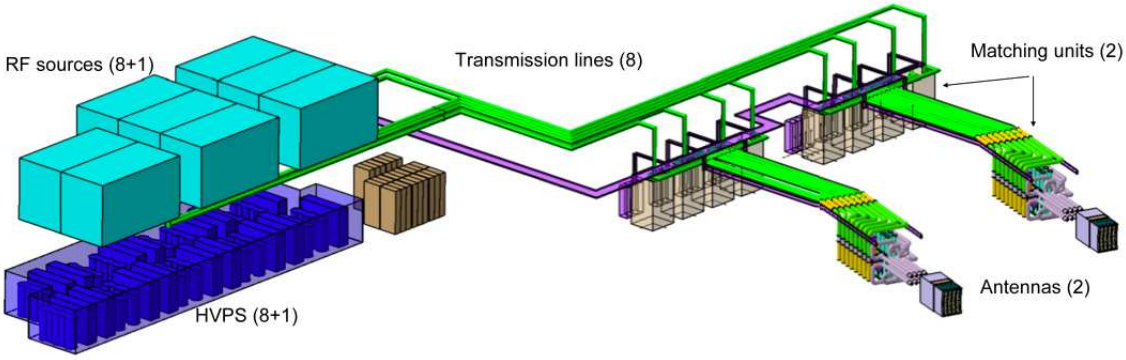

Figure 6.1: Layout of the ITER ICRH Externally Matched system [85]

ions coulomb scatter with other ions in the plasma, kinetic energy is shared amongst the scattering species, thus heat is injected into the plasma. The source of the RF radiation is produced externally to the plug and is supplied from gyrotrons/klystrons beyond the bioshield. The RF radiation is propagated along Vacuum Transmission Lines (VTL) which run from the RF sources to the rear of the ICRH. The ITER ICRH & Current Drive (CD) system, shown in Figure 6.1 is designed to couple 20 MW of power from two antennae in the frequency range of 40-55 MHz for a variety of ITER plasma scenarios. ICRH is expected in the majority of ITER plasma scenarios; without the 20 MW contribution of the ICRH system it is not possible to enter the high confinement plasma regimes required for ITER. This requires the system to operate reliably within the burning plasma environment [85]. The design concept proved the basis for the ITER-like ICRF antenna currently installed in JET. The ICRH system is to be installed in 2 of the 16 ITER equatorial ports, and thus represents 1/8th of the equatorial port plug shielding.

Two different designs of ICRH system were analysed in this work, namely the Internally Matched Option (IMO) and the Externally Matched Option (EMO). The EMO has the frequency matching system beyond the port plug, whereas the IMO has the equipment which matches the impedence of the VTLs to the plasma internal

to the port plug.

6.2.1 ICRH Externally Matched Option

The ICRH system is designed for insertion into an equatorial port, the geometry of the ICRH system is shown in Figure 6.2. The VTLs that carry the Radio Frequency (RF) radiation, run from the rear of the plug to the front and are only broken by a vacuum window. The VTLs extend throughout the entire length of the system, ending at the front face where the VTLs connect to the radiating straps. The VTLs are surrounded by a vacuum which extend over the same length. The ICRH VTL runs throughout the assembly, the junction box where the VTL separates into 8 junction boxes (4 upper and 4 lower).

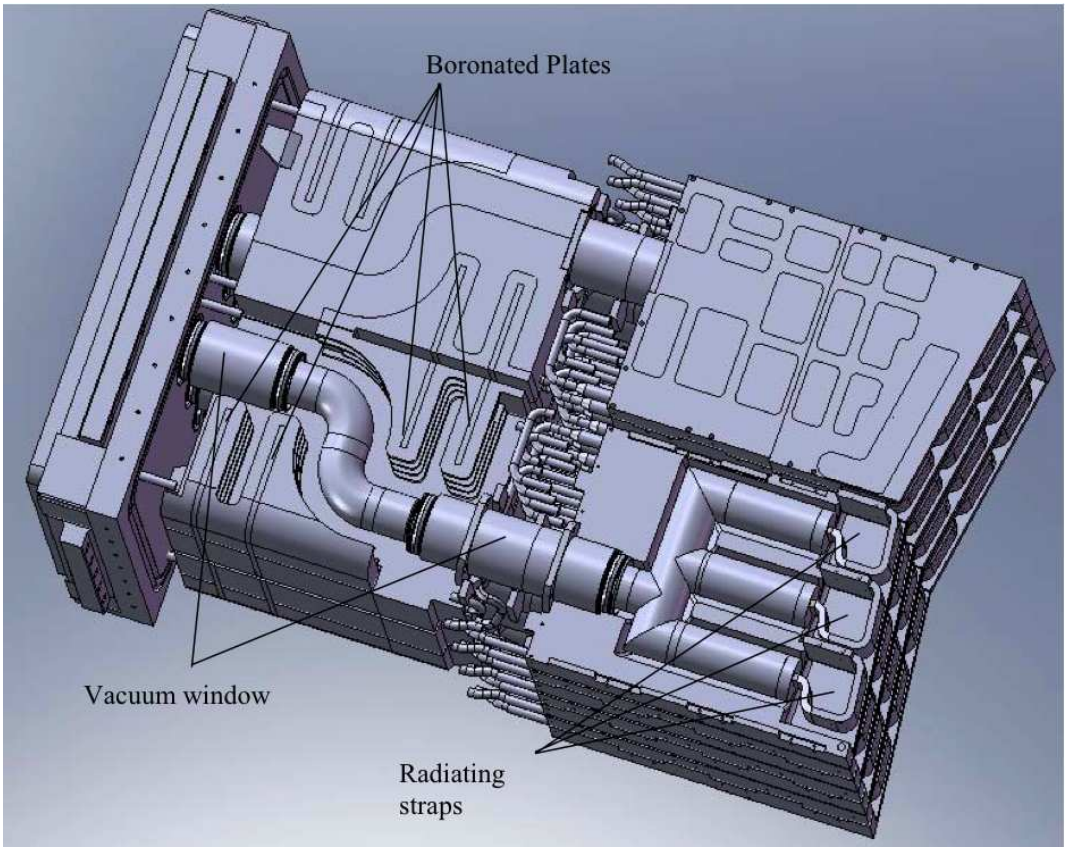

Figure 6.2: Geometry of the ITER ICRH EMO v2 [86]

6.2.2 ICRH Internally Matched Option

The IMO is the alternative proposed ICRH solution for ITER and is shown in Figure 6.3. The tuning capacitors of the IMO are located internally to the port plug. The

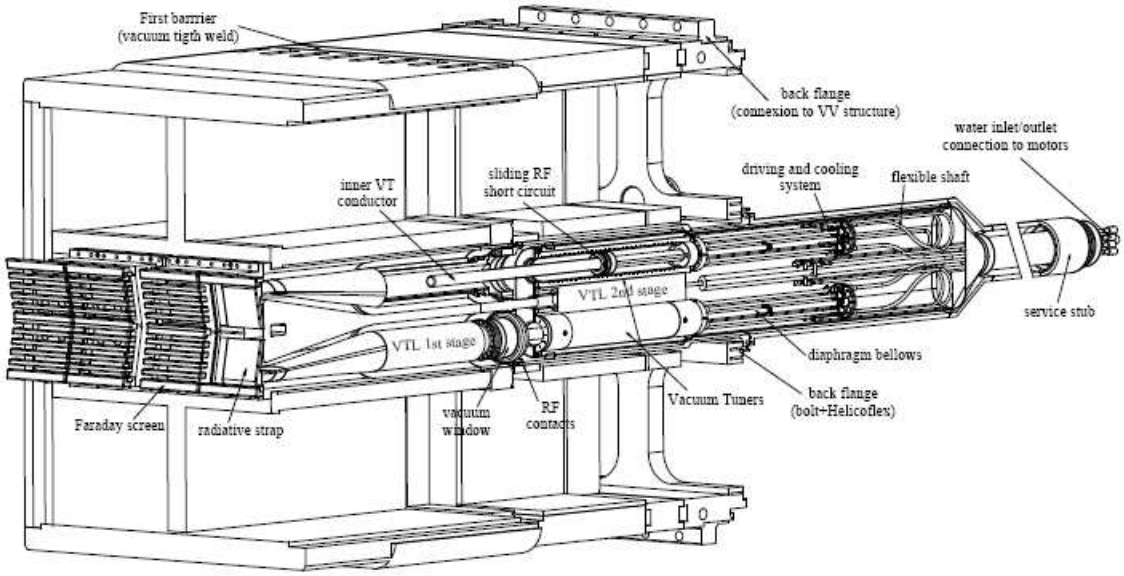

Figure 6.3: Geometry of the ITER ICRH IMO v1 [87]

antenna consists of six similar modules, as in Figure 6.3, and each module is made up of four identical antennas. An individual antenna measures 0.32m in height, 0.4m in width and 3.5m in length. The first stage of the system is under a vacuum, which extends from the Faraday screen until the Beryllium Oxide (BeO) vacuum window. Beyond the vacuum window lie the second stage units such as the RF tuning system and the diaphragm bellows. There is double bend in the vacuum transmission line (VTL) approximately 0.7m from the Faraday screen. At the rear of the unit, where the VTL second stage ends and the port plug flange begins, there is a large volume where there is no shielding material. The shielding material in the first section is 50 % (vol) 316 L stainless steel and 50 % (vol) water and in the rear the ratio increases to 70 % (vol) 316 L stainless steel and 30 % (vol) water. These stainless steel to water ratios approximately coincide with the recommended fractions [88].

The front of the unit has an angled RF antenna, the angle of which matches the curvature of the last closed magnetic flux surface. The antenna is centred on the equatorial plane of the torus and the front face will be subject to large neutron and heat fluxes, this means that water cooling will be required throughout the port plug. The presence of water is beneficial to the neutronics of the port plug, as hydrogen is an excellent moderator of neutrons.

6.2.3 Project Programme

The development schema of the two different designs is shown qualitatively in Figure 6.4. At the begining of the ICRH development program the two concept designs

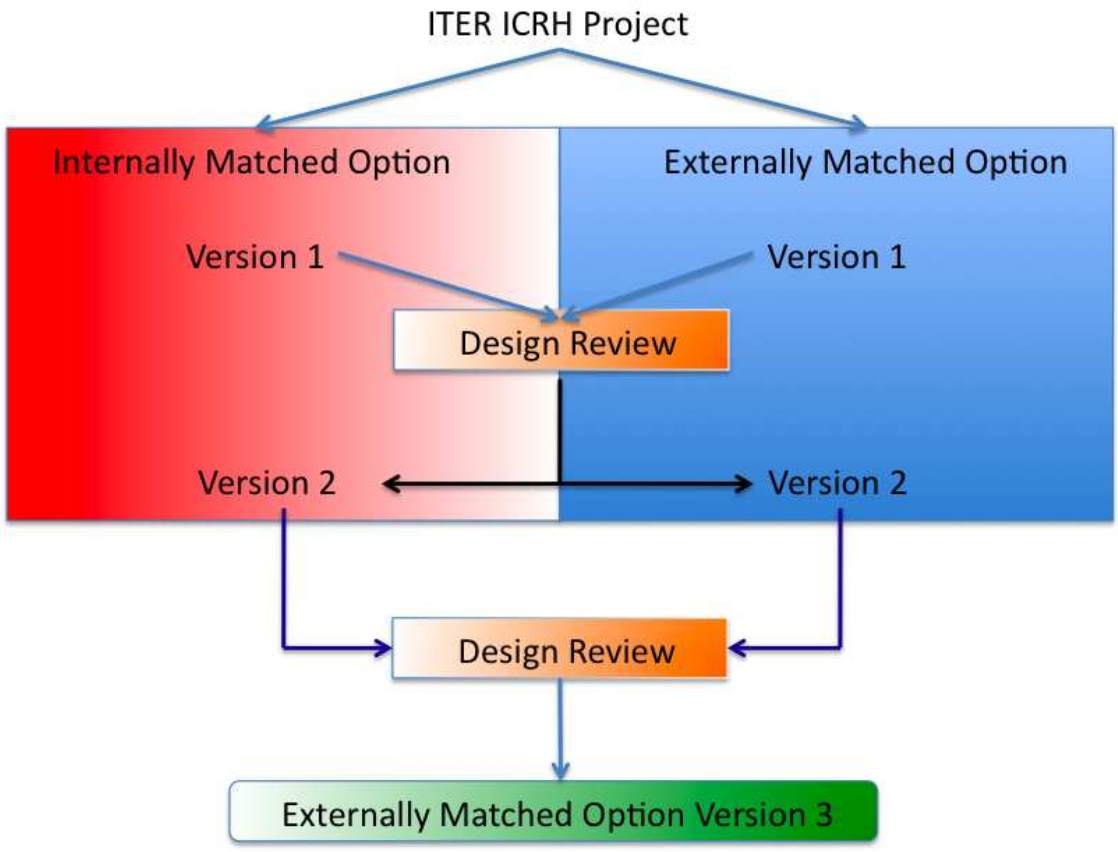

Figure 6.4: Flow chart showing the development of the ITER ICRH system

were analysed. Following these analyses, which encompassed nuclear, engineering and RF design, a second round of analysis was performed which rectified some of the design issues from the initial designs. The design review following the second version of the designs ultimately resulted in the cancelling of the internally matched design in favor of the externally matched option, which was deemed less of an engineering challenge.

6.2.4 Computational Approach

Neutronics calculations for the different design options described above, were performed with a parallel version of MCNP5 running on the Linux based Aethelwulf (Beowulf type) cluster at UKAEA Culham. FENDL-2.1 neutron and photon cross sections were used in the analysis. Two different source modeling methods were used: a parallel plane wave of neutrons defined at or near the front surface of the problem (hereinafter parallel source), and a parametrically defined fully toroidal neutron source described in Chapter 2 Section 2.5 (hereinafter torus source).

Source Modelling

The parallel source was used in scoping calculations and represents a pessimistic view of the radiation shielding of the system. For the torus source, a blank toroidal geometry was set up, with the plasma defined inside the torus. A centre column was set up to terminate neutron tracks that entered. The plasma had ITER dimensions; major radius 6.2 m, minor radius 2.0 m, vertical elongation 1.7, triangularity 0.33 and a peaking factor of 3.0. In all cases the energy distribution of neutrons was described by a Muir-Gaussian spectrum [3] peaked at 14.1 MeV and with a spread appropriate to an ion temperature of 20 keV.

Source Normalisation

In each case the neutron current passing through the front face of the ICRH was normalised such that the total neutron power incident is 0.78 MW m^{-2} (equivalent to a 14.1 MeV neutron current of 3.45×10^{13} n cm^{-2} s^{-1}), which is the peak neutron loading expected in the equatorial port regions of ITER [51].

Geometric Simplifcation

All the MCNP models were simplified to some level due to the inherently complex nature of engineering designs, that include small details that would have no influence on the neutron transport of the model. Where simplifications were made, they are discussed in detail.

Placement of the ICRH model

The ICRH geometry is placed in an equatorial port like region, with regions to terminate neutron tracks that do not enter the front of the ICRH directly. In the case of the parallel source runs, the source is defined along the front surface of the geometry, where the source neutrons are directed normal to the front face. Reflecting planes are used on the sides of the unit, to mimic the effect of the material surroundings.

Tally Uncertainties

In all cases investigated the MCNP runs were performed such that the statistical uncertainty in all tallies was less than 10%, except in the case of mesh tallies where this is difficult to maintain.

Shutdown Dose Calculations

In all cases investigated the shutdown gamma ray dose rate is the key parameter that determines the acceptance of the ICRH design. There were two methods used to calculate the shutdown gamma ray dose rate namely the FISPACT contact dose-rate and the MCR2S system.

For all examples of ICRH investigated the systems were irradated for a single ITER year. An ITER year is the average neutron production over the course of a year of ITER operations, which is assumed to be three thousand 400 s pulses at a power level of 500 MW. This is modelled as a single long irradiation at a lower flux, ϕ_{eq}, level which is the average flux of 2980 pulses over 363 days, which equates to

$$\phi_{eq} = \frac{\phi_A \times 2980 \times 400}{363 \times 24 \times 3600} \tag{6.1}$$

This long irradiation is followed by twenty 400 s pulses at full power, ϕ_A. The last few pulses are to correctly account for the build up of short lived nuclides, as shown in [52].

6.2.5 ICRH Version 1

Externally Matched Option

The initial neutronic scoping studies were performed on a simplified neutronic model of the EMO. The major structural details of the engineering design were homogenised in the neutronic model. The Faraday screen and the VTLs at the front of the system were simplified. The geometry used of the ICRH system is shown in Figure 6.5. The parameters that must be determined are the neutron flux and resultant activation at the rear of the port plug at the port interspace. As part of ITER ALARA principles, the guidelines state that if the dose to workers exceeds 100 μSv hr^{-1} then a detailed

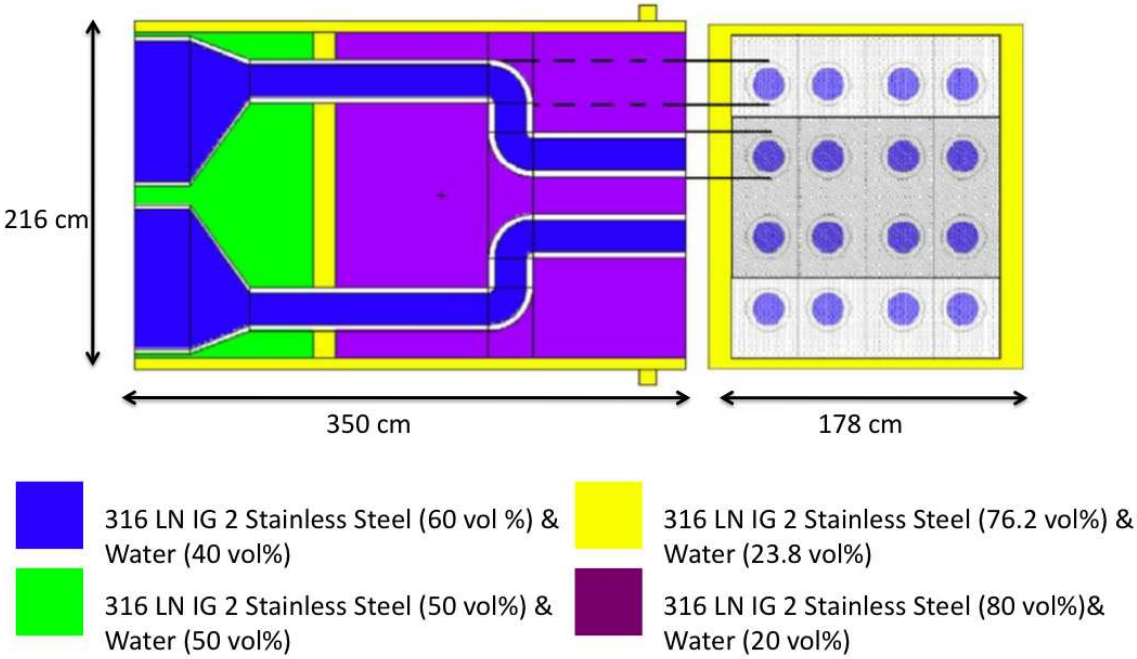

Figure 6.5: ICRH v1 MCNP geometry

investigation into the shielding design must be carried out.

The model was irradiated with the parallel source located at the front face of the antenna. A numeric description of the total neutron flux as a function of thickness was determined by performing a series of MCNP neutron runs. In each subsequent run the shielding thickness was increased by 10 cm. At each thickness the neutron spectrum was determined so that a FISPACT inventory calculation could be performed. The total neutron flux for each thickness interval and for each of the two tallying locations are shown in Figure 6.6 The dose arising from such irradiation at each thickness interval is shown in Figure 6.7.

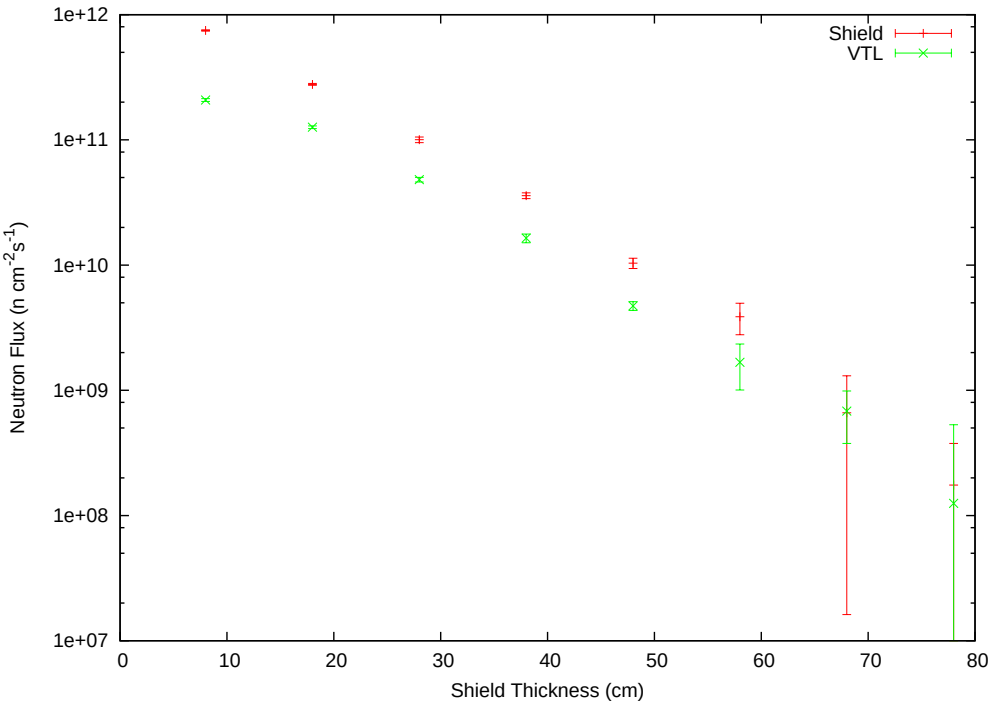

Figure 6.6: Total neutron fluxes at the rear of the ICRH v1

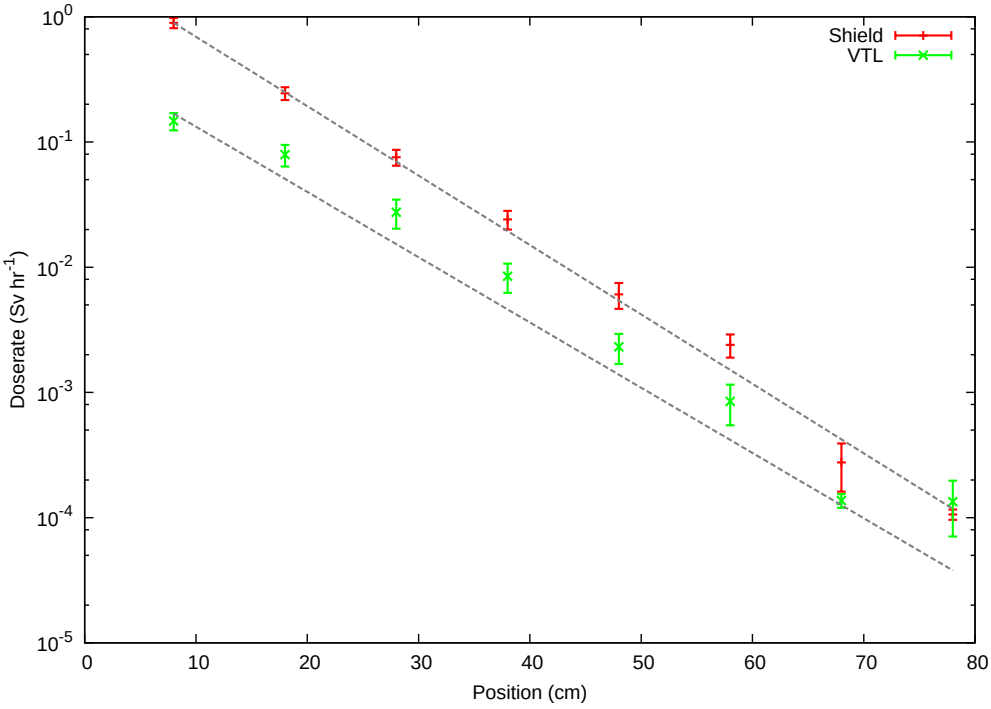

Figure 6.7: Shutdown contact gamma ray doses at the rear of the ICRH v1

By extrapolating the data in Figure 6.7 to the full length of the VTL, the analysis showed that the dose is lower than 100 μSv hr^{-1} which is the nessessary critereon of this design.

Internally Matched Option

A MCNP model was created from CAD drawings supplied by the CEA. This model along with the materials information supplied make a complete model. In keeping with the analysis of the EMO a parallel plane source was used due to the early design stage of the design. Due to the complex geometry in certain elements of the IMO design a number of modelling simplifications had to be made;

- MCNP is not capable of precisely recreating the outer VTL first stage, which has a cross-section which varies from circular to lozenge shaped. Instead, this section is replaced with a square cross section inclined at the same angle. This leads to a slight overestimate in shielding (reduced dose rate)
- For simplicity, reflecting planes were put in the model, this has the same effect as if 4 antennas were modelled as a single unit
- The louvrés in the Faraday screen were neglected as they are neutronically thin, and the gaps replaced with material identical to the surrounding material
- The materials are assumed to be a homogenous mix of its constituent nuclides, which is due to the early stages of the design

The geometric model is used in conjunction with materials data and MCNP to calculate the neutron spectrum and flux leaving the rear of the antenna system. Two cases were considered, shown in Figure 6.8,

1. The model as per the schematic (case A)
2. The model with additional rear shielding (case B)

In case B the rear section is filled with the same steel and water mix as in the adjacent material cells. In reality this region will be filled with complex water cooled steel components with an effective reduced density. These two cases therefore enclose the likely effective shielding of a complete model. The neutron spectra leaving

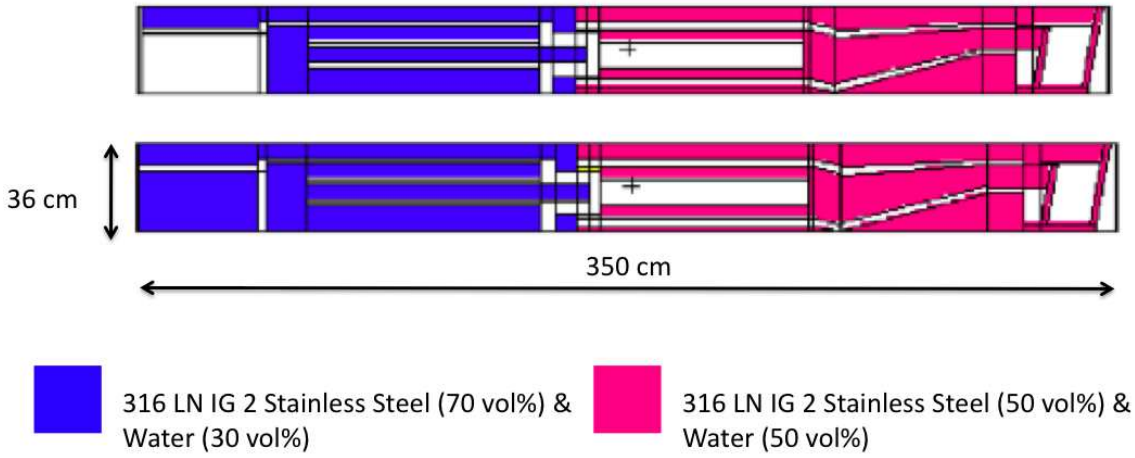

Figure 6.8: MCNP Models of ICRH V1 IMO (A [upper] and B [lower])

the rear of the unit in cases A and B have no significant differences in energy, however the intensity is smaller in case B. The integral fluxes at the rear of the antenna are:

Case A: 7.512×10^9 n cm^{-2}s^{-1} $\pm$ 0.85%

Case B: 1.535×10^9 n cm^{-2}s^{-1} $\pm$ 1.92%

The dose rate calculations were performed with FISPACT. Using the spectra calculated by MCNP the induced activity can be calculated. During the neutron transport calculations the material in which the neutron flux is determined, is some mixture composed of steel and water, however, this is not appropriate for the activation calculation since water is removed from the system during maintence. Thus the activation calculation should proceed with a given mass of steel with a density

Nuclide	Percentage dose rate
^{58}Ni(n,p)^{58}Co	55.23
^{55}Mn(n,2n)^{54}Mn (43.27%) ^{54}Fe(n,p)^{54}Mn (56.68%)	21.3
^{181}Ta(n,γ)^{182}Ta	14.58
^{59}Co(n,γ)^{60}Co (45.27%) ^{60}Ni(n,p)^{60}Co (53.63%) ^{63}Cu(n,α)^{60}Co (0.624%)	4.64

Table 6.1: Dominant dose causing nuclides after 14 days decay time in 316(L)N-IG2 at rear of ICRH V1 IMO

lowered to account for the removal of water, which would otherwise reduce the dose rate due to additional attenuation.

The dose rate in case A is 5.64±0.86 mSv hr^{-1}

The dose rate in case B is 1.09±0.20 mSv hr^{-1}

These are a factor of 57 and 11, respectively, too high. It should be noted that the addition of the 46 cm of extra shielding in case B reduces the dose rate by a factor of 5.14. In either case the attenuation of the system needs to be increased by at least an order of magnitude in order to be acceptable by ITER.

Further calculations [86] showed that there was excessive amounts of neutron streaming in the first design of the IMO. Recommendations were passed to the engineers of the CEA regarding this. The four highest contributors to the dose after 14 days cooling time are the reaction products ^{54}Mn, ^{58}Co, ^{182}Ta and ^{60}Co. The percentage contributions to the dose are given in Table 6.1. ^{182}Ta is a significant dose rate contributor, but is only 0.07% of SS316L(N)-IG2 by mass. The specific composition of the steel could be tuned in order to reduce the doserate from specific isotopes, but this must be done within limits.

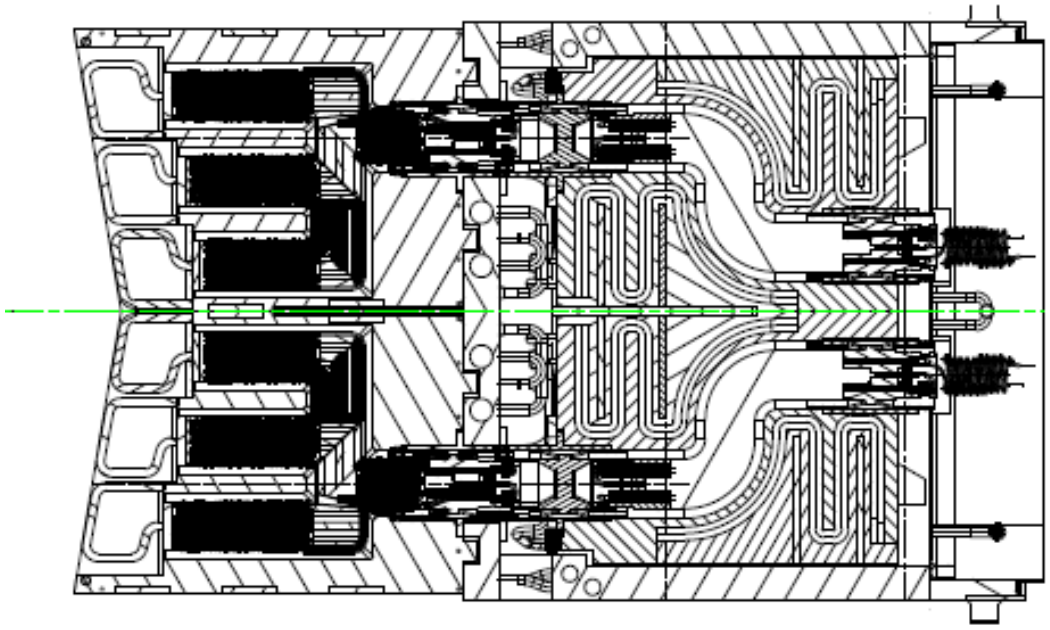

Figure 6.9: CAD Drawing of the ICRH v2 [89]

6.2.6 ICRH Version 2

Externally Matched Option

The ICRH v2, shown in Figure 6.9, was an evolution of the v1 design, and hence the vast majority of the lay-out remained unchanged. The entire unit was encased in a water cooled cowling. The VTLs extended throughout the geometry and were only broken in the void between front and rear modules by a vacuum window. The VTLs began in a trident formation which then merge into a junction box roughly 1 m from the front of the system. The front module of the ICRH system was constructed of a complex series of water chambers and baffles and hence was required to be modelled in some detail. Beyond the vacuum window the VTLs had a dogleg, additionally in this design boron carbide plates were inserted in pairs before and after the dogleg. The model used in the calculations is shown in Figure 6.10, and comparing this with Figure 6.9 the amount of simplification can be seen. The on-load neutron dose

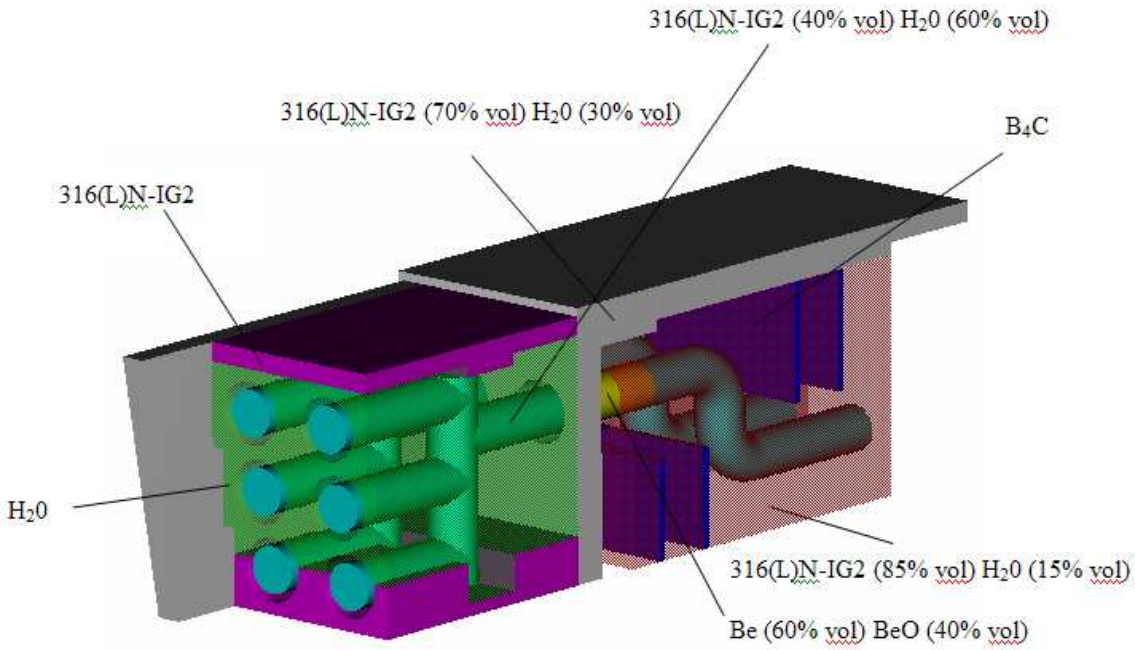

Figure 6.10: Sabrina[90] rendering of the MCNP model for ICRH v2

rate is calculated by transporting neutrons through the geometry and calculating the neutron spectrum at the rear of the geometry. The three-dimensional neutron flux distrubution is shown in Figure 6.12. There is evidence in this figure for neutron streaming down the shield-core conductor annulus. The dogleg in the geometry helps to reduce the effect of neutron streaming. The boronated plates before and after the dogleg absorb some of the thermal neutron flux present and reduce the activation of the region around the plates. The effect of the tetra-boron carbide plates on the neutron flux spectra can be seen in Figure 6.11. The boron carbide plates are 2.5 cm thick with a distance between plates of 19 cm. The thermal region of the neutron spectrum is significantly affected by the boronated plates. Immediately after the plate, the spectrum is "hardened" i.e. it is more dominated by energetic neutrons. The neutron spectrum is then folded with full body frontal irradiation fluence-to-equivalent dose conversion factor [37], thus providing an estimate of the effective dose equivalent rate present in the regions behind the ITER ICRH exter-

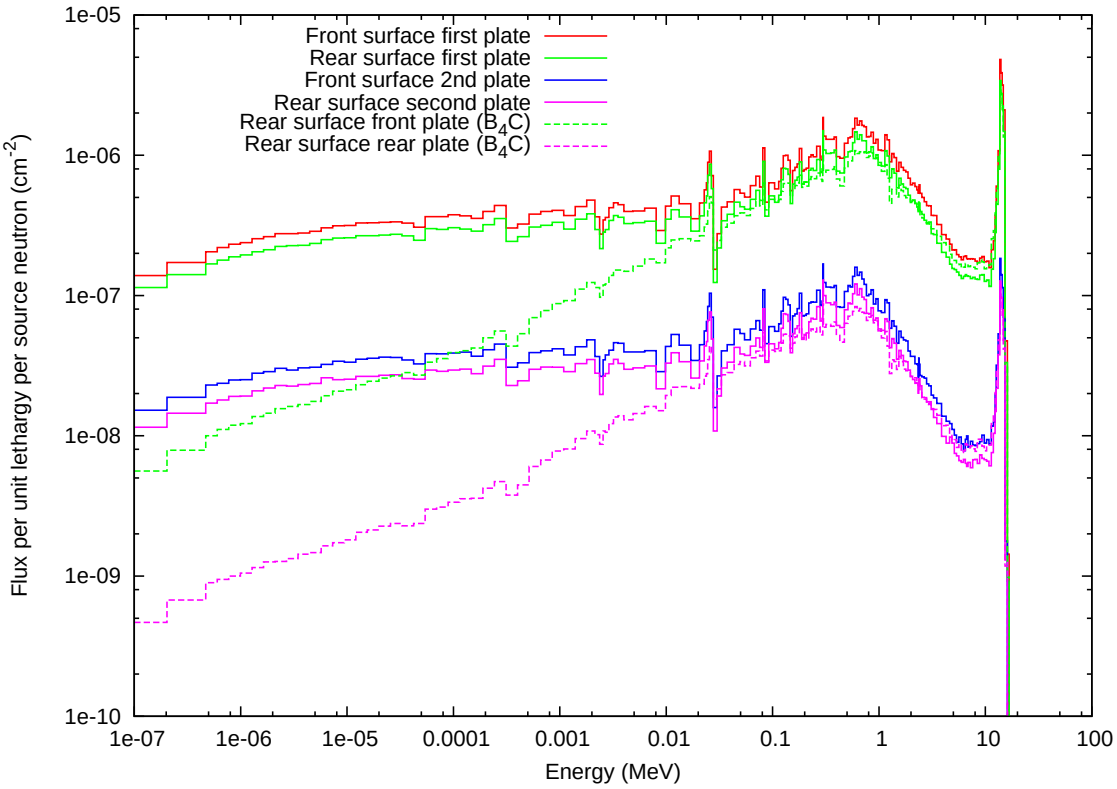

Figure 6.11: Hardening of the neutron spectrum due to B_4C plates

nal matching option. The onload neutron effective contact dose equivalent rate is 176±74 mSv hr^{-1} and the onload photon effective contact dose equivalent rate is 116.4±4.9 μSv hr^{-1} . The doserate is not an issue to personnel as no maintainence will be carried out while the device is onload, however this doserate may be useful for estimating potential damage to electrical equipment in the port interspace.

The neutron induced heating in the ICRH system was also investigated, shown in the upper part of Figure 6.13, and it was found that the largest amount of neutron heating is in the core conductor and the stainless steel cowling around the ICRH unit. There is some additional heating in the boronated plates due to the boron capture reaction $^{10}B(n,\alpha)^{7}Li$.

All photons that contribute to the photon heating, shown in the lower part of Fig-

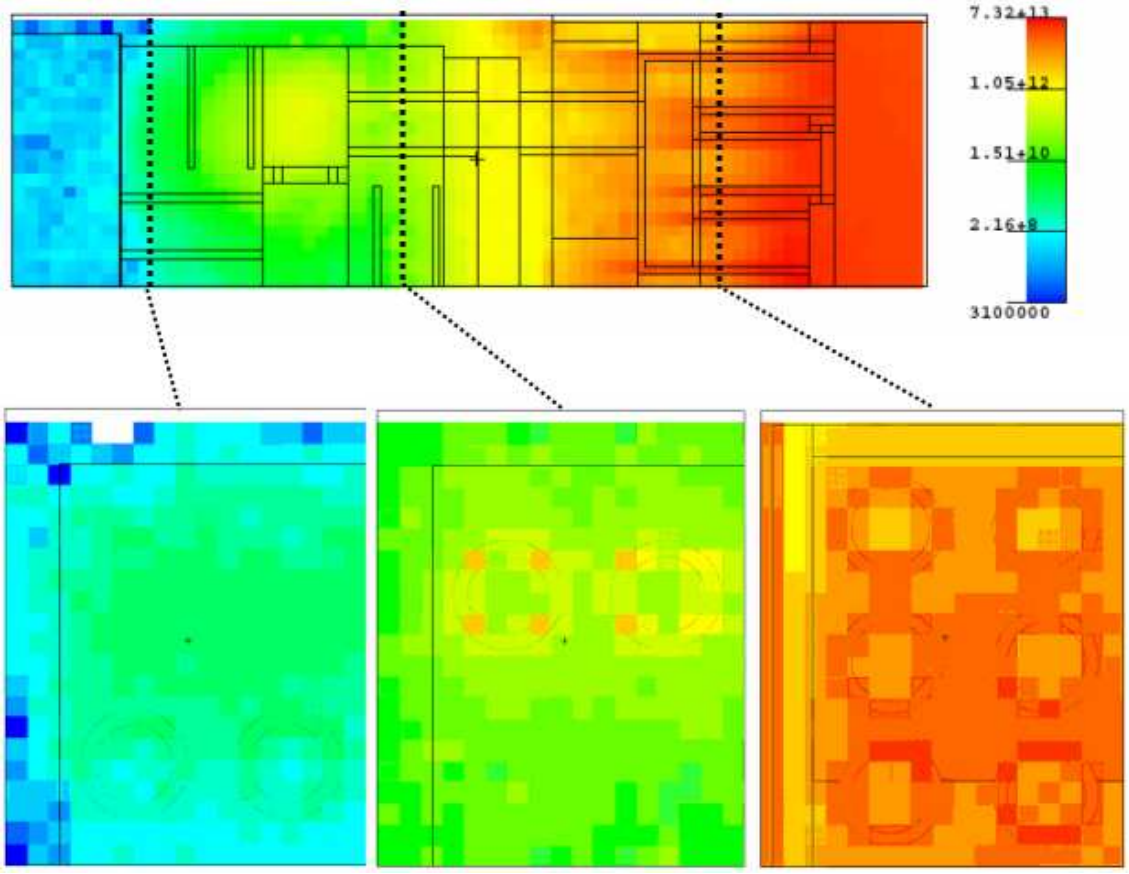

Figure 6.12: Onload neutron flux distribution ($cm^{-2}s^{-1}$) in the ICRH V2

ure 6.13 are produced from inelastic scattering and radiative capture of neutrons. These photons then deposit some or all of their energy via Compton scattering, photoelectric effect or pair production interactions. This deposition of energy ultimately manifests itself in the form of heat. The amount of energy deposited is a strong function of atomic number, hence why the amount of photon heating drops in B_4C plates since the atomic number and density is less than the surrounding steel.

Due to the physics of neutron transport the distribution of activation in a shield follows an approximate exponential trend with increasing depth. One of the consequences of this is that the strongest source of photons, that nearest the neutron source, has the most thickness of shielding to pass through in order to contribute to

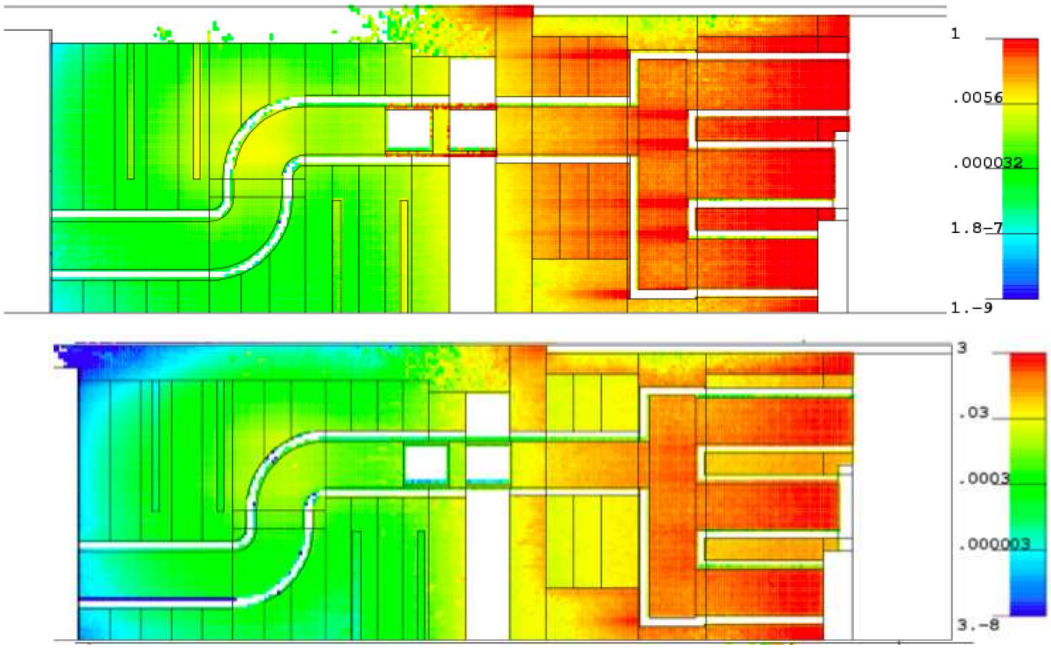

Figure 6.13: Neutron heating (upper) and Photon heating (lower) (W/cc) of the ICRH v2

dose at the rear of the shield. However, the least activated part of the shield (that furthest from the neutron source), in general, contributes the most dose at the rear of the shield. This effect is known as self shielding.

The shutdown γ-ray doserate was calculated using MCR2S and a MCNP photon mesh tally is placed in the void region at the rear of the ICRH unit to determine the shutdown gamma ray dose. The fluence-to-effective dose equivalent conversion factor [37] is then folded with the MCNP results to provide the effective dose equivalent rate as a function of position, shown in Figure 6.14. The total dose rate is greater than the 100 μSv hr^{-1} that is specified by ITER requirements, but the dose rate decreases with increasing position, and is below 100 μSv hr $^{-1}$ at 35 cm.

The French nuclear industry radiation level zonings are shown in Figure 2.4. Green zoning has a 25 μSv hr^{-1} dose limit and the rear of the ICRH cannot be classed as such, but it passes the conditions for a Yellow zone of 2 mSv dose limit and dose rate

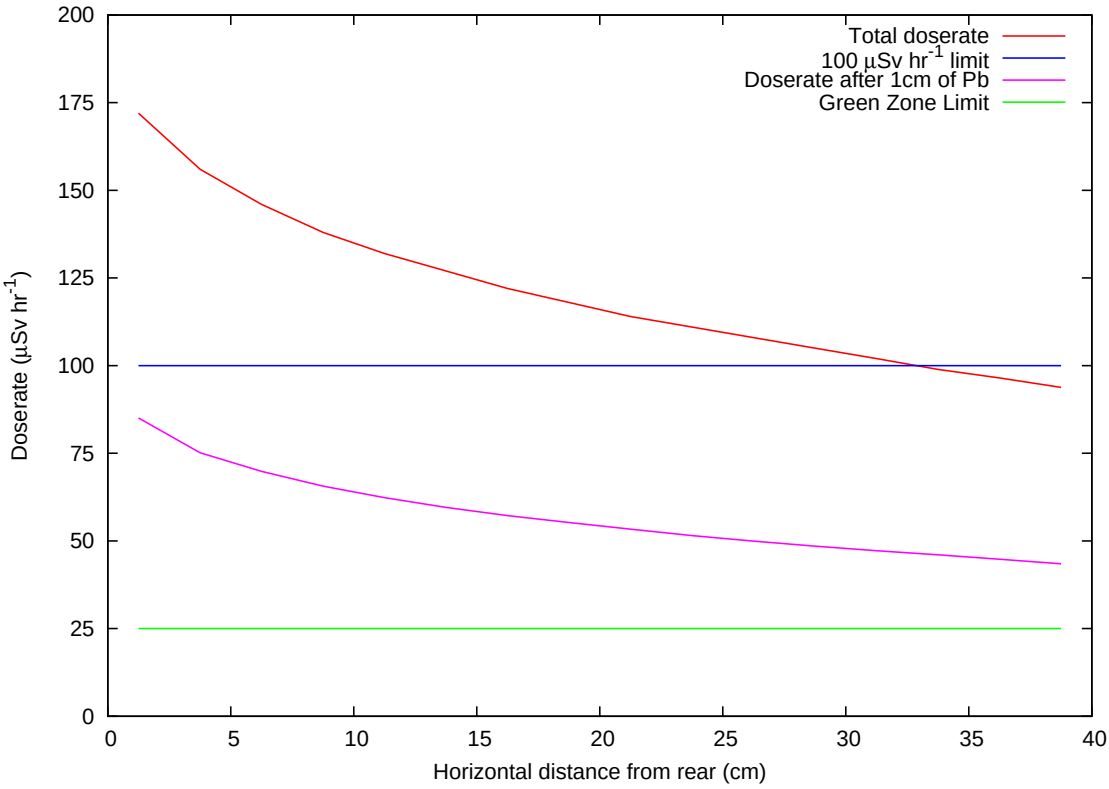

Figure 6.14: Doserate results for the ICRH v2 after 14 days decay time

less than 2 mSv hr^{-1}. The addition of 1 cm of lead, as can been seen in Figure 6.14, reduces the dose rate below the 100 μSv hr^{-1} dose rate limit, but remains above the Green zone limit. An addition of another 1 cm of lead reduces to the doserate to Green zone levels by $\sim$ 30 cm away from the rear of the system.

Comparison of the ICRH EMO v1 and v2 designs show that by including more precise geometric details and material distributions as the design has progressed has increased the doserate. This is not unsuprising as the v1 design was approximate with the exception of streaming paths.

Internally Matched Option

The neutronic calculations for the 2nd version of the Internally Matched antenna were not performed by the author and are only mentioned for completeness. The ICRH model was created from CAD drawings and the calculations were performed by M J Loughlin and were reported in [86].

6.2.7 Comparison of parallel and toroidal irradiations

One of the main assumptions used in the analysis of the v1 and v2 designs was the use of a parallel beam irradiation. It was assumed that the parallel irradiation was representative of the neutron flux entering an ITER equatorial port. In order to verify this, the ICRH EMO v2 model was incorporated into an ITER equatorial port location and both a toroidal and parallel beam neutron source were used.

The ICRH v2 model was analysed using both the parallel and torus source in order to compare how the neutron transport calculations differ between a parallel irradiation and a tokamak type neutron source. Under the presence of a parallel beam irradiation, shielding with penetrations that run parallel to the incident radiation will show the least attenuation. MCNP mesh tallies are the only choice of tally for gaining neutron flux data across the entire model. The dimensions of each volume element are 1 cm $\times$ 1 cm $\times$ 1 cm. The total neutron flux in the parallel and toroidal irradiation cases are shown in Figure 6.15. It can be seen in Figure 6.15 that the attenuation profiles are quite different. Firstly the toroidal irradiation results in less streaming along the waveguide-shielding annulus: this is because of the smaller solid angle projected by these voids to the strongly angular dependent torus neutron source. Secondly, despite the torus source and the parallel beam source having the same energy distribution, the spatial distributions of flux in the plug are different, due to the differing transport of the source neutrons, and hence this is primarily due

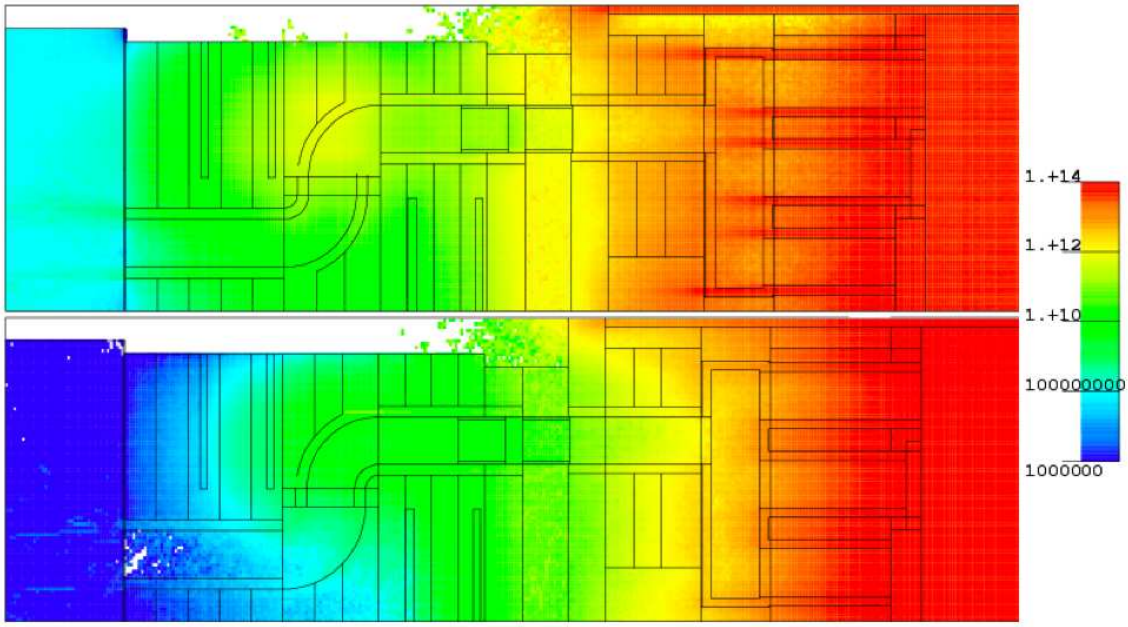

Figure 6.15: Total neutron flux data for the parallel (upper) and toroidal (lower) irradiations ($cm^{-2}s^{-1}$)

to the differing angular source distributions. In the case of the parallel irradiation, the neutron heating is shown in Figure 6.16. It is observed that the greatest heating is at the front of the module, however there are local maxima in heating in the boron plates and at the dogleg knee, where neutron streaming along the vacuum annulus is the cause. The maximum neutron heating peaks at 3.7 W cm^{-3}. In order to calculate the shutdown gamma ray contact dose rate, the neutron spectrum at the rear of the system must be calculated in fusion weighted 175 neutron energy groups. The spectrum is then passed to FISPACT along with materials, irradiation and cooling specificiations. The result of the calculation is the shutdown gamma ray contact dose rate at the location specified. The torus source model shows a significantly lower activation induced dose rate, shown in Table 6.2. Integral nuclear heats are comparable in both models. The results show that the parallel beam is a poor approximation to a toroidal source, and the full toroidal source should be used in future work where absolute values are required.

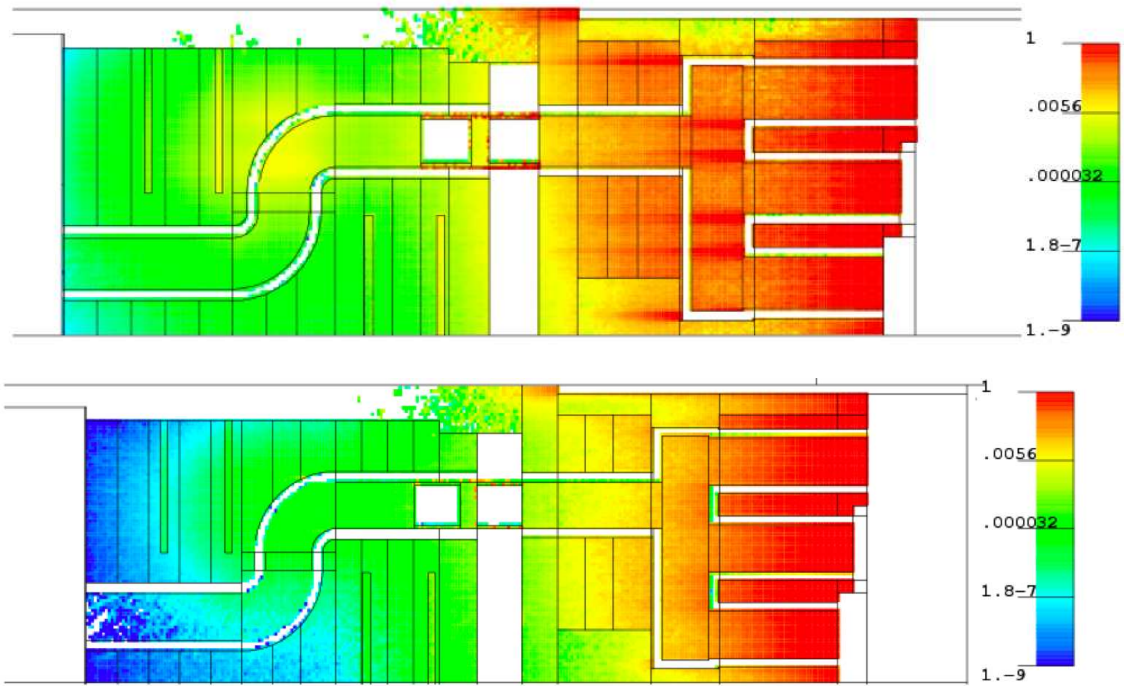

Figure 6.16: Neutron heating of ICRH v2 under parallel irradiation (upper) and toroidal irradiation (lower) (W cm^{-3})

Irradiation type	Shutdown Contact Dose rate (μSv hr^{-1})
Parallel	8590±603
Toroidal	0.5±0.3

Table 6.2: Comparison of shutdown gamma ray dose rates due to differing neutron sources

6.2.8 ICRH Version 3

The ICRH v3, shown in Figure 6.17 is a departure from the designs previously investigated. The RF engineering of the dog-leg bends proved troublesome and so the internal layout of the port plug was altered to simplify the engineering challenge. The VTLs are altered to a straight through penetration, similar to the IMO v1, however to provide sufficient neutron attenuation, the internal annulus is made smaller in chamfered steps. The vacuum window design [91], is more complete than in previous designs. The vacuum window is composed of a number of exotic materials such as Ti_6Al_4V and BeO/Be. The rear section of ICRH v3 is composed of

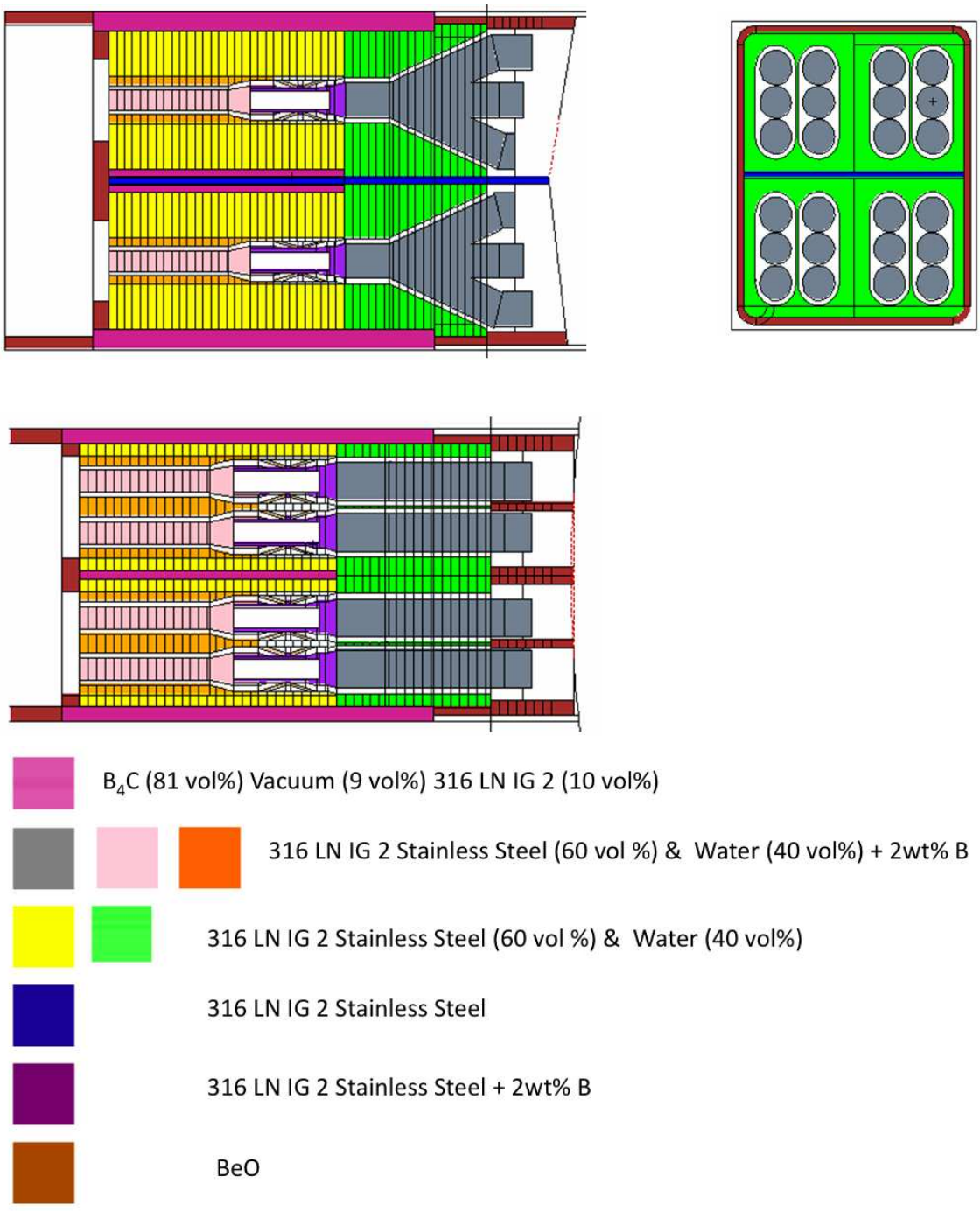

Figure 6.17: MCNP model of the ICRH v3

a removable pill type section to facilitate maintenance of the VTLs of the ICRH system. It would simplify maintenance if the entire pill section could be removed to a hotcell where workers could have access to the system.

The neutron transport properties of the new design were investigated to ascertain the flux distribution throughout the ICRH plug. In addition, during the course of the analysis a number of other parameters were requested by the ICRH design team, namely the vacuum window fast neutron fluence and an estimation of the cadmium production in the vacuum window brazes, made of silver, the location of the vacuum window is shown in Figure 6.18. The radiation transport model was created from engineering CAD drawings and material compositions were supplied by the ICRH design team.

The following criteria must be met

- Activation dose rate after 1 year of D-T operation and 14 days cooling time must be less than 100 μSv/hr
- The fast neutron fluence to the vacuum windows must be less than 10^{20} n cm^2 after 4 years of D-T operation

The fast neutron fluence across the vacuum window (VW) is one of the key parameters for the operation of the ICRH. The fast neutron vacuum window fluence over 4 years of ITER operation must be limited to 10^{20} n cm^{-2} to avoid embrittlement [92]. The VW is composed of two conical annuli which must support the weight of the VTLs during operation. The four year fast neutron fluence was calculated and was determined to be $1.00\times10^{18} \pm 10$ % n cm^{-2}. Cadmium production in the silver brazes of the vacuum window (VW) was estimated. Cd is produced from neutron absorption in Ag. Cd is also a plasma and cyropump poison and hence its quantity must be limited in regions such as the VW, which has a plasma side vacuum. The total number of Cd atoms produced, calculated using FISPACT, were determined to be 6.73×10^{17} atoms per VW after a 1 years irradiation and 2.70×10^{18} atoms per VW after 4 years irradiation. The number of cadmium atoms produced were deemed acceptable by the design team.

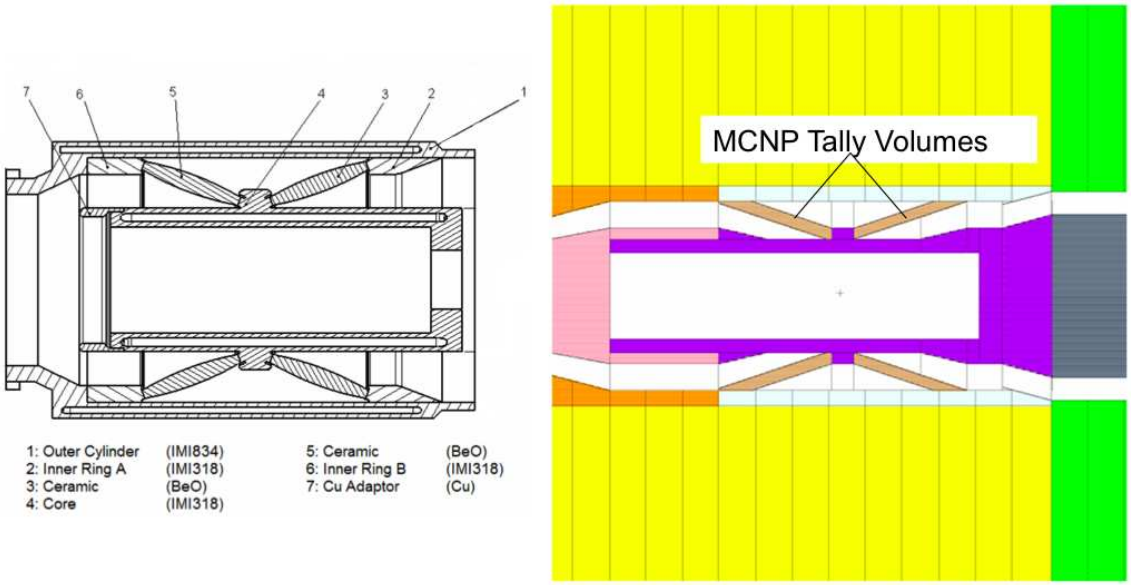

Figure 6.18: Schematic of the ICRH v3 vacuum window [91] (left) and MCNP equivalent (right)

Finally, estimation of the shutdown gamma ray dose for the ICRH v3 model was also made. In addition to FISPACT's contact dose, MCR2S was used. Using MCR2S, the shutdown gamma ray dose rate at the rear of the ICRH v3 was determined to be 52 ± 4 μSv hr^{-1} after 14 days cooling time. The 14 day shut down gamma ray dose rate as a function of the thickness is shown in Figure 6.19. It shows the contribution to the gamma ray dose from each 1 cm thick volume at the rear of the system. The purple curve is the integral of the incremental dose to that thickness. It can be seen that the dose as a function of position decreases exponentially with thickness. The integral of the incremental dose, "Sum < distance" trace asymptotically approaches a constant value of $\sim$ 52 μSv hr^{-1}. However, $\sim$ 90% of the dose eminates from the rear 26 cm of the ICRH system. The value calculated by FISPACT using the contact dose approximation, which assumes the same activation level throughout, was 30 μSv hr^{-1}. This underestimation was expected, as explained in Section 4.1.1.

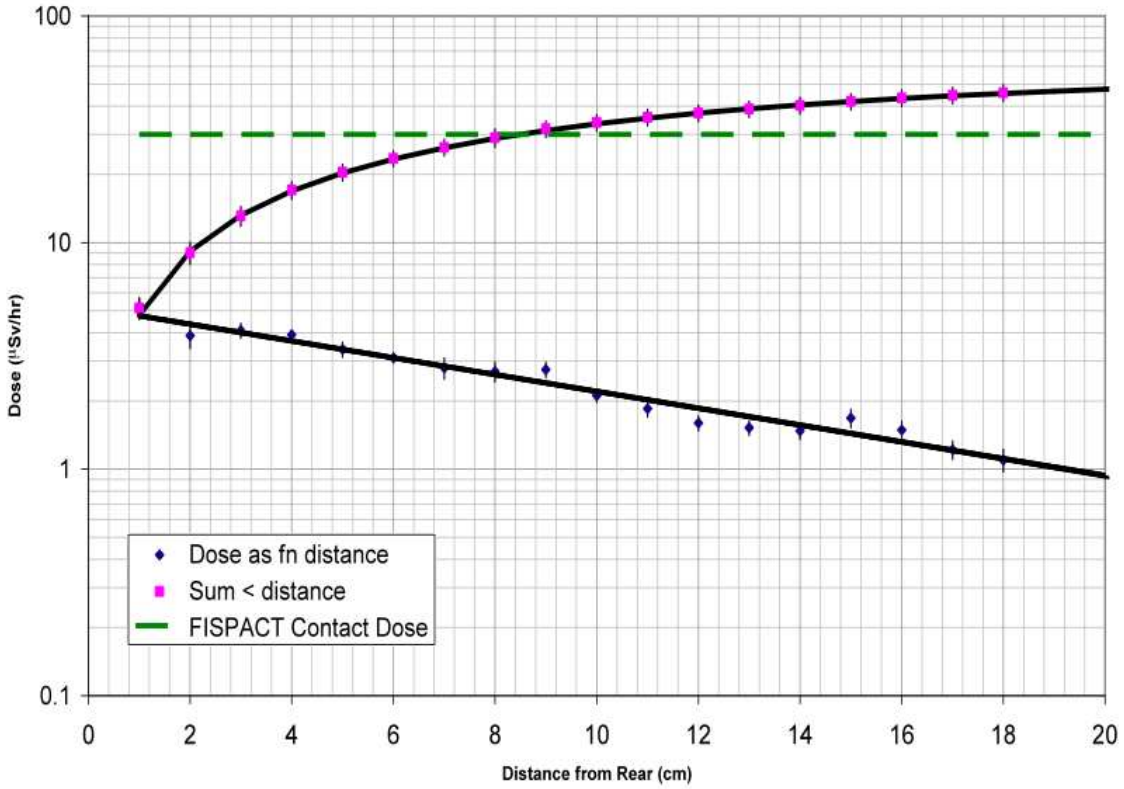

Figure 6.19: Doserate results for the ICRH V3 after 14 days decay time

Thus in a well behaved radiation shield, the dose leaving the rear of the shield is in the major part dominated by gamma ray emission from the last 4 or 5 gamma ray mean free path (mfp). This is because the gamma ray mfp is smaller than the neutron mean free path, and thus the transport of photons are the rear of the system becomes the dominating factor. However, in the case where there are a large number of penetrations, or a large area through which photons can exit, the exponential decrease shown in Figure 6.19, will be much flatter.

6.3 The ITER LIDAR Diagnostic

The Light Imaging Detection and Ranging (LIDAR) diagnostic system is located within one of the ITER equatorial ports. The ITER LIDAR system, a CAD drawing of which is shown in Figure 6.20, is composed of a large "Z" shaped penetration down which laser light is shone. The system works by producing laser light external to the cryostat, which is then shone down beampipes via a series mirrors to the back plate of the LIDAR system. The light then passes through the mirror holder and into the plasma. Laser light is then Thompson scattered by the plasma and then re-enters the LIDAR plug and bounces off the two mirrors in the apex of the "Z" shaped penetration. The layout of the ITER LIDAR system is shown in Figure

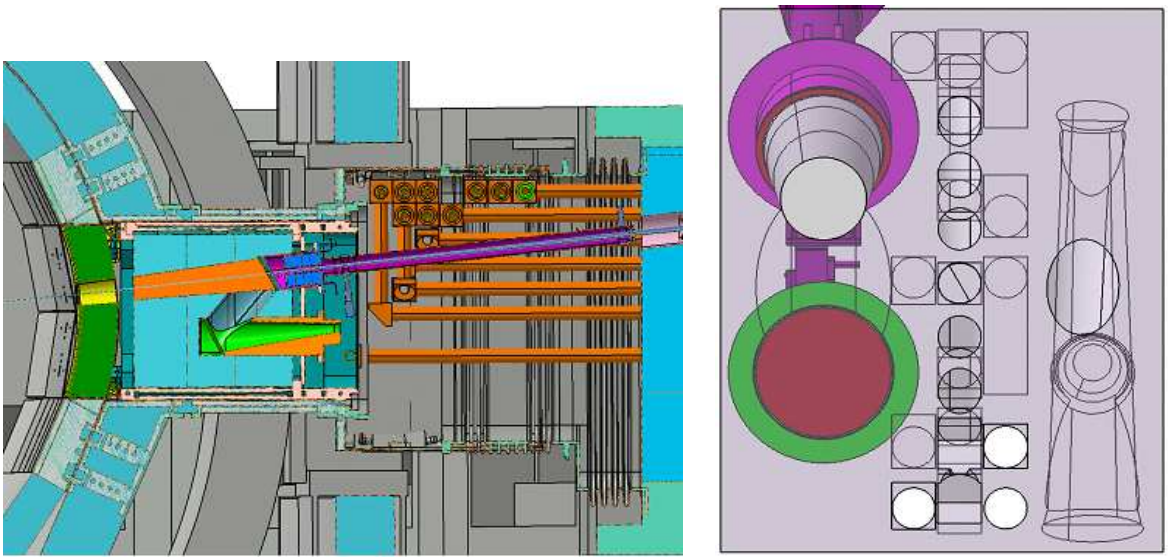

Figure 6.20: CAD Rendering of the ITER LIDAR System, cross section (left), port interspace flange (right)

6.20. It is composed of a "Z" shaped channel with highly polished stainless steel mirrors lying in the apex of the corners. The mirror holder lies at the first apex and this is where the laser beam is channeled into the plasma. The construction of the plug and internal material is the standard ITER grade 316 L(N) stainless steel. There will have to be some provision of water cooling to the plug, which must be introduced in a neutronically acceptable way.

The LIDAR shares similar computational issues as other diagnostic and heating systems in that neutron deep penetration and streaming occur simultaneously. The ITER LIDAR has gone through a number of design changes from its original inception. The original system called for a fan like arrangement of penetrations down which laser light was shone. The original calculations performed on this system used MCFISP for the estimation of the shutdown dose [51].

6.3.1 Shutdown Dose Calculations

Person access is required to the rear of the plug on the same timescales to that of the ICRH system, i.e. 14 days after machine shutdown, the dose at the rear of the plug must be less than 100 μSv hr^{-1}. During initial scoping studies the length and angle of the "Z" shape was optimised by [93]. The material definitions and standard ITER Alite model were used [94]. Alite is the official ITER supplied 3D neutronics model so that every ITER party has this model in which to perform analysis. The official ITER neutron source [95] was used in place of the typical plasma neutron source described in Chapter 2 Section 2.5, Equations 2.17, 2.18 and 2.19.

An MCNP model of the LIDAR system was inserted into the official ITER MCNP model. The simulation then determined the neutron flux and spectrum across the important part of the model; the port plug and around the equatorial port.

LIDAR was initially investigated for an ITER pulsing schedule corresponding to the full projected ITER lifetime (20 years). If the shutdown effective dose is less than the limit after 20 years irradiation, then should maintainence be required at any irradiation time less than 20 years, then the dose is limited to be less than the 20 year value.

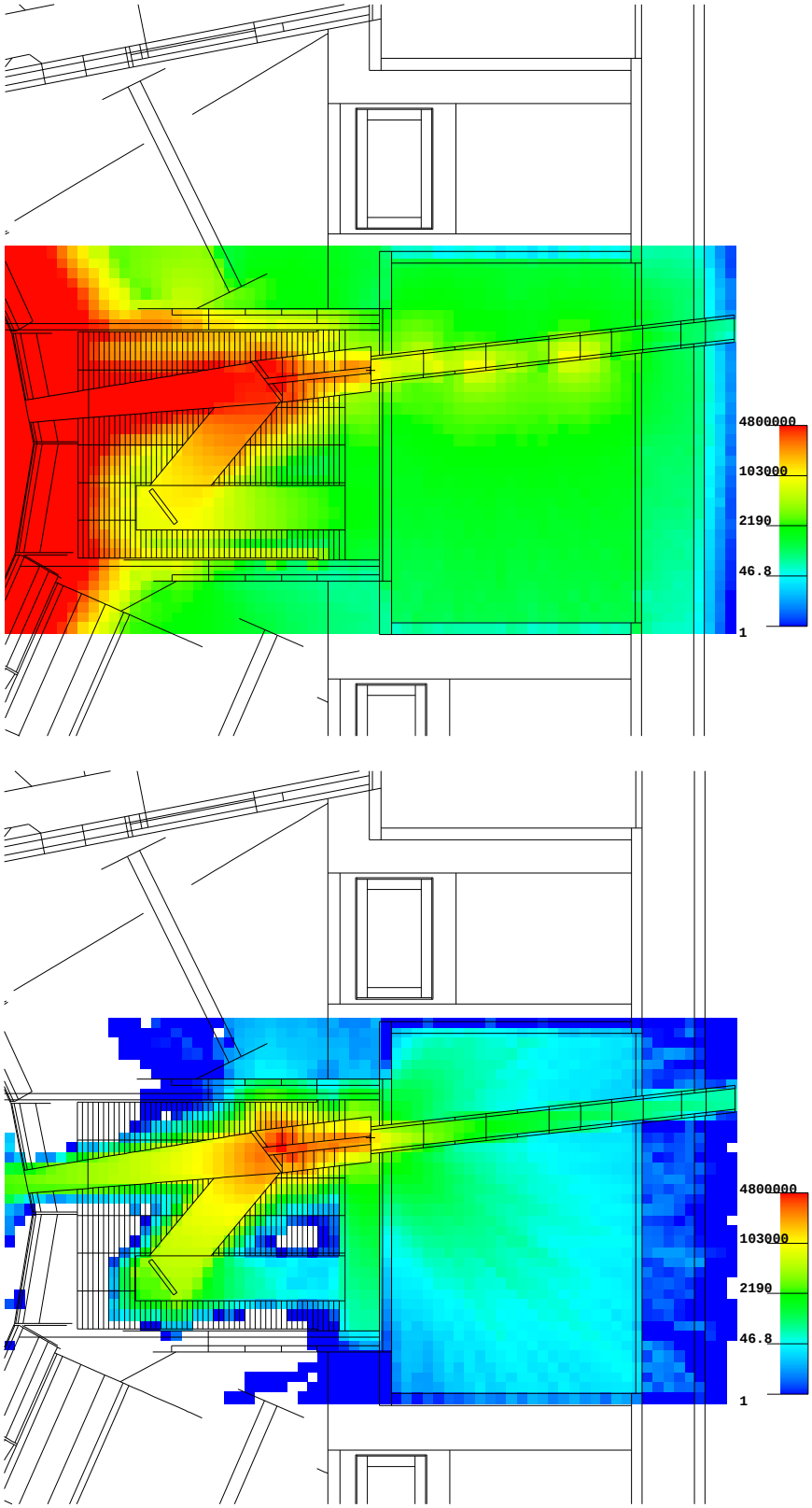

Figure 6.21: The shutdown dose rate in the ITER LIDAR system 14 days after shutdown (μSv hr^{-1}) - lower subfigure shows source contained in mirror only

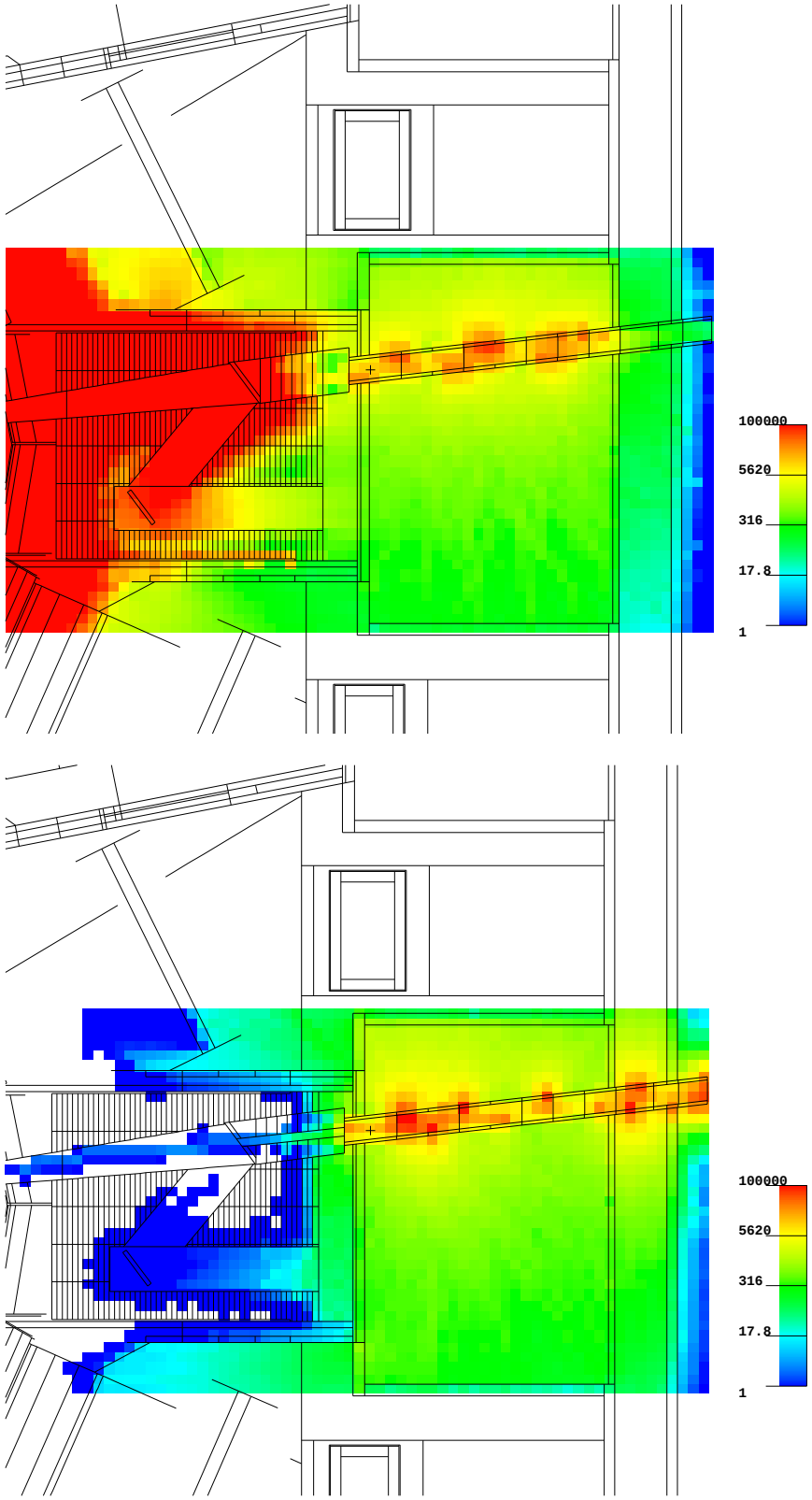

Figure 6.22: The shutdown dose rate in the ITER LIDAR system 14 days after shutdown (μSv hr^{-1}) - lower subfigure shows source contained in beam pipe only

One of the main advantages of MCR2S over preceeding software is the ability to compute shutdown dose analysis for specific components with ease. This is demonstrated in Figures 6.21 and 6.22. The source plotting function of MCR2S allows viewing of the activation photon source. In plots like that shown in Figure 6.23, hotspots like those seen along the beam pipe can be viewed. It can be seen in Figure 6.21 that the mirror holder is excessively activated, and indeed dominates dose at the port interspace flange. The amount of dose is caused by the activation of everything except the mirror holder shown in the upper part of Figure 6.22. The next highest contribution is from the beam pipe, which is 2.5 cm thick stainless steel piping which serves as a vacuum boundary. Considering Figure 6.22 it would seem unlikely that such a thin pipe could be such a strong source of potential dose. There are a number of possible solutions to the high dose rate from the beam pipe.

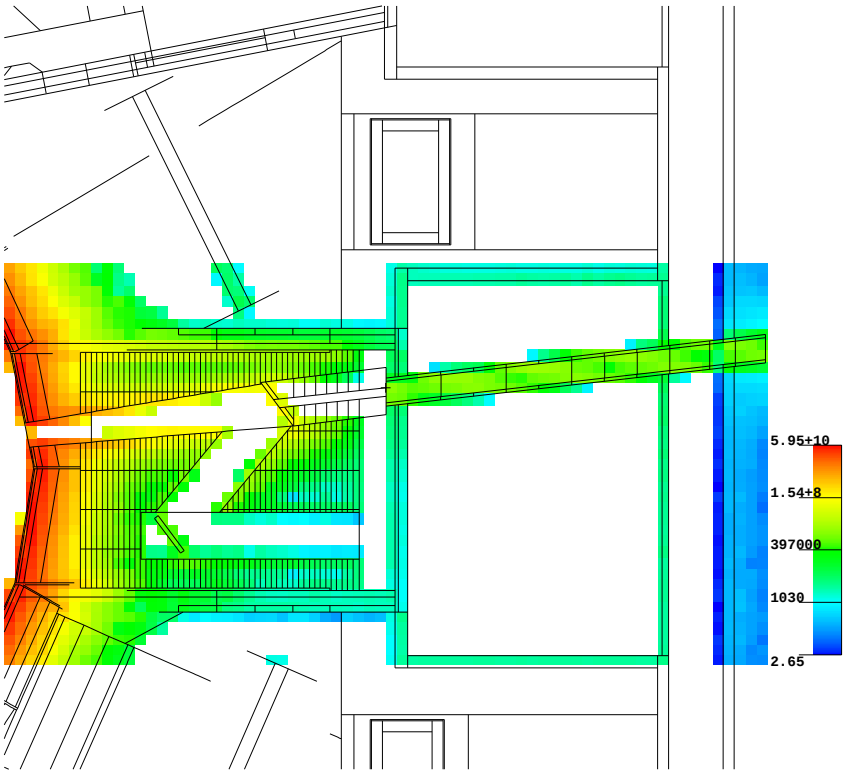

Figure 6.23: The shutdown photon source in the ITER LIDAR 14 days after machine shutdown (p s^{-1})

Either it can be shielded or the material altered. By changing the material from the current 316 L(N) stainless steel to some material with a lower activation cross section such as Aluminium or Vanadium, the dose rate could drop by a factor of 100. The other alternative is to shield the steel pipe with concrete, which should prove quite attenuating. However, there are a number of engineering challenges to overcome, for example will the steel pipe be able to withstand the weight of the concrete without failing.

Chapter 7

CONCLUSIONS AND FURTHER WORK

7.1 The MCR2S System

The MCR2S system is a tool for the analysis of activation dose in ITER and fusion devices based on the rigorous-2-step formalism, MCNP5 mesh tallies and the FISPACT nuclear inventory code. It couples transport and activation calculations in an integrated manner, allowing for the necessarily fine energy and spatial resolutions required for these kind of analyses and overcoming limitations of previous similar tools. In particular, it allows for very high spatial resolution independent from the transport geometry, and much faster analysis response owing to the parallelisation of the activation module. Due to the portable nature of the photon source definition, MCR2S is suitable to perform post-dismantling activation dose analysis (e.g. during transport or hot cell operations).

The results from the ATTILA-ASG system were compared against MCR2S. MCNP5 v1.4 was used with the mesh tallying feature to determine the neutron flux in 60

spatial and 175 energy bins. The equivalent was generated using ATTILA in 29 neutron groups. The agreement between the MCNP and ATTILA generated neutron flux map was within 3% at all locations. This finding agreed with other neutron transport benchmarks between MCNP and ATTILA. Neutron spectra were calculated for the front and rear slabs and were found to have a high degree of correlation. MCR2S used the MCNP generated mesh tally data to produce a spatially dependent shutdown gamma ray source for 4 decay times, namely 1 hour, 1 day, 10 days and 1 year. The ATTILA-ASG was used to perform the equivalent calculation and performed a shutdown gamma ray transport calculation. Shutdown photon flux profiles through the assembly were compared and were found to match well. In the worst case MCR2S predicted photon fluxes 25% higher than the ATTILA-ASG. Shutdown contact doses were calculated for the front and rearmost stainless steel block and the doses compared for all four decay times. It was found that MCR2S results are typically higher than those of the ATTILA-ASG, however this difference is no larger than 20%.

It was decided the MCR2S system should undergo an experimental benchmark excercise, and the most fusion relevant benchmark with the most complete data was found to be in the T-426 ITER benchmark shutdown gamma ray doserate experiment conducted at the Frascati Neutron Generator. The benefit of using this benchmark was the inclusion of calculations performed using the MCFISP ASG as well as experimentally determined doserate and other activation data. The neutron transport calculations were performed using MCNP5 with FENDL-2.1 transport cross sections. The initial irradiation campaign found that MCR2S data when folded with ANS-1977 data initially match the experimental data very well but over longer decay times over-estimate the dose. Conversely the MCR2S data when folded with ANS-1991 data initially underestimate the dose, but over longer decay times

match the experimental data well. It was determined that the data found in the benchmark report for the first irradiation campaign was not complete, there was a conversion factor missing from the MCNP dose calculation methodology. The second irradiation campaign allowed proper comparison of MCFISP, MCR2S and experimentally determined neutron spectra, gamma ray spectra and doserates. It was found the MCR2S, MCFISP and experimentally determined gamma ray spectra agree very well over all the decay times investigated. The agreement between MCR2S and MCFISP data when folded with the ANS/1977 data agree within 15% at early decay times and the agreement increases towards longer decay times where the dose data are within 5%. In the temporal region of interest the MCR2S system predicts doserates within 3% of experimental data.

The system has been used at CCFE to assist the design of several ITER components such as the ICRH heating system and LIDAR diagnostic.

7.2 Further Work

The MCR2S system developed over the course of this thesis has been benchmarked and shown to provide reliable shutdown gamma ray dose rates over a large range of decay times. However, there is much development still to be done on the system.

1. Benchmarks
2. Multi-platform support
3. Graphical User Interface
4. Parallelisation
5. Individual Material Activation

6. Coupled Uncertainties

7. FISPACT Modifications

8. Future Extensions

Benchmarking

As with any new computational method or code, the greater the number of comparisons and bencharks the more certain we can be of the answer and the uncertainty in the answer. Thus far MCR2S has compared well against the ATTILA-ASG and MCFISP. However, there are only a limited number of codes available for fusion relevant calculations. There are two remaining fusion relevant experimental benchmarks, that of the Fusion Neutron Source (FNS) in Japan (which provides both foil activations and shutdown gamma ray doserates), and the JET shutdown doserate benchmark (which provides TLD and GM tube dose measurements). However FISPACT, which is an integral part of the MCR2S system, is capable of performing calculations with fission products and many other actinide problems. There are many fission or accelerator relevant benchmarks which could be performed with MCR2S.

A complex geometry benchmark is also required by ITER. The JET benchmark has a number of issues which affect the uncertainty in the answer. The MCNP model was created more than 10 years ago. In this time there have been substantial changes to the JET device. A further limitation is the definition of the impurities in the materials that JET is composed of. These were defined by [96], and do not have accurate enough impurity definition. There has been critisism from some corners regarding the lack of a complex geometry benchmark. ITER will be constructed from well defined materials with known impurity levels, hence this is not an issue for the ITER device, whereas the complex geometry critisism is well placed. It is

time for a new FNG benchmark with a complex geometry, like that shown below in Figure 7.1. This will allow a number of transport phenomena to be investigated

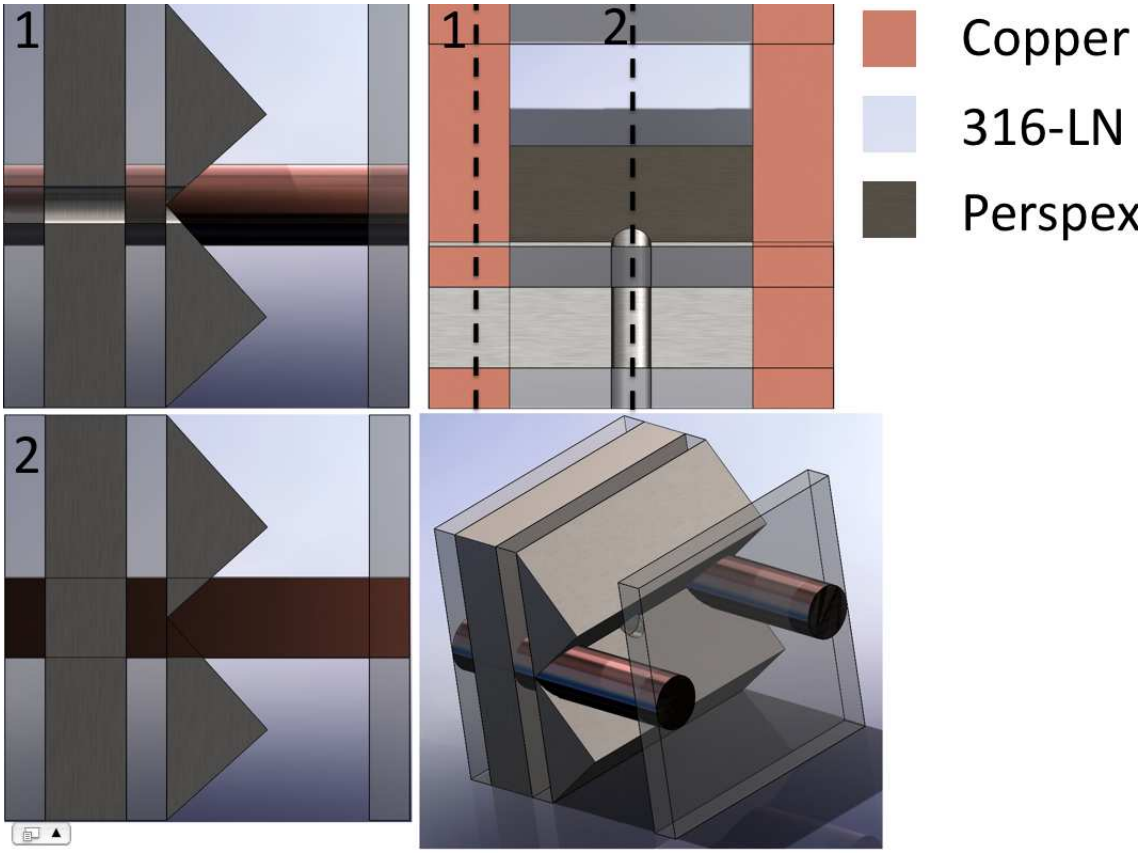

Figure 7.1: Suggested new FNG Dose rate benchmark

such as photon and neutron streaming, photon leakage from surfaces, and a large number of dose measurement locations.

Multiplatform Support

Currently the MCR2S system will only work with Linux/Unix type systems and on Windows via the Cygwin compatibility layer. The code should be re-written fully in C++ or Fortran so that any system with the correct compiler will be able to run the code.

Graphical User Interface

A Graphical User Interface (GUI) should be created to make the code easier to use. Currently MCR2S is terminal driven with a user defined input file, which can be quite labour intensive. The GUI should make use of the most modern programming techniques and make the creation of input files and the execution of the code trivial from the users point of view.

Parallelisation

The code is currently psuedo-parallelised in that each node of UKAEA's in house cluster is individually assigned a certain number of tasks. This solution only works when every node has a scratch drive that can be accesed. Most parallel computers have a queue submission system such as qsub or torque. The current methodology is not compatable with such queue submission systems. Therefore it is thought that rewriting the code in C++/FORTRAN, other than it being an added benefit to increase portability, parallelisation across many different system is then possible using either the Message Passing Interface (MPI) or Open Message Passing (OMP) parallelisation languages.

Individual Material Activation

One of the issues related to the accuracy of an MCR2S calculations is the voxel averaging technique. Firstly the the material composition is determined stochastically and secondly when input into MCNP the photon source is sampled across that entire voxel. The accuracy associated with the stochastically determined material fraction is a function of the number of particles sampled in the ptrac run. The more particles that are sampled, the lower the uncertainty in material fraction. This dominates the uncertainty in the material composition and hence photon spectra and strength.

A potential fix to this problem is to perform a calculation for every material that lies within that voxel, so rather than create an average material for that voxel, a FISPACT calculation is performed for every material in that voxel. Using the information already available from the ptrac/posmat file, the cells, material and volume fraction of materials that exist in that voxel are already known. Hence a calculation could be performed for material 1, if the irradiation of a single kilogram of material is considered, then the volume fraction of material 1 and the density of material 1 can be used to determine the strength of the source due to material 1. This process can then be performed for every material that lies under the voxel. The sum of the product of photon density, the volume fraction of the material and the voxel volume, gives the source normalisation. This method should be investigated and possibly introduced into the next version of MCR2S.

Coupled Uncertainties

The uncertainty in neutron spectrum and cross section from activation should be propagated through the calculation to the individual voxel gamma ray spectra and hence through to the shutdown gamma ray dose rate at the end of the calculation. There are a number of challenges associated with this. Firstly, the uncertainty in the material compositions of the voxel needs to be determined, this is generated from the ptrac file and is determined by Poisson statistics. The next step is the uncertainty in the cross section, taken from the EAF libraries. The two error sources combine to form the uncertainty in the source due to the specific voxel. The uncertainty in dose, therefore, is due to a combination of all voxels that contribute to the dose. This means that three calculations must be performed, these being the standard calculation, and two where the uncertainties are taken to their $\pm$ 1σ upper and lower bounds.

FISPACT Modifications

The current method essentially creates multiple FISPACT input files which are then processed one by one. FISPACT also processes calculations in three stages;

1. A "collapse" run where the neutron spectrum being analysed is folded with all neutron cross sections in the database.

2. An array run, where all cross sections are stored in an array.

3. The actual inventory calculation.

Each one of these steps is costly with regards to the length of the calculation, as every step requires numerous and large files to be read and written from hard drive. FISPACT should be modified such that this can all be done in a single step thus removing costly disk access time. This should be done by mimicing the steps the FISPACT goes through with actual code, and ensure that all reading of data is done at the start of program executing, even before FISPACT "knows" what step it should be performing. This method will allow the speed enhancements of the modifications to be asessed and the rigorous FISPACT testing procedure to be completed. These speed enhancements will not be noticed when performing individual FISPACT runs. This modified version of FISPACT, with the working title FISPACTION, should be developed and purposefully integrated into MCR2S. This will allow vast time savings along with the parallelised calculation. The time savings are the result of a single read of data, rather than a reading of data for every single calculation.

Future extensions

There are also a number of possibilites that may or may not be useful to the MCR2S code, and these include; the use of gamma ray line data, removal of un-required calculated parameters, and not collapsing cross section data for every voxel.

The use of gamma ray line data is of dubious use. Currently MCR2S operates with the FISPACT 24 photon energy groups, the uncertainty that this method introduces is simple to calculate by taking the increase or decrease in dose by considering the extreme boundaries of the energy groups and the effect this has on the dose response function shown in Equation 2.13. The main issue with moving MCR2S to use line data is that a typical activated 316LN stainless steel has around 1000 different gamma ray lines present at decay times of 14 days. If photons can be sampled uniformly by energy then in order to have a 10% accuracy from a single voxel we need to sample 100 photons. However, this will not give uniform sampling across all possible gamma ray lines. Hence 10^5 samplings are required from an individual voxel in order to guarentee 10% accuracy from every gamma ray line. Typically in situations where MCR2S has been used, there were around 40,000 voxels, which implies if line data were used, then 10^9 samplings would have been required, which is at the upper limit of 32 bit MCNP. An efficient compromise may be to increase the number of gamma groups covering isotopes important to dose.

7.3 ICRH and LIDAR

7.3.1 The ITER ICRH System

A number of different designs of the ITER ICRH system were analysed, namely the Externally Matched and Internally Matched options. Each system was analysed from early design stages through to concept designs. The different designs were analysed by creating an MCNP model from CAD drawings, then performing a neutron transport calculation. Dose is then determined by passing the neutron spectrum to FISPACT or to MCR2S. All dose calculations were performed for a single year of ITER operation and 14 days decay time. All calculations were normalised to a front neutron wall loading of 0.78 MW m^{-2}.

	v1 PAR	v2 PAR	v2 TOR	v3 TOR
Ave. Rear Neutron Flux ($cm^{-2}s^{-1}$)	1.98×10^{7}	9.2×10^{7}	0.49×10^{6}	12.6×10^{6}
Integral Nuclear Heating (MW)	N/R	2.9	3.19	3.46
Shutdown Gamma Contact Dose Rate (μSv hr^{-1})	54	N/R	0.5±0.3	30±4
Shutdown Gamma Dose rate (MCR2S) (μSv hr^{-1})	N/R	171±3	N/R	52±4

Table 7.1: Summary of results from the neutronics calculations of the ITER ICRH EMO Systems

A summary table of all results for the Externally Matched Option can be found in Table 7.1.

The first design of the Externally Matched Option (EMO) was analysed and it was found that the shutdown gamma ray contact dose rate was less than the 100 μSv hr^{-1} limit.

The ICRH IMO was also analysed and it was determined that under the same irradiation conditions as the v1 EMO design, the IMO design did not meet the required dose rate limits. The failure to meet the dose limits was due to a large direct line of sight streaming path from the front of the system to the rear. The average neutron flux at the rear of the IMO v1 was ~ 50 times higher than that of EMO v1. The contact dose rate at the rear of the IMO v1 was found to be 5.64±0.86 mSv hr^{-1} 14 days post shutdown.

The EMO v2 design was investigated and it was found that the shutdown gamma ray dose rate was greater than that of the EMO v1 design. This was attributed to the greater detail in the model including things like cooling water baffles and

additional shielding plates. The nuclear heating was also calculated in order to determine if sufficient provision of cooling was supplied to the plug. The shutdown gamma ray dose rate was determined to be 171±3 mSv hr^{-1} 14 days post shutdown.

Following a design meeting the IMO branch of ICRH was cancelled due to a number of engineering concerns and development work focussed on the EMO. The dose rate was determined by MCR2S and was found to be 54±3 μSv hr^{-1} after 14 days decay time. A number of other parameters were determined, neutron and photon heating, and the neutron and photon flux distributions within the ICRH system. Total neutron heating was determined to be 3.46 MW.

7.3.2 Further Work

There is also some further work to be performed on the ITER ICRH system. With regards to geometric design this is a work in progress. As more work is performed by design, RF, and structural engineers the overall layout and geometry will change and hence the neutron transport properties of the design will change.

The system design should be optimised to further reduce the dose according to ALARA principles, however there are some features of the ICRH system that cannot be changed such as the geometry of the VTL, the length of which is determined by the RF engineering of the system. The material properties of the system could be changed to further reduce the shutdown gamma ray dose rate, possibly with the use of advanced shielding materials such at the metal hydride shields. However, any new shielding material must be acceptable to ITER.

In addition to any changes in future designs, the current design should be incorporated into the so called reference ITER 3D MCNP model. This will allow a full

description of the radiation fields at the rear of the ICRH to be determined.

7.3.3 The ITER LIDAR System

The ITER LIDAR system was investigated to determine the system's response to neutron irradiation. The LIDAR system is incorporated into an ITER equatorial port plug, the bulk of which consists of a 316 LN-IG2 stainless steel. There is, however, a "Z" shaped penetration running from the front of the system to the rear. The LIDAR system was incorporated into the reference ITER 3D MCNP model and used the official ITER plasma neutron source. The LIDAR system is considered to be an ITER "lifetime" system and as such is expected to last the full duration of ITER without being changed, hence the irradiation was considered over 20 years. Following machine shutdown the dose rate was determined after 14 days decay time and was not found to be below 100 μSv hr^{-1}. In some places the doserate was 10s of mSv hr^{-1} an hour. The new source plotting feauture of MCR2S allowed the strongest soruces of gamma emission to be determined and were found to be the mirror holder and the laser beam pipe.

7.3.4 Further Work

As the LIDAR design progresses further, all new features should be incorporated into the modelling process. The main outstanding issues with regards to LIDAR modelling are to add the remaining diagnostics such as the polarimeter and the bolometer. This will give a more accurate answer for the shutdown gamma ray dose rate.

The amount of material in the laser beam pipe should be reduced to a minimum in order to reduce the amount of activated material that can contribute to the gamma ray source. There is little optimisation that can be performed on the mirror holder

except reduce the diameter of the laser penetration that runs through the middle of the system and make the shield behind the mirror holder slightly thicker.

Appendix A

ITER OPERATIONAL PARAMETERS

The parameters that define an ITER plasma are shown below in Table A.1.

Total Fusion Power	500 MW
Q fusion power/additional heating power	> 10
Average 14 MeV neutron wall loading	0.57 MW/m^2
Plasma inductive burn time	> 400 s
Plasma major radius (R)	6.2 m
Plasma minor radius (a)	2.0 m
Plasma current (I_p)	15 MA
Vertical elongation @ 95% flux surface/separatrix (κ_{95})	1.70/1.85
Triangularity @ 95% flux surface/separatrix (δ_{95})	0.33/0.49
Safety factor @ 95% flux surface (q_{95})	3.0
Toroidal field @ 6.2 m radius (B_T)	5.3 T
Plasma volume	837 m^3
Plasma surface	678 m^2
Installed auxiliary heating/current drive power	73 MW

Table A.1: ITER parameters [1]

Appendix B

ANSI/ANS-6.1.1-1991 DOSE CONVERSION FACTORS

The ANSI/ANS-6.1.1-1991 C coefficients used in this thesis, are shown below in Table B.1.

Photon Energy	C_0	C_1	C_2	C_3	C_4
E≤0.15 MeV	2.30402	0.75167	-1.04725	-0.50091	-0.06302
E>0.15 MeV	1.52070	0.79329	-0.07261	0.01228	0.00347
Neutron Energy	C_0	C_1	C_2	C_3	C_4
E≤0.01 MeV	3.43089	0.7725710	0.09834081	4.903466×10^{-3}	8.149667×10^{-5}
E>0.01 MeV	4.952167	0.6644235	-0.1017445	-1.496004×10^{-3}	3.636748×10^{-3}

Table B.1: ANSI/ANS-6.1.1-1991 Dose C Coeffients for photons and neutrons

Appendix C

ATILLA ASG - MCR2S BENCHMARK

C.1 Steel composition

Element	wt%
C	0.8
Co	0.1
Si	1.0
Ni	12.0
Cr	17.0
Cu	0.2
Mn	2.0
Mo	2.5
Fe	balance

Table C.1: Stainless steel composition used in the ATILLA-MCR2S benchmark

C.2 ATTILA-MCR2S Dose per unit lethargy graph

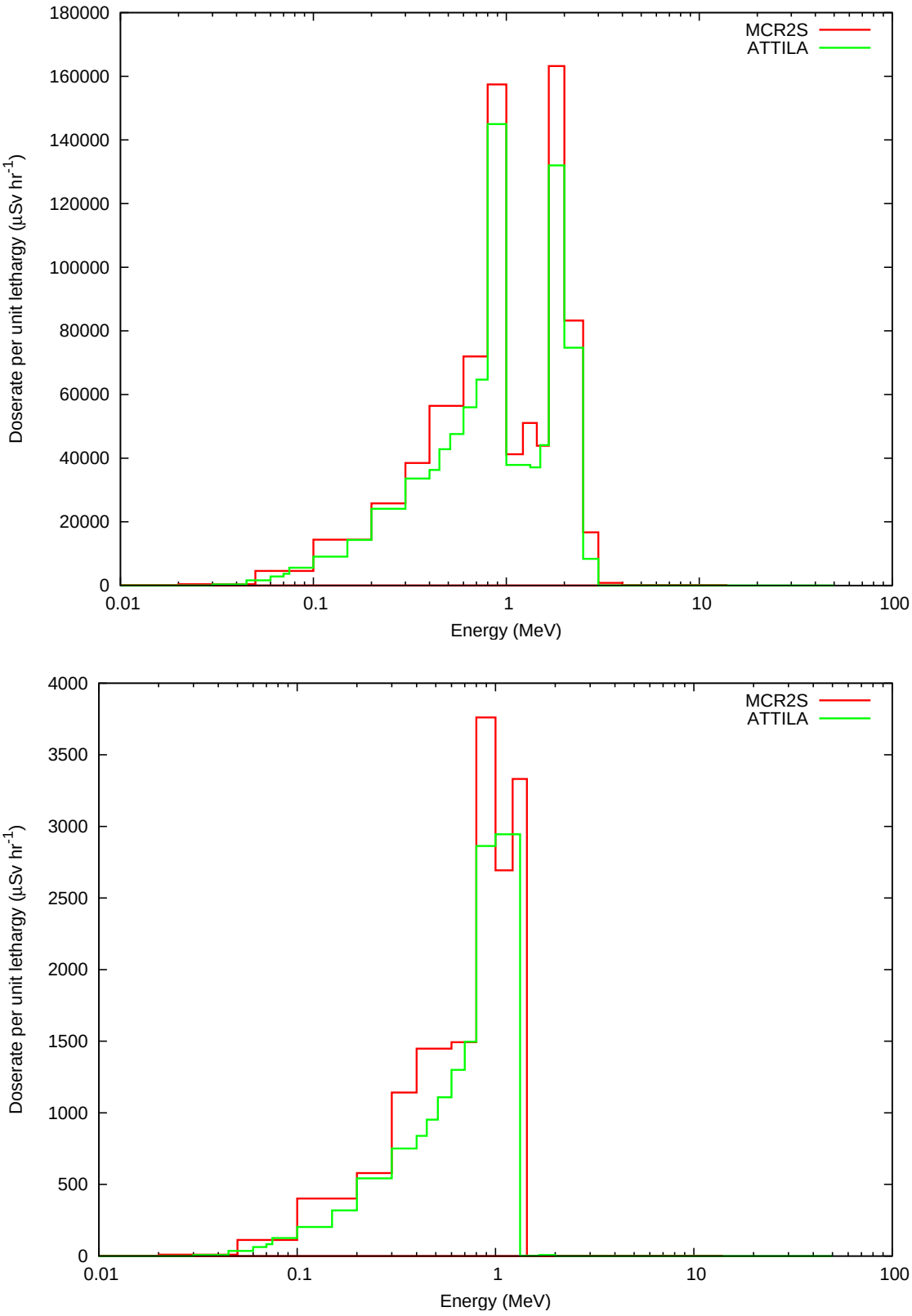

Figure C.1: Photon dose per unit lethary calculated by ATTILA and MCR2S for 1 hour decay time (upper) and 1 year decay time (lower)

Appendix D

THE MAGIC METHOD

Modern computing and computers mean that larger models can be created than in the past. Larger models inherently result in more complex models, which are very difficult to modify by hand. Previously it was left to the end user to define a so called "Importance Map". The concept of importance was introduced in Chapter 3. There are a number of different approaches being taken by researchers worldwide. The most popular of which uses a discrete ordinates code such as Attila to create a weight window mesh.

One of the most popular (by number) solutions is to use a deterministic code such as Attila or ANSYSN to determine the neutron flux distribution prior to running the main transport problem with MCNP. Knowing the neutron flux a priori allows a weight window mesh (WWM) to be produced. There are a number of limitations associated with the use of WWM, the main one being the size of message required when communicating with Message Passing Interface (MPI). The so called MCNP Automatic Generation of Importances in Cells (MAGIC) method is an innovative solution to the variance reduction problem in complex models. As mentioned previously there is a limit when using the parallel version of MCNP compiled with MPI which is determined by the maximum message size that MPI can handle, which is

Range of R	Quality of the Tally
0.5 to 1.0	Not meaningful
0.2 to 0.5	Factor of a few
0.1 to 0.2	Questionable
< 0.10	Generally reliable
< 0.05	Generally reliable for point detectors

Table D.1: MCNP tally uncertainty bounds

typically half of the available system memory. It was determined that when using the Alite model with a moderate resolution WWM (27 cm^3) this message limit was reached meaning the problem could not be run.

However if we consider that a flux tally in MCNP is given by

$$\phi = \frac{1}{NA} \sum_i w_i \tag{D.1}$$

Where

ϕ is the flux of particles per unit source particle

N is the number of particles simulated

A is the area of the surface across which the flux was calculated

w_i is the weight of particles crossing area A

The uncertainty of the tally, which is not to be understood as an uncertainty in the measurement, it is more correctly understood to be an equivalent of a convergence critereon, below in Table D.1 are the MCNP rules on tally uncertainties. In the trivial case to reduce the tally uncertainty it is simply a matter of running more particles in the transport problem, which is absolutely correct when dealing with small models (of less than 100 cells). To reduce the tally error by a factor of n one must run n^2 more particles. However, when running large models $\sim$ 3000 cells, this is no longer a viable solution due to the increase in runtime. Techniques known as

Variance Reduction (VR) must be employed. As the title suggests, these techniques reduce the variance and hence uncertainty in results.

A new method developed during the course of this thesis is known as the MAGIC method. This method involves peforming a long analog run, i.e. with no variance reduction. The average particle weight is then determined in every cell. Some cells may not have any particle enter them. This is not a particularly bothersome issue and is addressed in the next run. It is known that the average particle weight in a cell, w, is inversely related to the cell importance;

$$w = \frac{1}{I} \tag{D.2}$$

Hence taking the inverse of the particle weight in every cell in the problem gives the importance map for the entire problem. It is critical to note that, in order to use this method, the analog run must be performed with the MCNP keyword `print`, which makes MCNP print additional output information. From `print table 110`, which contains information regarding the weights entering, exiting and destruction in every cell in the problem. From this list the weight exiting the cell is the important part of information. However, MCNP outputs this as a negative amount, thus multiplying the amount by -1 and taking the reciprocal of this value results in the importance of the cell. This method was used in the analysis of the MCR2S FNG benchmark, the ITER LIDAR system and determining the ALITE neutron importance map. Comparisons between various VR methods were performed by R Pampin et al [97], and found that the MAGIC method generates a better importance map and hence results with a lower uncertainty quicker than other methods.

Appendix E

VITAMIN-J NEUTRON BIN STRUCTURE

The Vitamin-J neutron energy binning structure used in this thesis is shown below in Table E.1.

1.0000E-07	4.1399E-07	5.3158E-07	6.8256E-07	8.7643E-07
1.1254E-06	1.4450E-06	1.8554E-06	2.3824E-06	3.0590E-06
3.9279E-06	5.0435E-06	6.4760E-06	8.3153E-06	1.0677E-05
1.3710E-05	1.7604E-05	2.2603E-05	2.9023E-05	3.7267E-05
4.7851E-05	6.1442E-05	7.8893E-05	1.0130E-04	1.3007E-04
1.6702E-04	2.1445E-04	2.7536E-04	3.5358E-04	4.5400E-04
5.8295E-04	7.4852E-04	9.6112E-04	1.2341E-03	1.5846E-03
2.0347E-03	2.2487E-03	2.4852E-03	2.6126E-03	2.7465E-03
3.0354E-03	3.3546E-03	3.7074E-03	4.3074E-03	5.5308E-03
7.1017E-03	9.1188E-03	1.0595E-02	1.1709E-02	1.5034E-02
1.9305E-02	2.1875E-02	2.3579E-02	2.4176E-02	2.4788E-02
2.6058E-02	2.7000E-02	2.8501E-02	3.1828E-02	3.4307E-02
4.0868E-02	4.6309E-02	5.2475E-02	5.6562E-02	6.7380E-02
7.2025E-02	7.9499E-02	8.2503E-02	8.6517E-02	9.8037E-02
1.1109E-01	1.1679E-01	1.2277E-01	1.2907E-01	1.3569E-01
1.4264E-01	1.4996E-01	1.5764E-01	1.6573E-01	1.7422E-01
1.8316E-01	1.9255E-01	2.0242E-01	2.1280E-01	2.2371E-01
2.3518E-01	2.4724E-01	2.7324E-01	2.8725E-01	2.9452E-01
2.9721E-01	2.9849E-01	3.0197E-01	3.3373E-01	3.6883E-01
3.8774E-01	4.0762E-01	4.5049E-01	4.9787E-01	5.2340E-01
5.5023E-01	5.7844E-01	6.0810E-01	6.3928E-01	6.7206E-01
7.0651E-01	7.4274E-01	7.8082E-01	8.2085E-01	8.6294E-01
9.0718E-01	9.6167E-01	1.0026E+00	1.1080E+00	1.1648E+00
1.2246E+00	1.2874E+00	1.3534E+00	1.4227E+00	1.4957E+00
1.5724E+00	1.6530E+00	1.7377E+00	1.8268E+00	1.9205E+00
2.0190E+00	2.1225E+00	2.2313E+00	2.3069E+00	2.3457E+00
2.3653E+00	2.3851E+00	2.4660E+00	2.5924E+00	2.7253E+00
2.8651E+00	3.0119E+00	3.1664E+00	3.3287E+00	3.6788E+00
4.0657E+00	4.4933E+00	4.7237E+00	4.9659E+00	5.2205E+00
5.4881E+00	5.7695E+00	6.0653E+00	6.3763E+00	6.5924E+00
6.7032E+00	7.0469E+00	7.4082E+00	7.7880E+00	8.1873E+00
8.6071E+00	9.0484E+00	9.5123E+00	1.0000E+01	1.0513E+01
1.1052E+01	1.1618E+01	1.2214E+01	1.2523E+01	1.2840E+01
1.3499E+01	1.3840E+01	1.4191E+01	1.4550E+01	1.4918E+01
1.5683E+01	1.6487E+01	1.6905E+01	1.7333E+01	1.9640E+01

Table E.1: 175 Group Vitamin-J Neutron energy bin boundaries

Appendix F

FNG APPENDIX

F.1 FNG MCNP Neutron Source

The source is described using the data shown in Figure 5.13, and is used in the MCNP source definition thus

```
 SDEF POS=0.0 0.001 0.0 RAD=D22 EXT=D23 VEC=0 1 0 DIR=D1 ERG=FDIR=D2
SI1 A -1 -0.98481 -0.93969 -0.86603 -0.76604 -0.64279 -0.5 -0.34202
-0.17365 0 0.17365 0.34202 0.5 0.64279 0.76604 0.86603 0.93969 0.98481
1
SP1 0.94764 0.94842 0.95073 0.95452 0.95969 0.96609 0.97354 0.98184 0.99075
1 1.00932 1.01842 1.02701 1.03484 1.04162 1.04715 1.05124 1.05374
1.05459
DS2 S 4 5 6 7 8 9 10 11 12 13 14 15 16 17 18 19 20 21
SI4 A 13.1635 13.1719 13.1804 13.189 13.1977 13.2066 13.2156
13.2248 13.2341 13.2436 13.2532 13.263 13.273 13.2832
13.2935 13.3041 13.3149 13.3259 13.3371 13.3486 13.3603
13.3724 13.3847 13.3973 13.4103 13.4236 13.4373 13.4515
13.466 13.4811 13.4967 13.5129 13.5297 13.5472 13.5655
13.5847 13.6049 13.6263 13.649 13.6734 13.6998 13.7288
13.7611 13.7982
SP4 0.01434 0.01494 0.01554 0.01614 0.01674 0.01752 0.01831
0.019 0.0197 0.02063 0.02157 0.02274 0.02391 0.02502
0.02613 0.02759 0.02904 0.03014 0.03123 0.03265 0.03409
0.03522 0.03638 0.03724 0.0381 0.03825 0.0384 0.03757
0.03672 0.03469 0.03258 0.02982 0.02696 0.02351 0.01989
0.01651 0.01289 0.01008 0.00703 0.00509 0.00293 0.00195
0.00077 0.00045
```

The source shown above fully describes the intensity change as a function of angle, but there is only one neutron spectrum shown for the first angular bin. In the full source used there were 21 angular bins.

F.2 Frascati Neutron Generator benchmark material compositions

Element	316 SS	316 SS (15)	316 SS (Box)	Perspex
H	-	-	-	8
B	0.0035	0.005	0.002	-
C	0.04	0.03	0.023	60
O	-	-	-	32
Na	-	-	-	$<$ 1 appm
Mg	-	-	-	$<$ 1 appm
Al	-	$<$ 0.03	$<$ 0.03	$<$ 1 appm
Si	0.45	0.69	0.49	4 appm
P	0.022	0.021	0.039	-
S	$<$ 0.006	$<$0.01	$<$ 0.01	4 appm
K	-	-	-	$<$ 1 appm
Ca	-	-	-	2.6 appm
Ti	-	$<$ 0.01	$<$ .005	$<$ 1 appm
V	0.16	0.12	0.04	-
Cr	16.8	17.8	17.2	-
Mn	1.14	1.64	1.58	-
Fe	68.32	66.22	68.102	$<$ 1 appm
Co	0.14	0.07	0.011	-
Ni	10.7	11.3	9.9	
Cu	0.09	0.09	0.42	-
As	-	$<$ 0.01	$<$ 0.01	-
Zr	-	$<$ 0.03	$<$ 0.03	-
Mo	2.12	2	2.07	-
Sn	0.004	$<$ 0.01	0.016	-
Pb	0.001	$<$ 0.01	$<$ 0.01	-

Table F.1: Elemental composition of materials in the FNG

F.3 FNG Campaign 2 Decay times

Incremental Decay time	Total Elapsed Decay Time
1.216666667	1.216666667
0.5	1.716666667
0.363333333	2.08
1.136666667	3.216666667
1.583333333	4.8
2	6.8
2.666666667	9.466666667
3.25	12.71666667
3.183333333	15.9
4.252777778	20.15277778
5.047222222	25.2
11.46666667	36.66666667
22.33333333	59
37	96
37.13888889	133.1388889
63.66666667	196.8055556
94.86111111	291.6666667
172.2222222	463.8888889
11.11111111	475

Table F.2: Decay times used in the second FNG Campaign

Appendix G

MATERIAL COMPOSITIONS FOR ICRH ANALYSIS

With the exception of 316L(N)-IG2, all materials definitions were calculated via stoichiometry. The steel definition comes from ITER Material Assesment Report G 74 MA 10 W0.3.

Element					
	316L(N)-IG2	H_20	Be/Be0	Ti_6Al_4V	B_4C
H	-	11.11111	-	-	-
Be	-	-	36.000	-	-
B	0.001	-	-	-	78.262
C	0.030	-	-	-	21.737
N	0.080	-	-	-	-
O	-	88.88889	67.000	-	-
Al	-	-	-	40.000	-
Si	0.500	-	-	-	-
P	0.025	-	-	-	-
S	0.010	-	-	-	-
Ti	0.070	-	-	47.400	-
V	-	-	-	12.600	-
Cr	18.000	-	-	-	-
Mn	2.000	-	-	-	-
Fe	63.654	-	-	-	-
Co	0.050	-	-	-	-
Ni	12.500	-	-	-	-
Cu	0.300	-	-	-	-
Nb	0.010	-	-	-	-
Mo	2.700	-	-	-	-
Ta	0.070	-	-	-	-

Table G.1: Elemental Compositions of materials used in the ICRH analysis, all materials except 316L(N)-IG2 calculated via stoichiometry

References

[1] ITER Consortium, "ITER Plant Description Document", Tech. Rep. G A0 FDR 1 01-07-13 R1.0, ITER, 2001.

[2] A A Harms et al., *Principles of Fusion Energy*, 2000.

[3] Muir D W, "Sensitivity of fusion reactor average cross sections to thermal broadening of the 14 MeV neutron peak", Tech. Rep. LA-5411-MS, Los Alamos, 1973.

[4] Max-Planck Institut für Plasmaphysik, ", http://www.ipp.mpg.de/ippcms/eng/for/projekte/w7x/index.html, 2009.

[5] M. Tobin et al., "Target Area Design Basis and System Performance for the National Ignition Facility", in *11th Topical Meeting on the Technology of Fusion Energy*. American Nuclear Society, 1994.

[6] N Fleurot et al., "The laser mgajoule (lmj) project dedicated to inertial confinement fusion: Development and construction status", *Fusion Engineering and Design*, vol. 74, no. 1-4, pp. 147 – 154, 2005, Proceedings of the 23rd Symposium of Fusion Technology - SOFT 23.

[7] S. Atzeni et al., "Studies on targets for inertial fusion ignition demonstration at the HiPER facility", *Nuclear Fusion*, vol. 49, pp. 7pp, 2009.

[8] S Ishizaka, "Project Specification", Tech. Rep. ITER D 2DY7NG v1.0, ITER, 2008.

[9] J How, "Plant Description", Tech. Rep. 2X6K67, ITER, 2009.

[10] UKAEA Fusion/ERM/KMS, "Reference geometry for the ITER ICRH (External matching option", 2005.

[11] J Wesson, *Tokamaks*, Oxford University Press, 3rd edition, 2004.

[12] ITER, "ITER Technical basis", Tech. Rep. G A0 FDR 1 01-07-13 R1.0 Plant Description, ITER, 2001.

[13] D A Humphreys and A G Kellman, "Analytic modeling of axisymmetric disruption halo currents", *Physics of Plasmas*, vol. 39, pp. 2742, 1999.

[14] *Principles of Fusion Energy*, chapter 13.6, p228, World Scientific, 2000.

[15] A. Caldern et al., "Effects of the gamma-ray irradiation on the optical absorption of pure silica core single-mode fibres in the visible and NIR range", *Nuclear Instruments and Methods A*, vol. 538, no. 3, pp. 810–813, 2005.

[16] J Ferziger, *The Theory of Neutron Slowing Down in Nuclear Reactors*, Elsevier, 1966.

[17] W M Stacey, *Nuclear Reactor Physics*, Wiley, 2001.

[18] K S Krane, *Introductory Nuclear Physics*, J Wiley and Sons, 1988.

[19] G R Satchler, *Introduction to Nuclear Reactions*, 1980.

[20] G.F. Knoll, *Radiation Detection and Measurement*, 2000.

[21] T Rockwell (III), *Reactor Shielding Design Manual*, 1957.

[22] Judith F Briesmeiser, "MCNP^{TM} a General Monte Carlo N-Particle Transport Code", Tech. Rep. LA-13709-M, Los Alamos National Laboratory, March 2000, MCNP 4C3.

[23] Geant 4 Team, ", *Nuclear Instruments and Methods A*, vol. 506, pp. 250–303, 2003.

[24] F Salvat et al., "PENELOPE: A Code System for Monte Carlo Simulation of Electron and Photon Transport", in *Proceedings of a Workshop/Training Course*. OECD/NEAD, November 2001, number NEA/NSC/DOC(2001)19.

[25] D.S. Billington, *Radiation Damage in Solids*, 1961.

[26] Michael Nastasi, *Ion Implantation and Synthesis of Materials*, Springer, Berlin, 2006.

[27] T Burchell, "Neutron Irradiation Damage in Graphite and Its Effects on Properties", in *Carbon '02*. Beijing, China, September 2002.

[28] R A Forrest, *FISPACT 2007: User manual*, UKAEA Fusion, Culham Science Centre, Oxfordshire, OX14 3DB, 2007.

[29] A Holmes-Siedle and L Adams, *Handbook of Radiation Effects*, 2003.

[30] M Martone, "IFMIF Conceptual Design Activity", Tech. Rep., ENEA Frascatti, 1996.

[31] H Wilson et al., "A proposed component test facility", in *Proceedings of the 20th IAEA Fusion Energy Conference*. International Atomic Energy Agency, 2003.

[32] M.H. O'Brien, *Materials Aspects of Future Fusion Systems*, PhD thesis, The University of Birmingham, 2007.

[33] P. Jongenburger, "The Extra-Resistivity Owing to Vacancies in Copper", *Physical Review Letters*, vol. 90, no. 4, pp. 710–711, May 1953.

[34] T Nishitani et al., "Radiation-induced thermoelectric sensitivity in the mineral insulated cable of magnetic diagnostic coils for ITER", *Journal of Nuclear Materials*, 2004.

[35] International Comission on Radiation Protection, *ICRP Publication 60*, 1990.

[36] ANS-6.1.1 Working Group M E Battat (Chairman), "American National Standard Neutron and Gamma-ray Flux-to-Dose Rate Factors", Tech. Rep. ANSI/ANS-6.1.1-1977 (N666), American Nuclear Society, 1977.

[37] "Neutron and Gamma-Ray Fluence-to-Dose factors", Tech. Rep. ANSI/ANS-6.1.1-1991, American National Standard, 1996.

[38] Her Majesties Goverment, "Statutory Instrument 1999 No. 3232 -The Ionising Radiations Regulations 1999", 1999.

[39] Nuclear Energy Agency, "Nuclear Law Bulletin", Tech. Rep. Number 71, Nucear Energy Agency, 2003.

[40] B T Price, *Radiation Shielding*, Pergamon Press, 1959.

[41] Y Wu et al., "Analysis on Nuclear Heating in the Superconducting Coils of HT-7U Tokamak Fusion Device", in *Symposium on Fusion Research*, 2003, vol. 22.

[42] V. Khripunov, "The ITER first wall as a source of photo-neutrons", *Fusion Engineering and Design*, vol. 56-57, pp. 899 – 903, 2001.

[43] Los Alamos National Laboratory, "www.mcnp-green.lanl.gov/lanlreports.html".

[44] P Wilson and D Henderson, *ALARA: Analytic and Laplacian Adaptive Radioactivity Analysis - Technical Manual*, University of Wisconsin Fusion Technology Institute, volume 1 edition, January 1998.

[45] ORNL, "ORIGEN-2, Isotope Generation and Depletion Code", Tech. Rep. ORNL TM-7175, Oak Ridge National Laboratory, 1980.

[46] T R England, "CINDER - A One Point Depletion and Fission Product Program", Tech. Rep., Bettis Atomic Power Laboratory, 1962 rev 1964.

[47] J M Perlado, "ACAB Manual", Tech. Rep., Institute of Nuclear Fusion (Polytechnical University of Madrid.

[48] R F Burstall, "A Computer Code for Nuclide Inventory Calculations", Tech. Rep. ND-R-328(R), 1979.

[49] A B Pashchenko E T Cheng, R A Forrest, "Report on the second international activation calculation benchmark comparison study", Tech. Rep. INDC(NDS)-300, International Atomic Energy Agency, February 1994.

[50] J Sidell, "EXTRA - A digital computer program for the solution of stiff sets of ordinary value, first order differential equations", Tech. Rep. AEEW-R-799, AERE Harwell, 1972.

[51] ITER Consortium, "ITER Project Description Document - Nuclear Analysis Report", Tech. Rep., ITER, 2001.

[52] R Forrest, "EASY - A Tool for Activation Calculations", *Fusion Engineering and Design*, vol. 37, no. 1, pp. 167–174, 1997.

[53] Mahmoud Youssef, Anil Kumar, Mohamed Abdou, Hesham Khater, Mohamed Sawan, and Douglas Henderson, "Assessment of dose rate profiles and accessibility inside the building of the experimental fusion reactor, iter, during

operation and after shutdown", *Fusion Engineering and Design*, vol. 42, no. 1-4, pp. 155 – 172, 1998.

[54] E. Ciattaglia, L.C. Ingesson, D. Campbell, G. Saibene, C. Walker, L. Doceul, P. Dirken, L. Petrizzi, and R. Heidinger, "Iter diagnostic port plug engineering design analysis in the eu", *Fusion Engineering and Design*, vol. 82, no. 5-14, pp. 1231 – 1237, 2007, Proceedings of the 24th Symposium on Fusion Technology - SOFT-24.

[55] L. Petrizzi, L. Auditore, G. Cambi, D.G. Cepraga, and R. Villari, "Helium-cooled lithium lead: Activation analysis of the test blanket module in iter", *Fusion Engineering and Design*, vol. 83, no. 7-9, pp. 1244 – 1248, 2008, Proceedings of the Eight International Symposium of Fusion Nuclear Technology - ISFNT-8 SI.

[56] M. Angelone, L. Petrizzi, M. Pillon, S. Popovichev, and R. Villari, "A dose rate experiment at jet for benchmarking the calculation direct one step method", *Fusion Engineering and Design*, vol. 82, no. 15-24, pp. 2805 – 2811, 2007, Proceedings of the 24th Symposium on Fusion Technology - SOFT-24.

[57] L. Petrizzi, M. Angelone, P. Batistoni, U. Fischer, M. Loughlin, and R. Villari, "Benchmarking of monte carlo based shutdown dose rate calculations applied in fusion technology: From the past experience a future proposal for jet 2005 operation", *Fusion Engineering and Design*, vol. 81, no. 8-14, pp. 1417 – 1423, 2006, Proceedings of the Seventh International Symposium on Fusion Nuclear Technology - ISFNT-7 Part B.

[58] R G Jaeger (Editor), *Radiation Shielding Design Manual volume 2*, vol. Volume 1, Springer-Verlag, 1976.

[59] R Pampin and A Davis, "Novel Tools for Estimation of Activation Dose: Description, Preliminary Comparison and Nuclear Data Requirements", Tech. Rep. UKAEA FUS 549, UKAEA Fusion, 2008.

[60] D Valenza et al., "Proposal of shutdown dose estimation method by Monte Carlo code", *Fusion Engineering and Design*, , no. 55, pp. 411–418, 2001.

[61] D Valenza et al., "Proposal of shutdown dose estimation method by Monte Carlo code", *Fusion Engineering and Design*, vol. 55, no. 4, pp. 411 – 418, 2001.

[62] "Rigorous based shutdown dose rate calculations: computational scheme, verification calculations and application to ITER, journal =".

[63] A Serikov et al., "Nuclear Safety and waste managment aspects of the EP ECRH upper launcher for ITERmore", *Fusion Engineering and Design*, vol. 84, pp. 1751–1754, 2009.

[64] J M McGhee et al., "ATTILA V6.2 user manual", Tech. Rep., Transpire Inc.

[65] J C Ryman and O W Hermann, "Origen-s data libaries", Tech. Rep. Technical Report NUREG/CR-0200, Revision 6, Volume 3, Section M6, ORNL/NUREG/CDS-2/V3/R6, Oak Ridge National Laboratory, 2000.

[66] F Wasastjerna, *Using MCNP for fusion neutronics*, PhD thesis, Helsinki University of Technology, 2008.

[67] E. Sartori I. Kodeli and B. Kirk, "SINBAD Shielding Benchmark Experiments Status and Planned Activities", in *The American Nuclear Societys 14th Biennial Topical Meeting of the Radiation Protection and Shielding Division, Carlsbad New Mexico, USA.*, 2006.

[68] A Davis and R Pampin, "Benchmarking the MCR2S system for high resolution shutdown dose analysis", *Fusion Engineering and Design*, vol. 85, no. 1, pp. 87–92, 2010.

[69] M Z Youseff, "Comparing the Prediction of "Attila" Code to the Experimental Data of Fusion Integra Experiments and to the Results of MCNP code", *Fusion Science and Technology*, vol. 52, no. 4, pp. 801–806, 2007.

[70] D S Lucas et al., "Comparison Of The 3-D Deterministic Neutron Transport Code Attila To Measure Data, MCNP and MCNP-X For The Advanced Test Reactor", INL Report INL/CON-05-00662, Idaho National Laboratory, September 2005.

[71] R Pampin and M J Loughlin, "Evaluation of a three-dimensional discrete ordinates radiation transport tool for the support of iter design", *Fusion Engineering and Design*, vol. 82, no. 15-24, pp. 2008 – 2014, 2007, Proceedings of the 24th Symposium on Fusion Technology - SOFT-24.

[72] Mahmoud Z. Youssef, Russell Feder, and Ian M. Davis, "Neutronics analysis of the international thermonuclear experimental reactor (ITER) MCNP "Benchmark CAD Model" with the ATTILA discrete ordinance code", *Fusion Engineering and Design*, vol. 83, no. 10-12, pp. 1661 – 1668, 2008, Proceedings of the Eight International Symposium of Fusion Nuclear Technology - ISFNT-8 SI.

[73] P Batistoni et al., "Experimental validation of shut down dose rates - Final Report", Tech. Rep., ENEA Frascati, 2001.

[74] Y. Morimoto et al., "Shutdown dose evaluation experiment for ITER", *Fusion Engineering and Design*, , no. 69, pp. 643–648, 2003.

[75] M Angelone M Martone and M Pillon, "The 14 MeV Frascati neutron generator", *Journal of Nuclear Materials*, , no. 212-215, pp. 1661–1664, 1994.

[76] M Pillon et al., "Characterisation of the source neutrons produced by the Frascati Neutron Generator", *Fusion Engineering and Design*, , no. 28, pp. 683–688, 1995.

[77] P Batistoni and L Petrizzi, "Task T426 - Neutronics Experiments - Experimental Validation of shut down dose rates - 1st Intermediate Report on Experiment Pre-analysis", Tech. Rep., ENEA Frascati, 2000.

[78] L Petrizzi P Batistoni, M Angelone and M Pillon, "Benchmark Experiment for the Validation of Shutdown Activation and Dose Rate in a Fusion device", *Journal of Nuclear Science and Technology*, vol. 2, 2002.

[79] K Seidel et al., "Measurement and analysis of dose rates and gamma ray fluxes in an ITER shut-down dose rate experiment", *Fusion Engineering and Design*, vol. 63-64, pp. 211–215, 2002.

[80] H Freiesleben et al., "Measurements of dose rates, decay /*gamma*-rays and neutron flux", Tech. Rep., TU Dresden, Institut fur Kern und Teilchenphysik, 2001.

[81] M Tichy, "Description and Users Guide", Tech. Rep. PTB-7.2-193-1, Physikalisch-Technische Bundesanstalt Braunschweig, 1993.

[82] M Z Youssef et al., "Benchmarking the Three-Dimensional CAD-Based Discrete Ordinates Code "ATTILA" Using Integral Dose-Rate Experiments and Comparison to MCNP Results", *Fusion Science and Technology*, vol. 56, no. 2, pp. 718–725, 2009.

[83] A Borthwick et al., "Mechanical design features and challenges for the ITER ICRH antenna", *Fusion Engineering and Design*, vol. 84, pp. 493–496, 2009.

[84] A Davis, R Pampin and S Zheng, "Use of the MCR2S system for High-resolution Occupational Radiation Exposure Estimate in ITER", *9th IAEA Technical Meeting on "Fusion Power Plant Safety"*, 2009.

[85] P U Lamalle et al., "Status of the ITER IC H and CD System", *18th RF Topical Conference Proceedings*, 2009.

[86] A Davis and M J Loughlin, "Neutronics Analysis of ICRH Antenna", Tech. Rep. EFDA/06-1397 (TW6-TTMN-NAS1), UKAEA Fusion, 2007.

[87] K Vulliez et al., "Mechanical design of the ITER ion cyclotron heating launcher based on in-vessel tuning system", *Fusion Engineering and Design*, 2007.

[88] A Davis, "Preliminary Neutronic Investigation into optimum stainless steel to water ratios for ITER radiaiton shielding", Tech. Rep., UKAEA Fusion, 2006.

[89] D Lockley, "CAD Model of the ICRH EMO v2", Tech. Rep., UKAEA Fusion.

[90] J T West(III), "SABRINA: An Interactive Three Dimensional Geometry Modelling Program for MCNP^{TM}", Tech. Rep. LA-10688-M, Los Alamos National Laboratory, 1986.

[91] C Hamlyn-Harris et al., "Engineering design of an rf vacuum window for the iter icrh antenna", *Fusion Engineering and Design*, vol. 84, no. 2-6, pp. 887 – 894, 2009, Proceeding of the 25th Symposium on Fusion Technology - (SOFT-25).

[92] K J Leonard et al., "Neutron irradiation effects on the dielectric properties loss tangent of ceramic insulators", in *13 International Conference on Fusion Reactor Materials*. Nice, France, 2007.

[93] R Pampin, M J Loughlin and M J Walsh, "Radiation Transport Analyses for Design Optimisation of the ITER Core LIDAR Diagnostic", *Fusion Science and Technology*, vol. 56, no. 2, pp. 751–755, 2009.

[94] M Loughlin, "ALITE official ITER neutronics model revieved", ITER Project Office, January 2008.

[95] E Polunovskiy, "D-T neutron emission rate for standard neutron source for ITER nuclear analysis with MCNP code", Tech. Rep. INAR-005, ITER, 2008.

[96] J C Sublet, *Activation Considerations Relevant to the Decommissioning of Fusion Reactors*, PhD thesis, The University of London, 1989.

[97] R. Pampin et al., "Comparison of Global Variance Reduction methods", in *Monte Carlo Users Group Meeting*. Oxford, UK, 2009.